Tidewater glacier flow of Helheim Glacier, Greenland, 2006-2008, using high-rate GPS

Julia de Juan Verger

ADVERTIMENT. La consulta d'aquesta tesi queda condicionada a l'acceptació de les següents condicions d'ús: La difusió d'aquesta tesi per mitjà del servei TDX (**www.tdx.cat**) ha estat autoritzada pels titulars dels drets de propietat intel·lectual únicament per a usos privats emmarcats en activitats d'investigació i docència. No s'autoritza la seva reproducció amb finalitats de lucre ni la seva difusió i posada a disposició des d'un lloc aliè al servei TDX. No s'autoritza la presentació del seu contingut en una finestra o marc aliè a TDX (framing). Aquesta reserva de drets afecta tant al resum de presentació de la tesi com als seus continguts. En la utilització o cita de parts de la tesi és obligat indicar el nom de la persona autora.

ADVERTENCIA. La consulta de esta tesis queda condicionada a la aceptación de las siguientes condiciones de uso: La difusión de esta tesis por medio del servicio TDR (**www.tdx.cat**) ha sido autorizada por los titulares de los derechos de propiedad intelectual únicamente para usos privados enmarcados en actividades de investigación y docencia. No se autoriza su reproducción con finalidades de lucro ni su difusión y puesta a disposición desde un sitio ajeno al servicio TDR. No se autoriza la presentación de su contenido en una ventana o marco ajeno a TDR (framing). Esta reserva de derechos afecta tanto al resumen de presentación de la tesis como a sus contenidos. En la utilización o cita de partes de la tesis es obligado indicar el nombre de la persona autora.

WARNING. On having consulted this thesis you're accepting the following use conditions: Spreading this thesis by the TDX (**www.tdx.cat**) service has been authorized by the titular of the intellectual property rights only for private uses placed in investigation and teaching activities. Reproduction with lucrative aims is not authorized neither its spreading and availability from a site foreign to the TDX service. Introducing its content in a window or frame foreign to the TDX service is not authorized (framing). This rights affect to the presentation summary of the thesis as well as to its contents. In the using or citation of parts of the thesis it's obliged to indicate the name of the author.

Tidewater glacier flow of Helheim Glacier, Greenland, 2006–2008, using high-rate GPS

PhD Thesis
Doctoral Program of Earth Sciences

Julia de Juan Verger

Advisor: Dr. Pedro Elósegui Larrañeta
Tutor: Dr. Jaume Calvet Porta

Institut de Ciències de l'Espai (ICE)
Consell Superior de Investigacions Científiques (CSIC)

Institut d'Estudis Espacials de Catalunya (IEEC)

Unitat de Tecnologia Marina (UTM)
Consell Superior de Investigacions Científiques (CSIC)

Departament de Geodinàmica i Geofísica
Facultat de Geologia
Universitat de Barcelona (UB)

TIDEWATER GLACIER FLOW OF HELHEIM GLACIER, GREENLAND, 2006–2008, USING HIGH-RATE GPS

by

Julia de Juan Verger

PhD Dissertation
Submitted to the Geodynamics and Geophysics Department of the
University of Barcelona in partial fulfillment of the requirements for
the degree of Doctor of Philosophy

Signature:

Barcelona, January 2011

(Defense: 14 March 2011)

Contents

Acknowledgments

This thesis was completed with the support and encouragement from many people. First of all, I would like to express my most sencire gratitude to my supervisor, Pedro Elósegui. I am indebted to him for giving me the opportunity to work in this exciting team project. His expertise, enthusiasm, patient guidance, and kindness have added considerably to my graduate experience. His always positive spirit and encouraging words have been specially helpful over these four years of research.

He has also given me the opportunity to work with other exceptional researchers. I would like to thank specially Meredith Nettles and Jim Davis for their clever guidance, suggestions, and constructive criticism that always help to improve my work. Thanks to both for, together with Pedro, teaching me how to "do Science." Thanks to Meredith for her endless energy and meticulous inputs and recommendations. Thanks to Gordon Hamilton, Leigh Stearns, Morten Andersen, Tine Larsen, Göran Ekström, and the rest of the Helheim project team members, without all of whom this thesis would never have been possible. Thanks to Emma Hill for sharing with me her processing skills and for the always lovely AGU dinners. I am grateful to Meredith and Göran for hosting me at Lamont. Thanks to Pedro and Meredith for giving me the opportunity of seeing Helheim with my own eyes and collaborating in one of the field campaigns. Thanks to Meredith, Leigh, Morten, Gordon, Kristin, and Steve for the Tasiilaq experience.

Voldria expressar el meu agraïment al meu tutor, Jaume Calvet, per la seva ajuda i disponibilitat.

Vull donar també les gràcies de forma especial a l'Alberto, el Pep, el Nacho, la Laura, el Marc, el Markus, el Ferran i l'Ismael, amb els que he compartit despatx, el meu dia a dia a l'IEEC i moltes rialles. Com oblidar les llargues, i en masses ocasions surrealistes, converses a l'hora del dinar amb tots vosaltres. O el sempre simpàtic "que pasa quillo" del Nacho. Ni tampoc el "procrastination time" del Pep i l'Alberto que interrompien la meva concentració, però que, teníeu raó, han enriquit molt més, sinó la tesi, els meus dies a l'IEEC. Gràcies Laura, per compartir amb mi més d'aprop l'experiència (i els sentiments) del doctorat, també per ajudar-me en els començaments de la recerca i sempre que ho he necessitat.

També, gràcies a tantes altres persones que d'una manera o altre m'han donat el seu suport durant el desenvolupament de la tesi. Gràcies Magdalena i Quico pel vostre

interès, recolzament i consell. També, als meus amics i companys de carrera Lorena, Llucia, Víctor i Miquel. Tot i no compartir la tesi d'aprop, l'hem compartida sempre que he tornat a "sa roqueta", casi sembla que no sapiguem parlar d'altra cosa. Gràcies Lorena per compartir els nervis en els congressos de l'EGU i les passejades per Viena. Un molt especial agraïment al Javi, ets en part responsable de fins on he arribat, gràcies pel teu recolzament i per sempre interessar-te pel meu treball, aquesta tesi és en part teva.

Voldria transmetre el meu més sincer agraïment a la meva família. Al meu pare, un home de lletres, li he d'agrair que em convencés per a que jo fos una dóna de ciències. També, per sempre saber escoltar i donar consell, tranquil·litat i afecte. A la meva mare, pel seu suport i estimació incondicionals, pel seu positivisme i per la plena confiança que sempre diposita en mi. A la meva germana Claudia per intentar entendre el que faig, encara que a vegades sembli difícil, i per escoltar-me i parlar-me. Al meu germà Emili per ser el petit de la família i per ser com és.

Marc, gràcies per la nostra amistat, per alleujar els moments difícils i per compartir-ne els millors, per fer-me sentir acompanyada, recolzada i estimada en tot moment. Al teu costat sempre tot sembla més fàcil, incloent-ne l'escriptura d'aquesta tesi.

Finalment, aquesta tesi i la meva estada al Lamont Doherty Earth Observatory (LDEO) no hauria sigut possible sense el finançament d'una beca predoctoral I3P del Centre Superior de Investigacions Científiques (CSIC). La meva assistència a congressos de la European Geophysical Union (EGU) i l'American Geophysical Union (AGU), així com la meva participació en una de les campanyes de recollida de dades a Groenlàndia ha sigut possible gràcies al suport del projecte POL2006-07076 del Ministeri de Ciència i Innovació (MiCiNN). Gràcies a l'Institut de Ciències del Espai (ICE), a l'Institut d'Estudis Espacials de Catalunya (IEEC), i a la Unitat de Tecnologia Marina (UTM/CMIMA) per acollir-me durant els anys en que s'ha dut a terme aquest treball.

Abstract

Greenland's main outlet glaciers are highly sensitive to climate conditions, and have been recently observed to experience rapid dynamic changes. However, they remain poorly monitored and understood. This study presents an analysis of high-rate Global Positioning System (GPS) observations from a dense network installed at Helheim Glacier, east Greenland, during the Arctic summers of 2006–2008, that results in a new data set of glacier flow. To obtain optimal estimates of spatio-temporal variations of glacier flow, an investigation of errors of the high-rate GPS technique in glaciology is undertaken. The resulting high-precision (cm level) and high-rate (15 s) position estimates reveal the surface expression of glaciological signals, occurring from sub-hourly to daily time-scales and beyond, enabling the characterization of glacier deformation at temporal resolutions not achievable with most standard techniques employed in glaciology. Particular emphasis is placed on the study of the response of Helheim Glacier to ocean tidal forcing.

This study is part of a multidisciplinary project that investigates the dynamics of tidewater fast-flowing glaciers in Greenland using high-rate GPS along with other geophysical sensors. The new data set of glacier flow contributes to an improved understanding of Helheim Glacier in various ways. First, estimates of mean flow of Helheim Glacier during the 2006–2008 period are presented, which ranged from ∼24 m/d near the terminus to ∼4 m/d ∼37 km upglacier, with 2007 flowing faster, showing more variability, and exhibiting the largest number of glacial earthquakes. Then, sub-seasonal to sub-daily flow variations are presented. In particular, we present a detailed study of the semi-diurnal variations in the flow of the lower ∼12–16 km of Helheim Glacier due to hydrostatic pressure changes at the glacier terminus caused by ocean tides. An admittance analysis shows that the amplitude of the tidal response decays exponentially with distance from the calving front in the three components of flow, and that the response of the glacier is delayed with respect to the ocean tides by 1–2 h. Moreover, the analysis shows that the tidal response in the along-flow component is highly time varying, both on long timescales, with a non-linear response of ∼15 days periodicity, and on short timescales, with abrupt changes associated with calving events and glacial earthquakes. For example, the along-flow tidal response after a glacial earthquake increases abruptly, by a factor of as much as ∼2.5, and recovers after 1–2 days, which could be explained by the disruption of the subglacial drainage system and a concomitant reduction in flow resistance. Last, variations of Helheim Glacier's flow for two important glacier dynamic processes are also presented. These include flow variations associated with glacial earthquakes and calving events, and with the potential drainage of supraglacial meltwater lakes.

This thesis demonstrates that the analysis of the high-rate, high-precision GPS observations acquired at the surface of Greenland fast-flowing outlet glaciers provides valuable information pertaining to their dynamics, including their response to small and constant forcings, such as the ocean tide, and also to large and sudden changes in the glaciers boundary conditions, such as those related to glacial earthquakes and meltwater pulses.

List of Figures

List of Tables

Tidewater glacier flow of Helheim Glacier, Greenland, 2006-2008, using high-rate GPS

Julia de Juan Verger

ADVERTIMENT. La consulta d'aquesta tesi queda condicionada a l'acceptació de les següents condicions d'ús: La difusió d'aquesta tesi per mitjà del servei TDX (**www.tdx.cat**) ha estat autoritzada pels titulars dels drets de propietat intel·lectual únicament per a usos privats emmarcats en activitats d'investigació i docència. No s'autoritza la seva reproducció amb finalitats de lucre ni la seva difusió i posada a disposició des d'un lloc aliè al servei TDX. No s'autoritza la presentació del seu contingut en una finestra o marc aliè a TDX (framing). Aquesta reserva de drets afecta tant al resum de presentació de la tesi com als seus continguts. En la utilització o cita de parts de la tesi és obligat indicar el nom de la persona autora.

ADVERTENCIA. La consulta de esta tesis queda condicionada a la aceptación de las siguientes condiciones de uso: La difusión de esta tesis por medio del servicio TDR (**www.tdx.cat**) ha sido autorizada por los titulares de los derechos de propiedad intelectual únicamente para usos privados enmarcados en actividades de investigación y docencia. No se autoriza su reproducción con finalidades de lucro ni su difusión y puesta a disposición desde un sitio ajeno al servicio TDR. No se autoriza la presentación de su contenido en una ventana o marco ajeno a TDR (framing). Esta reserva de derechos afecta tanto al resumen de presentación de la tesis como a sus contenidos. En la utilización o cita de partes de la tesis es obligado indicar el nombre de la persona autora.

WARNING. On having consulted this thesis you're accepting the following use conditions: Spreading this thesis by the TDX (**www.tdx.cat**) service has been authorized by the titular of the intellectual property rights only for private uses placed in investigation and teaching activities. Reproduction with lucrative aims is not authorized neither its spreading and availability from a site foreign to the TDX service. Introducing its content in a window or frame foreign to the TDX service is not authorized (framing). This rights affect to the presentation summary of the thesis as well as to its contents. In the using or citation of parts of the thesis it's obliged to indicate the name of the author.

Chapter 1

Introduction

1.1 Overview

This thesis presents a study of the application of Global Positioning System (GPS) techniques to the study of the dynamics of Helheim Glacier, one of the fastest-flowing outlet glaciers in the world, located on the southeast coast of Greenland.

In this chapter we first present the background to this study reviewing the state of the cryosphere, focusing on polar ice sheets, the dramatic changes they have undergone in recent years, and their effect on global sea level rise. Then we describe the role played by Greenland outlet glaciers in the development of such changes, and we discuss several factors by which recent warming air temperatures and ocean waters have affected their dynamics. Next, we give a more extended revision of the characteristics and recent evolution of Helheim Glacier, which is the subject of this study. Subsequently, we describe the project conducted at Helheim Glacier by an international and multidisciplinary group. The project consisted in several field-based campaigns, carried out during the Arctic summers of 2006–2010, where we collected GPS measurements and additional geophysical observations. Finally, we discuss the thesis motivation and objectives, and give an overview of the structure of the thesis.

1.2 State of the cryosphere

The cryosphere stores approximately 75% of the world's freshwater (Lemke et al., 2007). It comprises snow, river and lake ice, sea ice, glaciers, ice caps, ice shelves, ice sheets, and frozen ground. The cryosphere is a natural sensor of climate variability and, in the past, has undergone significant changes over both long and short timescales. Most recently, there has been a general decrease in total ice mass coinciding with increasing summer air temperatures and warmer ocean waters, with a concomitant increased contribution of the cryosphere to sea level rise (Lemke et al., 2007). For example, the two present-day ice sheets, Greenland and Antarctica, contributed about 0.21±0.07 mm/yr and 0.21±0.35 mm/yr, respectively, to sea level rise between 1993–2003 (Bindoff et al., 2007), and constitute the largest potential source of future sea level rise. Their volumes, if melted completely, would be equivalent to ~7 m and ~57 m of global sea level rise, respectively (Lemke et al., 2007), although sea level would not rise equaly everywhere due to self-attraction and loading (e.g., Milne et al., 2009). Recent observations show that the ice-sheets contribution to sea level rise is increasing at an accelerated rate (Rignot & Kanagaratnam, 2006; Velicogna, 2009). The release of fresh water from the ice sheets to the oceans not only increases sea level, but influences the climate in a complicated manner, including coupled oceanic and atmospheric responses, such as changes in ocean circulation and variations in the fluxes of heat and fresh water to the atmosphere.

Ice sheets grow by continual accumulation of snow that, where it is not melted over the summer, forms successive layers of snow that are gradually compressed into solid ice. In its interior, ice sheets are formed of thick grounded ice that rests on more or less solid bed. The ice spreads under the force of gravity towards lower altitudes and eventually the oceans. Near the coast, flow is typically concentrated in thin, fast-flowing channels that drain the ice sheet. Such channels are either narrow outlet glaciers confined by rock margins, or fast-moving ice streams surrounded by slow-moving ice. The Antarctic ice sheet is mainly drained by ice streams that normally spread into the ocean to form extensive, floating ice shelves that are attached to the ice on land. Instead, the Greenland ice sheet is drained by fast-flowing outlet glaciers which flow into floating ice tongues, or directly into the ocean. Outlet glaciers in Greenland can flow several times faster than Antarctic ice streams. Since they are typically located at lower latitudes than Antarctic ice streams, Greenland tidewater glaciers are also more sensitive to a warming climate.

Rapid changes in the ice sheets associated with the actual climate conditions are observed mainly in coastal areas, where outlet glaciers and ice streams interact with the ocean and warmer air temperatures. These outlet glaciers and ice streams drain the Greenland and Antarctic ice sheets through ice melting and iceberg calving, which in steady state conditions balance snow input, so that the height of the ice sheet remains approximately constant. In the Greenland Ice Sheet, summer surface melt drains into the ocean either through surface runoff or subglacial channels. The latter has the potential to lubricate outlet glacier beds, increasing their flow speed. Increased ice flow, in turn, increases ice discharge to the ocean through iceberg calving, which is the other large component for outflow from Greenland. Mass loss from the Antarctic Ice Sheet takes place mostly by calving off the ice shelves and by basal melting. In contrast to Greenland, since Antarctica remains cold even in summer, very little of its mass is lost by surface melting.

Although the Greenland and Antarctic ice sheets are thickening in their interior due to relatively high rates of snowfall (e.g., Johannessen et al., 2005; Davis et al., 2005), it has been shown that losses by melting and ice discharge from outlet glaciers exceed accumulation of snowfall. The contribution of the Greenland Ice Sheet to sea level rise has more than doubled over the past decade at an accelerated rate (Rignot & Kanagaratnam, 2006; Chen et al., 2006; Velicogna & Wahr, 2006). Its mass loss increased from 90 to 220 cubic kilometers of ice per year, during the period 1996–2005, as shown by

Interferometric Synthetic Aperture Radar (InSAR) surveys (Rignot & Kanagaratnam, 2006). Measurements from the Gravity Recovery and Climate Experiment (GRACE) showed that the Antarctic Ice Sheet lost mass during the period 2002–2005 at a rate of 150 cubic kilometers of ice per year (Velicogna & Wahr, 2006). Continuous observations from GRACE over a longer time period, 2002–2009, confirmed that the mass loss from the Greenland and Antarctic Ice Sheets is accelerating at a rate of 30±11 and 26±14 Gt/yr^2, respectively (Velicogna, 2009).

Flow speed has increased for some Greenland and Antarctic outlet glaciers, followed by thinning, reduction or loss of ice shelves and floating glacier tongues (e.g., Joughin et al., 2004; Howat et al., 2005; Scambos et al., 2004; Payne et al., 2004). It has recently been noted that current models for future predictions of sea level rise do not take into account rapid dynamic changes of ice streams and outlet glaciers (Lemke et al., 2007; Milne et al., 2009). The observations that these glaciers can experience rapid changes in velocity, implies that predictions of sea level rise by current models are underestimated, and highlights the need for understanding the mechanism for fast-flowing outlet glaciers in a changing climate.

1.3 Greenland outlet glaciers dynamics

Observations indicate that the recent accelerated mass loss from the Greenland Ice Sheet is mainly due to dynamic changes at the ice sheet's outlet glaciers (Howat et al., 2005; Rignot & Kanagaratnam, 2006; Stearns & Hamilton, 2007; Howat et al., 2008). InSAR surveys confirmed that variations in total mass budget of the Greenland Ice Sheet are dominated by variations in ice discharge (Rignot et al., 2008). Indeed, during the past 1–2 decades there has been a marked increase in flow speed and rate of ice discharge from large outlet glaciers (Joughin et al., 2004; Luckman & Murray, 2005; Howat et al., 2005; Luckman et al., 2006; Stearns & Hamilton, 2007) and also smaller glaciers located in the southeast coast (Howat et al., 2008; Moon & Joughin, 2008; Murray et al., 2010). Also, observations indicate that the acceleration is expanding north (Rignot & Kanagaratnam, 2006).

Current projections of sea level rise are only based on the balance between accumulation and melting and have not taken into account rapid dynamical changes in ice flow (Alley et al., 2005a; Lemke et al., 2007). Therefore, the understanding of the mechanisms by which these glaciers are dynamically behaving and its connection to the changing climate is critical for future predictions of sea level rise.

The high-elevation interior of the Greenland Ice Sheet is growing slowly due to increased snowfall associated with higher temperatures (Johannessen et al., 2005). However, such growth is offset by mass loss from the coastal areas. Repeated laser-altimeter surveys indicate that the Greenland Ice Sheet is thinning at the coastal regions (Krabill et al., 2004). Thinning can occur by melting, either at the surface by warm air temperatures or along the submerged faces of the glaciers termini in contact with warm ocean waters. Thinning also occurs as a response to dynamic processes linked to acceleration and associated with longitudinal stretching.

Satellite observations during the last decade have shown dramatic changes in dynamics at the largest and most active outlet glaciers in Greenland, Jakobshavn Isbræ, located in the west coast (Joughin et al., 2004; Luckman & Murray, 2005), and Helheim and Kangerdlugssuaq glaciers, in the east coast (Howat et al., 2005; Luckman et al., 2006; Howat et al., 2007; Stearns & Hamilton, 2007). These three glaciers combined drain a large fraction (~28% in 2005) of the total mass discharged by the Greenland Ice Sheet (Rignot & Kanagaratnam, 2006). Typical flow speeds at the calving front of these three glaciers range between ~20–35 m/d (Joughin et al., 2004; Howat et al., 2005; Luckman et al., 2006; Nettles et al., 2008; Amundson et al., 2008; Joughin et al., 2010). Figure 1.1 shows a map of the flow speed of the Greenland ice sheet and outlet glaciers, indicating the location of these three glaciers, which recently have exhibited increased flow speeds, accompanied by thinning, and retreat of several kilometers in their calving-front position.

Jakobshavn Isbræ has received much attention during the last decade, since it transitioned from slow thickening to rapid thinning of up to ~15 m/yr in 1997 (Thomas et al., 2003; Joughin et al., 2004). These changes were associated with doubling of its flow speed, up to ~35 m/d at its terminus, and the disintegration of its floating ice tongue (Joughin et al., 2004; Luckman & Murray, 2005). Helheim Glacier experienced similar acceleration and retreat to that seen at Jakobshavn Isbræ, increasing its flow speed from ~20 m/d to ~30 m/d at its terminus from 2000 to 2005. The changes observed at Helheim Glacier were followed by Kangerdlugssuaq Glacier, which doubled its speed between 2004 and 2005 (Howat et al., 2005; Luckman et al., 2006). During this period the calving front of these two glaciers also retreated by several kilometers (Howat et al., 2005; Luckman et al., 2006). Such accelerations caused rapid ice volume loss and extensive dynamic thinning of tens of meters per year, with thinning rates increasing towards the front of the glaciers (Stearns & Hamilton, 2007). Furthermore, the changes at these two eastern margin glaciers occurred nearly synchronously, suggesting a response to a common regional forcing (Luckman et al., 2006; Murray et al., 2010). Over the same period, several smaller glaciers, particularly those located along Greenland's southeast coast (south of Kangerdlugssuaq), sped up and retreated synchronously (Rignot et al., 2004; Rignot & Kanagaratnam, 2006; Howat et al., 2008; Moon & Joughin, 2008; Murray et al., 2010). Changes were less evident further north (Stearns et al., 2005), but even in some areas such as along Greenland's northwest coast, airborne altimetry data showed substantial rates of thinning (Abdalati & Steffen, 2001; Krabill et al., 2004). The marked face of acceleration of the southeast Greenland tidewater glaciers in the early 2000s was followed after 2005 by a synchronous and widespread slowdown, accompanied by a decrease in the thinning rates, and stabilization of the terminus position, further suggesting a response to regional forcing (Murray et al., 2010). Still, Helheim and Kangerdlugssuaq glaciers continued to flow ~40 to 60% faster than in 2001 (Murray et al., 2010).

There are many evidences that during the past 1–2 decades acceleration, retreat and associated thinning have caused significant volume loss from Greenland outlet glaciers, and in turn, from the Greenland Ice Sheet that continuously feeds them and contributes to

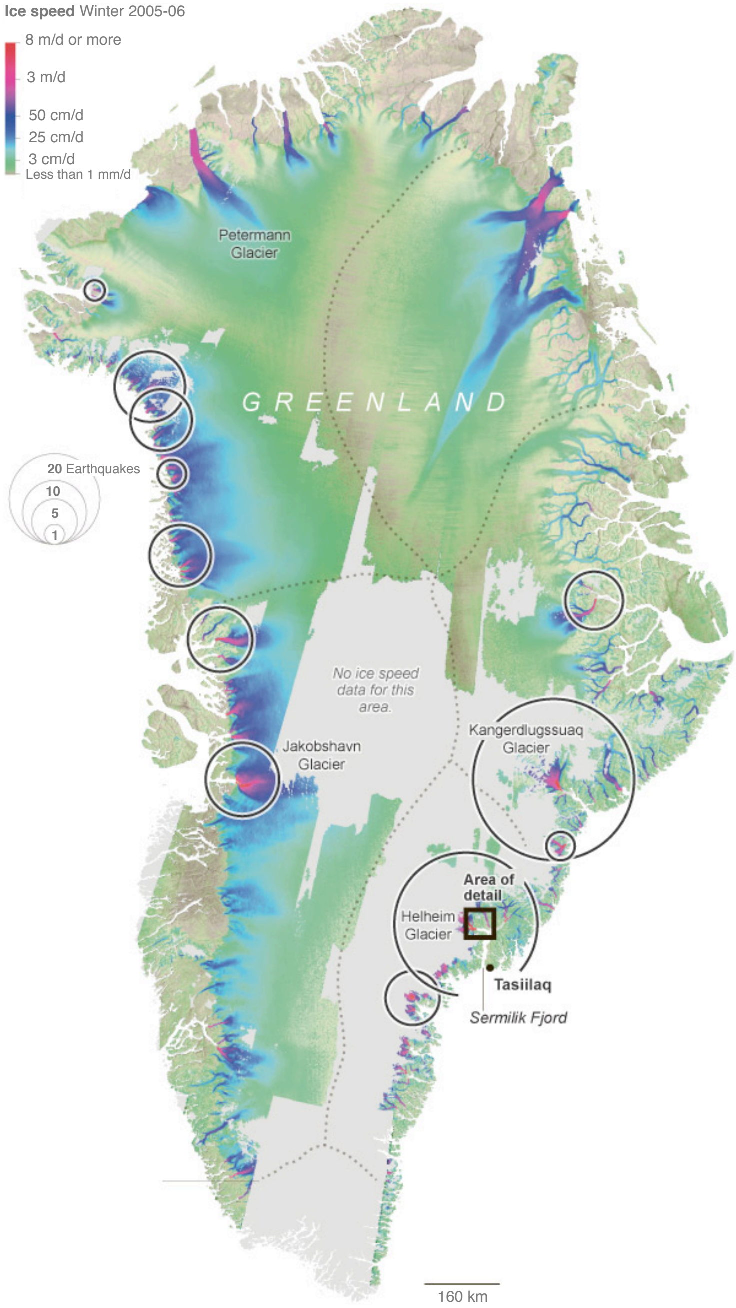

Figure 1.1: Map of Greenland showing the location of Jakobshavn Isbræ in the west coast, Kangerdlugssuaq Glacier and Helheim Glacier in the east coast, and Petermann Glacier in the north coast. Dotted lines mark the approximate location of Greenland's main ice divides (or boundaries between ice drainage basins). Colors show the flow speeds of Greenland's ice sheet and outlet glaciers for the winter of 2005–06 from RADARSAT data (Joughin et al., 2010). Circles show the number of glacial earthquakes through 2005 (Ekström et al., 2006). (Adapted from Jonathan Corum and Xaquin G.V., The New York Times, November 12, 2010).

their re-advance. The observations suggest that these glaciers can respond rapidly to variations in ocean and atmospheric conditions and associated changes in the glacier's boundary conditions. The mechanisms that cause the observed dynamic changes in Greenland outlet glaciers are still not fully understood. However, there are several processes that are believed to have an important influence on the flow speed and ice discharge of these glaciers: (1) the lubrication of the ice sheet's and the glacier's bed due to surface meltwater runoff, (2) the loss of resisting forces at the glacier's terminus due to calving front retreat, and (3) the presence of warm ocean waters in the fjords. Next, we give an overview of the effect on glacier dynamics of these three processes, which have been the subject of numerous studies during recent years.

1.3.1 Surface meltwater runoff

Surface melting caused by warmer air temperatures is responsible for a large part of the ice-sheet thinning (Krabill et al., 2004). Most of the meltwater is accumulated at the surface of the ice sheet filling crevasses, or either forming supraglacial lakes and streams, and ends up penetrating the ice sheet through surface-to-bed conduits, called moulins, or by fracture propagation of crevasses. Observations at the slow-moving ice sheet at Swiss Camp (near Jakobshavn Isbræ, in the west coast margin of the ice sheet, see Figure 1.1) revealed that the intensity of surface melting correlated with seasonal speedups of 5 to 28% (Zwally et al., 2002), indicating that meltwater accumulated at the surface, when entering the ice, is capable of reaching the bed. Lubrication of the ice-bedrock interface, as meltwater is drained to the subglacial drainage system, causes flow acceleration through increased basal water pressure, weakening the ice-bed contact, and leading to ice acceleration (Zwally et al., 2002). This process thus provides a mechanism for rapid response of ice flow to a warming climate. There is a large evidence for the occurrence of such mechanism in the ice sheet along the western margin (Zwally et al., 2002; Joughin et al., 2008a; Das et al., 2008). In summer 2006 the drainage of a large supraglacial lake (with a volume of 0.04 km^3) at the west margin of the ice sheet, on slow-moving ice, was registered to happen in less than 2 hours, leading to the ice sheet uplift and acceleration; the event lasted approximately 24 hours (Das et al., 2008). The vertical uplifts of the ice sheet coinciding with these events are indicative of changes in the basal water pressure (Zwally et al., 2002; Das et al., 2008).

It has been shown that fast-flowing outlet glaciers can also respond to fluctuations in melt (Joughin et al., 2008a; Andersen et al., 2010), although their velocity is less sensitive than that of ice sheets to enhanced meltwater input. A study on a larger region on the west margin, spanning ice sheet to outlet-glacier flow, revealed summer speedups linked to melting of 50 to 100% on the ice sheet, but of less than 15% at outlet glaciers (except for the faster flowing Jakobshavn Isbræ, whose velocity was found to be correlated with ice-front position, rather than with melt) (Joughin et al., 2008a). The rapidity of the dynamic response to these events suggests that there exists an efficient drainage conduit system that channels meltwater to the bed of the ice sheet and distributes the water subglacially (Zwally et al., 2002; Das et al., 2008).

Meltwater is at first temporally accumulated on the surface of glaciers and ice sheets. The water is stored in the firn layer (or partially-compacted layer of snow) in the accumulation zone, flowing in streams formed on the ice until they encounter a crevasse or moulin, or stored in supraglacial meltwater lakes until a connection to the englacial hydraulic system is established. It is still not well understood how surface meltwater penetrates to the bed of the ice sheet, but theoretical studies show that fracture of water-filled crevasses can rapidly propagate all the way to the bed if meltwater supply maintains the crack full of water (van der Veen, 2007; Alley et al., 2005b; Fountain et al., 2005). The englacial drainage system connects, through a series of steep conduits (Fountain & Walder, 1998), the surface of the glacier with the subglacial drainage system, formed by channelized conduits and/or linked cavity systems. The basal hydraulic system can be formed by low-pressure large channels that provide fast drainage. High discharge in such tunnels favors low pressure, so that low-discharge tunnels collapse in favor of the high-discharge ones (Röthlisberger, 1972). A different type of subglacial drainage is the one provided by distributed systems at high-pressure. Distributed systems consist of cavities that form in the lee of bedrock bumps where the ice is detached from the bedrock, and are linked by narrow passageways that provide slow drainage (Kamb, 1987).

The nature of the drainage system varies from glacier to glacier, and also within the glacier. Most likely, the drainage system is formed by a combination of both types of systems. The flow speed of the glacier and the amount of water supplied to the bed, among other factors, control which type of system is active. Both systems can be disrupted by the flow of ice, and meltwater can transition from one to the other. Transition between the two systems happens depending on the sliding speed, the bed geometry, and the water discharge (Kamb, 1987; Fowler, 1987). Such transitions are involved in the process of surging in some glaciers (Kamb et al., 1985; Kamb, 1987). Observations at glaciers in Alaska indicate that it is the increase in water supply (especially in a pulse-like mode), when it exceeds the capacity of the existing subglacial conduits, that drives the water to the linked cavity systems, filling them and thus increasing the basal water pressure, providing the mechanism for acceleration (Kamb, 1987; Bartholomaus et al., 2008). It has been suggested that such mechanism could explain the accelerations observed at Greenland outlet glaciers (Bartholomaus et al., 2008).

Recent models suggest that it is not the steady supply of large volumes of meltwater that drives glacier acceleration, but the variability in the water input (Schoof, 2010). It is the short-term increases in water input that lead to high water basal pressure and ice acceleration, while a high and steady supply of meltwater can favor channelization.

Although it has been shown that the ice sheet and glaciers respond to meltwater variability (Zwally et al., 2002; Das et al., 2008; Joughin et al., 2008a; Andersen et al., 2010), a connection between the observed dynamic changes at large outlet glaciers in Greenland and meltwater runoff has still not been shown. Instead, such glaciers seem to be more sensitive to changes in the boundary conditions at their terminus, in contact with warming ocean waters.

1.3.2 Calving front retreat

The low sensitivity of fast-flowing glaciers in Greenland to melt (Joughin et al., 2008a; Andersen et al., 2010) suggests that their recent acceleration is not dominated by an increase in meltwater runoff. Instead, observations indicate that the increase in flow speed is related to the ice-front retreat and the associated reduction in back-stress at the terminus (Joughin et al., 2004; Thomas, 2004; Howat et al., 2005; Nettles et al., 2008). A similar acceleration of ice streams in Antarctica has been observed following loss of ice-shelf buttressing (Scambos et al., 2004; Rignot et al., 2004; Dupont & Alley, 2005). Both, observations and modeling suggest that dynamic changes at Greenland outlet glaciers begin at the calving front and propagate upglacier (Howat et al., 2005; Stearns & Hamilton, 2007; Amundson et al., 2008; Nettles et al., 2008; Nick et al., 2009). Force balance analyses show that loss of ice mass at the calving front reduces the along-flow resistance generated from drag at the bed and/or the fjord walls near the terminus and concentrates the gravitational driving force over smaller area, causing glacier speedup. This acceleration causes dynamic thinning of the glacier due to longitudinal stretching, that steepens the glacier surface and further increases the driving stress, causing the acceleration to propagate upglacier (Thomas, 2004; Howat et al., 2005; Nick et al., 2009).

Iceberg calving from large outlet glaciers occurs primarily in summer (Joughin et al., 2008b; Amundson et al., 2008), because in winter the growth of sea ice strengthens the ice mélange immediately in front of the glaciers, increasing back-stress and preventing the occurrence of large calving events (Amundson et al., 2010), and because a lower level of meltwater in the surface crevasses reduces the calving rate (Nick et al., 2010). The ice mélange is formed by small and large pieces of ice calved from the glacier that are closely compacted in the glacial fjord. The main controls on calving are crevasse or fracture formation, and fracture propagation (Benn et al., 2007a; Otero et al., 2010; Nick et al., 2010). Crevasse formation is driven by the high longitudinal strain rates that fast-flowing glaciers experience associated with large-scale velocity gradients. The propagation of the crevasses responds to local stress imbalance. Other controls include melting at the submerged face of the terminus and bending in response to ocean tides (Benn et al., 2007a). Hydro-fracturing of water-filled crevasses also plays a role in some calving events (Sohn et al., 1998; Benn et al., 2007b; Otero et al., 2010; Nick et al., 2010). This is a clear mechanism by which higher air temperatures can have an impact on calving rates, and thus, glacier flow.

Observations indicate that water depth at the terminus of a glacier strongly affects its rate of calving, so that calving rate is smaller when the glacier terminates into shallow water (e.g., Meier & Post, 1987). Therefore, when glaciers retreat over bathymetric depresions, such as those caused by moraine sedimentation, they tend to increase their rate of calving as they retreat into deeper waters, causing rapid retreat, until they calve back to shallow waters. This constitutes a classic pattern whereby tidewater glaciers undergo cycles of slow advance followed by rapid retreat. However, recent models have investigated crevasse-depth calving criteria (Benn et al., 2007b; Otero et al., 2010; Nick et al., 2010). In such models the rate of calving is controlled by the penetration of surface, or surface and basal crevasses, which in turn depends on longitudinal strain rates and the water level in the surface crevasses. These models, which unlike height-above buoyancy calving models, apply to floating and grounded termini, suggest that basal topography is not as a controlling factor on calving as previously thought, and that terminus stabilization can be achieved on a reverse bed slope (Nick et al., 2010). They also provide better explanation for the seasonal variation in terminus position of Greenland outlet glaciers, which is mainly controlled by seasonal variations in surface melting and in concentration of sea ice in front of the terminus (Nick et al., 2010).

Two types of icebergs are calved off from the large Greenland outlet glaciers: large (km-scale) tabular icebergs associated with floating ice fronts, and slab-like icebergs (∼100 m in the along-flow direction) associated with grounded termini that are unstable and overturn shortly after calving (Joughin et al., 2008b). The calving and overturning of the latter type of icebergs has been associated with glacial earthquakes (Joughin et al., 2008b; Nettles et al., 2008; Amundson et al., 2008).

Data from the global seismic network (GSN) revealed a previously unknown kind of non-tectonic teleseismic earthquakes located beneath several large tidewater glaciers in Greenland, Antarctica, and Alaska (Ekström et al., 2003, 2006; Tsai & Ekström, 2007). These so-called "glacial earthquakes" are characterized by large seismic magnitudes (between 4.6 and 5.1) and, unlike tectonic earthquakes, long-period waves (35–150 s). During the period from 1993 to 2005, 184 glacial earthquakes were detected in Greenland. The number of events per year began to increase in 2002, with 2005 producing more events than the combined 1993-to-1996 total. Furthermore, there is a strong seasonality in the rate of occurrence of these events. They occur in each month of the year but are more frequent during late summer months. The seasonality and increasing frequency of glacial earthquakes, and its coincidence with the changes in behavior of Greenland outlet glaciers, suggested a connection between these two mechanisms (Ekström et al., 2006). Modeling showed that these earthquakes could be generated by large and sudden glacial-sliding motions (Ekström et al., 2003, 2006; Tsai & Ekström, 2007). However, the occurrence of such displacements has been discarded by observations (Nettles et al., 2008). Instead, the earthquakes have been shown to be temporally linked to calving of large slab-like icebergs that roll when they calve (Joughin et al., 2008b; Nettles et al., 2008; Amundson et al., 2008; Nettles & Ekström, 2010), suggesting that the earthquakes are generated by the calving process. Although the mechanism by which they arise is not fully understood yet, several models that involve the interaction of such icebergs with the Solid Earth at the sea bed of the fjord have been proposed (Tsai et al., 2008). Step-wise increases in glacier speed have been observed coincident with such calving events (Nettles et al., 2008), demonstrating that these glaciers can respond nearly instantaneously to a change in their boundary conditions.

1.3.3 Glacier-ocean interaction

New observations highlight the importance of warm surface ocean waters for their contribution to ice mass loss from outlet glaciers in Greenland. Such warm waters, when entering the glacial fjords become in contact with the glaciers termini. Warm waters influence the glacier's dynamics through melting beneath floating tongues and submerged faces of the glaciers termini (Holland et al., 2008; Rignot et al., 2010). They also play a role in triggering the disintegration of the calving front and the ice mélange that forms in front of these tidewater glaciers, that in turn affect their dynamics through reduction of the back-stress (Motyka et al., 2003; Nick et al., 2009; Amundson et al., 2010). And they also cause changes in water circulation within the fjord (Motyka et al., 2003).

Hydrographic data showed that the changes at Jakobshavn Isbræ that initiated after 1997 were most likely triggered by the arrival of warm waters into the glacial fjord (Holland et al., 2008). Such warm waters were originated from the Irminger Current (IC) and probably caused the melting and disintegration of the floating ice tongue. The IC is a branch of the North Atlantic Current carrying warm, high-salinity waters that travel from the southwest coast of Iceland southwards along the southeast coast of Greenland, and northwards along its southwest coast. A study at outlet glaciers in the central west coast revealed that summer submarine melting rates were two orders of magnitude larger than surface melting, but comparable to rates of ice discharge through calving (Rignot et al., 2010), identifying this mechanism as an important factor for Greenland glaciers destabilization. Measurements at Helheim Glacier's fjord, in the east coast, during summer 2008 also revealed the presence of subtropical waters throughout the fjord, suggesting that submarine melting at the glacier terminus has played a role in the recent acceleration of outlet glaciers in this region (Straneo et al., 2010).

Murray et al. (2010) showed that the synchronous acceleration of glaciers located in the southeast coast of Greenland coincided with the weakening of the East Greenland Coastal Current (EGCC), and subsequent arrival of warm, high-salinity, subtropical waters from the IC. The EGCC is a cold, fresh water current that starts at approximately the latitude of Kangerdlugssuaq Glacier (see Figure 1.1) and travels southwards along the coast. This ocean current has an important contribution of water input from the ice sheet, both from meltwater runoff and iceberg calving. The slowdown that followed in 2006, accompanied by a decrease in thinning rates and re-advance of the calving front, occurred synchronously throughout the southeast coast when the EGCC was reactivated after 2005. Murray et al. (2010) hypothesized that the acceleration, thinning, and retreat of the glaciers was partially responsible for the synchronous slowdown of the glaciers. The dynamic processes at these outlet glaciers caused an increase in the fresh, cold water discharge to the ocean, that was likely partially responsible for the re-strengthenning of the EGCC after 2005, which resulted in the slowdown. This relationship between the EGCC strength and the glaciers runoff, would act as a negative feedback that prevents the outlet glaciers against continued acceleration and fast loss of ice, re-stabilizing the dynamics of the glaciers if their discharge increases substantially.

Although also of oceanographic origin, ocean tides represent a different type of interaction (i.e., periodic forcing) between tidewater glaciers and the ocean. Not only can the terminus of some tidewater glaciers be floating and thus vertically responding to ocean tides, but also the flow velocity of some tidewater glaciers is modulated in a regular way by ocean tidal forcing at the terminus on both sides of the grounding line (Anandakrishnan et al., 2003; Gudmundsson, 2006; Murray et al., 2007; de Juan et al., 2010b). In this thesis, such dynamic responses are subject to detailed analysis at Helheim Glacier. The effect of the ocean tides on tidewater glacier flow is expanded on Chapter 4.

1.4 Helheim Glacier

This thesis focuses on the study of the dynamics of Helheim Glacier during the period 2006–2008. Here we introduce Helheim Glacier, its characteristics, and the changes it has undergone during the last few years.

Helheim Glacier is the third largest fast-flowing tidewater glacier in Greenland and is responsible for a significant fraction of the mass loss from the Greenland Ice Sheet through calving. The glacier is located on the southeast coast (66.4°N, 38.5°W), and drains its icebergs to the Atlantic Ocean (see Figure 1.1). The 100-km-long Sermilik Fjord connects Helheim Glacier with the Atlantic Ocean (Figure 1.2). The glacier is about 7-km wide at its terminus, flows from northwest to southeast, with its main trunk following a bend marked by the glacier margins of approximately 135 degrees. It has two main tributaries, the one feeding the main trunk from the south is larger and flows relatively fast, the smaller one entering from the north flows much slower (Howat et al., 2005). There is a bathymetric depression of $\sim$200 m in height at the fjord bedrock below the region where the calving front has been fluctuating during the past decade (see Figure 1.3) (Gogineni et al., 2001; Howat et al., 2007), that has likely played a role on the recent retreat of the glacier (Howat et al., 2007; Joughin et al., 2008b; Howat et al., 2008). However, models also show that the retreat and advance of Helheim Glacier, and specially its seasonal variation, can not be solely controlled by the bed topography, rather also by factors controlling the propagation of basal and surface crevasses, like variations in surface melting and in back pressure provided by concentration of sea ice in front of the glacier terminus (Nick et al., 2009, 2010).

The glacier has experienced significant changes during the last decade. It has undergone periods of extensive retreat, acceleration, and thinning (Howat et al., 2005; Rignot & Kanagaratnam, 2006; Stearns & Hamilton, 2007), synchronously to the changes observed at Kangerdlugssuaq Glacier and other southeast outlet glaciers in Greenland. The mass balance of Helheim Glacier decreased from positive ($\sim$4 km^3 ice/year) during the period 1996–2000 to negative (-12 km^3 ice/year) in 2005, which represented 5% of the Greenland Ice Sheet total mass loss during that year (Rignot & Kanagaratnam, 2006). The glacier spedup at its terminus from 22 m/d to 30 m/d between 2000 and 2005 (Howat et al., 2005). During this same period, the calving front position retreated by about 7.5 km, as the terminus moved over the reverse slope of the bedrock over-deepening and

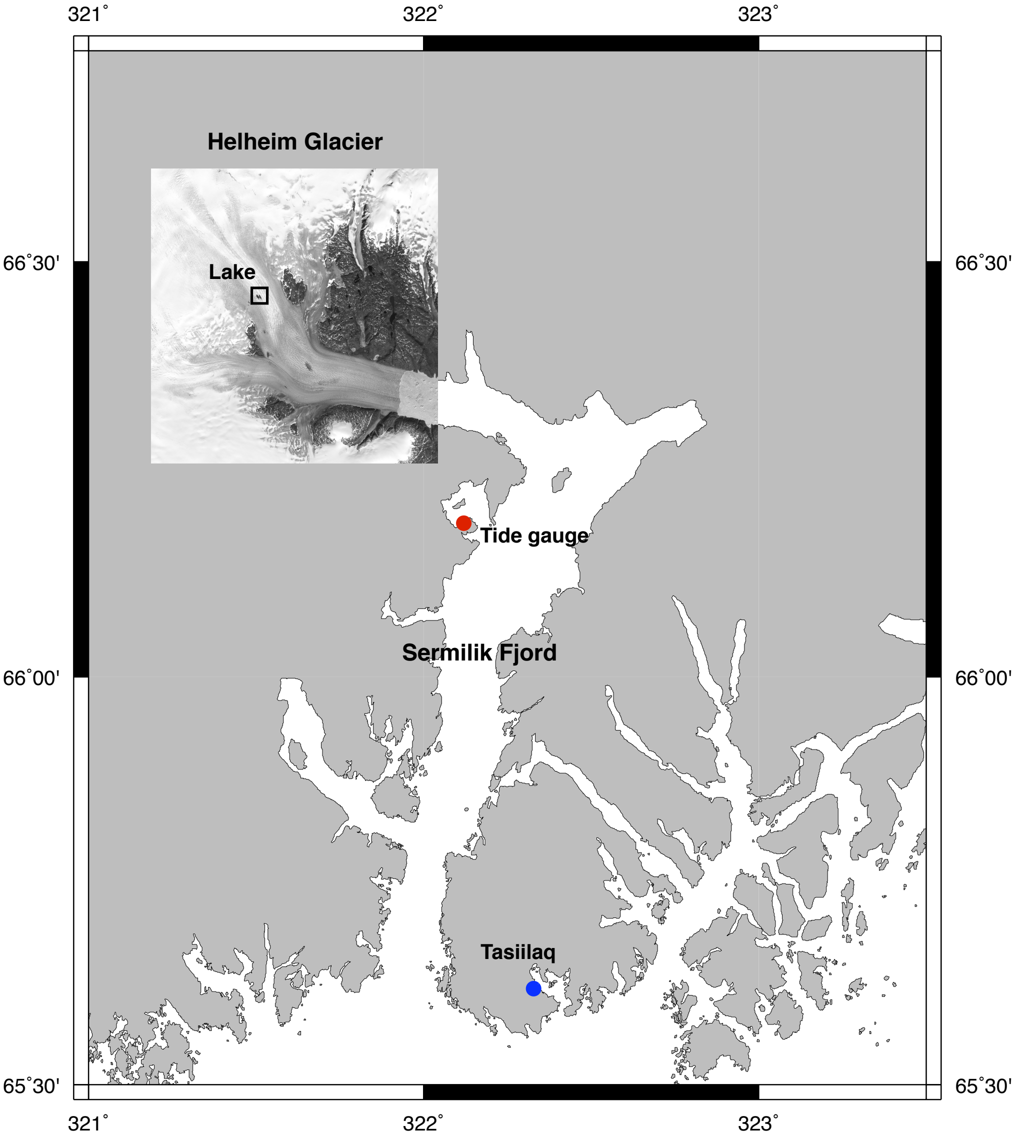

Figure 1.2: Landsat satellite image of Helheim Glacier overlain on a map of Sermilik Fjord. The locations of the town of Tasiilaq, a water-pressure tide gauge deployed in the fjord, and a meltwater lake on the surface of the glacier were also a water-pressure gauge was opearted (referred to later in the text) are indicated.

thus into deeper water. Most of the changes at Helheim Glacier took place during the summer of 2003, and during 2005 (Howat et al., 2007), coinciding with the presence of warm ocean waters in southeast Greenland fjords (Murray et al., 2010). Large thinning rates coincided with the periods of maximum retreat, with a mean of 44 m/yr between 2002–2003, and 60 m/yr between 2004–2005 on the region within 20 km from the ice front (Stearns & Hamilton, 2007). Figure 1.3 shows the elevation profile of the lower ∼13 km of the glacier at several times during 2001–2006, and the bed elevation below the

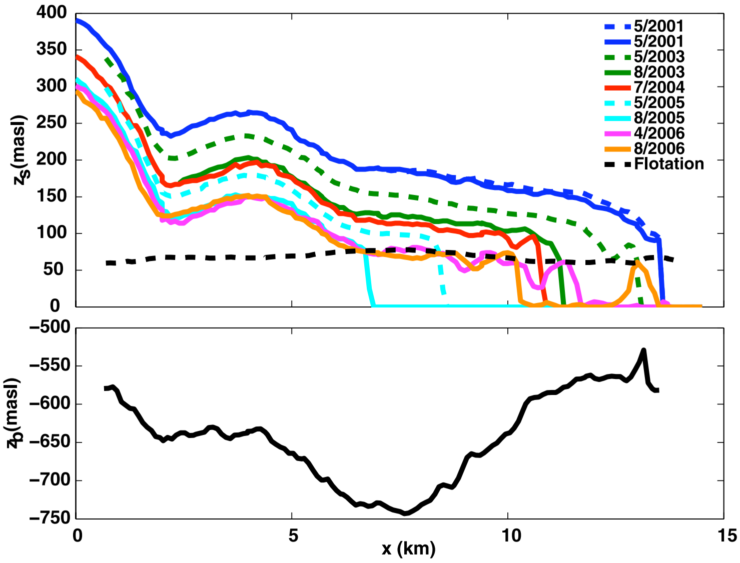

Figure 1.3: (Top) Elevation profile of the lower, west-east section of Helheim Glacier, in meters above sea level (masl), for several time periods between 2001 and 2006. A black dashed line shows the flotation threshold, below which the ice is floating. (Bottom) Bed elevation showing the bathymetric depression below the glacier (from Joughin et al. (2008b)).

glacier. During the period 2000-2005 the front of Helheim appears to have been grounded (Rignot et al., 2004; Howat et al., 2005; Joughin et al., 2008b). In 2001 the glacier was 100-m above the flotation thickness (Howat et al., 2007; Joughin et al., 2008b). However, the large retreat in 2005 moved the calving front past the bathymetric depression in the bedrock topography, which added on to the high thinning rates caused the terminus to be at or near flotation.

This period of rapid changes at Helheim Glacier and increased ice discharge was likely driven by the ocean-glacier interaction, through the weakening of the EGCC, that transports cold water along the coast and within the fjords, which allowed the entrance of warm waters from the IC in the fjord. In 2006, when the glacier had retreated over the other end of the bedrock over-deepening and thus into shallower waters, it decreased its rate of thinning, slowed down, and readvanced. In 2006, after 5 years of increasing ice discharge, the glacier's mass balance returned to 2000 values (Howat et al., 2007). The glacier's front probably re-grounded on the other end of the bathymetric over-deepening by the end of summer 2006, mantaining a stable position for the latter part of 2006. At the same time, flow speeds upglacier were mantained to high values, resulting in a compressional flow zone behind the terminus and thus causing thickening of the glacier (Joughin et al., 2008b). The slowdown, thickening, and re-advance observed after 2005 happened synchronously at other tidewater glaciers in the east coast, south of Kangerdlugssuaq Glacier, and coincided with the re-strengthening of the EGCC (Murray et al., 2010). Such slowdown of the glaciers in the southeast Greenland sector lasted at least until 2008. However, during July and August in 2007, Helheim Glacier, unlike the rest of glaciers, experienced a slight reactivation, possibly related with high ocean temperatures registered during this period offshore of Greenland, between Iceland and Greenland (Murray et al., 2010).

The acceleration and retreat of Helheim Glacier coincided with the increase in number of glacial earthquakes located at this glacier, that escalated from 1 in 1993 to 12 in 2005 (Tsai & Ekström, 2007), however the glacier produced no earthquakes during 2006 (Nettles et al., 2006). During the retreat of the terminus in the period 2001–2005, nearly all of the calving episodes observed in satellite images coincide (within 24 hours) with the times of one or more glacial earthquakes (Joughin et al., 2008b). In 2006, when no glacial earthquakes were detected at Helheim, the front of the glacier was close to flotation and produced tabular-like icebergs, suggesting that glacial earthquakes were associated with non-tabular icebergs that overturn when they calve (Joughin et al., 2008b). Some of the tabular-like icebergs have been also observed in winter or early spring, suggesting that the glacier develops a short floating tongue during these periods. Also, the calving front position seems to be stable during winter or slightly advancing, with most of the retreat taking place between May and September (Joughin et al., 2008b). The seasonal variation in terminus position is possibly regulated by the sea ice extension and strength of the ice mélange (Amundson et al., 2010), and less presence of meltwater in surface crevasses (Nick et al., 2010)

Modeling also suggests that Helheim Glacier adjustes very rapidly to changes in its boundary conditions at the calving front, where dynamic changes of this glacier are originated, propagating then upglacier through dynamic coupling (Nick et al., 2009).

Helheim's dynamics seems to have a high sensitivity to sea surface and atmospheric temperature. As indicated above, its periods of acceleration and deceleration during 2000–2008 coincided with the presence in Sermilik Fjord of warm waters from the IC and cold waters from EGCC origin, respectively. Oceanographic data collected in Sermilik Fjord in summer 2008 revealed the presence of subtropical waters throughout the fjord (Straneo et al., 2010), suggesting that warm ocean waters are still a controlling factor for the glacier's dynamics. These waters are advected from the shelf adjacent to the fjords and renewed through wind-driven exchange. Their temperature and circulation indicate that they cause enhanced submarine melting at the tidewater margin of Helheim. Also, its recent epoch of substantial retreat occurred when temperatures recorded at Ammassalik ($\sim$100 km from Helheim) were above mean, and during its subsequent re-advance in 2006 summer temperature was lower than the 2002-2005 mean (Joughin et al., 2008b).

To address the dynamics of Helheim Glacier in high detail we use data from a GPS network that we operated on the surface of the glacier continuously for various periods of time during the summers of 2006–2008. The high precision of high-rate GPS observations collected on the surface of water-terminating glaciers enables the study of sub-daily deviations from mean flow, such as glacier response to ocean tides, and sub-daily changes in glacier velocities related to processes involving meltwater runoff or large-scale calving events.

Among the overall findings of the Helheim Glacier project, some of which represent the core of this thesis, are that (1) the lower part of the glacier presents semi-diurnal flow variations due to the hydrostatic pressure changes at the glacier's terminus caused by ocean tides (de Juan et al., in preparation(a)), (2) large-scale calving events and glacial earthquakes are linked to step-wise speed increases of the glacier of up to ∼18% (Nettles et al., 2008) and sudden increases in tidal response by a factor of as much as ∼2.5 (de Juan et al., 2010b), (3) velocity variations of up to ∼5% are correlated with melt fluctuations with a 1-day time lag (Andersen et al., 2010), and (4) the drainage of supraglacial lakes can cause the uplift and acceleration of the glacier (de Juan et al., in preparation(b)).

1.5 The Helheim Glacier project

The discovery of glacial earthquakes and their relation to glacier flow and climate motivated the consolidation of a multidisciplinary project to study the behavior of large tidewater glaciers in East Greenland. This project involves scientist experts in Glaciology, Seismology, Geodesy, and Meteorology from several institutions in the United States, Denmark, and Spain. (See Nettles et al. (2008) and/or de Juan et al. (2010b) for project participants and project support.) During the Arctic summers of 2006–2010, we carried out extensive field campaigns at Helheim Glacier to record with high spatio-temporal resolution the dynamics of the glacier. The spatial coverage of the networks we deployed on this highly-crevassed, fast-flowing glacier surface, and the time duration of glacier monitoring make this experiment a world first of its kind.

1.5.1 Motivation

When this project was conceived, glacial earthquakes were believed to be caused by large, sudden, and short-lived glacier-sliding motions. In order to test this hypothesis, high temporal resolution data of glacier motion was needed. Satellite observations, widely used for observations of glacier dynamics, provide high spatial resolution, but lack temporal resolution since images can be taken at most once or twice every day, depending on the platform and sensor, and on atmospheric conditions. Global Positioning System (GPS) measurements can provide high-rate position estimates with high accuracy (cm-level). This project was designed to collect GPS data, among other geophysical measurements, at several locations on the surface of a large outlet glacier in Greenland during boreal summer seasons. The investigation of the physical mechanism triggering glacial earthquakes, combined with the increasing interest in Greenland tidewater glaciers dynamics, and its connection with climate change motivated the consolidation of this multidisciplinary project.

The aim of the project is to improve our understanding of the dynamics of large tidewater glaciers in Greenland and their response to climate change by monitoring the surface ice velocity. The main objectives are (1) the characterization of the mean flow of the glacier and its variability from monthly to seasonal timescales; (2) the study of the rapid changes in glacier dynamics and the timescale in which they occur; in particular, the characterization of the physical mechanism involved in a glacial earthquake event and its effect on the dynamics of the glacier; and (3) the analysis of sub-daily to monthly changes in glacier flow associated with ocean tides, melt variability, and other external forcings.

Helheim Glacier was selected for this project for several reasons. It has a recent history of rapid change though, unlike Jakobshavn Isbræ, the dynamics of Helheim Glacier had not been studied before with ground-based techniques; it had a high productivity of glacial earthquakes in the period 1996-2005 (12 earthquakes were detected at Helheim Glacier during 2005); and it is logistically less complex than other glaciers, since it is at a relatively short distance from an airport connected to Iceland and a regional heliport located in the largest East Greenland town, Tasiilaq (∼2000 inhabitants) (see Figures 1.1 and 1.2).

The project represents the first long-term occupation of a Greenland outlet glacier by a GPS receiver network, and addresses questions of flow variation on earthquake to interannual timescales.

1.5.2 GPS networks

During 2006–2010 we deployed a network of continuously recording GPS receivers at Helheim Glacier, along with a variety of auxiliar geophysical sensors including water-pressure sensors, seismic instrumentation, time-lapse cameras, and automatic weather stations. Most of these measurements took place for periods of ∼2 months during the Arctic summer seasons. However, starting in 2008, we also deployed a network of single-frequency GPS systems to operate year-round. We also deployed a mix of single and dual-frequency receivers in Kangerdlugssuaq Glacier in 2008–2009. This thesis focuses on the analysis of the data acquired from the GPS network and water-level sensors operated during summer seasons of 2006–2008 at Helheim Glacier, thus this will be the focus of this section.

The continuously recording network of GPS receivers provide high-rate position measurements of the glacier's surface motion. The networks deployed during summers 2006–2008 comprised a series of 12–23 geodetic-quality, high-precision GPS systems distributed at several locations on the surface of the glacier's main trunk (and in some cases on the main tributary), and 2–3 systems at nearby locations on the glacier margins that serve as static reference stations. Appendix A contains specifications for the GPS systems deployed, and Appendix B contains a list of the sites deployed in each of the summer campaigns. Figures 1.4–1.6 show the location of the GPS systems on ice and bedrock at Helheim Glacier for each of the observing periods in 2006–2008, respectively.

The GPS receivers on the glacier surface spanned a distance of 1–30 km behind the calving front, with positions both on and offset from the center flowline of the glacier. They recorded observations every 1–5 seconds continuously during the duration of the campaigns, a limitation imposed by the storage capacity of the receivers. The reference static stations were deployed on nearby rock sites (see Figures 1.4–1.6). Reference stations NUN1 and NUN2 were assembled every summer at a location between the upstream and downstream ice stations, on the southern and northern margins, respectively. A permanent station, HEL1, is located closer to the downstream ice stations on the northern margin, and was used as reference site for the project during summer 2006. Another permanent station, HEL2, located very near to the location of HEL1 was used as reference site in summer 2008. All the GPS systems involved geodetic-quality, dual-frequency receivers and geodetic-quality antennas. Photovoltaic panels and batteries provided power supply to the systems. (See Appendix A for details on the systems.)

The glacier presents high flow speeds and high longitudinal strain rates since it flows faster at the terminus than further upglacier, thus the surface of the glacier is highly crevassed, specially near the terminus. Also, there is a high deformation zone near the glacier bend, caused by an important change in the glacier's bed slope and flow speed. The harsh environment on the surface of the glacier makes the deployment of the GPS systems extremely difficult. The systems have to be deployed on spots where a helicopter can land, since this is the only way of accessing the glacier surface. The deployment and retrieval of the instruments is controlled by crevasse visibility. For safe landing of the helicopter, the glacier surface must be relatively free of snow, which limits the time of deployment and retrieval to the Arctic summer seasons. The GPS receivers that were deployed on the glacier surface were secured on the ice surface by anchoring the different components (GPS antenna and box with receiver, batteries, and solar panels) to a pole drilled a few meters deep in the ice (see Figure A.1). Also, the surroundings of a GPS antenna can suffer high deformation after its deployment, therefore some antennas can turn sideways, partially sink into meltwater, or fall in a crevasse, which can highly affect the quality of the data or even cause data loss. For this reason we carried out mid-campain field visits to perform maintenance work on the GPS systems, and in some cases to retrieve or relocate them further from the calving front in order to prevent GPS loss to calving. The data from the GPS systems was manually downloaded on maintenance and retrieval visits.

We deployed a total of 20, 12, and 23 systems on the glacier surface in 2006, 2007, and 2008, respectively (see Figures 1.4–1.6). In 2006, the sites were distributed mostly upstream, spanning ∼20 km from a point ∼15 km behind the calving front (sites IS01–IS19), in a relatively slow-moving and slightly deformed section of the glacier. These sites operated for a period of maximum 60 days, from June 29 to August 28 (days of year 180–240). Most of the sites went off after a few days following their deployment due to power supply problems that were fixed in a maintenance visit on days 204–209. These power problems caused many data gaps during the entire campaign for some of the stations. Sites IS03, IS05, IS09 and IS18 were retrieved in the mid-campaign visit. Because it was our first experiment and we did not want to risk the equipment, we only operated some sites near the terminus (up to ∼8 km behind the calving front) during two short-time periods (2 sites, SN03 and SN04, during days of year 204–205; and 4 sites,

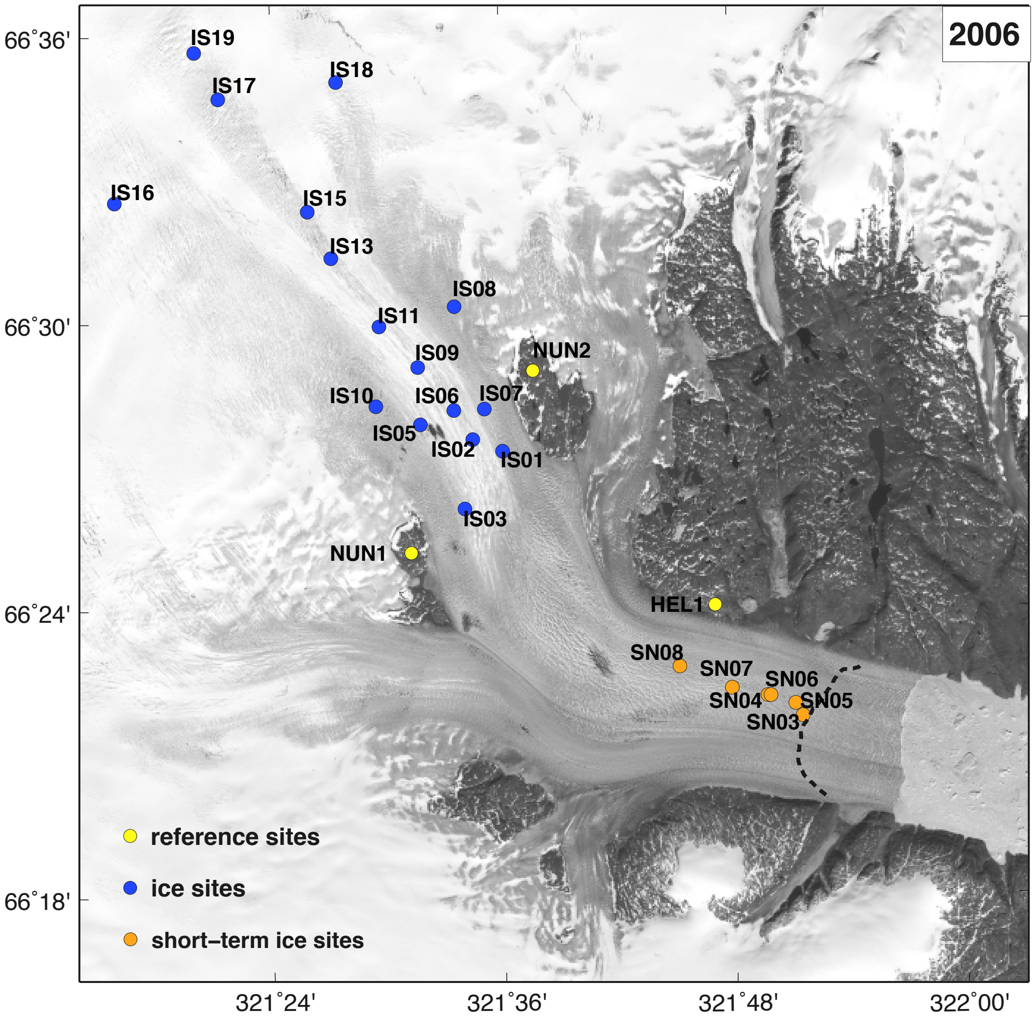

Figure 1.4: Deployment locations of GPS stations at Helheim Glacier in the summer of 2006, overlain on a 2001 LANDSAT image. A black dotted line shows the approximate position of the calving front on August 30.

SN05–SN08 during the period 238–241).

Building on the experience acquired during 2006, in summer 2007 we were able to obtain a higher quality data set. As a result of the knowledge on the velocity of the glacier and its surface deformation gained from the 2006 observations, we could distribute the GPS sites along the entire length of the glacier and closer to the calving front. In addition, we ruggedized the systems after the lessons learned in the field during 2006, which resulted in a 2007 data set significantly more complete than in 2006. We used the same locations for the static sites as in 2006. In this case all of the sites were deployed for a period of ~50 days, from July 4 to August 24 (days of year 185–236). However, the four stations installed closest to the calving front (IS20–IS23) were repositioned

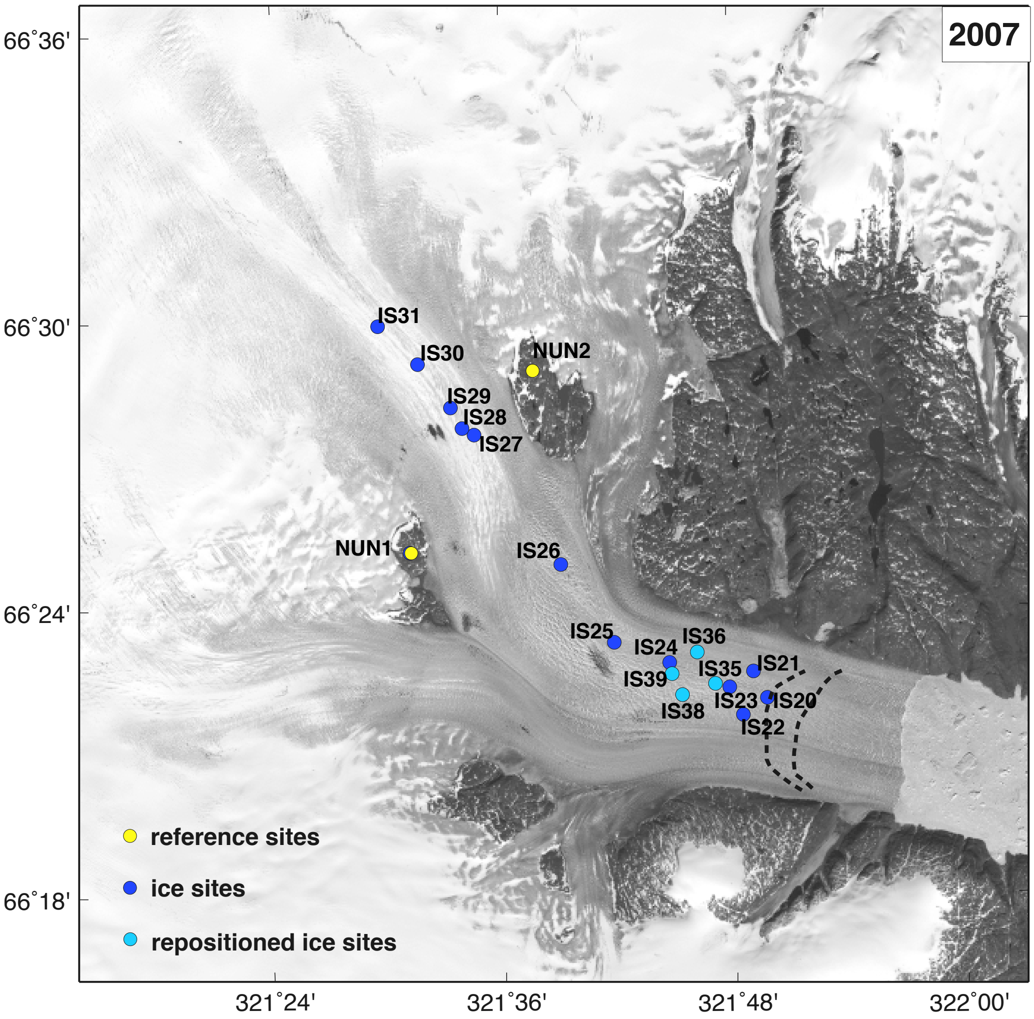

Figure 1.5: Same as in Figure 1.4, except here for 2007. Dotted lines show the terminus position at two times during the summer (easternmost line, July 4; westernmost line, August 24).

∼3 km upglacier in a mid-campaign field visit on day 207 (and renamed to IS35–IS39, respectively) to prevent receiver loss to calving. Also, at the same time, site IS24 was retreived.

In 2008, most of the site locations from 2007 were roughly re-ocupated, and some new locations were added: two sites were deployed in the downstream area (IS46 and IS47), one more in the area near the bend in the glacier (IS60), two other sites in the upstream area furthest from the calving front (IS54 and IS55) where some sites were placed in 2006, and finally 6 sites were deployed along the main tributary (IS48, IS49, and IS56–IS59). The length of this campaign season was ∼50 days, from June 27 to August 20 (days of year 179–233). Most of the sites operated continuously for the majority of this period.

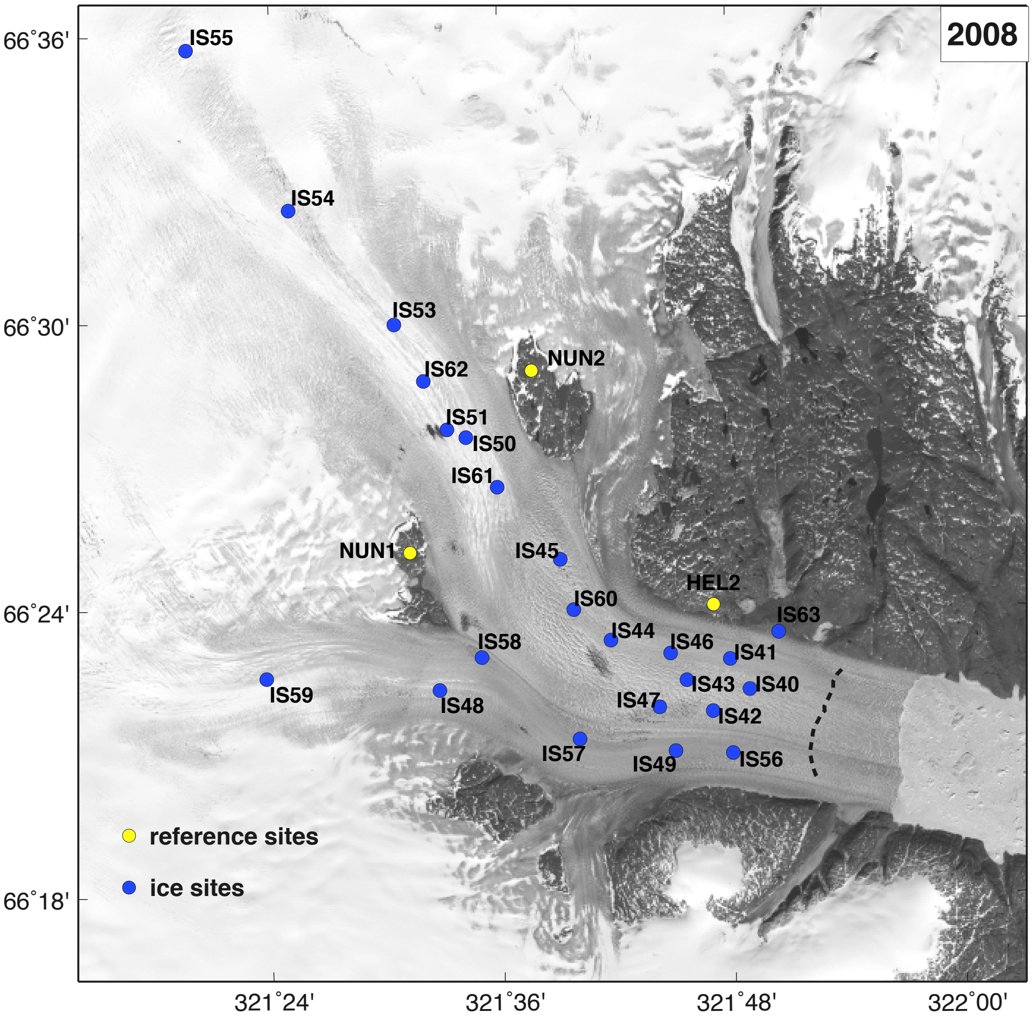

Figure 1.6: Same as in Figure 1.4, except here for 2008. Dotted line shows the position of the calving front on July 31.

However, IS40 was retrieved on day of year 207 (i.e., July 25, 2008) and some sites (IS56, IS46, IS54) were retrieved in a mid-campaign field visit during days 211–213, but were not repositioned. Site IS63 was deployed at this time and operated until the end of the season.

With the intention of extending our observing period over winter and to reduce time of deployment of the GPS systems, as part of this multidisciplinary project, we developed an accurate, robust, and inexpensive polar GPS system (Elosegui et al., 2008). We sought a system that was robust and lightweight to facilitate its deployment and retrieval, and thus reduce costs and maximize safety. At the same time, we wanted the system to be low-cost since, owing to the high flow speed and deformation rates of the glacier, it is possible for unattended equipment to be destroyed. Finally, in order to download data remotely, we provided the systems with two-way radio communications. This allowed us, starting in summer of 2008, to have some systems deployed on the glacier surface throughout the year, downloading the data via satellite link (Elosegui et al., 2009). The data acquisition from these systems is limited by daily insolation and snow cover. The systems shut down in the fall and wake up again in spring, when snow melts and insolation increases. For the systems to be low-cost, we restricted them to single-frequency (L1-only) capability, and thus they are more sensitive to potential ionospheric errors, compared to the rest of systems deployed during the summer, which are dual-frequency. A software for processing single-frequency data is currently under development, thus the analysis of the data collected by these new systems is out of the scope of this thesis.

1.5.3 Complementary geophysical observations

To complement the GPS estimates we also used several geophysical sensors, which we describe here. During most parts of the GPS observing period, we also operated a water-pressure gauge in a Sermilik Fjord cove, at a distance of ∼35 km from the glacier terminus (see Figure 1.2), to obtain a record of ocean tide heights. The pressure gauge had a nominal mm-level resolution and was operated to acquire one observation every minute. The pressure gauge operated continuously, except for some (sometimes fairly significant) hiatus due to battery failure. The gauge operated during days of year 203–221 in 2006, 186–218 in 2007, and 183–202 and 213–238 in 2008. It recorded a predominant semi-diurnal tidal variation at Sermilik Fjord and a fortnight variation ranging between ∼3 m (spring tide) and ∼1 m (neap tide) amplitude, peak-to-peak.

In summer 2009 a water-pressure gauge was operated as well in a large meltwater pond which forms every year at a location on the glacier surface in the upstream region (see Figure 1.2), and has been known to drain in several occasions. The water-pressure gauge, which has similar characteristics to the ones used in the fjord except that it is intended for freshwater, recorded the water level of the lake from its deployment on day of year 178 (June 27) until it drained on day 217 (the tide gauge was found lying on ice at a time when the melt pond had drained). (More specifics on these instruments can be found in Appendix A.)

We use satellite imagery from the Helheim Glacier region to monitor the position and geometry of the calving front and the presence of meltwater ponds on the glacier surface. We use cloud-free, visible-band images from the Moderate Resolution Imaging Spectroradiometer (MODIS), acquired by NASA's Terra and Aqua satellites, to digitize the position of the calving front with 250-m spatial resolution at daily intervals when atmospheric conditions allow it. The different spectral signature of glacier ice and the iceberg–sea-ice mélange allows to determine the boundary between the two surfaces. Also, MODIS images are inspected to detect the presence of supraglacial melt ponds.

We installed several time-lapse cameras on the glacier margins with viewing range of the calving front, taking pictures typically once every 4–8 minutes. We use these images to document calving events with higher temporal resolution than that provided by satellite imagery (Hamilton et al., 2008).

We also use data from the Global Seismographic Network (GSN), filtered in the 35–150 s period range, to detect glacial earthquakes located at Helheim Glacier throughout the duration of the project, using the approach of Ekström (2006). Some glacial earthquakes are too small for detection with this standard algorithm, thus we also inspect the GSN array stacks in an interactive mode to identify such earthquakes (M. Nettles, private communication).

A variety of other measurements, of great interest to the project but not direct application to this thesis, were performed at Helheim Glacier during the same time period. For example, regional broadband seismic stations were operated on the nearby locations of Tasiilaq, Kulusuk, and Isortoq (90–100 km from the glacier), and also on the glacier margins in subsequent years, to constrain the details of the glacial earthquakes source process. The glacier ice surface was also mapped using airborne laser altimetry in summer 2007. In 2006 weather data was obtained from an automatic weather station (AWS) in Tasiilaq. During following years, we installed a AWS on the glacier surface, in the upstream region, near the location of the monitored melt pond. The AWS at Helheim Glacier recorded wind speed and direction, aspirated air temperature, snow surface height, short- and long-wave radiative fluxes, station tilt, and surface ablation. These data were used to conduct a study on the effect of melt on ice dynamics at Helheim Glacier (Andersen, 2010; Andersen et al., 2010).

The research work presented in this thesis focuses on the geodesy component of the Helheim Glacier project, evaluating the accuracy of the position estimates obtained with a GPS network in a glacier environment and studying the physical information that can be obtained from these data sets on the dynamics of a large fast-flowing Greenland outlet glacier.

1.6 Thesis motivation and objectives

The research work presented in this thesis is integrated in a multidisciplinary project that investigates the dynamics of tidewater fast-flowing glaciers in Greenland. This thesis presents a study of glacier flow using position estimates from a Global Positioning System (GPS) network installed during the Arctic summer seasons of 2006–2008 at Helheim Glacier, East Greenland. The primary reason for undertaking this study is to improve our understanding on the dynamics of fast-flowing glaciers at temporal resolutions that are not achievable with most standard techniques employed in glaciology, such as satellite imagery. The use of high-rate GPS techniques to study glacier flow is a relatively novel procedure. Therefore, the accuracy and precision of these techniques in a fast-flowing glacier environment needs to be assessed.

This thesis focuses on the geodesy component of the project. As part of the thesis work, we obtained a complete and consistent set of timeseries for the different GPS sites deployed in each of the summer campaigns. One of the purposes of this thesis was to assess the precision of the position estimates acquired from a GPS network in a glacier environment. Quantifying the precision of the estimates and having the ability to distinguish between data or processing artifacts and real geophysical signals is the first requirement to undertake the analysis of the geophysical signals present in the GPS data, which constitutes the second part of the study presented here.

The high-rate, high-precision GPS measurements acquired at several locations on the surface of Helheim Glacier during the summer seasons of 2006–2008 allow us to analyze the dynamics of the glacier with high temporal resolution at the locations where the GPS sites were installed. The use of satellite images to study velocity fields of glaciers and their annual to seasonal velocity changes is very extended. However, satellite images cannot provide the almost continuous sampling that can be achieved with glacial GPS networks. GPS glaciology allows to study the dynamics of glaciers from inter-annual to sub-hourly timescales. It is at the sub-daily timescales where the advantages of using GPS networks to measure glacier flow become clear.

This thesis focuses on the analysis of the glacier's sub-daily position deviations from mean flow and its spatio-temporal variation. In this respect, one of the main goals of this thesis was to use the extensive positioning data set for the characterization and analysis of the flow response of Helheim Glacier to the ocean tides. We observe that the flow of the lower part of the glacier is modulated by the ocean tides. Several studies on the response of Antarctic Ice Streams to ocean tides exit. However, due to data sparsity a detailed study of the response of a Greenland's outlet glacier to ocean tidal forcing was lacking. The tidal response of the glacier is also analyzed in relation to sudden changes in the speed of the glacier that occur as a response to large calving events and glacial earthquakes. The characterization of the glacier's dynamic signature in relation to glacial earthquakes was one of the main goals of the Helheim Glacier project. Here, we describe the spatio-temporal character of the speed changes related to glacial earthquakes, and we analyze the tidal response during these periods. Finally, other changes in flow speed driven by other geophysical processes, presumably meltwater runoff, are also presented and characterized.

1.7 Thesis outline

This chapter has given an introduction to the state of the cryosphere and glacier dynamics, focusing on Helheim Glacier, and we have presented the measurements acquired as part of the Helheim Glacier project and the motivation of this thesis.

Chapter 2 introduces the basics of the Global Positioning System, it details the high-rate processing methods used to estimate the position of the GPS sites at Helheim Glacier, and assesses the precision and error sources in the estimated position timeseries.

Chapter 3 presents results pertaining to the mean flow of Helheim Glacier and analyzes the spatial and temporal trends of its behavior, focusing on timescales that range from seasonal to daily.

Chapter 4 presents the characterization of the flow response of Helheim Glacier to the ocean tides during each of the summer seasons, analyzing its spatial and temporal behavior.

Chapter 5 further examines the high-rate position estimates of the glacier sites at some specific times surrounding the time of glacial earthquakes and associated calving events. We describe the dynamic response of the glacier to such events, which is characterized by a the step-wise increase in speed of the glacier and an abrupt change in tidal response.

Chapter 6 examines a different type of change in glacier speed that we hypothesize to be associated with the drainage of supraglacial melt ponds, and show the evidence for the occurrence of such events.

Chapter 7 gives a summary of the work presented in this thesis and an overview for future work.

Chapter 2

The technique of high-rate GPS for glaciology

The Global Positioning System (GPS) has become a widely used tool in geodetic studies of the Earth as it can provide accurate position estimates, and their temporal variation, for a site anywhere on the globe, at any time. During the last decade or two, GPS observations have been applied to the study of several disciplines in Geophysics such as plate tectonics, postglacial rebound, and atmospheric sciences, to name a few. In these studies, GPS measurements are used mainly to obtain the temporal variation of daily estimates of site position on timescales that range from a few days to several years. As the precision of GPS estimates of position continues to improve, the detection of smaller and faster geophysical signals has become feasible. This new GPS technique, known as high-rate GPS, has been used, for example, in seismology to measure ground motions due to earthquake-induced shaking. GPS has also been employed for some years in glaciology mostly as a surveying tool for ice flow. The use of high-precision geodetic methods in high-rate GPS to study fast flowing glaciers represents, however, one of the most recent applications of this technique. This chapter contains an introduction to the GPS technique and describes the processing methods we have used to analyze the GPS data acquired at Helheim Glacier. References Teunissen & Kleusberd (1998) and Hofmann-Wellenhof et al. (1994) have been used to document Section 2.1.

2.1 The Global Positioning System (GPS)

2.1.1 GPS constellation and signal structure

GPS positioning is based on trilateration, by which the unknown position of a point is determined by measuring its distance to points at known coordinates. GPS positioning requires distance measurements to at least 4 satellites with known coordinates to determine the three components of the position of the receiver plus the unknown receiver clock error.

The GPS constellation is composed of at least 24 operational satellites (31 as of this writing, December 2010) distributed among six circular orbits, at an altitude of approximately 20200 kilometers above the surface of the Earth. All orbital planes are inclined 55° with respect to the equatorial plane and rotated by 60° with respect to their neighboring planes. Each of the satellites completes two full revolutions each sidereal day, with an orbital period of 11hr 58min, such that the constellation of satellites observed from a given point on the Earth repeats every sidereal day. The orbits are arranged so that at least six satellites are always within line-of-sight from almost anywhere on the Earth's surface.

Each GPS satellite transmits pure sinusoidal-wave signals or carriers, centered on two microwave radio frequencies. These lie in the L-band, 1575.42 MHz (wavelength of 19.0 cm), referred to as Link 1 or simply L1, and 1227,60 MHz (wavelength of 24.4 cm), referred to as L2. Such carriers are phase modulated by apparent random sequences of binary values which repeat after some chosen interval time, known as pseudorandom noise (PRN) codes. Since exactly the same code sequences are independently replicated in a GPS receiver, the PRN codes enable to measure the exact number of cycles that lie between the satellite and the receiver by aligning the replicated with the received sequence. Knowing the time the signal was transmitted, which is encoded on the signal, and when it was received, measured by the receiver clock, allows to compute the range or distance between the satellite and the receiver.

The key of the accuracy of the system lies on the fact that all the components of the satellite signal are precisely controlled by atomic clocks. The differences in satellite clock timing is tracked by GPS ground station monitors and included in the satellite message. However, the receiver clocks are comparatively inaccurate, and hence, the receiver clock error needs to be estimated along with the station coordinates.

Two different PRN codes are transmitted by each satellite: the C/A code or coarse acquisition code and the P or precision code. The P-code has a shorter wavelength, which enables a higher precision of the range measurement. The C/A code, with an effective wavelength of $\sim$300 m, is modulated on the L1 carrier whereas the P code, with an effective wavelength of $\sim$30 m, is transmitted on both L1 and L2. The GPS system is in the process of modernization and by 2014 it is expected that the new satellites GPS III will carry, among other technological innovations, C/A on L2 or L2C. Each satellite generates its own unique PRN codes, which are highly orthogonal to any other codes from a different satellite.

In addition to the PRN codes, the navigation or broadcast message is modulated onto both carriers, which includes among other system parameters, the orbit parameters or satellite ephemerides, from which the receiver can compute the satellite coordinates. The satellites atomic clocks are carefully monitored and the amount by which they drift from GPS system time is also supplied in the broadcast message.

Thus, the signal transmitted by a GPS satellite antenna is a combination of three components: carrier wave, ranging codes, and navigation message. The signal is transmitted with enough power to ensure a minimum signal power level at the Earth's surface.

2.1.2 GPS observables

A GPS receiver can make basically two kinds of measurements based on the comparison between received signals and receiver generated signals: code pseudorange, and carrier phase. Both measurements are biased by satellite and receiver clock errors, and thus the distances derived from them are denoted as pseudoranges.

The code pseudorange is a measure of the range or distance between the satellite antenna and the antenna feeding a GPS receiver, and is determined using the PRN codes. The receiver makes this measurement by determining the time shift required to align the replica of the code generated in the receiver with the received code from the satellite, which multiplied by the speed of light gives the pseudorange. Since the transit time is measured in the satellite time frame and the reception time in the receiver time frame, this measurement is biased by the lack of time synchronization between the satellite and receiver clocks. As its is further explained below, it also suffers from several other effects including ionospheric and tropospheric delay of the signal, multipath, and receiver noise. These biased time delay measurements are thus referred to as pseudoranges, and can be expressed as

$$P_1 = \rho + c\,(dt_s - dt_r) + T + I_1 + \epsilon_{P1} \tag{2.1}$$

$$P_2 = \rho + c\,(dt_s - dt_r) + T + I_2 + \epsilon_{P2}, \tag{2.2}$$

where P_1 and P_2 are the pseudorange observables in L1 and L2, ρ is the unknown geometric range from the satellite to the receiver, c is the speed of light, dt_s and dt_r are the satellite and receiver clock offsets from GPS time, respectively, I_1 and I_2 are the ionospheric delays, T the delay introduced by the troposphere on an electromagnetic signal that propagates through it, and ϵ_{P1} and ϵ_{P2} contain the rest of error sources, including multipath and receiver noise. Note that the ionospheric delay (which is dispersive), multipath, and receiver noise depend on the frequency and thus are different for L1 and L2. Most of these contributions to the delay can be accurately modeled and estimated along with the position coordinates.

The carrier phase observable is the phase of the received carrier from a satellite with respect to the phase of the carrier generated by an oscillator in the GPS receiver. The precision of the carrier phase is much higher than the precision of the code pseudorange because its wavelength is much shorter (∼20 cm versus tens of meters). However, because the receiver cannot distinguish one cycle of a carrier from another, the initial phase is undetermined by an integer number of cycles, or ambiguity N, which must be determined along with the station coordinates. Multiplying the measured carrier phase in cycles, L, by the carrier wavelength, λ, we obtain its equivalent in distance units or pseudorange,

$$L_1\lambda_1 = \rho + c\,(dt_s - dt_r) + \lambda_1 N_1 + T - I_1 + \epsilon_{L1} \tag{2.3}$$

$$L_2\lambda_2 = \rho + c\,(dt_s - dt_r) + \lambda_2 N_2 + T - I_2 + \epsilon_{L2} \tag{2.4}$$

Note that, because the ionosphere is a dispersive medium, it delays groups of waves (the PRN codes) but advances phase carriers, thus the ionospheric delay in the carrier phase pseudorange is equal in magnitude but opposite in sign to the code pseudorange delay. Also, the residual errors such as multipath and random noise are different for code and carrier phase observables.

2.1.3 GPS positioning biases and errors

The code and phase pseudoranges are affected by systematic errors, or biases, and random noise. Biases affecting GPS solutions can be classified into three broad categories: (1) satellite related errors, (2) signal propagation and observation related errors, and (3) station related errors.

Satellite-related errors include biases in the satellite ephemeris or satellite clock timing, which are normally uncorrelated between satellites. Biases induced by the propagation of the signal through the atmosphere comprise ionospheric and tropospheric refraction. Biases related to the observation method of such signals are those caused by ambiguity resolution and cycle slip (or phase break) detection and fixing. Finally, errors associated with the station are receiver clock biases, multipath, and antenna phase-center variations.

In relative positioning, some of these errors, such as orbital errors or satellite and receiver clock biases, can be eliminated or greatly reduced using differenced observables, an approach detailed in 2.1.4. Differencing either eliminates some of the errors because they are common to the differenced ranges, or reduces the rest of the errors because of their spatial and temporal coherence. With respect to atmospheric refraction, differenced observables only reduce their effect for short baselines, where the satellite signals are affected very similarly.

Some of the errors can be either eliminated using a combination of the two different frequency observables, like the ionospheric delay, or modeled, such as the troposphere refraction and antenna phase-center variations. However, others such as multipath can not be easily corrected. All of these error sources are explained in detail below.

Finally, some of the biases that affect GPS positioning can not be modeled but, given enough available satellites, can be estimated as extra parameters along with the position coordinates. For example, this method is used to estimate ambiguities, and also clock errors.

2.1.3.1 Ionospheric refraction

Dual-frequency observations are crucial for eliminating one of the major sources of error in GPS positioning, the ionospheric refraction. The ionosphere is the region of the atmosphere where there is a high content of free electrons, making it a dispersive medium with respect to radio waves. The delay of an electromagnetic signal as it travels through this ionized medium is proportional to the inverse square of its frequency f,

$$I_P = -I_L \sim \frac{40.3\ TEC}{f^2}. \tag{2.5}$$

where P denotes code pseudorange, and L carrier phase. The magnitude of delay, in the case of the code pseudorange, or advance, for the carrier phase, caused by the ionosphere depends on the total electron content, TEC, and can range from tens of centimeters to tens of meters.

Dual-frequency positioning systems take advantage of the dispersive nature of the ionosphere for correcting for its effect, as the first-order ionospheric effect can be eliminated by forming a linear combination of dual-frequency GPS observables in L1 and L2, which is called the ionospheric-free combination. The resulting phase observable is L_C,

$$L_C = \frac{f_1^2}{f_1^2 - f_2^2} \left(L_1 - \frac{f_2}{f_1} L_2 \right), \tag{2.6}$$

where L_1 and L_2 are the phase observables in L1 and L2. The corresponding ionospheric-free code observable is P_C,

$$P_C = \frac{f_1^2 P_1 - f_2^2 P_2}{f_1^2 - f_2^2}. \tag{2.7}$$

One can solve the equations for estimating the station coordinates using the ionospheric-free observables, which is a very common procedure in GPS processing that allows to remove most of the ionospheric effect (non-corrected effects are of centimeter-level) certainly away from the peaks of the ~11-year solar cycles. (State-of-the-art estimators include corrections for second- and third- order ionospheric effects as well (e.g., Hoque & Jakowski, 2008).)

2.1.3.2 Tropospheric refraction

The atmospheric delays caused by the refraction of the neutral parts of the Earth's atmosphere, which include the troposphere and other regions up to 80 km in altitude, such as the stratosphere, are all of them referred to as tropospheric delay due to the dominant contribution of the troposphere. Unlike the ionosphere, this is a non-dispersive medium, so that group and phase delays are the same, and dual-frequency observations can not be used to eliminate its effect.

The atmospheric effects on radio signals are typically taken into account by estimating the delay in the zenith direction and mapping this value for the elevation and azimuth angles of the satellite. The delay in the zenith direction is of ~2.5 m at sea level and has a component due to the constituents in the atmosphere that are in hydrostatic equilibrium ("dry" delay), which accounts for ~90% of the tropospheric refraction, and a component due to water vapor in the atmosphere ("wet" delay), which accounts for the rest (Davis et al., 1985). The hydrostatic component can be generally well modeled with an accuracy of a few millimeters using surface pressure data, or in the absence of it, using standard atmospheric pressure (Elgered et al., 1991). On the other hand, the wet component is highly variable spatially and temporally. However, this residual tropospheric bias can be parametrized and estimated along with the position coordinates. Finally, several mapping functions have been developed to evaluate such zenith delays for all elevation and azimuth angles (e.g., Marini, 1972; Davis et al., 1985; Herring, 1992; Niell, 1996).

2.1.3.3 Antenna phase-center offset and variations

The electrical phase center of the antenna is the point to which the position estimates are referenced. However, the phase center is not a physical point that can be measured to, so the offset of the phase center from a physical point on the antenna must be known. The phase center is different for L1 and L2 frequencies. Moreover, because only ideal point-like antennas have spherical equi-phase surfaces, with origin at the antenna phase center, signals arriving from different azimuth and elevation angles to the real antenna phase center will experience different delays. The variations of the phase (or delay) with angle of incidence is commonly known as phase-center variations (e.g., Schmid et al., 2005). Such variations can be of the order of millimeters to a few centimeters in the case of geodetic quality antennas.

The exact position of the phase center is modeled and tabulated for each type of antenna, including a phase-center offset, which describes the vector from the receiver antenna reference point to the mean phase center, and a phase-center variation, which provides zenith- and/or azimuth-dependent corrections to get the actual phase-center position. However, in relative positioning, as long as the same model of antenna is used for both systems and the antenna separations are $\sim$100 km or less, the position of the phase center is usually not important at the mm level.

2.1.3.4 Multipath

Multipath is the phenomenon whereby the direct signal that reaches the receiver's antenna interferes with other signals, usually weaker, reflected from objects present in the vicinity of the antenna. The difference in path lengths causes the signals to interfere, which adds noise to the estimated positions, generally of the order of several centimeters, and of higher amplitude in the vertical component. There is no general model of the multipath effect because of arbitrarily different geometric configurations surrounding the antenna, and it can not be differenced out due to its highly site-specific nature. The most efficient way to mitigate the effect of this phenomenon is avoiding reflecting surfaces in the neighborhood of the antennas or placing a microwave absorbing material on the surface close to the antenna (e.g., Elosegui et al., 1995). Also, since multipath has a larger impact at low elevation angles, employing an elevation angle cut-off of 7-15° is a typical procedure in standard GPS data processing to reduce its effect on the position estimates. However, since the multipath effect in a particular location at a given time depends on the satellite configuration in the sky, and satellite geometry repeats every sidereal day, the multipath error is highly correlated across subsequent days. Therefore, one can apply filtering to the position estimates to help minimize this error, in a method know as sidereal filtering (e.g., Choi et al., 2004).

2.1.3.5 Random Noise

There are also observational errors associated with the receiver's electronics which are of random character. For modern geodetic-quality receivers the internal phase noise is less than ∼1mm (Park et al., 2004). This random noise is proportional to the wavelength of the signal, and therefore, the noise level is higher for the pseudorange code observables rather than the carrier phase observables, and within each of these, it is higher for the L2 rather than the L1 observables (e.g., Thompson et al., 1986). Furthermore, although the use of the ionospheric-free combination observables is warranted in order to correct for the ionospheric delay, the noise level in this observable is higher, since it adds the noise from both frequencies. Therefore, for relative positioning and a short baseline, where the ionospheric effect is largely mitigated by using differenced observables, it is recommended to compute the position solutions using the L1 observable.

2.1.4 Relative positioning

In differential or relative positioning, the coordinates of one or more GPS systems are determined relative to a fixed GPS system, whose absolute coordinates are already known. Because many effects and errors will affect the absolute positions of the simultaneously observing GPS systems to almost the same extent, these errors largely cancel out when differential positioning is used, thus resulting in a higher positioning accuracy.

Relative positioning enables to use, among other differenced observables, the double-differences approach, which eliminates clocks biases and reduces other sources of error. The single-difference observables "Δ" are the difference at a given time between observables from two different receivers (A and B) and the same satellite (j), for example, for the carrier phase pseudorange:

$$\Delta L_{AB}^{j}\lambda = \Delta\rho_{AB}^{j} - c\Delta\left(dt_r\right)_{AB}^{j} + \lambda\Delta N_{AB}^{j} + \Delta T_{AB}^{j} - \Delta I_{AB}^{j} + \epsilon. \tag{2.8}$$

This procedure eliminates the satellite clock error, and if the baseline length between receivers is small compared to the satellite orbit altitude, the effect of orbital errors are also largely mitigated.

The double-difference, "∇Δ", which is the difference at a given time between two single-differences corresponding to the same pair of receivers (A and B) but different satellites (j and k), eliminates the receivers clock errors:

$$\nabla\Delta L_{AB}^{jk}\lambda = \nabla\Delta\rho_{AB}^{jk} + \lambda\nabla\Delta N_{AB}^{jk} + \nabla\Delta T_{AB}^{jk} - \nabla\Delta I_{AB}^{jk} + \epsilon'. \tag{2.9}$$

For short baselines, single-differences also remove some of the atmospheric biases ($\Delta T_{AB}^{j} \sim 0$; $\Delta I_{AB}^{j} \sim 0$) since for two receivers located nearby, the signals arriving to both receivers travel through approximately the same path, and therefore suffer similar atmospheric delay.

2.2 Data processing

GPS data processing is based on the inversion problem, in which a group of parameters is to be estimated from physical observations by inverting the equations that relate the observables to the parameters. For positioning purposes, the primary parameters of interest are the receiver coordinates, but there are many other unknown parameters such as clock, atmospheric, and phase ambiguity biases that are solved for simultaneously. The equations that relate observations ($P_{1/2}$, $L_{1/2}$) and parameters (ρ, dt_s, dt_r, T, $I_{1/2}$, $N_{1/2}$), the so-called observation equations, (equations 2.1–2.2 for the code pseudorange and equations 2.3–2.4 for the carrier phase) can be written in matrix form,

$$Y = f(X) + \epsilon \tag{2.10}$$

where Y is a vector of the observables, X is the vector of parameters, and ϵ are the observational errors. These set of equations need to be inverted to solve for the parameters. However, the observation equations are not linear on the parameters because the geometric range ρ is a nonlinear function of the receiver coordinates,

$$\rho = \|\overrightarrow{r}_s - \overrightarrow{r}_r\| = \sqrt{(x_s - x_r)^2 + (y_s - y_r)^2 + (z_s - z_r)^2}, \tag{2.11}$$

where $\overrightarrow{r}_r$ and $\overrightarrow{r}_s$ are the three-dimensional receiver and satellite position vectors, respectively, in a given reference frame and $\|\|$ is the absolute value. In order to linearize the observation equations, we need approximate values (or a prioris) for the parameters. Then, one can rewrite the observation equations substituting all parameters for increments to the a priori values, X_0, and the observations for the observed-minus-computed observations, where the computed observable, Y_0, is determined using the a priori parameter values. These increments are of a sufficient small value so that we can replace the ones that are nonlinearly related to the parameters of interest with their first order approximation:

$$Y = Y_0 + A\,(X - X_0) + \epsilon, \tag{2.12}$$

where A is the matrix of partial derivatives evaluated at $X = X_0$,

$$A = \left.\frac{\partial y}{\partial x}\right|_{X=X_0}. \tag{2.13}$$

The inversion of the linearized observation equations can then be accomplished using standard optimal estimation methods such as least squares or Kalman filters. One needs sufficient number of observations to simultaneously solve for the receiver coordinates but also for the other unknown parameters. Redundant observations generally result in improved parameter estimates. One can iterate on this method as necessary using the estimates from a prior solution to progressively improve the a priori parameter values and thus, the estimates, until reaching convergence.

In the static positioning, the average position during a given time is estimated using all the recorded observations during that time at a given interval sampling. This approach provides redundant observations, overdetermined solutions, and thus a higher accuracy of the determined position.

On the other hand, in kinematic solutions, a high-rate processing method is needed, where only the observations recorded at each epoch are used to estimate the position of the receiver at that epoch, using as constrains for each of the epochs the estimated position and variance/covariances at the previous epoch. This inverting procedure can be either a Sequential Least Squares or a Kalman filter. The accuracy of the solutions is lower that those obtained in the static mode. However, the accuracy can be improved by performing relative positioning.

2.3 Processing of GPS data from Helheim Glacier

2.3.1 The TRACK software package

Processing of the GPS data acquired at Helheim Glacier has been done using TRACK, the kinematic component of the GAMIT/GLOBK software package, open-source code by MIT (Chen, 1998). This code was originally written to determine the trajectory of an aircraft with respect to a ground reference station and can use the high-precision, carrier-phase observables. This package is thus suitable for kinematic applications relying on differential GPS techniques over small-scale networks, such as those employed in GPS glaciology. As the separation between the static and kinematic site increases, the differential ionospheric and tropospheric delay increases. The program performs best for separations between the static and kinematic sites of less that ∼10 km, between ∼10 and ∼100 km, although more difficult it is often successful, and over ∼100 km the performance of the program depends critically on the quality of the data collected (Herring et al., 2008).

The core algorithm for data inversion used in TRACK is a Kalman filter (Kalman, 1960; Chen, 1998), which estimates the geophysical parameters of interest (GPS station coordinates) from geophysical measurements (GPS observations) in the presence of observational errors. This type of algorithm minimizes the estimation error employing all measured data plus prior knowledge about the system (a priori coordinates of the stations and their covariance matrix). The Kalman filter includes an estimation procedure that enables the geophysical parameters of interest that we estimate to change during the interval in which data is collected. The inversion is applied on an epoch-by-epoch basis, using in each case as a priori information the estimated positions from the epoch before, except for the first epoch, for which the a priori is given externally. In TRACK's Kalman filter, the position variations for the kinematic site are modeled as a random-walk stochastic process, whose white-noise generating variance can be user selected.

The equations for estimating the positions are solved using double-difference observables, which, as shown in Section 2.1.4, eliminate satellite and receiver clock errors and reduce satellite orbit and atmospheric delay errors for stations separated by a short distance.

TRACK includes a solid Earth tide model, and correction for phase-center offsets and tropospheric delays. However, ocean tidal loading is not taken into account since the effect over short distances is assumed to be sub-mm. The tropospheric dry and wet zenith delays are computed using Saastamoinen's model (Saastamoinen, 1972), based on the pressure calculated from the height above sea level of the station and a standard atmosphere (i.e., pressure 1013.25 mbars, temperature 20°C, and relative humidity 50%). The uncorrected atmospheric delay can be modeled in TRACK as a random walk process in the zenith direction and estimated in the Kalman filter along with the coordinates of the receiver, mapping to the elevation angle of the incoming GPS signal. The mapping functions used for the dry and wet tropospheric delay are the MTT mapping functions (Herring, 1992).

The cycle ambiguities must be correctly resolved, ideally by fixing them to integer values, in order to convert the phase observations into the precise ranges before estimating positions. Ambiguity resolution is necessary in three occasions: the beginning of a session, the occurrence of cycle slips, and when a new satellite becomes visible and its observations are included into the position processing. TRACK's ambiguity algorithms use dual-frequency GPS observables to account for the effects of the ionosphere and utilize geometry or position-free combination of observables (Chen, 1998). Ambiguities are solved using the Melbourne-Wubena wide lane (MW-WL) observable, which removes both the effects on the ionospheric delay and changes in range by using the pseudorange measurements to estimate the difference in phase between L1 and L2,

$$L_{MW-WL} = L_1 - L_2 - \frac{f_1 - f_2}{f_1 + f_2}\left(\frac{P_1}{\lambda_1} + \frac{P_2}{\lambda_2}\right) = N_1 - N_2. \tag{2.14}$$

Thus, the MW-WL observable gives the difference between the L1 and L2 cycles. Then, a combination of techniques is used to determine the individual cycles N_1 at L1 and N_2 at L2 separately (Chen, 1998). The program then tries to fix the ambiguities to integer values iteratively. It uses floating point estimate with LC, MW-WL, and ionospheric delay constraints to determine the integer biases and the reliability with which they are determined. This sequence is repeated until an iteration where no new biases can be fixed (Herring et al., 2008). For short baselines ($\lesssim$10 km) for which ionospheric delay is negligible, L1 and L2 ambiguities can be resolved separately.

The software allows to choose the data type to be used in generating the position estimates: L1-only phase, L2-only phase, LC or ionospheric-free combination phase, the same for the pseudoranges or a combination of these data types. For short baselines ($\lesssim$2–3 km), the differential ionospheric delay between the static and the kinematic site can be neglected and, thus, positioning can use L1 and L2 separately to reduce random noise. For longer baselines, this is no longer true and the use of the ionospheric-free combination observable should be used.

A Kalman filter smoothing can be used, whereby the Kalman filter solution is run forwards and backwards in time and then a smoothing filter is carried out. This approach is recommended specially if there remains some non-fixed ambiguities, or if atmospheric delays are estimated (Herring et al., 2008).

2.3.2 Processing method

TRACK runs using a command file. The basic inputs needed in such file, without which the program can not run, are the location and name of the observation files (RINEX format) for the static and the kinematic sites, and the orbit files (SP3 format) for the period being processed. Although the program has default values for most of the processing parameters, there is a level of parameter tuning that is required to produce the best solution for a specific experiment or configuration, since there is some level of subjective decision that is built on experience and training. The strategy used for the processing of the GPS data from Helheim Glacier is detailed below, along with the parameters and information we tune in TRACK's command file. This strategy was consolidated after a comprehensive study involving quality control error analysis and extensive testing. This study was necessary since the scientific goals of the Helheim Glacier project required a level of kinematic GPS accuracy over a wide range of timescales, that had never been attempted before in glaciology.

1. We process each day independently, using 24-hours-long observation files, which is a standard procedure in GPS data analysis. TRACK uses the Receiver Independent Exchange Format (RINEX) observation files. Our receivers originally record daily (24 h) binary files, which we convert to daily RINEX.

2. We process single baselines by recommendation of the software developers (T. Herring, private communication). We use as reference site, the static site that has the better quality and most continuous data throughout the summer season, which in 2006 was HEL1, and in 2007 and 2008 was NUN1 (see Figures 1.4–1.6 for the location of the sites on the glacier's margins).

3. We use precise satellite orbits and clocks (final products) of the International GNSS Service (IGS) in Standard Product 3 (SP3) format. IGS analyzes and combines satellite coordinates and clocks from various agencies, such ad MIT, JPL, NGS, and SIO. We choose to use these combined orbits instead of orbits from a specific agency because these undergo extensive intercomparison and quality control and thus are generally of higher quality. These orbits are in 24-hours files with state estimates every 15 minutes. Because of the way TRACK interpolates the orbits, it needs 2 hours prior to the beginning of the RINEX and 2 hours subsequent to its end. Since we process 24 hours of data, we concatenate together the last and first 3 h of the SP3 files from preceding and following days, respectively, with the SP3 file from the day that is being processed.

4. We always compute the solutions using carrier-phase observables since these are of higher precision. In most cases, the best solution is obtained when using the L_C observable, i.e., the ionospheric-free phase observable, since most baselines are

long enough (between 10 and 15 km) for the ionosphere to have a perceptible effect. Therefore, we have computed all solutions using L_C, hereinafter referred to as "LC solutions".

5. We process the solutions with a sampling interval of 15 seconds, i.e., we obtain an estimate of the kinematic site position with respect to the reference site every 15 seconds. We chose this sampling interval as a balanced compromise between computer CPU time and the period of the geophysical signals of interest. The receivers installed at Helheim Glacier recorded data every 1–5 seconds. However, since the duration of a typical glacial earthquake is 30–60 seconds, a 15-s sampling interval satisfies the Nyquist criteria, and we consider that we do not need to process at higher rates unless we observe very short timescale events in the results from this processing.

6. We use a fairly standard 10 degrees satellite elevation angle cut-off, which means that any observations arriving to the antenna with an elevation angle less than 10 degrees are not used in the solution. This is done to mitigate multipath effects which are typically more severe at low elevation angles.

7. In the random-walk stochastic model used for the position variations, we use a variance that allows for displacements of 0.04 m between epochs (15 seconds apart). This statistic is $\sim$10 times looser than the actual observed average position change between epochs at Helheim Glacier, since the maximum velocity we observe is $\sim$24 m/d (or 4 mm every 15 seconds). This variance is consistent with the dynamic parameter defined in Elósegui et al. (1996) to neither over- nor under-constrain a kinematic solution.

8. In all the solutions we present in this work, we have chosen not to estimate atmospheric parameters, since otherwise the quality of the position estimates is considerably reduced. This is because, when estimating atmospheric parameters, we are introducing an extra solve-for parameter for each site and epoch, which makes the site position estimates highly unstable. Tests performed comparing estimates with and without solving for atmospheric parameters show that when estimating atmospheric parameters the RMS of the solution increases by $\sim$50–80%. Also, the difference between both solutions is of less than $\sim$1 cm in the horizontal components, and of $\sim$1-2 cm in the vertical component. Therefore, we find that these tests do not warrant solving for atmospheric parameters since, over the short baselines of interest, their effect on position estimates is small but the noise increases considerably.

9. We use absolute phase-center offsets for the specific antenna type from the International GNSS Service. The offsets are different for L1 and L2.

10. The most critical part of the processing lies in the resolution and fixing of ambiguities. TRACK allows to choose the type of data to be used in resolving and

fixing ambiguities to integers. One can either use L1 and L2 phase data separately, under the assumption that ionospheric delay is small, and works best for short baselines ($\lesssim$3 km), or use the ionospheric-free observable L_C, which works best for long baselines. We have tested both procedures and even for our longest baselines ($\sim$20 km), there are some ambiguities that are only fixed when using LC, and some other only fixed when using L1 and L2 separately. TRACK is able to read a table of ambiguities. Therefore, one can give as an input to the program the table of ambiguities from a previous run, in which case TRACK will use the ambiguities that had been fixed in the previous run and will try to fix the ones that was not able to fix before. After some testing, we concluded that the best approach was to process the data in two iterations: (1) in iteration 1 we fix the ambiguities with L1 and L2, and (2) in the second iteration we give the resulting table of ambiguities from iteration 1 as an input, and fix the ones that remain non fixed using LC.

11. A crucial part prior to the resolution of the ambiguities is correctly detecting the cycle slips. TRACK searches for cycle slips using the extra wide lane or ionospheric delay ($L_1 - L_2 f_1/f_2$). The default tolerance or largest jump allowed in the ionospheric delay before it is considered a cycle slip is by default set to 0.5 cycles. For some stations/days (but not all) we have found that it is useful to increase such tolerance, as the cycle-slip detector is too sensitive and thus flags and tries to fix cycle slips that are not real. After some testing, we concluded that increasing the ionospheric tolerance to 1.3 cycles was what worked best in such cases. But this is only true in some cases, in others it can prevent a true cycle slip from being flagged. Therefore, our procedure consists in running two separate cases: (a) default ionospheric tolerance (0.5 cycles), and (b) increased ionospheric tolerance (1.3 cycles), and then choosing between (a) and (b). Note that each of these runs, (a) and (b) is a result of two iterations, one fixing ambiguities with L1 and L2, and the second, with LC. Choosing between these two solutions needs to be done manually by visual inspection of each of the individual solutions and selecting the one that has less position offsets associated to the non resolution of an ambiguity. It can not be done automatically by comparing the number of non fixed ambiguities because the number of flagged ambiguities is always higher in (a). The question lies on whether such ambiguities are either true or an artifact associated with the sensitivity of the data cleaning process.

12. We run the Kalman filter forwards and backwards and then run a smoothing filter. This way we obtain a higher-quality and smoother solution.

2.4 Post-processing of GPS position solutions from Helheim Glacier

2.4.1 Reference frame

TRACK outputs position estimates as geodetic coordinates (i.e., latitude, longitude, and height) in the World Geodetic System 1984 (WGS84 ellipsoid). We convert these coordinates to a more practical system for our application, a NEU topocentric reference frame with north, east, and vertical (positive up) directions, centered on the position of the kinematic station at a reference epoch.

A natural coordinate system for the glacier is defined by the glacier flow direction. For each site and timeseries, we rotate the position estimates to a local right-handed coordinate system with the 1-axis in the along-flow direction (positive in the direction of flow), the 2-axis in the cross-flow direction, and the 3-axis in the vertical direction (positive up). In this system, the along-flow component is defined as the direction of maximum daily-averaged horizontal velocity, and the orthogonal to this direction in the horizontal plane, referred to as cross-flow component, is thus the direction of mean daily zero velocity. The rotations are performed by minimizing the misfit to a linear model, in a least-squares sense. In rotating the coordinate system, the uncertainties in the position estimates are taken to be the formal uncertainties from TRACK root-sum-squared with a term accounting for the degree of ambiguity fixing at that epoch. The rotation to the along-flow, cross-flow, and vertical (ACU) coordinate system, is usually performed on a daily-solution basis, however it is occasionally conducted over longer or shorter time periods as needed, for example to characterize the response to glacial earthquakes. In these cases the cross-flow component is the direction of mean zero velocity over the duration of such time periods.

The conversion of the position solutions to the ACU coordinate system allows us to investigate the dynamics of each of the sites in a coherent mode, since almost all the dynamics of the site occurs in the along-flow component. However, because sites can change its direction of flow during the day, for example as they navigate around glacier bends or are jostled around by the ocean tide, cross-flow variations are sometimes present. In the longer term, the direction of flow of a site can also change with time and, of course, is different for the various sites. However, we are more interested in the character of along-flow position estimates rather than in the flow direction at each moment.

2.4.2 Analysis of the dynamics of the glacier

The timeseries of position estimates from Helheim Glacier show high background velocities, characteristic of ice flow of a Greenland outlet glacier. We estimate the mean daily velocity by fitting a linear model to the along-flow position estimates, which allows us to investigate the temporal dependence of the glacier's mean dynamics.

In addition, the high precision of high-rate GPS observations enables us to study in great detail the spatio-temporal variation of sub-daily position deviations from mean flow.

To do this, we subtract a linear model fitted to the horizontal and vertical components of the timeseries, obtaining the relative position of each of the GPS sites to their mean speed. The lower amplitude signals superimposed to the background velocities obtained with this procedure can represent either systematic errors, such as multipath, or real dynamic behavior of the glacier. We analyze the residuals to the linear fit to search and quantify short-term velocity changes related to glacial earthquakes or other geophysical processes, as explained in Chapters 5 and 6. We also investigate the response of the glacier to ocean tides by analyzing the semidiurnal signals in the position residuals, as further detailed in Chapter 4.

2.5 Characterization of errors in the position solutions

In this section we assess the precision of the position estimates and discuss the sources of error of most relevance to GPS glaciology.

2.5.1 Precision of the position estimates

The aim of the work presented in this section is to assess the precision of the high-rate position solutions for GPS systems on a fast-flowing glacier environment, like Helheim Glacier, processed with the method described above (see Section 2.3.2). We cannot test the accuracy of the solutions since we lack an external method for this purpose. However, we analyze the precision of the TRACK solutions by examining, for a set of solutions, the position residuals to a model that describes the mean kinematics of each site, and the post-fit phase residuals statistics as a function of time.

The post-fit phase residual for a satellite-station pair at a given epoch is the difference between the observed phase and the phase computed using the estimated values of the site's position parameters. These residuals include the effect of clock errors, multipath, phase-center variations, and the atmospheric non-modeled effects. They are typically found to be zero mean, otherwise they indicate that the solution contains systematic errors. The root-mean-square (RMS) of the post-fit phase residuals decreases with increasing elevation angle, since at lower elevation angles multipath and atmospheric errors have a larger effect. On the other hand, a dependence of the phase residuals with time indicates that some source of error has a time-dependent pattern.

Here we present the residuals as a function of time, since the temporal patterns are more relevant for the purpose of this work. In addition, we quantify the level of precision of our solutions by computing the RMS of the position estimates with respect to a mean kinematic model for each site. We analyze these results for three cases of increasing complexity: (1) a zero-baseline experiment that allows us to estimate a low-bound error for our processing method; (2) a $\sim$9-km baseline between two static reference sites at Helheim Glacier; (3) two kinematic baselines between a static site on rock and ice sites flowing with the glacier, representative of low-noise and high-noise solutions. The examples shown here are of solutions where all ambiguities are fixed to integer numbers, errors arising from this source are described in Section 2.5.4.

2.5.1.1 Statistics for a zero-baseline laboratory experiment

We ran a zero-baseline (ZBL) test at the roof of our office building with GPS systems similar to the ones operated in Greenland. In a ZBL test the GPS signal from a single GPS antenna is split in two and fed to two receivers, thus forming a two-element baseline of effectively zero distance (e.g., Park et al., 2004). The only difference in the path travelled by the signal recorded by each receiver is the cable with which each of them is connected to the antenna splitter. When processing zero-baseline observations in a differential GPS mode, all errors with origin between the GPS satellite and the splitter cancel out exactly. These include satellite errors, atmospheric delays, and site-dependent errors such as multipath. Only the noise due to the signal traveling through different cables and receiver-dependent errors, such as receiver thermal noise and clock error, do not cancel. Therefore, ZBL tests are normally performed to assess the accuracy of a GPS receiver system or a processing method. Here we present a high-rate processing of a ZBL experiment, applying the processing method described in section 2.3.2, which we use as a calibration experiment. We take the precision of this solution as a low-bound error of our data processing strategy.

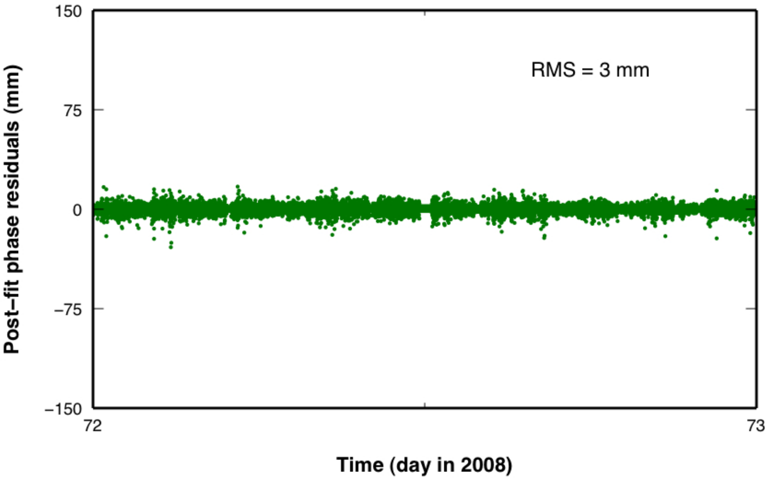

Figure 2.1: Post-fit phase residuals as a function of time for a static GPS system in a zero-baseline test carried out on the roof of our office building in Barcelona. (There are some data segments which have been edited out by the processing software due to low data quality. They show up in this figure as zero post-fit phase residuals (e.g., approximately, in the middle of the day).)

The post-fit phase residuals of this calibration test are shown in Figure 2.1 as a function of time. Each point in this graph is the residual for a specific satellite and an individual site at a given time. The RMS of the phase residuals statistics is 3 mm. A typical RMS value for an LC static or point-positioning solution of a ZBL test is usually ~1 mm (e.g., Park et al., 2004). A kinematic solution is slightly noisier, since it estimates the receiver coordinates every 15 seconds, thus, using much less observations in each estimation than a static processing method (where the estimation of a unique average position of the receiver is sought). The phase residuals are essentially zero-mean ($6\ 10^{-5}$ mm) and randomly distributed around zero, therefore indicating the absence of systematic errors.

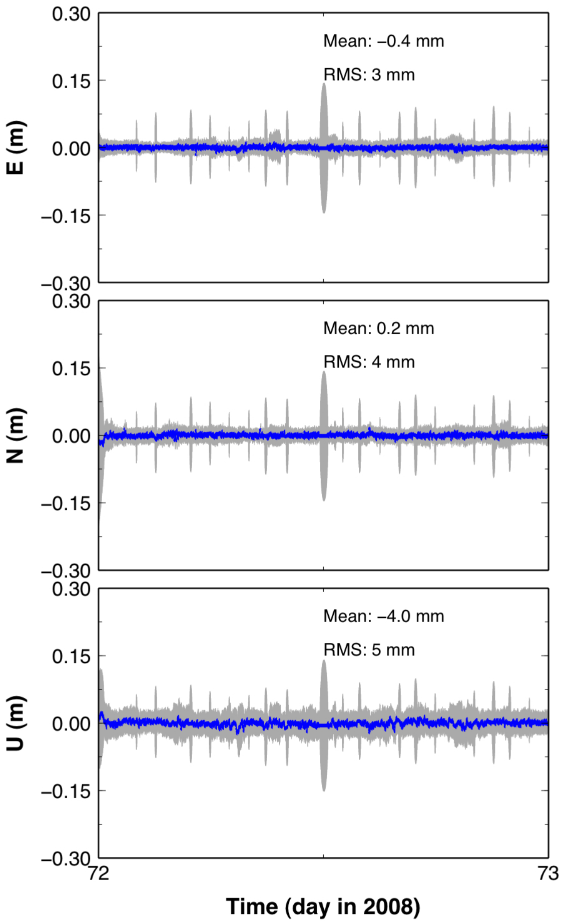

Figure 2.2: Blue dots show position estimates relative to mean position in east (top), north (middle), and vertical (bottom) components for a zero-baseline experiment. Estimates uncertainties are shown as error bars in grey. The mean position and the root mean square (RMS) of the position residuals to the mean are written above the estimates. (Low quality data segments have been edited out by the processing software. The solution corresponding to these data segments have larger error since the software simply propagates forward the solution by maintaining the position fixed.)

Figure 2.2 shows the position estimates of the kinematic site in the ZBL test with respect to the reference site and relative to the mean position in the east, north, and vertical components. The RMS of the position residuals to the mean is less than 6 mm in all three components, indicating that the error of our processing method plus hardware noise is less than 6 mm, that is, that the precision of our processing method and GPS systems is at the mm-level. The mean baseline length is less than 4 mm in the vertical, and less than 1 mm in the horizontal component, which is a lower bound for the accuracy of our processing method. This is the only type of experiment where we can assess the accuracy of the processing method and GPS system since we have ground truth information, that is, the baseline length, which is zero mm.

Unfortunately, small segments of data during the day that this experiment lasted are edited by the processing software because of bad quality. (The reason for the decreased quality is not known.) Since a Kalman filter propagates the solution (i.e., position and covariance matrix) forward, and random walk errors increase as the square root of the processing interval time, epochs with larger uncertainties indicate reduced number of observations or data gaps. Nevertheless, the impact of these bad estimates is not too relevant to the purpose of this study.

2.5.1.2 Statistics for a static ∼9-km baseline at Helheim Glacier

Here we present the solution for a baseline between two static sites at Helheim Glacier, NUN1, located in the southern margin and used as reference site in this experiment, and NUN2, located in the northern margin, both upstream from the bend at Helheim Glacier and separated by ∼8.5 km (see Figures 1.4–1.6). This serves as an additional calibration experiment that is somewhat different from the ZBL experiment for several reasons. This data, although not on the ice, it was collected in Greenland, on the glacier margin of Helheim Glacier, therefore in a high-latitude polar environment. On the other hand, the test using these observations is affected by more error sources than the ZBL test such as atmospheric delays and multipath since in this case the antennas are located several kilometers apart and on different surfaces. But still, this is a quite controlled experiment because the GPS systems are anchored to bedrock and are, therefore, static.

We have performed exactly the same processing as in the ZBL test and for the rest of solutions from the Helheim Glacier data set (Section 2.3.2). Figure 2.3 shows an example of post-fit phase residuals from this processing. Because this experiment has more error sources, the noise level has increased from 3 mm to 8 mm. As in the case of the zero baseline, the post-fit residuals are essentially zero mean ($-3\ 10^{-6}$ mm) and do not present any relevant structure, therefore, not showing signs of significant systematic errors. The corresponding position estimates, shown in Figure 2.4, have an RMS less than 6 mm in the horizontal components, slightly higher than in the zero-baseline test, and of ∼12 mm in the vertical component. The RMS is higher in the vertical component, as one would expect, because the atmospheric delay errors have a larger impact on the vertical position (e.g., Davis et al., 1985).

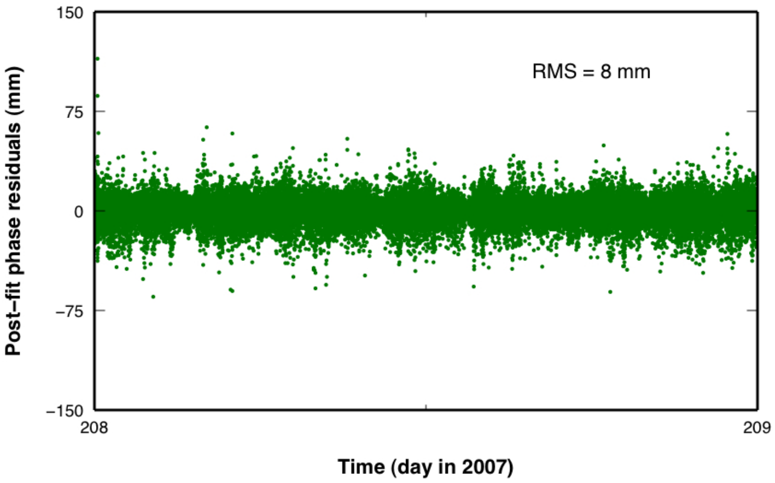

Figure 2.3: Post-fit phase residuals as a function of time for a static GPS system (NUN2, see Figures 1.4–1.6) located at ∼9-km distance from the static reference site (NUN1) on the glacier margin of Helheim Glacier, East Greenland.

2.5.1.3 Statistics for kinematic baselines at Helheim Glacier

Heretofore, we have showed results for static GPS receivers. Hereafter, we present results for baselines between a static reference system on the glacier margin (NUN1) and a site on the glacier flowing several meters per day. Such baselines are the focus of the study in this thesis.

Figures 2.5 and 2.6 show results for two examples of kinematic baselines, the first is representative of the lowest-noise solutions in our data set, and the second corresponds to a case of higher-noise data. (Higher noise levels are typically associated with systematic errors. For example, we have seen that the noise increases significantly over time only to find that upon visiting the site, the antenna, which is supposed to remain upright, had fallen on its side.) Here, the data is processed with the same method as for the previous tests (see Section 2.3.2). In this case, in order to quantify the RMS of the position estimates we need to model the mean kinematics of the glacier site. For this reason, the examples shown here correspond to sites located far from the glacier terminus, since the farthest upglacier, the less complex the dynamics of the glacier is, as will be presented in later chapters. The daily dynamics of the sites shown here, sites IS29 from 2007 (Figure 1.5) and IS53 from 2008 (Figure 1.6), can be approximated by a linear model, with accelerations being negligible.

Figure 2.5 and 2.6 show, respectively, the post-fit phase residuals versus time, and the position of the sites relative to mean speed. The RMS of the post-fit phase residuals and the position residuals to the linear model have increased with respect to the static baseline, as one would expect, since the sites are deployed on a deforming ice surface, located at a larger vertical distance from the reference site, and moving with respect

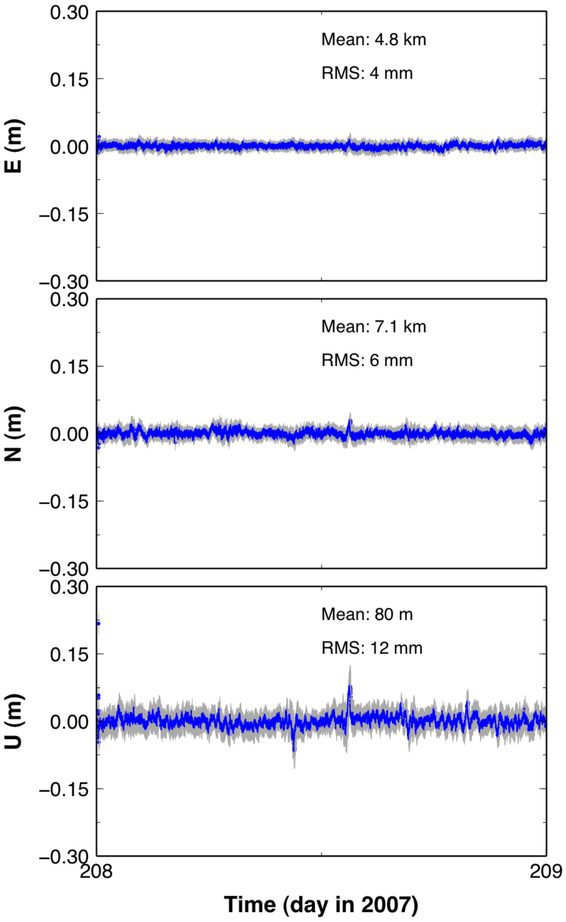

Figure 2.4: Same as in Figure 2.2, except here for the static site NUN2 with respect to the reference site NUN1, on day of year 208, 2007.

to it. Hence, this adds to the problem high background velocities, higher atmospheric differential delays, and possibly larger multipath effects from a reflective ice surface. The RMS of the post-fit phase residuals increase considerably in the example of higher-noise data. Moreover, the phase residuals in this case show a time-dependent pattern, indicating that the noise is dominated by a systematic error, which also increases the noise in the corresponding position estimates. The repetition of the noise pattern in the position estimates from preceding and following days (not shown) suggests that the systematic error is dominated by multipath (e.g., Elósegui et al., 1996). The effect of multipath in the position estimates of kinematic baselines at Helheim Glacier is shown and further discussed in Section 2.5.6.

In summary, the high-rate position solutions of fast-flowing ice sites at Helheim Glacier, processed with respect to a static reference site on the rock margin with TRACK and the method described in Section 2.3.2, have a precision of ∼1–2 cm in the horizontal component, and ∼2–5 cm in the vertical component. Lacking external methods to

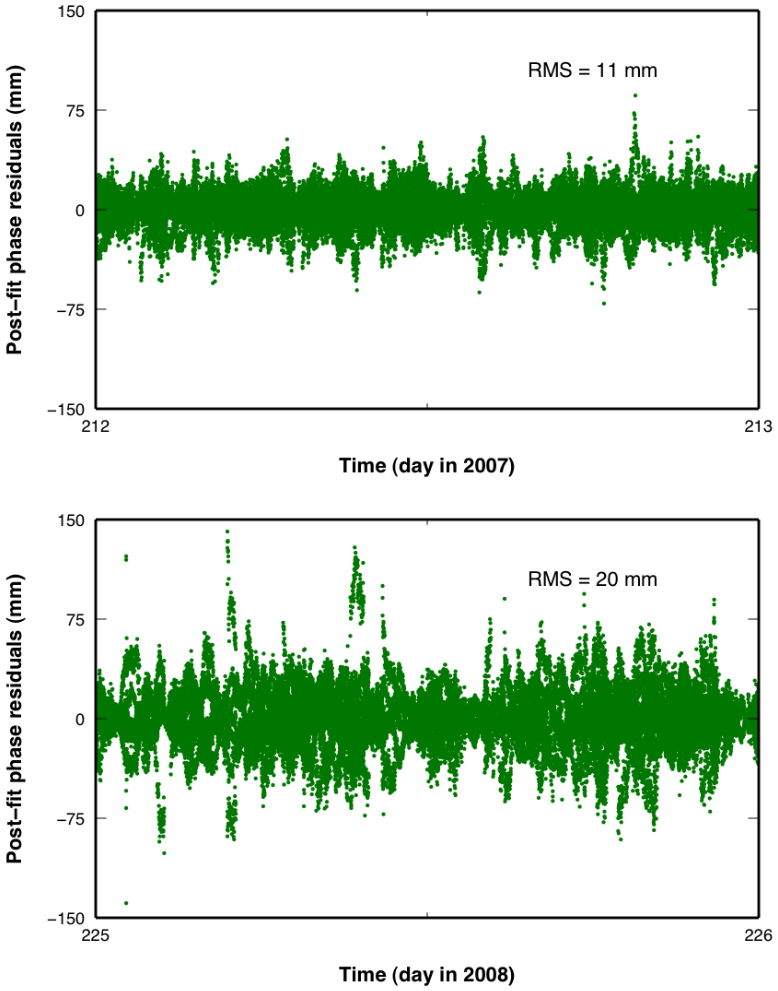

Figure 2.5: Post-fit phase residuals as a function of time for (top) an example with low-noise data (site IS29 on day of year 212, 2007), and (bottom) an example of high-noise data (site IS53 on day 225, 2008), both located on the upstream part of Helheim Glacier, and flowing at a velocity of ∼12–13 m/d.

quantify the accuracy and precision of our position estimates of glacier flow, we take the RMS of the position residuals of the ZBL test as the lower bound of the precision of our processing method, as indicated in 2.5.1.1.

2.5.2 Ionospheric errors

For the purpose of analyzing the precision of L1 kinematic solutions in a glacier environment, we have processed the dual-frequency observations collected at Helheim Glacier during the 2007 summer campaign, using only the L1 observable. The direct comparison between position estimates from the LC and L1 solutions enables to assess the importance

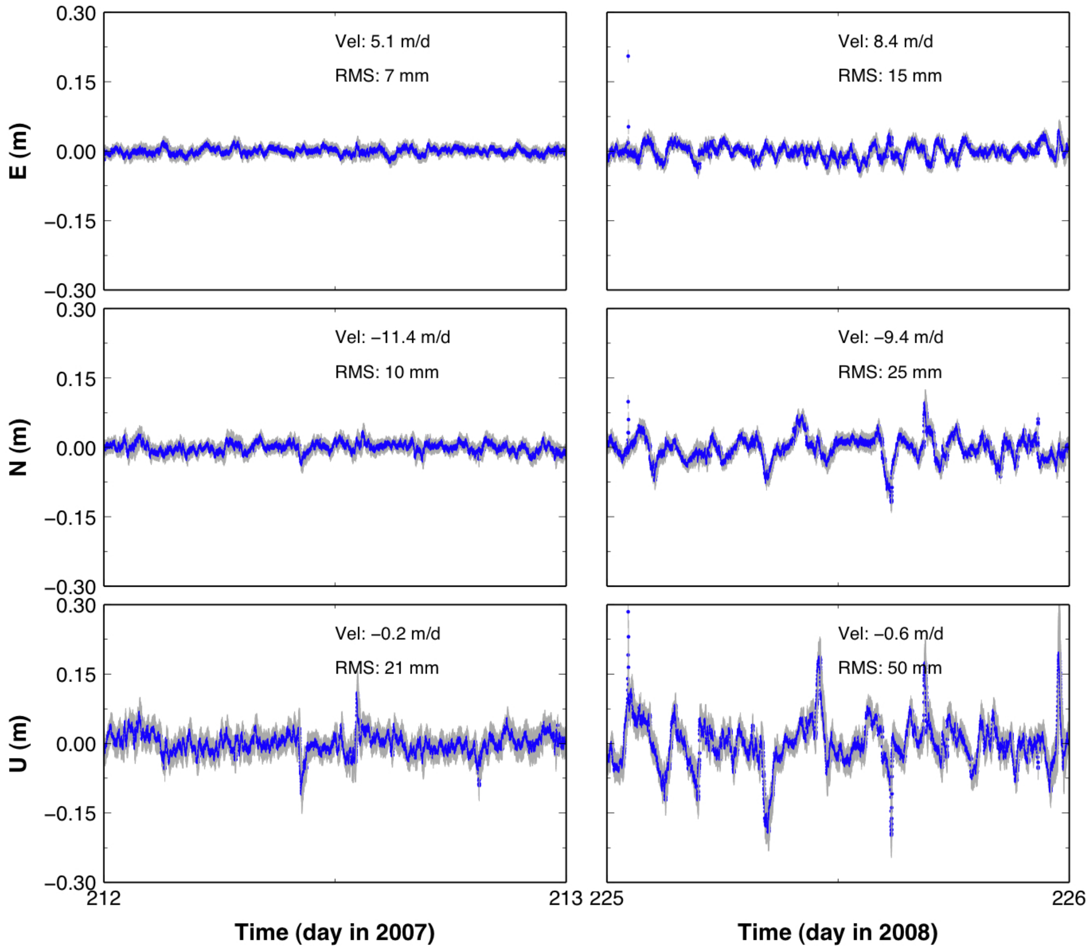

Figure 2.6: Blue dots show position estimates relative to mean daily speed in the east (top), north (middle), and vertical (bottom) components for (left) an example with low-noise data (site IS29 on day of year 212, 2007), and (right) an example of high-noise data (site IS53 on day 225, 2008). Estimate errors bars are shown in grey. The daily speed in each of the components is written above the estimates, along with the root mean square (RMS) of the position residuals to such speeds.

of the ionospheric delay in the position estimates from Helheim Glacier.

Figure 2.7 shows the RMS of the post-fit phase residuals as a function of baseline length for all glacier sites with respect to the two reference sites deployed in 2007, NUN1 and NUN2. Baselines during this year range from ∼3 to ∼15 km. Each point in this figure corresponds to a glacier site – static site pair for a given day of the 2007 campaign. The figure shows a clear difference in behavior between the LC and L1 solutions. The RMS of the LC solutions is approximately baseline independent and covers a range from ∼6 to ∼23 mm. On the other hand, the RMS of the L1 solutions increases with increasing baseline length. We have fitted a simple linear model to the L1 RMS results,

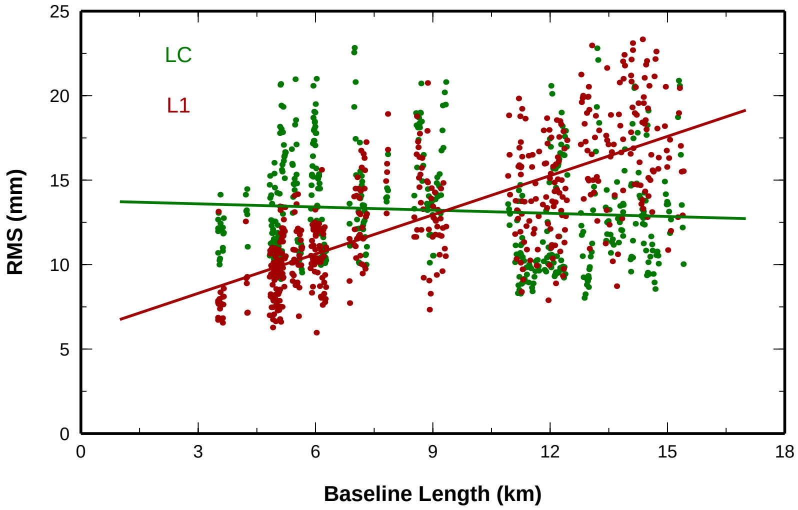

Figure 2.7: RMS statistics of daily post-fit phase residuals versus baseline length for LC solutions (green) and L1 solutions (red) of all glacier site – reference site pairs and all days of observation in the 2007 summer campaign. Lines are best-fit linear model to the LC and L1 phase residuals.

which shows that the RMS increases at a rate of a 0.8 mm per km of baseline (with a correlation coefficient of 0.7, significant at the 95% level), whereas the slope of a linear fit to the LC RMS statistics is -0.06 mm per km (with a correlation coefficient of 0.1). This behavior suggests that ionospheric errors have an important effect for baselines larger than ~9 km, when the LC solutions are more precise than the L1 solutions. For shorter baselines the L1 solution is more precise, presumably because the ionosphere does not change much over this distance, and thus a higher degree of cancellation is achieved when using differential positioning. Moreover, the LC combination amplifies the noise level of the solution because it is a linear combination of two observables, L_1 and L_2. Applying the error propagation law and assuming the same noise for both phases ϵ, the noise of L_C, ϵ_{L_C} is higher by a factor of ~3,

$$\epsilon_{L_C} = \frac{f_1^2}{f_1^2 - f_2^2}\sqrt{1 + \left(\frac{f_2}{f_1}\right)^2}\,\epsilon \sim 3\,\epsilon. \tag{2.15}$$

Therefore, the receiver noise is amplified in L_C with respect to L_1. Of course, to compute this factor correctly, one must take into account the different noise levels (L2 is typically noisier than L1). For this reason L1 solutions are more precise for baseline lengths for which the ionosphere has a small effect. Nevertheless, for consistency, in the processing of the Helheim Glacier GPS data sets from summers of 2006–2008 we chose to process LC solutions for all baselines.

2.5.3 Reference frame errors

Here we aim to investigate local reference frame errors in our position estimates. In order to do this, we compare the position estimates of a site on ice using two different static sites as reference. Figure 2.8 shows the difference between position estimates of site SN05, processed with respect to reference sites NUN1 and HEL1 (see Figure 1.4 for the location of these sites at Helheim Glacier). The two reference sites are separated by ∼16 km. The mean daily difference between both solutions is of less of 1 mm in each of the components, north, east, and vertical, well below the lower bound of the precision of our processing method (see Section 2.5.1). The RMS of the difference is of less than ∼7 mm in the horizontal components, and ∼16 mm in the vertical component, thus consistent with results in Figures 2.4 and 2.6, as one would expect. The variation in the difference in position is probably dominated by errors in the observations of the reference sites, since the errors from the site on ice cancel to first order.

2.5.4 Systematic errors associated with non-fixed phase ambiguities

Resolving and fixing to an integer value the phase ambiguities (which include first observations, rising of new satellites above the elevation angle cutoff, and cycle slips) is the most challenging part of the processing method. The largest inaccuracies in our solutions are observed associated with non fixed ambiguities. This issue becomes critical for noisy data associated with, for example, a GPS antenna that turned upside-down or fell in a crevasse and still continued collecting data. (We have tried to understand the quality of such data, instead of editing it out.) In such cases many ambiguities remain unresolved, and therefore the solution becomes unreliable.

Figures 2.9 and 2.10 show a set of timeseries that illustrate the effect of non-resolved ambiguities on the position estimates (position estimates are hereafter shown in the local reference frame defined at each site, along-flow, cross-flow, and vertical, see Section 2.4). Figure 2.9(a) shows an example where all of the ambiguities were resolved and fixed to integer values, thus the smoothness of the position estimates. (The semidiurnal signature in the along-flow component is tidal in origin, as discussed in Chapter 4). Figure 2.9(b) shows a case where the data is so noisy that almost all of the estimates involve observations from non-fixed segments of data. Figure 2.10 is an intermediate case, showing two examples in which part of the solution is affected by non-fixed biases. The RMS of the residuals to mean flow are shown for each of the components of motion.

TRACK outputs, along with the estimated position coordinates, the number of non-fixed ambiguities at each epoch of data. More specifically, the quantity it outputs for each epoch is the number of observations used in generating the position estimate that pertain to a segment of data with an initial ambiguity that TRACK has not been able to fix. The estimates from epochs for which this number is different from zero should be treated with caution, since the non-fixed biases weaken the solution. All of the estimates from epochs pertaining to a segment of data with a non-fixed ambiguity are affected by it, and therefore, these “conflictive” estimates are not isolated, but continuous fragments

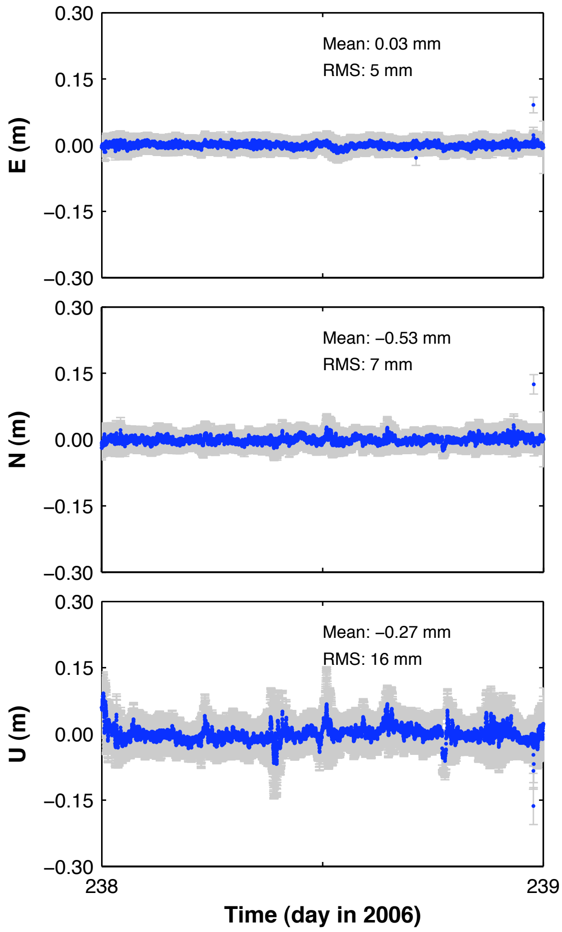

Figure 2.8: Blue dots show difference between position estimates of site SN05, on day of year 238 (2006), processed using as reference the static site NUN1 and the static site HEL1, in the east (top), north (middle), and vertical (bottom) components. The mean difference and the root mean square (RMS) of the difference in position is written above the estimates.

of estimates that can last several minutes or hours. In the figures, the epochs that involve non-fixed biases are plotted in a lighter color to indicate that they should be treated with caution.

As mentioned in the section on the processing method, we run the program in two iterations with different approaches for the resolution of ambiguities in each of them. The second iteration (2) fixes many ambiguities that are not fixed in the first iteration (1) (∼40–70% of the biases not fixed in (1) are fixed in (2)). However, this does not always mean that the solution improves from (1) to (2). For certain solutions, some offsets in the position estimates are corrected in (2) with respect to (1). However, in many cases the position estimates remain unchanged although more biases are fixed. This happens probably because the biases that are not fixed in (1), are however resolved to a value very close to the “true” integer number of cycles, which results in a good solution. And

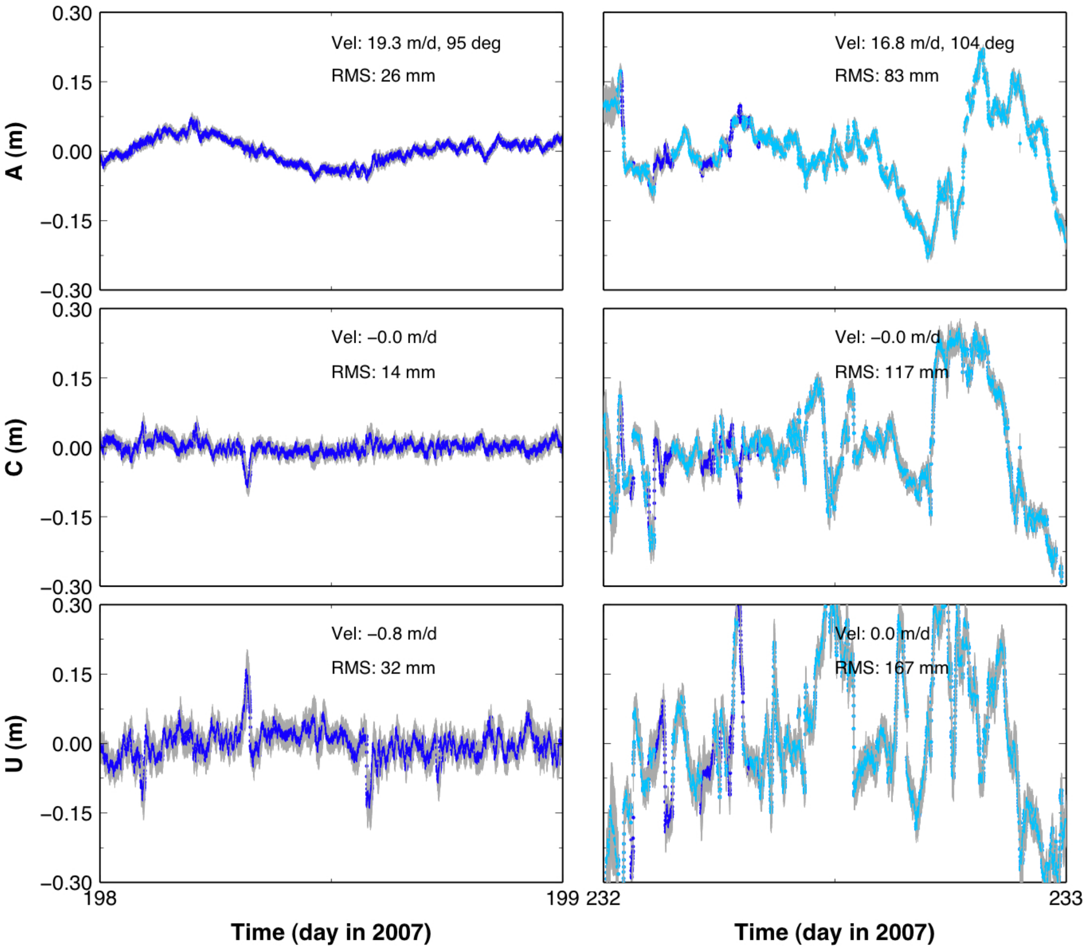

Figure 2.9: Blue dots show position estimates relative to mean daily speed in the along-flow (top), cross-flow (middle), and vertical (bottom) components for (left) an example with all ambiguities fixed (site IS24 on day of year 198, 2007), and (right) an example of very noisy data (site IS25 on day 232, 2007). Position estimates pertaining to non-fixed segments of data are plotted in light blue, good estimates are plotted in dark blue. Estimate errors are shown with grey bars. The daily speed in each of the components is written above the estimates, along with the RMS of the position residuals to such speeds, in the top panel the direction of flow with respect to the north direction is also written.

only in the cases where the resolved value is far from the true value, it produces an offset or jump in the position estimates that is sometimes repaired once the bias is fixed in (2).

This implies that we should not rule out all of the estimates that are part of non-fixed segments of data, since they may be resolved to a value very near to the “true” integer ambiguity, and hence be good estimates. However, it is not always easy to determine if such non-fixed segments of estimates are good or either should not be taken into account. The non-fixed ambiguities affect the position estimates in basically four different ways (examples for each of them are shown in Figure 2.10):

1. The entire non-fixed segment is simply offset with respect to the rest of the solution, but the segment has continuity and can last for a couple of hours and be offset by no more than a few cm (e.g., last ∼3–4 h from the example shown in Figure 2.10(a)).
2. The non-fixed segment presents a different time-dependent "shape" than it should but is continuous with the rest of estimates and simply converges to the true "shape" (e.g., first ∼2–3 h from the example shown in Figure 2.10(b)).
3. Less frequently, the non-fixed segment shows as outliers or a few estimates that are completely offset from the solution and have no continuity (some of these are observed during the first hour from the example shown in Figure 2.10(a)).
4. Although they are marked as non-fixed, they seem to be good estimates. This is usually recognized because they are consistent with position timeseries from preceding and following days, and in general with the typical behavior of the glacier (e.g., the short segments observed in both examples in Figure 2.10). Many of the solutions have a few short segments that are marked as non fixed but are perfectly continuous with the rest of the solution.

Cases 1 and 3 are easily recognizable as bad estimates. However, it is more difficult to distinguish between 2 and 4, specially for days when unusual dynamic signals are measured, such as sudden changes in flow speed. Nevertheless, most of the times, by having a sense of what the typical dynamics of a given sites is, the dubious estimates can be accepted as good estimates or either discarded.

2.5.5 Systematic errors near day boundaries

We process the data for each UT day independently. This is a natural choice since standard GPS products by the IGS are tailored to UT data processing. Some of the timeseries present poor results near day boundaries due to non-resolved ambiguities that cause position outliers just after or before the day boundary. This can be particularly problematic when we need to combine several daily timeseries to analyze a relevant geophysical signal that happened close in time to the day boundary. The two examples in Figure 2.10 show such problem at the beginning of the day.

Some tests involving the processing of 12–24 hours across the day boundaries, by means of concatenating consecutive-days RINEX and orbit files, yielded no improvement to such position solutions. Thus, we discarded the possibility of this problem being a product of the processing method at the beginning of the solution, or poor a priori information available for the first epoch. Instead, after examination of the observations, we concluded that it was a result of poor satellite geometry at those times, which provided less data constraints. For example, at the beginning of day 226 there were 6 satellites visible (with both L1 and L2 observations) from the location of our GPS network at Helheim Glacier, 8–9 satellites were visible at 12:00 UT on day 226, and 7 satellites were visible at the end of the same day (see Figure 2.10). This problem is further compounded

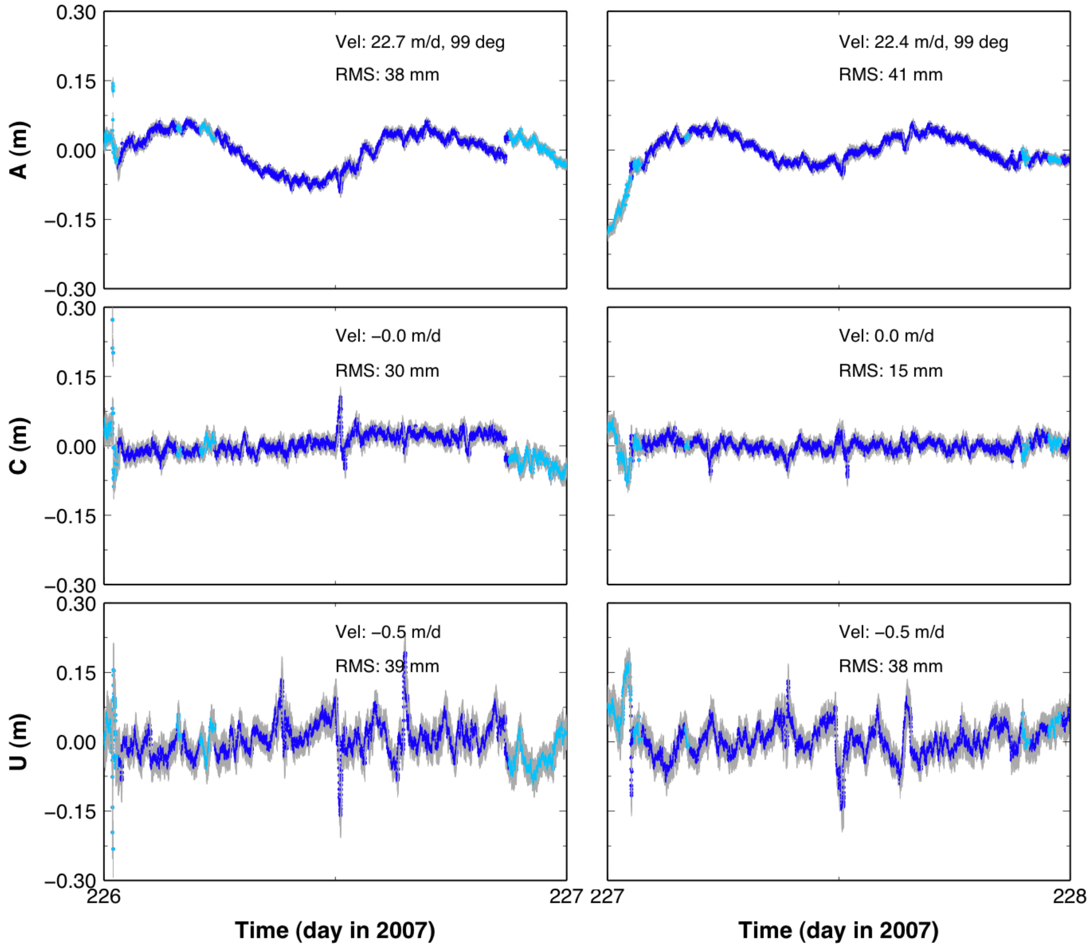

Figure 2.10: Same as in Figure 2.9, except here for two examples for which part of the position estimates are affected by non-fixed ambiguities. Examples are for site IS36 and days of year (left) 226 and (right) 227, 2007.

by the filter whose uncertainty estimates are also larger at the beginning and end, even after smoothing, than in the center because of initialization and convergence.

2.5.6 Systematic errors associated with multipath

All of the sites, including the ones located in relatively slow and less active zones of the glacier present a high-frequency, low-amplitude structure that is site dependent and most of which repeats approximately from day-to-day for each site. It has been shown (e.g., Elósegui et al., 1996) that repeatability is a clear indication of multipath errors. This is particularly true for the vertical component of site position estimates. This suggests that a substantial part of the systematic error in the timeseries from Helheim Glacier is caused by multipath. Figure 2.11(a) shows the position timeseries for one of the sites and 4 consecutive days in 2007, Figure 2.11(b) shows the position estimates for the same days but a different site. It can be inferred from visual inspection of the timeseries that the high-frequency structure approximately repeats from day to day at around the same time for each of the sites, and that such structure is different for the two sites. This is consistent for the rest of the data collected at Helheim Glacier. Because the surface on which the sites are anchored is approximately the same every day (except when significant deformation occurs due to crevassing or others), and because the geometry of the satellites in the sky repeats every sidereal day, the reflections of the GPS signals on the surrounding ice happen in the same way every day, and hence the multipath systematic error in the data repeats. A sidereal filtering technique (e.g., Choi et al., 2004), which is standard in high-precision GPS seismology or geodynamics for static sites is not desirable here because glaciological signals of interest would be washed out if applied. For example, the response of glacier flow to tidal forcing has a semidiurnal signature that also repeats from day to day (see Chapter 4).

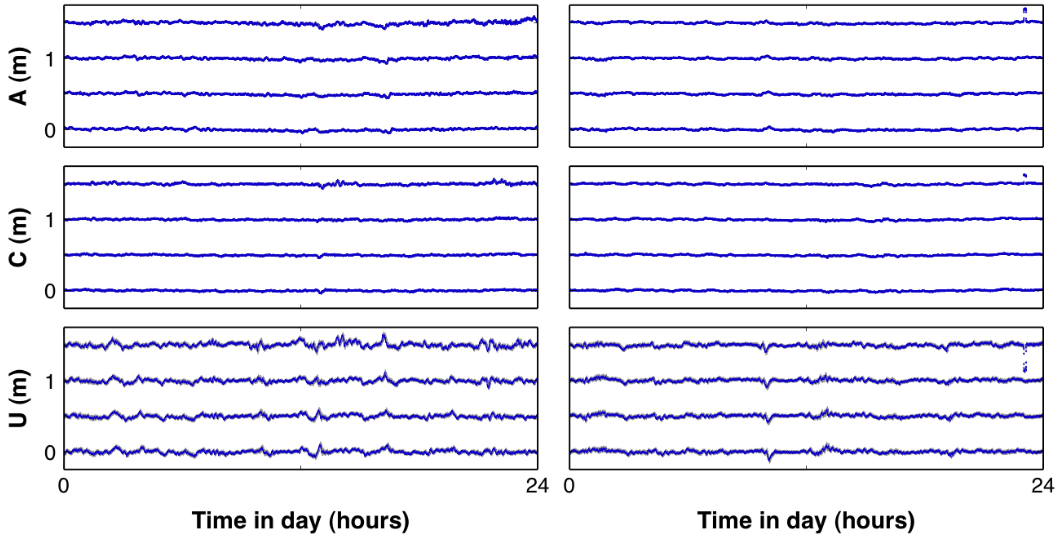

Figure 2.11: Position estimates relative to mean speed in the along-flow (top), cross-flow (middle), and vertical (bottom) components for (left) site IS28 and (right) site IS29, and 4 days, 214–217 (2007). The timeseries for each of the different days are offset by an arbitrary amount for clarity, from day 214 (bottom in each of the panels) to 217 (top in each of the panels).

2.5.7 Summary

We have obtained a lower bound for the accuracy of the processing method and GPS system, by performing a zero-baseline test, of 1 mm in the horizontal components and 4 mm in the vertical component, and a lower bound for the precision of the processing method and GPS system of less than 6 mm. A study of high-rate position timeseries of fast-flowing GPS sites on ice at Helheim Glacier yield a precision for such solutions of ∼1–2 cm in the horizontal component, and ∼2–5 cm in the vertical component.

A comparison between position solutions using the L_C observable and the L_1 observable, yield that even though L1 solutions are more precise for short baseline lengths, ionospheric errors become important for baselines larger than ~9 km. On the other hand, a comparison between solutions using two different reference sites show that local reference frame errors are well below the accuracy of the processing method. Non-fixed segments of data should be taken with caution, however, in most cases, bad position estimates can be visually detected, given a certain knowledge about the mean dynamics of the site. Less data constraints near to day boundaries can sometimes cause bad position estimates at the beginning or end of a day. And, finally, most of the position solutions present a low-amplitude, high-frequency structure caused by errors of multipath origin.

Chapter 3

Mean kinematics of Helheim Glacier during summers of 2006–2008

The main scientific objectives of the project at Helheim Glacier required high-temporal resolution and high-accuracy data of glacier motion. Satellite remote sensing offers image coverage over large spatial regions in areas where it is difficult and expensive to access by field-based programs, and provides a broad view, spatially and temporally, of glacier velocity (e.g., Murray et al., 2010). However, measurements of flow velocity obtained with cross-correlation feature-tracking techniques on satellite-based radar or visible-band images are limited by the availability of pairs of images, and generally yield one measurement of velocity per season. Moreover, such velocity measurement is a mean value of a dynamic system over two dates separated from several days to several months (e.g., Howat et al., 2005; Luckman et al., 2006; Howat et al., 2007). In such studies, where inter-annual variations in speed are investigated, the results suffer from the effect of seasonal and inter-seasonal speed variations, when taking one measurement as representative of an entire year or season.

On the other hand, the time resolution provided by ground-based GPS data at the locations where GPS sites are installed far exceeds the resolution that is possible from satellite imagery, and produces velocity estimates of higher accuracy (though the time span of such data is limited to the duration of field campaigns). It was not the main objective of this project to investigate inter-annual variations in speed, rather to characterize sub-seasonal to sub-daily to sub-hourly behavior, which cannot be observed with any other technique. However, the GPS data collected along and across Helheim Glacier also provides the opportunity to characterize the general state of the glacier's flow. The goal of this chapter is to give a broad view of the flow field of Helheim Glacier, and its variations, during 2006–2008 before immersing in the analysis of higher frequency flow characteristics. In this chapter we focus on (1) the spatial characterization of the mean summer flow of the glacier during 2006–2008 and its consistency from year to year, and (2) the temporal dependence of the mean daily velocity at each of the sites for the duration of the season and its spatial coherence throughout the glacier.

The flow speed of Helheim Glacier underwent dramatic changes between 2000 and 2005, increasing from 22 m/d to 30 m/d at the terminus, coinciding with a retreat of its calving front of several kilometers, and extensive thinning (Howat et al., 2005; Luckman et al., 2006; Stearns & Hamilton, 2007). The greatest changes took place in the summers of 2003 and 2005 (Howat et al., 2007). Here we extend these results to the subsequent years, 2006–2008, and we expand the temporal resolution of the speed estimates to daily measurements.

3.1 Method

The processing of the GPS data collected at Helheim Glacier produces position estimates every 15 seconds (see Chapter 2). In this chapter we examine the mean flow of the glacier from ∼2 months to daily timescales. We first compute the mean daily velocity and position of each site, and then use these estimates to obtain a mean summer velocity of the glacier at the locations of the GPS sites.

In order to obtain an estimate of mean daily velocity, we perform, for each site and each day independently, a linear fit to the 15-seconds-rate position estimates as a function of time for each of the three topocentric coordinates, i.e., north, east, and vertical components. This also yields an estimate of the mean daily position for each site (since we use the mid-day epoch as the reference time for the fit). Daily speeds range between 2 to 27 m/d, with formal errors in general of less than ∼1 mm/d. At a 1-day timescale, a simple linear model describes markedly well the daily kinematics of the glacier sites, with the RMS of the residuals to best-fit estimates ranging between ∼10 mm to ∼10 cm. Second-order terms in describing daily glacier's kinematics start to become important for sites close to the calving front, and include ocean tidal response, speed variations related to glacial earthquakes and changes in basal lubrication due to meltwater runoff, smaller constant accelerations, etc.. These second-order terms are not considered at this stage, but they are modeled and analyzed in greater detail in Chapters 4–6. Results for specific days for which an average speed can not be estimated with confidence are eliminated. These are cases for which there are too few observations or the observations result in a bad solution due to, for example, many non-fixed ambiguities.

We then compute the mean horizontal speed of each site over each summer by performing a quadratic fit to the daily position estimates in the north and east components. We observe that, in general, the glacier speeds up over the summer, as it is discussed later in this chapter. Therefore, at this longer timescale of ∼2 months, it is warranted to use a quadratic model to describe the kinematics of the glacier. Figure 3.1 shows two examples of timeseries of daily position estimates with respect to the estimated mean summer speed, for sites IS27 and IS22, located in the upglacier and downglacier area, respectively, in 2007 (see Figure 1.5). These examples clearly illustrate the need for an acceleration term when fitting the data. In general, a quadratic term over a 2-month

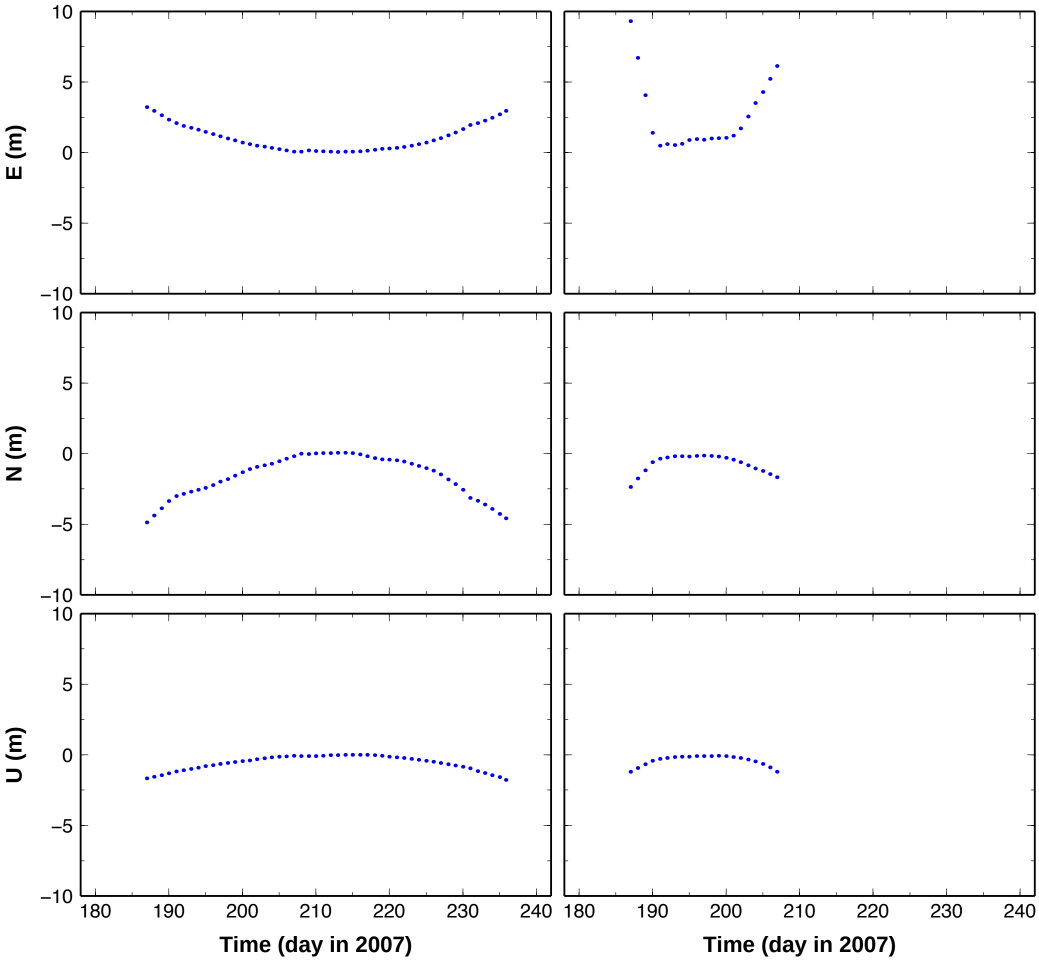

Figure 3.1: Daily position estimates relative to mean speed in the east (top), north (middle), and vertical (bottom) components for (left) site IS27 and (right) site IS22, and all days during which they operated at Helheim Glacier in summer 2007. The estimated mean speeds for these sites are 13.14±0.01 m/d for IS27 and 22.45±0.06 m/d for IS22 (see Appendix C). Error bars are in general less than ∼1 cm, thus smaller than the size of the markers. (The timeseries are offset from zero because the acceleration term in the fit to the data has not been removed.)

timescale describes well the data, since the boundary conditions are not expected to change significantly over this time period; longer timeseries would undoubtedly include seasonal variations, and thus, a quadratic model would not be sufficient. However, sites located near the terminus, where boundary conditions can change significantly over short timescales, present a more complicated behavior and would require a model that introduces more physics than what can be described by a simple quadratic form to obtain a more accurate speed estimate. Figure 3.1(b) shows an example for one of such sites, IS22, located very near the calving front in 2007. Despite the complex dynamics of Helheim, for consistency here we use the average velocity resulting from a quadratic fit to the daily position estimates over the summer and throughout the glacier to describe the mean summer flow of the sites. Departures at individual sites from such behavior are deferred to later chapters.

In this chapter we first discuss the mean summer flow of Helheim Glacier, Section 3.2 presents maps of the average flow field of the glacier during the summers of 2006–2008. (Appendix C contains a list of the mean summer horizontal speed and flow direction for each site.) Then, Section 3.3 discusses the daily variations in speed.

3.2 Mean summer flow of Helheim Glacier

Figures 3.3–3.5 show the mean summer horizontal velocity for the GPS sites installed at Helheim Glacier during the field campaigns of 2006–2008. Each of the arrows in these figures illustrates the mean horizontal speed and flow direction of each of the sites for the time period during which they remained on the glacier (see Appendix B for a list of the sites and the time periods during which they operated, and Appendix C for a table with their mean summer horizontal speed and flow direction). It is worth noting that the average for different years and for different sites in each of the years is not always done over the same time span nor period. Each of the three campaigns took place on slightly different dates, and in each year different sites were deployed during different time periods. Many of the results are averages over the entire duration of the campaign, however in other cases this is not true (see Figures 1.4–1.6 for the location of the sites referenced hereinafter). For example, the mean speed for sites SN05–08 is only representative of ∼4–5 days at the end of August 2006; the results for sites IS20–24 are the mean over the first half of the summer of 2007, while the results for sites IS35–39 are the average over the second half of the same summer; and the speed for site IS40 is the mean over the first half of the summer of 2008.

In general, these results show that the glacier flows fastest near the calving front and gradually slower the farther from the terminus, and therefore, that the glacier is overall under extensional regime as it flows towards the ocean. Also, the sites located offset from the center flowline of the glacier flow slower than those located on the center, with the speed rapidly decreasing towards the glacier margins. Such velocity gradients in the along-flow and cross-flow directions result in longitudinal and lateral strain rates, respectively, causing the glacier to continuously open fractures which eventually become large crevasses extended in various directions, in general perpendicular to the flow direction, visible on the glacier's surface (see Figure 3.2).

In each of the summer campaigns, the fastest GPS site was the one located closest to the calving front, flowing at a mean speed of ∼20–24 m/d. The fastest site during the three summer campaigns was IS20, from 2007, which flowed at a mean speed of ∼24 m/d. The slowest site flowing on the centerline of the glacier was the one located furthest upglacier in 2008, at ∼37 km behind the front, that flowed at ∼4 m/d. Nevertheless, the slowest sites on Helheim Glacier were the ones located offset from the centerline, being the slowest a site deployed near the northernmost glacier margin in 2006 that flowed at a mean speed of ∼2 m/d.

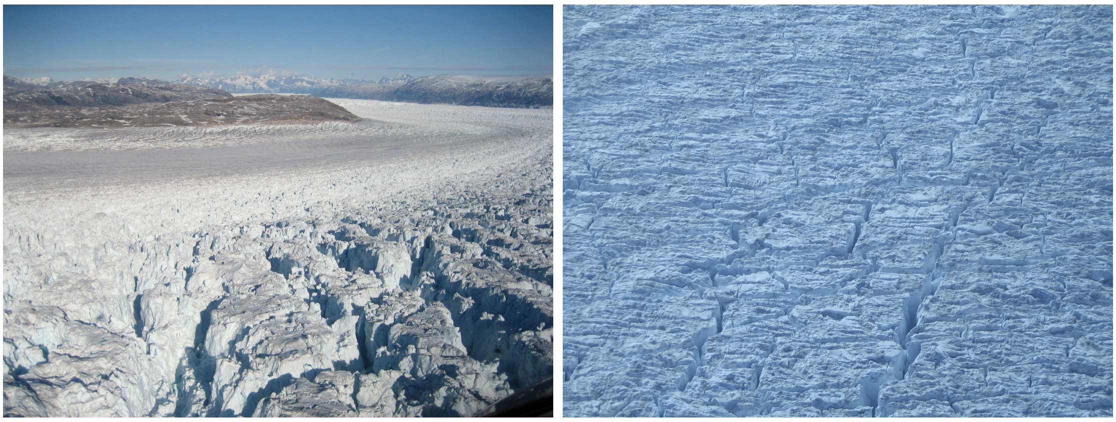

Figure 3.2: Pictures showing fractures on the surface of Helheim Glacier.

In general, the flow direction of the ice adapts to the glacier margins geometry, i.e., the direction is approximately parallel to the walls of the fjord. However, the sites located near the margins have an important flow component perpendicular to the glacier walls. The mean acceleration of the sites over the summer is always positive and ranges between ∼0–14 cm/d^2. This result yields from the quadratic fit to the daily position estimates that is used to compute the mean summer velocity of the sites. In general the acceleration of the sites is small (less than ∼2 cm/d^2) except for the downglacier sites in 2006 and, especially, 2007. In 2007, sites IS20–25 and IS35–39, located a few kilometers from the calving front, experienced a mean acceleration of ∼4–14 cm/d^2, which represents less than ∼1% increase in velocity over a day. Sites located in similar positions in years 2006 and 2008 present lower accelerations. The variation in speed of the sites over the summer is analyzed in greater detail in Section 3.3.

3.2.1 Average flow field in 2006

The average flow field of Helheim Glacier during the Arctic summer of 2006 is shown in Figure 3.3. (For sites names see Figure 1.4.) During the field campaign of summer 2006, a few sites were deployed in the downglacier area just behind the calving front for two short time periods, encompassing days of year 203–204, and 238–241. Of these downglacier sites, all of them positioned on the center flowline, the sites located closest to the calving front, SN03 in the first period and SN05 in the second period, flowed at a mean speed of ∼23–24 m/d; the site located ∼6 km behind the terminus in the second period, SN08, flowed at ∼18 m/d. Such a high velocity gradient results in high longitudinal strain rates near the glacier terminus (see Figure 3.6). Because ice in this area has undergone a high degree of deformation during its flow downglacier, this region it the most deformed and fragmented of the glacier.

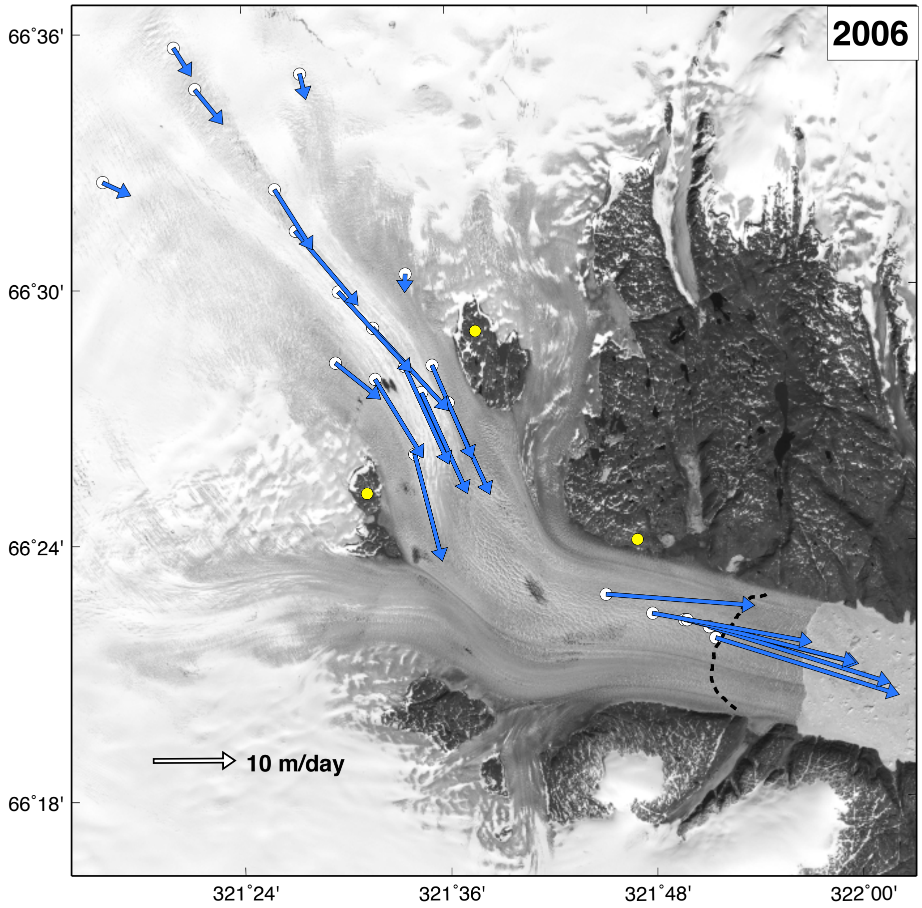

Figure 3.3: Mean summer horizontal velocity of glacier sites at Helheim Glacier in 2006. Dots indicate the deployment location of (white) ice sites, and (yellow) static reference sites. The direction of the arrows indicates the average direction of flow, and the mean horizontal speed is indicated by the length of the arrows. A 10 m/d scale arrow is given for reference at the bottom of the figure. The dashed line indicates the position of the calving front on August 30, 2006 (day of year 242).

However, during the 2006 campaign the ice sites were deployed mainly upglacier, in a configuration that included 8 sites positioned approximately on the glacier center flowline and 8 sites offset from the center, of which 4 were positioned closer to the southern margin and 4 closer to the northern margin. The sites on the glacier centerline spanned a length of ∼21 km from a distance of ∼16 km behind the calving front. Of such centered sites, the four located in the lower ∼6 km flowed at a speed of ∼13–14 m/d, so that this part of the glacier flowed relatively coherently compared to the downglacier area. More upglacier the speed gradient increased again, with the site located furthest upglacier flowing at a speed of ∼4 m/d. The sites located off the center flowline, but closer to the center rather than to the margins, flowed at a slightly slower speed than their closest centered sites, but still quite coherently, whereas the sites located closer to the margins flowed at a much slower rate. One particular site, IS08, that was positioned very near to the glacier rock margin and flowed at ~2 m/d, was the slowest of all the GPS sites operated on the glacier during 2006–2008. Two other sites operated at a larger distance from the center flowline but at the farther upglacier catchment area (where rock margins are not visible), flowed at ~3–4 m/d. The comparison between the speed of the lateral sites with the speed of their closest centered sites indicates that the cross-flow speed gradient increases as we approach the glacier margins, and is much higher in the areas where the glacier is restrained by rock margins, rather that in the catchment area, as one would expect.

3.2.2 Average flow field in 2007

The average flow field of Helheim Glacier during the Arctic summer of 2007 is shown in Figure 3.4. (For sites names see Figure 1.5.) In summer 2007, the sites on the surface of Helheim were deployed in a different spatial distribution compared to the previous year. The main difference is that during this campaign the focus was placed on the downglacier region rather than the upglacier. The five sites closest to the calving front, IS20–24 operated during the first half of the summer, and had to be retrieved during a mid-campaign field visit (to prevent receiver loss to calving). Four of them were repositioned a few kilometers upglacier and were renamed to IS35–36 and IS38–39. Also two sites, IS25 and IS26 were deployed in the center region where the glacier changes its main direction of flow. And finally, less focus was placed in the upglacier region compared to the previous year, with 5 sites occupying the region from ~18 to ~24 km behind the calving front. The sites were distributed mainly on the center flowline with only two sites deployed off the center, one in each of the sides and between the two centered sites located closest to the calving front. The four sites closest to the calving front flowed at a mean speed of ~22–24 m/d, with little difference between the sites located on and off the centerline, and similar longitudinal speed gradient than that observed in the previous year at the same region. The velocity gradient increased upglacier, with site IS24 (operated only during the first half of the summer), ~6 km from the calving front, flowing at ~19 m/d, and site IS25, ~8 km upglacier from the calving front flowing at ~16 m/d. The upglacier sites, IS27–31, flowed at ~13 m/d, a slightly slower rate than the sites located in the same area in the previous year but also in a low velocity gradient zone. However, the slowest site during the 2007 campaign, IS26, was located near the bend of the glacier at ~12 km from the calving front and flowed at an average speed of ~10 m/d. This site was located in a region where the glacier changes its direction of flow from southeast to mainly east direction, which causes the ice to compress before passing through the bend (where site IS26 is located) and extend once it has flowed passed the bend, hence first decelerating and then accelerating. No site was deployed in this region during 2006, and hence this feature of the glacier's flow field was not observed during the first year.

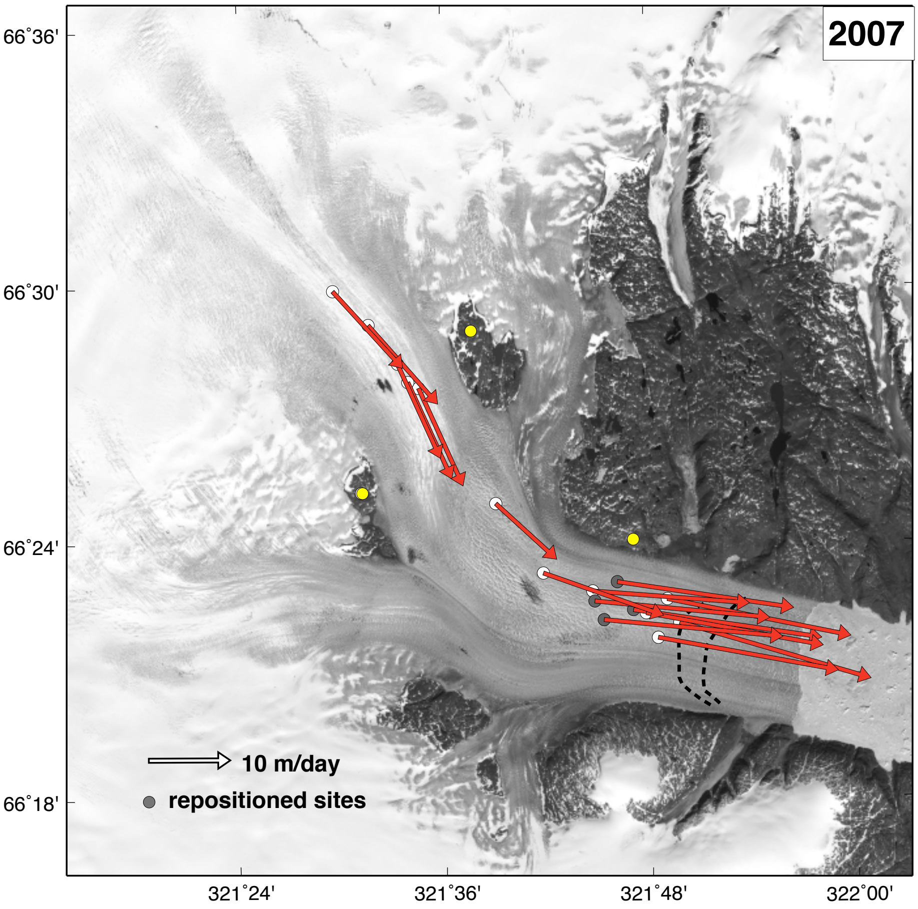

Figure 3.4: Same as in Figure 3.3, except here for sites in 2007. Relocated ice sites are indicated by grey dots. Dashed lines indicate the position of the calving front at two times during summer 2007 (easternmost line, July 4 (day of year 185); westernmost line, August 24 (day of year 236)).

3.2.3 Average flow field in 2008

The average flow field of Helheim Glacier during the Arctic summer of 2008 is shown in Figure 3.5. (For sites names see Figure 1.6.) The summer campaign of 2008 achieved a more evenly distributed network, with sites spanning from ~3 to ~37 km behind the calving front, with the uppermost site located at approximately the same position than the one in 2006. The sites were mainly positioned on the center flowline, with four sites in the downglacier area located offset from the center, and two other sites upglacier positioned slightly deviated from the center flow line. During this campaign, five sites were also deployed on the center line of Helheim's main tributary, that enters the main glacier from the south. Also, a site was deployed near the boundary between the tributary

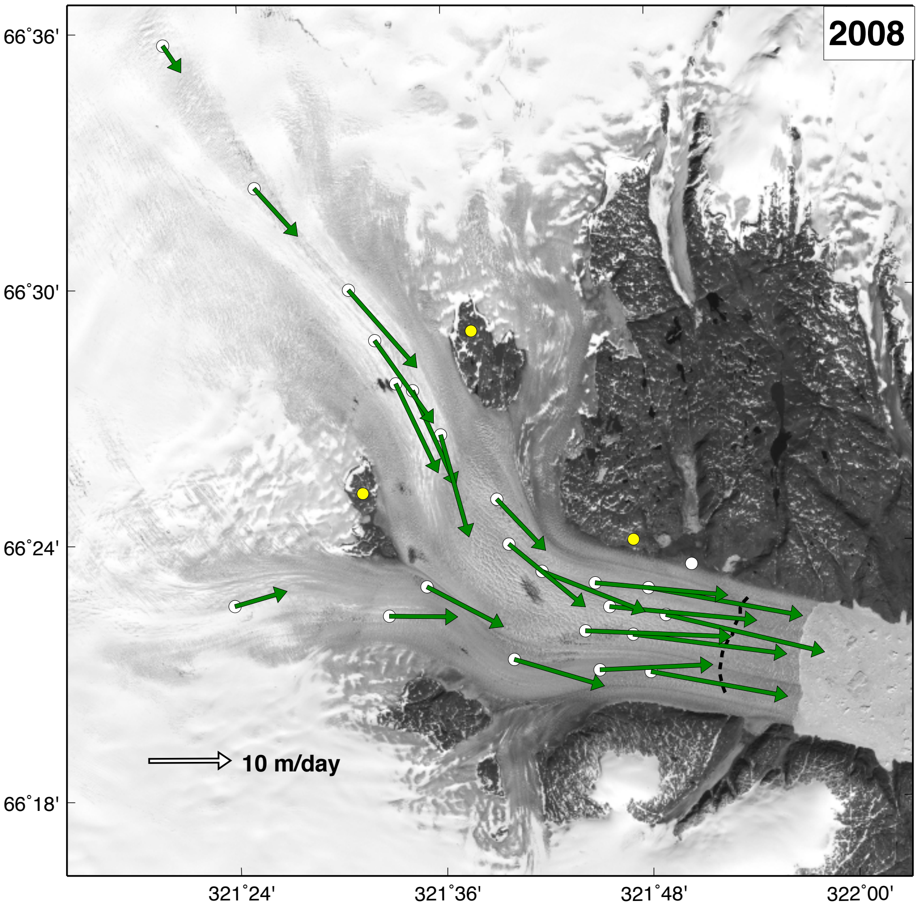

Figure 3.5: Same as in Figure 3.3, except here for sites in 2008. Dashed line indicates the position of the calving front on July 31, 2008 (day of year 213).

and the main glacier. In general, the glacier flowed slower than in the two previous years, specially in the downglacier region, with the site located closest to the calving front flowing at ∼20 m/d, ∼2–3 m/d slower than sites deployed in similar positions in previous years. However, the uppermost site, flowing at ∼4 m/d, exhibited a similar velocity than in 2006. The rest of sites distributed between the calving front and the catchment area showed a similar behavior to the previous years, although mean speed was lower in every region of the glacier, specially near the terminus. The sites deployed on Helheim's main tributary revealed that its speed was slower than the speed of the main glacier, with the site closest to the calving front (at approximately the same distance to the terminus than the closest site on the main trunk) flowing at a mean speed of ∼17 m/d, and that the speed rapidly decayed upglacier, with the site deployed furthest from the terminus in the tributary, at ∼21 km distance, flowing at just ∼7 m/d, while at the main glacier sites located at similar distances from the terminus flowed at ∼12 m/d.

3.2.4 Average flow and strain rate of the center flowline

Figure 3.6 shows the mean horizontal speed and the longitudinal strain rate of the sites on the center flowline of the glacier in each of the summer seasons during the period 2006–2008. The mean summer horizontal speed of the sites deployed approximately on the center flowline of the glacier is plotted with respect to their distance to a reference position of the terminus. The calving front positions shown in Figures 3.3–3.5 were derived from satellite images from days: August 30, 2006; July 4 and August 24, 2007; and July 31, 2008. Among these, the most advanced position of the calving front was the one on July 31, 2008. We have chosen this calving front position as the reference for the distances of the sites shown in Figure 3.6.

The figure also shows the approximate elevation profile on the center flowline, deduced from the estimated vertical positions of the GPS sites from 2008, when the sites were deployed in a more evenly distributed network compared to 2006 and 2007. Overall, there are small differences between the elevation profiles for 2006–2008 (not shown). Differences between elevation of sites roughly reoccupied in different years are discussed in Chapter 4. For the purpose of this section, this approximate elevation profile is sufficient.

The figure shows that the flow speed of Helheim Glacier was quite consistent for all three years. The largest differences are observed in the downglacier area, where also the variation in speed during the summer is higher (as indicated by the acceleration estimates, that are generally highest in this area, as further discussed in Section 3.3). Flow speed in the downglacier region (up to $\sim$12 km from the calving front position) was highest in 2007, followed by the flow speed at the end of August 2006 (the comparison between these two results should be taken with caution, since estimates in this area for 2006 are averages over only $\sim$4–5 days at the end of August). In 2008, the downglacier region flowed somewhat slower than in the two previous years ($\sim$20% slower at the calving front, compared to 2007). In the upglacier region extending between $\sim$16–24 km from the calving front, the flow speed was very consistent from year to year, with the speed in 2006 being slightly higher. In the upglacier region located between $\sim$26–37 km from the calving front, where very few measurements are available and limited to years 2006 and 2008, the flow speed is similar in both years.

The figure also shows the dependence of the longitudinal strain rate with distance from the calving front. Longitudinal strain rates are computed between each pair of consecutive sites, using their mean speed and the distance between both sites. The highest strain rates ($\sim$0.3–0.7 yr^{-1}) are observed in the downglacier part, extending up to $\sim$12 km behind the calving front, where the ice rapidly accelerates towards the terminus. The region just upglacier from the bend is a compression zone associated with the change in direction of the glacier's flow, where we estimate strain rates of up to $\sim$-0.5 yr^{-1}. This region coincides as well with the steepest surface slope that we observe at the glacier, as indicated by the elevation profile in Figure 3.6. As had been indicated above, the upglacier region comprised between $\sim$16–24 km, that flows at $\sim$13 m/d, presents very low longitudinal strain rates ($\sim$-0.1–0.1 yr^{-1}). And finally, the uppermost part of

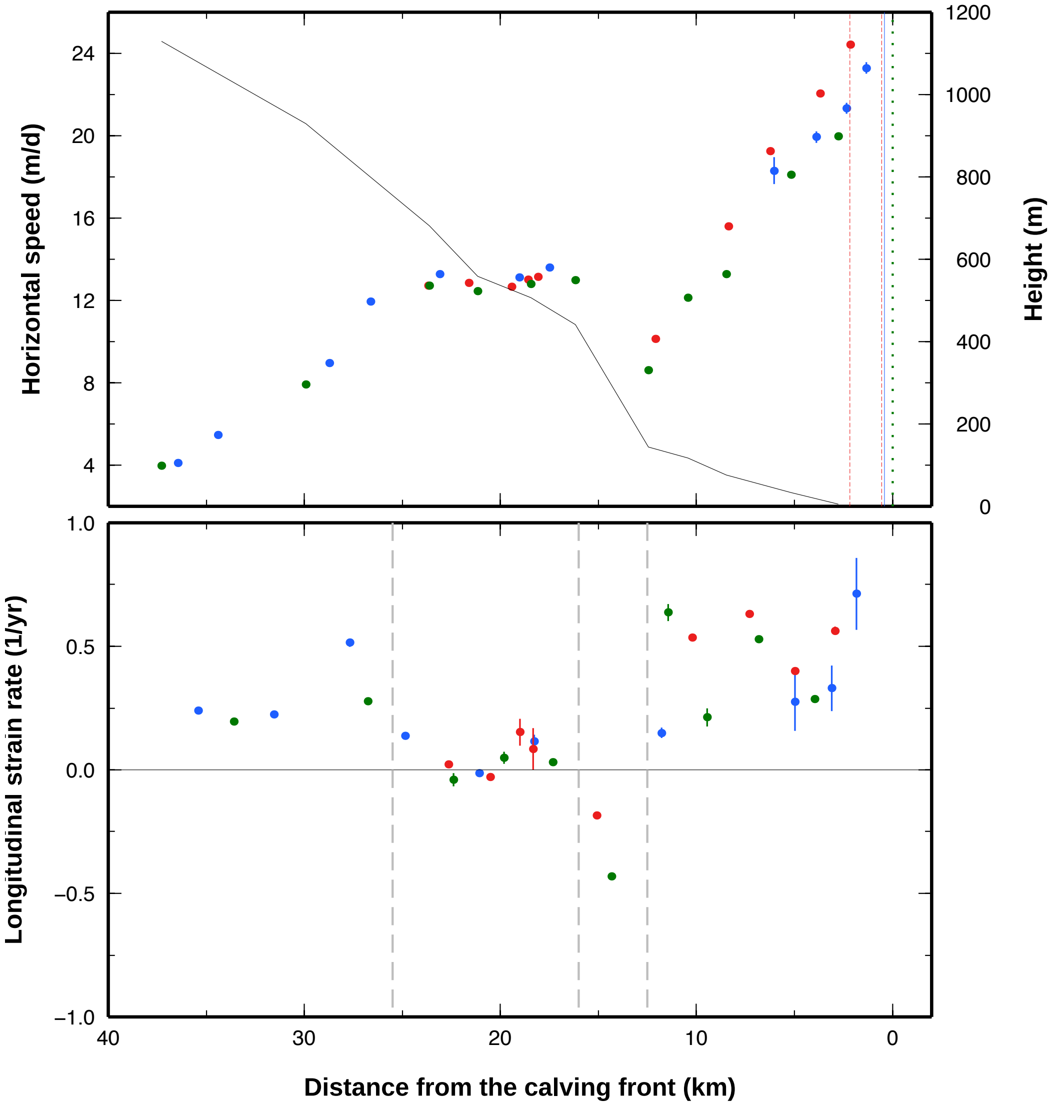

Figure 3.6: (Top) Dots: Mean horizontal speed of sites located approximately on the center flowline as a function of distance to a reference terminus position in 2006 (blue), 2007 (red), and 2008 (green). Error bars are in many cases smaller than the size of the symbols, except for some sites in 2006 where observations were made over a very limited time span. Solid line: elevation profile, as computed from the GPS sites positions from year 2008 (with respect to the vertical position of the site closest to the calving front), when sites were more evenly spaced throughout the glacier. Vertical lines: calving front positions on days shown in Figures 3.3–3.5 for 2006 (solid), 2007 (dashed), and 2008 (dotted) (color coded as dots). (Bottom) Longitudinal strain rate on the center flowline of the glacier between each pair of consecutive sites (color coded as in the pannel above). Dashed grey lines are drawn to separate zones in the glacier with different flow regime (referenced in the text). Distances are with respect to the calving front position on July 31, 2008 (day of year 213).

the glacier is also an extending flow zone, with strain rates slightly lower than in the downglacier region (∼0.2–0.5 yr^{-1}).

The elevation profile in Figure 3.6 shows that the surface slope of Helheim Glacier is relatively constant upglacier, that it increases markedly in the compression zone, and then flattens again where the ice accelerates downglacier. The calving front at the beginning of the summer of 2007 was approximately in the same position that it was at the end of summer 2006. During the 2007 summer Helheim's terminus retreated by ∼2 km, readvancing again over the winter, so that in midsummer 2008 it was approximately at the same location that at the end of summer 2006 and the beginning of summer 2007.

3.2.5 Discussion

The horizontal speed of Helheim Glacier ranges from ∼24 m/d near the terminus to ∼4 m/d ∼37 km upglacier. In general the flow speed gradually increases from upstream towards the calving front, so that extending flow dominates over the majority of the glacier's extension. Such high speed gradients, and associated high positive longitudinal strain rates are possibly caused by the ice flowing from the catchment area into the valley walls, which converge in the downstream direction, causing transverse compression of the ice that must be compensated by longitudinal extension (Paterson, 1994). Despite that in the lower ∼8 km the glacier walls widen compared to upglacier, two tributaries converge into the main flow a few kilometers upglacier, further restraining the flow of the main glacier. Also, changes in the boundary conditions at the terminus (the calving front can be highly dynamic, as obseved in MODIS images) may play a role in causing the high strain rates observed in the lower part of the glacier, as will be discussed in Chapter 5.

However, a compressing flow region exists in the vicinity of the bend in the glacier, where Helheim Glacier undergoes a significant change in flow direction from southeast to mainly east. This possibly causes the ice first to compress upglacier and flow slower, and to extend once it passes the bend, rapidly increasing its speed towards the terminus. (Due to the high deformation of the glacier surface in this area, which complicates its accessibility, we have very few observations in this region.) The variation in the flow regime from extension to compression and again to extension, as the ice flows downwards, is accompanied by a significant change in the slope of the surface of the glacier (see Figure 3.6), with a very steep surface around the compression zone compared to upglacier, that evolves in a much moderate slope as the ice accelerates and approaches the terminus.

Although few stations were positioned off the center flowline, the observations indicate that the horizontal speed varies little across the central part of the glacier, with sites located just ∼2–3 km offset from the center flowing at similar speed than those located on the center flowline. However, speed decreases rapidly near the margins, suggesting that lateral shear strain rates are high, and that friction on the glacier walls causes the ice closer to the margins to flow slower. The ice speed of many glaciers diminishes with increasing ice depth. Despite that our observations on the surface of the glacier can not be extrapolated to depth, the fact that the glacier presents a speed response to melt increase, as shown by Andersen et al. (2010), and to drainage of supraglacial lakes, discussed in Chapter 6, strongly suggests that the glacier flows mainly by basal sliding. And therefore, that the glacier is supported more strongly by friction near the sides than by basal friction.

The high longitudinal and lateral speed gradients cause important deformation on the glacier. The glacier flow field determines the location and direction of the crevasses that are opened in the ice due to longitudinal stretching. Some of these crevasses, when approaching the terminus, suffer stresses sufficiently high to cause them to propagate deep enough in the ice to isolate glacier blocks from the main glacier mass, that is, they are the fracture lines by which the glacier breaks off as icebergs (Benn et al., 2007b; Otero et al., 2010; Nick et al., 2010). The stresses in a crevasse are enhanced if they are filled by meltwater. This is a clear mechanism by which higher air temperatures can cause the retreat of glaciers by increasing their calving rate.

The location of the sites was not repeated exactly each year in the period 2006–2008, and average speeds were calculated over slightly different time periods. Thus, a very strict comparison between the glacier speed in each of the summers can not be undertaken. However, Figure 3.6 shows that overall the mean velocity of the glacier remained quite consistent from year to year in the period 2006–2008. The inter-annual variations during this period were less important than the variations reported in the period of 2000–2006 (Howat et al., 2007). However, in 2007 the lower $\sim$12 km of the glacier flowed slightly faster than in the previous and subsequent years. The speed was also more variable during 2007, as indicated by the larger acceleration estimates for that summer. A more detailed analysis of the day-to-day variations in speed and a comparison of the behavior of the glacier in the different years during the period 2006–2008 is presented in Section 3.3.

Documented estimates from satellite remote sensing show that during the period 2000–2005 Helheim Glacier experienced high acceleration and thinning rates, along with a large retreat of its terminus (Howat et al., 2005; Luckman et al., 2006; Howat et al., 2007; Murray et al., 2010). Most of these changes took place in 2003 and 2005 (Howat et al., 2007; Murray et al., 2010). Rather than such behavior being isolated, similar changes were observed to happen synchronously at other tidewater glaciers on the southeast Greenland coast, suggesting that they were driven by regional environmental factors (Luckman et al., 2006; Murray et al., 2010). The mean speed of Helheim Glacier during summers of 2006–2008, as estimated from the GPS observations, reveal that flow speed at the glacier was lower than in 2005 and similar to estimates from 2003. Peak velocities during summers 2006–2008 were $\sim$20% slower than peak velocities in 2005, but $\sim$20% faster than in 2000. This slowdown at Helheim that followed the period of acceleration is also consistent with the behavior of the rest of southeast Greenland glaciers. The deceleration was accompanied by a decrease in thinning rates and a readvance of the terminus position (Howat et al., 2007; Murray et al., 2010). The glacier terminus retreated by over 4 km between August 2004 and August 2005, but readvanced during 2006 by $\sim$3 km (Howat et al., 2007). The analysis of satellite images (Murray et al., 2010) shows that during the summer of 2007 the calving front retreated to almost the position of summer 2005, but readvanced again in 2008 to approximately the position of 2006.

This widespread and synchronous sequence of acceleration, thinning, and retreat, followed by a deceleration, decrease in thinning rates, and stabilization of the terminus, observed at the glaciers in southeast Greenland appears to have been regulated by an increase and subsequent decrease in the sea surface temperature (Murray et al., 2010). A decline in the East Greenland Coastal Current (EGCC), the ocean current transporting fresh, cold water southwards along the southeast coast of Greenland, during the period 2003–2004 caused warm waters, probably originated in the Irminger Current that transports high-salinity, warm waters from the Atlantic, to enter the glacial fjords and reach the glacier front margins. Such warm waters very likely caused the speed and the calving rate of the glaciers to increase (Murray et al., 2010), possibly through weakening of the terminus, melt beneath the glacier floating tongue, if any, reduction of the ice melange in the fjord, and changes in circulation at the glaciers fronts. Murray et al. (2010) hypothesized that, since the EGCC is partially originated by the input of fresh cold water from the ice sheet, the acceleration period of 2003–2005 may have been responsible, through its increased calving rates and ice-sheet runoff, for the reactivation of the EGCC, that drove in the subsequent years the deceleration of the glaciers back to pre-2003 values. Although the EGCC had reactivated in 2006, the presence of high-temperature ocean waters between Greenland and Iceland during summer 2007, with a strong warm water anomaly in July 2007, could explain the slight reactivation of Helheim's speed in summer 2007, which is not observed at other glaciers (Murray et al., 2010). This anomaly in the sea surface temperature rapidly recovered at the end of the summer of 2007. In summary, our observations of flow speed at Helheim Glacier, are in agreement with those reported by Murray et al. (2010) for the same period and thus suggest that the flow regime of Helheim Glacier is highly sensitive to ocean conditions.

3.3 Daily mean flow of Helheim Glacier

3.3.1 Results

Figures 3.7–3.9 show the daily horizontal speed of all sites during each of the summer campaigns, 2006–2008. These results show that in general the speed of a site increases gradually with time over the duration of the campaigns. Such increase is larger for sites closer to the calving front and smaller or nonexistent for sites located upglacier, and was also more significant in 2007, compared to 2006 and 2008. The sites also experience some larger step-like increases in speed, normally followed by partial or total decreases in speed, that are usually coherent throughout all or part of the glacier. The magnitude of these step-like variations also decreases with increasing distance from the calving front. In fact, sites located upglacier in general show less variation in speed that those located downglacier. The glacier presents, in general terms, a slight different behavior during the three years, with 2007 being the most active year in terms of speed increase over the summer and speed variations.

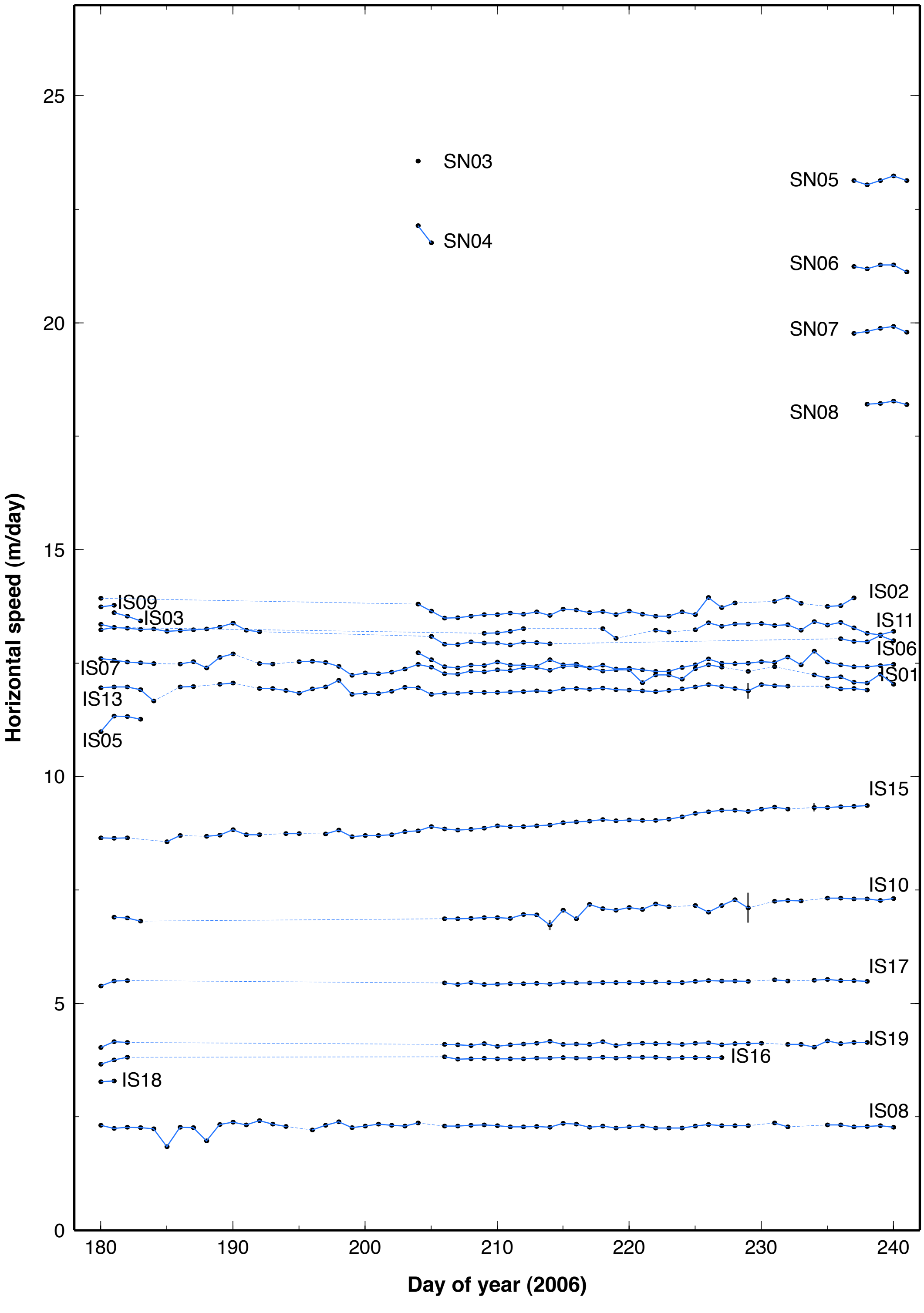

Figure 3.7: Mean daily horizontal speed of glacier sites operated at Helheim Glacier during the summer campaign of 2006, days of year 180–241 (June 29 to August 29). Estimates corresponding to each site are connected with a line for clarity, a solid line connects estimates from consecutive days, dashed lines are used when observations are missing or the quality of the data does not permit to estimate the speed with confidence. In most of the cases the error bars are smaller than the size of the symbols, except for few cases of poor data quality.

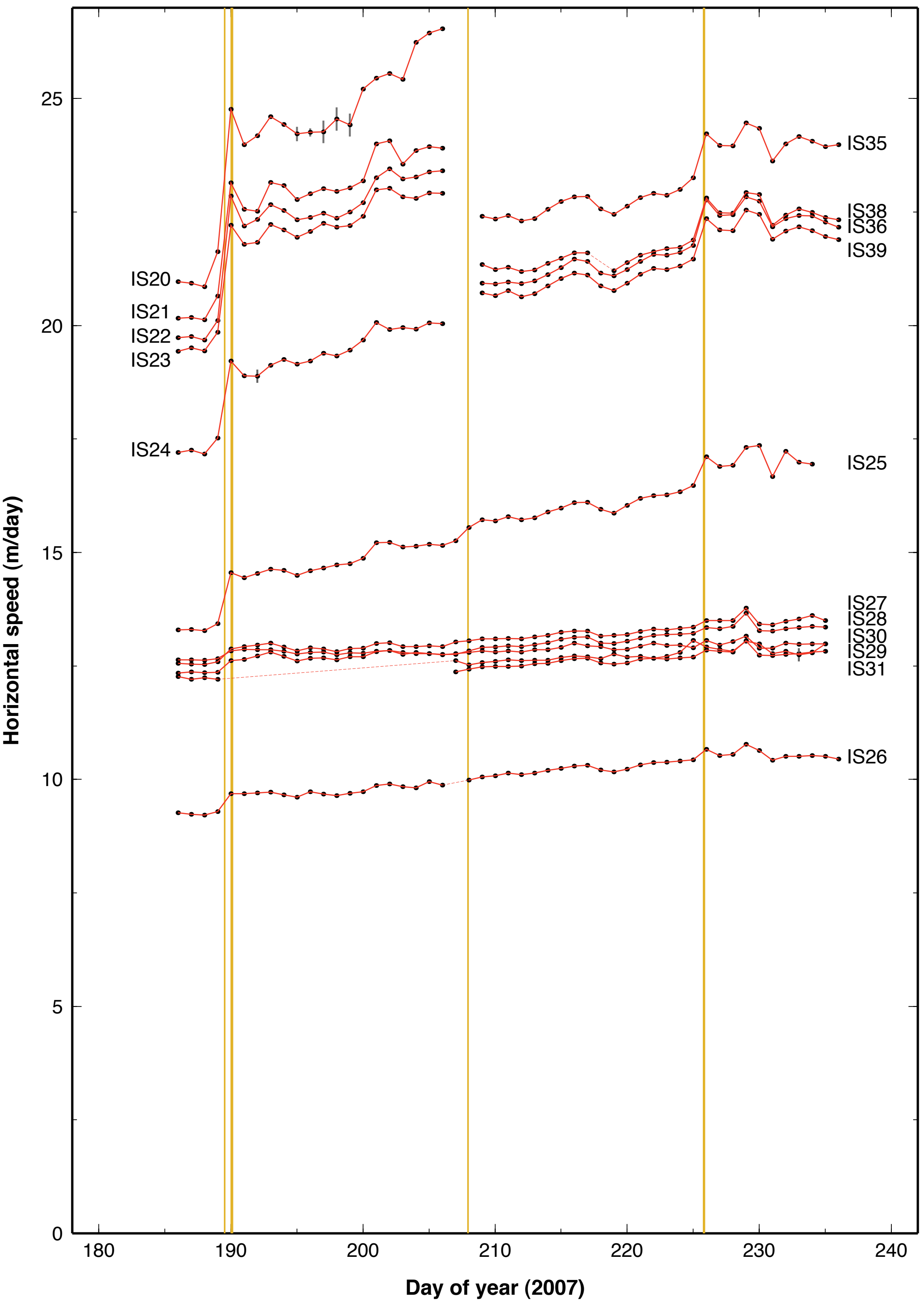

Figure 3.8: Same as in Figure 3.7, except here for glacier sites operated in 2007 during days of year 186–236 (July 5 to August 24). Yellow bars indicate time of teleseismically detected glacial earthquakes. The curves corresponding to the sites closer to the calving front are disconnected at days of year 207–208, when the sites where repositioned a few kilometers upglacier to prevent receiver loss to calving.

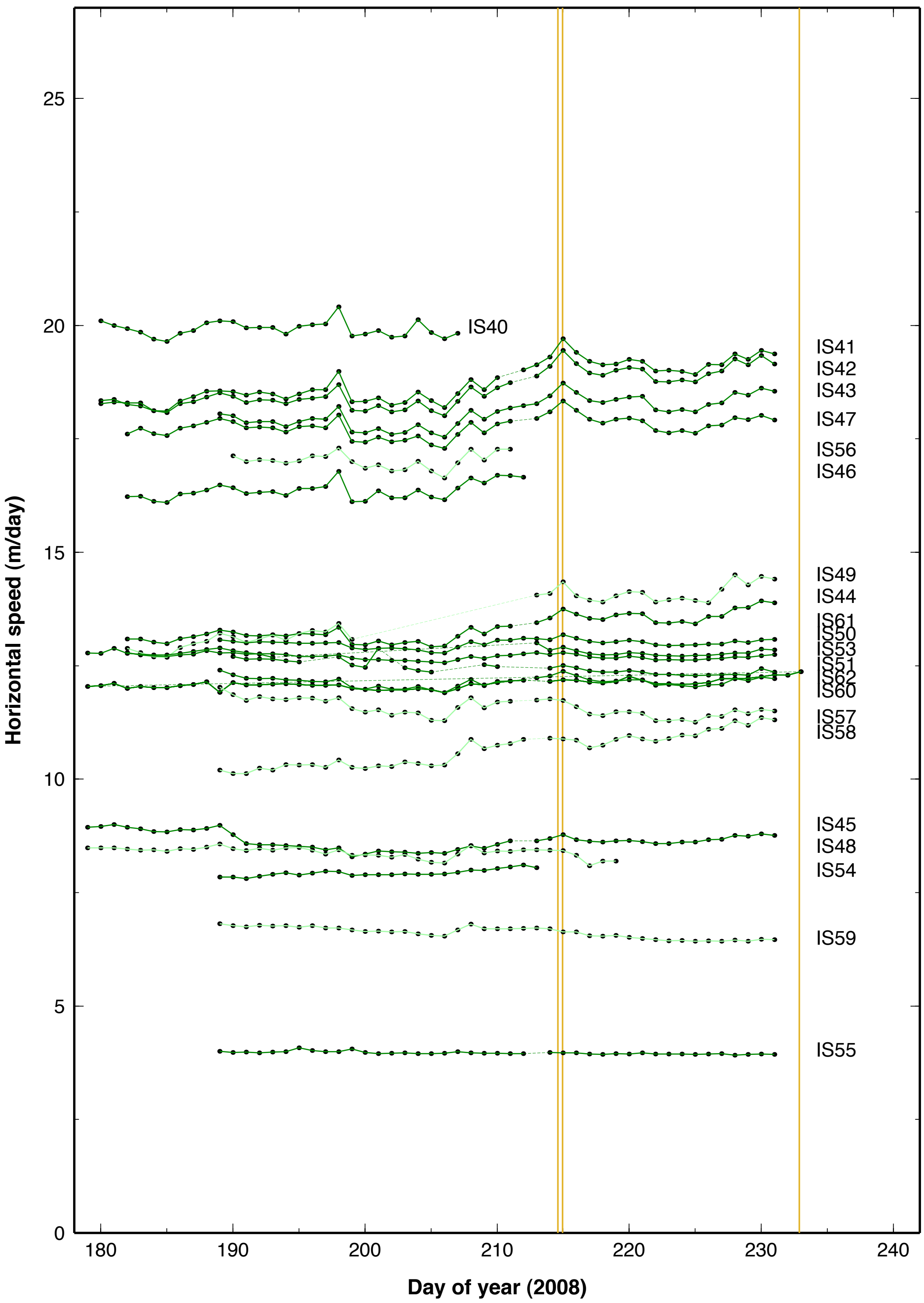

Figure 3.9: Same as in Figure 3.8, except here for glacier sites operated in 2008 during days of year 179–232 (June 27 to August 19). Sites on the glacier's tributary are shown with a lighter color.

In 2006 the focus of the campaign was concentrated in the upglacier part of Helheim, and the study in the downglacier and generally most active part was limited to short time periods. On the other hand, in 2007 the focus was shifted to the downglacier part and the locations farthest from the calving front had to be left unocupied. For this reason, the comparison between the results from 2006 and 2007 is mostly limited to the region of the glacier located between ∼16–24 km behind the calving front. However, the GPS network in 2008 extended over all the length occupied in the two previous years.

The results reveal that Helheim Glacier was most active during the summer of 2007 (Figure 3.8), which presents the highest positive trends in speed and the largest and most numerous sudden changes in dynamics. During this summer, the speed of the sites gradually increases as they flow downglacier, with the rate of increase being highest for the sites closest to the calving front and diminishing for sites farther from the front. During the time that this campaign lasted, the GPS sites also registered several large step-like increases in speed, most of them coherent throughout the length of the glacier that were followed, one or several days later, by a total or partial slowdown. The magnitude of these variations in speed is largest behind the calving front and decreases with increasing distance from the terminus. At a time close to some of these speedups, large calving events and glacial earthquakes, the time of which is indicated in the figures by yellow bars, occur. The summer of 2007 was also the most active of the three summers in terms of glacial earthquakes. The temporal link between large calving events, glacial earthquakes, and sudden accelerations is further discussed in Chapter 5.

In 2006 the sites present in general a more constant and less spatially coherent flow (see Figure 3.7). Most of the sites do not show a significant increase in speed over the summer. The sites located between ∼16–24 km from the calving front present lower increase rate compared to the sites deployed in similar locations in 2007. Surprisingly, the sites that show the largest speed trend are IS15 (located ∼29 km behind the calving front) and IS10 (at ∼21 km and close to the south margin). Also, the results indicate that the flow in this area was less coherent in 2006 compared to 2007, the variations in speed are in general site dependent in 2006, while the variations in 2007 happened basically coherently for all sites. However, it should be taken into account that, due to battery failure problems, many of the timeseries in 2006 extend over partial days (making the daily speed estimates equal to the average over these partial days), this could yield variations in speed which are fictitious. Although less coherent, the size of the speed variations in the area between ∼16–24 km have a similar magnitude than those in 2007. Since there are very few observations in the downglacier region in 2006, we are unable to determine if there were speed variations (uncorrelated to glacial earthquakes, since none occurred at the glacier during the field campaign of 2006) comparable to those in 2007.

In 2008, the speed of the sites also presents low increase rates compared to 2007 (see Figure 3.9). However, unlike the observations from 2006, the variations in speed are coherent throughout most of the glacier, but of smaller magnitude than those observed in 2007. One of such speedups is also coincident in time with two glacial earthquakes registered during the duration of this campaign, showing similar behavior to the events observed during the previous year, but again of smaller magnitude. The sites on the tributary, shown in the figure with a lighter color, present flow variations consistent with those in the main glacier. However, the site farthest upglacier in the tributary, unlike any other site, presents a negative speed trend.

3.3.2 Discussion

In most cases, the velocity of each site gradually increases through the season. The increase was much higher in 2007, when this long timescale acceleration was also observed throughout the extension of the glacier. In 2006 and 2008 the acceleration was much lower and only significant in the downglacier area. Such increase in speed may have two components, (1) the acceleration of the glacier over the summer due to external forcings, such as seasonal increases in temperature, changes in the boundary conditions, etc., and (2) the advection of the sites into regions of faster flow regime. Because we are estimating velocities of locations on the glacier which are progressively advancing downglacier, it is difficult to discern in these timeseries between acceleration due to advection and acceleration due to external forcings. The advection component should be highest in regions of highest speed and speed gradient, therefore in the downglacier area. Strain rate is also high in the uppermost part of the glacier, however speed is low in this area, and thus sites advance a shorter distance over the season, with advection having a lower impact. On the other hand, advection should probably not be relevant in the upglacier region between $\sim$16–24 km which flows at a relatively coherent speed of $\sim$13 m/d, as discussed in Section 3.2. However, in 2007, a quite significant trend is observed in this region of approximately constant speed, and also at site IS26, located near the compression zone of the glacier (see Figure 3.8). This, together with the fact that increase trends were lower during 2006 and 2008, suggests that a large component of the acceleration over the summer of 2007 was due to external forcing. Indeed, despite that in 2007 the presence of cold coastal waters had been reactivated along the southeast coast after the decline of the East Greenland Coastal Current (EGCC) in 2003–2004, the summer of 2007 presented anomalous high sea-surface temperature (SST) offshore, causing a minor reactivation of the glacier (Murray et al., 2010).

This characteristic of the glacier's flow in 2007 clearly differentiates its behavior during this summer with respect to the summers of 2006 and 2008. Also, 2007, in comparison with the previous and subsequent years, is the year with the most numerous and largest variations in speed, also coinciding with the highest occurrence of glacial earthquakes. Glacial earthquakes are related to calving front retreat, as will be further examined in Chapter 5. All of this suggests that the increase in flow speed observed during July and August, 2007, may be related to the highly varying boundary conditions at the calving front of Helheim Glacier likely driven by the presence of warm waters at the front of the glacier.

Most of the large and sudden speed increases are observed to occur temporally and spatially coherent throughout the glacier's length, indicating that a change in the boundary conditions, whether it is localized at the glacier terminus, like in the case of glacial earthquakes (Nettles et al., 2008), or upglacier, like in the drainage of a supraglacial lake (further discussed in Chapter 6), the speed response of the glacier is transmitted through all the length of the glacier, demonstrating that the glacier is capable of responding rapidly and coherently to external forcing. The nature of some of these speed variations is analyzed in more detail in Chapters 5 and 6.

3.4 Summary

The mean flow of Helheim Glacier was quite coherent during summer seasons of 2006–2008, with the glacier flowing slightly faster during 2007, and slowest during 2008. The glacier flows fastest near the calving front, with a maximum speed at the site behind the calving front of ∼24 m/d, and presents extending flow over most of its extension, with speed decreasing upstream, and the uppermost centered site flowing at ∼4 m/d. However, it also presents a compressing flow region near the bend in the glacier, where the direction of flow changes from southeast to mainly east. The ice decelerates once it enters this compression zone, and accelerates once it has passed it.

During these years, the flow speed of Helheim Glacier was ∼20% lower than in 2005, but higher than in 2000. The calving front position was also more stable during this period, compared to 2003–2005, with the terminus retreating over the summer and readvancing during the winter. These observations are in agreement with the hypothesis that the decline of the cold East Greenland Coastal Current (EGCC) during 2003–2004 caused higher than mean sea surface temperatures that came in contact with the glaciers and drove the widespread and synchronous acceleration and thinning of the southeast Greenland glaciers until the summer of 2005. Then the EGCC re-strengthened, making possible the slowdown of Helheim Glacier and the other southeast Greenland glaciers by summer 2006 (Murray et al., 2010).

During this three-year period, the glacier was most active during the summer of 2007, when the speed of the glacier increased over the summer more than it did during the previous and subsequent years, and also presented more variation in a daily timescale, in part associated with the glacier also producing more glacial earthquakes during this year. This reactivation of Helheim Glacier in 2007, not observed at other glaciers, could be explained by the presence of warm sea surface waters offshore, between Greenland and Iceland (Murray et al., 2010).

The speed of the glacier experienced step-like increases, normally followed by total or partial decreases, which happened in general coherently throughout the glacier, and with a magnitude that decreased upstream. Some of these rapid variations in speed are temporally linked to the occurrence of glacial earthquakes, others to the drainage of lakes formed by accumulated meltwater on the surface of the glacier, all of which will be addressed in later chapters.

Chapter 4

Ocean tides modulation of flow at Helheim Glacier

Greenland's main outlet glaciers have been shown to be most sensitive to changes at their calving terminus, which can initiate dramatic phases of acceleration, thinning, and retreat (e.g., Howat et al., 2005; Stearns & Hamilton, 2007; Amundson et al., 2008; Nettles et al., 2008; Nick et al., 2009). Characterizing the interactions between the cryosphere and the ocean is key to gain an improved understanding of this complex coupled system (Holland et al., 2008; Straneo et al., 2010; Rignot et al., 2010; Murray et al., 2010). Studying the effects on the flow of glaciers of well known perturbations applied at their weakest margin such as the ocean tide, can provide valuable information on the nature of the dynamic response and sensitivity of the glaciers to changes in their boundary conditions.

The vertical bending of glacier ice tongues and ice-shelf margins due to ocean tidal forcing has been investigated for many years. Of special interest is the flexure zone or hinge zone, i.e., the transition region from grounded to freely floating conditions. Measurements of the vertical response to ocean tides in this region provide information on the glacier response to a periodic forcing and is analyzed as well for its contribution to the formation of icebergs. In theoretical models of tidal flexure of floating glaciers, the glacier is usually modeled as a long elastic beam of uniform thickness, resting on elastic foundations (e.g., Holdsworth, 1969; Lingle et al., 1981). Vaughan (1995) showed that elastic beam theory with a single value of the ice elastic modulus ($E = 0.88 \pm 0.35$ GPa) successfully explained the tidal displacement data from several ice shelves in Antarctica. However, a data set from Jakobshavn Isbræ, West Greenland, measured by Lingle et al. (1981), could only be fitted by this model when using a much lower value of E (Vaughan, 1995), or when considering that the non-crevassed effective thickness of the glacier tongue was only $\sim$20% of the real thickness (Lingle et al., 1981). Reeh et al. (2000, 2003) observed a variation in the phase of the vertical response to ocean tides with distance from the grounding line within the flexure zone of Nioghalvfjerdsfjorden Glacier, northeast Greenland, and found that viscoelastic beam theory, rather than purely elastic, was needed to explain the observed amplitude and phase of the tidal deflection.

Observations of vertical tidal response at the short floating section of Jakobshavn Isbræ also showed that the glacier response was delayed with respect to the ocean tide by 35–40 min (Dietrich et al., 2007).

Ocean tides have also been shown to have an effect on the horizontal flow of outlet glaciers and ice streams. The flow speed of such glaciers can be modulated by the tides at a wide range of frequencies. Velocity fluctuations at diurnal and sub-diurnal frequencies are such that faster flow normally occurs during the falling tide and slower flow during the rising tide (e.g., Walters & Dunlap, 1987; Anandakrishnan & Alley, 1997; Anandakrishnan et al., 2003; Gudmundsson, 2006; Murray et al., 2007). Theoretical models show that this out-of-phase tidal response is due to the change in back pressure at the glacier terminus (Anandakrishnan & Alley, 1997; Thomas, 2007) or the change in ice-shelf back forces (Thomas, 2007) as the tide rises and falls. Anandakrishnan & Alley (1997), modeling the ice stream as an elastic beam lying on a viscous substrate, found that the amplitude of the tidal-modulated flow decayed exponentially with distance from the grounding line and that the response was further delayed the longer it traveled upglacier.

Velocity variations of periods longer than diurnal caused by ocean tides have also been observed in ice streams in Antarctica. The flow speed of Rutford Ice Stream, West Antarctica, is modulated by a wide range of frequencies, from semi-diurnal to semi-annual (Murray et al., 2007). This ice stream presents strong semi-monthly and semi-annual speed modulations (Gudmundsson, 2006; Murray et al., 2007; King et al., 2010), flowing faster during the spring tide and slower during the neap tide, and also faster during the equinoxes and slower during the solstices. The semi-monthly and semi-annual flow speed variations can be explained by a non-linear response to the ocean tidal forcing at semi-diurnal and diurnal frequencies, due to the non-linear relation between basal sliding velocity and basal shear stress (Gudmundsson, 2007; King et al., 2010). Furthermore, the amplitude of the semidiurnal variations in flow velocity has a seasonal and biweekly dependence (Murray et al., 2007). A different sort of complex response to the tides are stick-slip events paced by the ocean tides, observed at Whillans Ice Stream, West Antarctica (Bindschadler et al., 2003; Wiens et al., 2008). The sudden transient periods of rapid motion at this Ice Stream are paced by the ocean tides.

In contrast with the ample set of observations that are available from large ice streams in Antarctica, very little is known about the tidal effects on the flow of Greenland's outlet glaciers. Previous workers found tidally modulated variations in flow speed on a floating section of Kangerdlugssuaq Glacier, East Greenland (Hamilton et al., 2006; Davis et al., 2007), and the speed of the lower part of Jakobshavn Isbræ was observed to fluctuate by 35% at tidal frequencies (Echelmeyer et al., 1991), but characterization of the glacier response has been limited by data sparsity.

Here we use the extensive positioning data set collected at Helheim Glacier to characterize its tidal response. The high precision of high-rate GPS observations collected on the surface of this ocean-terminating glacier enables us to study in great detail the spatio-temporal variation of sub-daily deviations from mean flow, such as the glacier response to ocean tides over daily, to monthly, to seasonally timescales. In this chapter we present a characterization of the tidal signals observed in the GPS timeseries and an analysis of the floating conditions and tidal flow modulations at Helheim Glacier during this period. The record of tidally-modulated variations in horizontal flow presented here is the first ever documented for a Greenland outlet glacier to span more than a few days. The results presented here will be part of a manuscript that is currently in preparation (de Juan et al., in preparation(a)).

4.1 Tide observations and model prediction

During parts of the GPS observing periods, we operated a water-pressure tide gauge in a Sermilik Fjord cove, at a distance of ~35 km from the glacier terminus (Figure 4.1(a)), to obtain a record of ocean tide heights. We selected a side cove off the fjord and not at the glacier front to minimize the risk of losing the equipment to ice calving and scouring. The pressure gauge had a nominal mm-level resolution and was operated to acquire one observation every minute (see Appendix A). The pressure gauge operated continuously, except for some (sometimes significant) interspersed gaps due to battery failure. It operated during days 203–221 in 2006, 186–218 in 2007, and 213–238 in 2008.

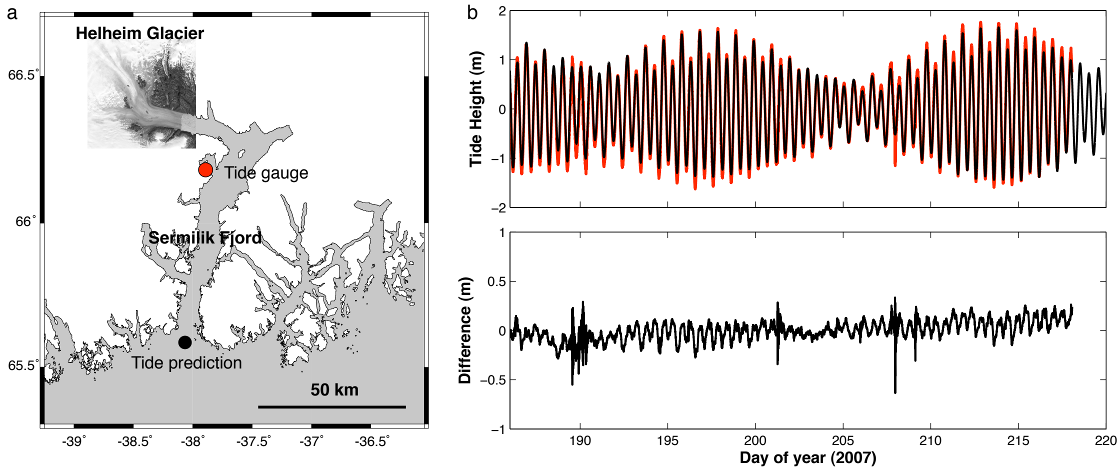

Figure 4.1: (a) Map showing the location of Helheim Glacier and Sermilik Fjord. Red dot: location of water-pressure tide gauge. Black dot: location of ocean tide prediction. The distance between the two locations is ~60 km. (b) Upper panel: Black line shows predicted ocean tide at the ocean location near the mouth of the Sermilik Fjord (black dot in a). Red line shows observed tide within the fjord. Lower panel: Difference between the predicted and observed tide. The RMS of the difference is ~10 cm. High-frequency water-height variations (e.g., around day of year 190) are caused by small tsunamis that follow large calving events (Nettles et al., 2008).

Since the water height records were not continuous throughout the GPS observing period, we also predict the ocean tide at an open ocean location near the mouth of the Sermilik Fjord using the ocean tide model AOTIM-5 (Padman & Erofeeva, 2004).

Figure 4.1(a) shows the location of the tide gauge in the Sermilik Fjord cove and the ocean location for the tide model prediction. The distance between the two locations is ~60 km, mainly in a NS direction. Figure 4.1(b) shows the comparison between the water height predicted by the AOTIM-5 model and the recorded tide in 2007. The 5 km resolution of the AOTIM-5 model lacks the coastline and bathymetry necessary to predict the tide at the specific location of the tide gauge. Nevertheless, the predicted and recorded tide gauge data in the fjord are consistent to the few cm level, and they are in phase to within 3 minutes. The root-mean-square (RMS) of the difference between the observed and predicted tide (shown in Figure 4.1(b)), for the entire 2007 record (days of year 186–218), is ~10 cm, which includes tsunami events due to glacial earthquakes (Nettles et al., 2008). The amplitude of the observed tide is higher than the amplitude of the modeled tide by ~5%. The tide predicted with AOTIM-5 agrees at the few cm level with other global ocean models such as CSR-4.0 (Eanes & Bettadpur, 1995) and TOPEX-7.2 (Egbert et al., 1994). However, though these last two global models are more recent than AOTIM-5, they do not include observations from local tide gauges, and are thus assumed to be of lower quality in this region.

Table 4.1: Eight main tidal constituents of the ocean tide at the Sermilik Fjord location 65.5°N, 38.2°W, as predicted by model AOTIM-5. Columns include Darwin name, diurnal/semidiurnal band ($n_i = 1/2$), harmonic frequency in cycles per day, $n_i f_i$, amplitude, b_i, and phase at the reference epoch (January 1, 1992 at 00:00 UT), $\phi_i(t_0)$.

Symbol	n_i	$n_i f_i$ **(cpd)**	b_i **(m)**	$\phi_i(t_0)$ **(degrees)**
Q1	1	0.8932440	0.01293	336.768
O1	1	0.9295356	0.07198	350.088
P1	1	0.9972621	0.04727	199.825
K1	1	1.0027381	0.15775	346.681
N2	2	1.8959820	0.17989	9.912
M2	2	1.9322736	0.99199	99.211
S2	2	2.0000000	0.38188	0.000
K2	2	2.0054756	0.10428	89.299

The ocean tide variations at Sermilik Fjord are predominantly semi-diurnal and have a fortnightly (i.e., 15-day period) modulation. The amplitude of the tide ranges between ~3 m (spring tide) and ~1 m (neap tide), peak-to-peak. The fortnight variation, with a dominant period of ~14.7 days, results principally from the beating of the two principal tidal constituents, M2 and S2 (see Table 4.1). The difference between the observed and modeled tides (Figure 4.1(b)) is dominated by a semidiurnal frequency and also shows high-frequency variations, caused by small tsunamis that follow large calving events (e.g., on days 189 and 190) (Nettles et al., 2008), which, obviously, AOTIM-5 does not model.

4.2 Observations of tidal flow variations

The mean flow velocity of Helheim Glacier over the area where our GPS network extends, ranges from ~2 m/d on the higher parts of the glacier and closest to the margins, to a maximum of ~24 m/d near the terminus, during the summers of 2006–2008. On a day with no "atypical" external forcings (e.g., no glacial earthquake events), as it is commonly the case, we observe no abrupt changes in the flow speed of the glacier. In those days, flow is characterized by small and gradual variations in speed, which are normally largest near the front of the glacier. In general, the cross-flow and vertical directions contain no relevant sub-daily variations that could be indicative of glacier behavior. Such variations are typically limited to the mean daily direction of flow or along-flow component.

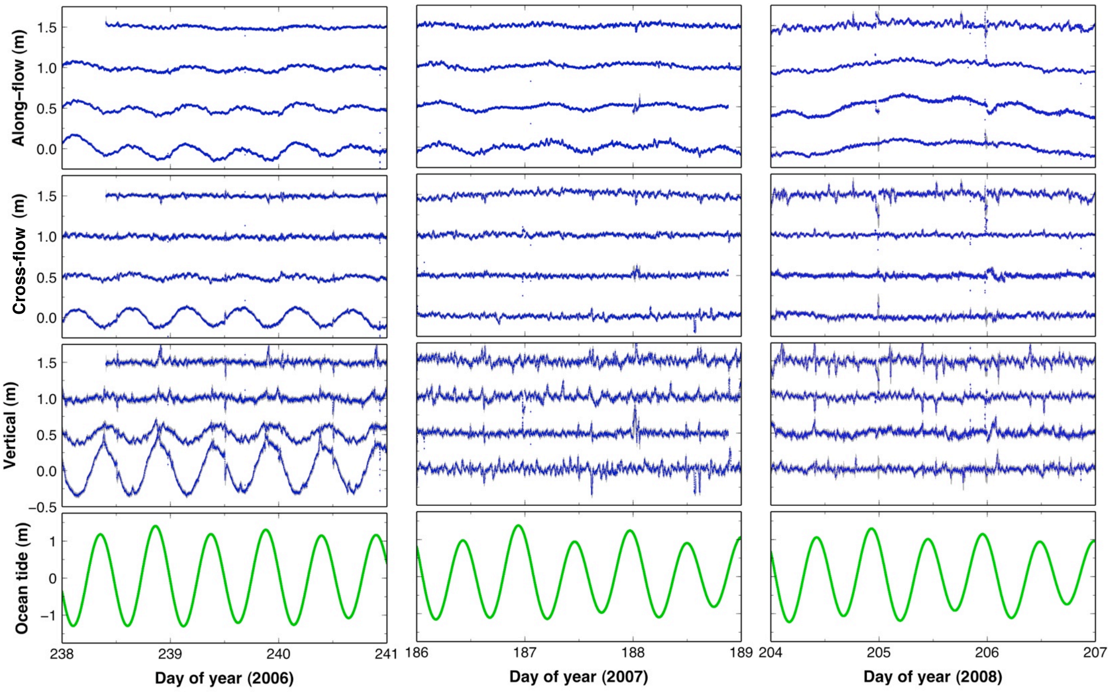

Figure 4.2: Dark blue dots: Example of along-flow (top), cross-flow (middle), and vertical (bottom) position of GPS stations relative to mean speed, estimated every 15 seconds. The four sites located on the centerline of the glacier and closest to the calving front are shown, for a period of three days in 2006 (left), 2007 (middle), and 2008 (right). Traces within each panel are arbitrarily offset for clarity, with stations plotted from closest to the calving front (bottom), to furthest upglacier (top). Green line: Predicted ocean tide using the AOTIM-5 model. Note the difference in scale between the tide and the position residuals.

At the sites located in the downglacier part of Helheim, located up to ~12–16 km from the calving front, the along-flow position residuals to linear motion present semi-diurnal sinusoidal variations (see Figure 4.2). During parts of the observing periods, the sites located closest to the calving front also present semi-diurnal variations in the vertical and cross-flow components. These variations correlate with the ocean tide but are delayed with respect to it. The possibility of such variations resulting from multipath or data processing artifacts is discarded for several reasons: (1) the semi-diurnal signal is present for sites in the lower section of the glacier but absent for the sites located furthest upglacier, while the electromagnetic environment for the two regions of the glacier is quite similar and the orbits and reference station used in the processing of all sites are the same, (2) the amplitude of the variations decays with distance from the calving front, suggesting a spatial decay of a response of a forcing acting on the calving front, (3) the amplitude of the signal varies over time coherently throughout the glacier, and (4) the signal is in phase for the sites that show it, which suggests that the signal is not site dependent. Therefore, we interpret these variations as the response of the glacier to ocean tidal forcing, which in the vertical direction manifests as bending, and in the horizontal direction of motion, as position variations with respect to mean flow. We deployed a total of 20, 12, and 23 systems in 2006, 2007, and 2008, respectively. This study focuses on those sites deployed on the lower ∼16 km of the glacier, closest to the terminus, since they are the most sensitive to ocean tidal forcing.

Figure 4.2 shows an example of site position estimates relative to mean speed, in the along-flow, cross-flow, and vertical components. The figure includes the four GPS sites on the centerline of the glacier that are located closest to the calving front, for a period of three days in each of the three summer campaigns, 2006–2008. During the three campaign years, at the sites located in the region that extends up to ∼12–16 km behind the calving front (see Figures 1.4–1.6), the displacement deviations from mean flow in the along-flow component present variations at tidal frequencies. The tidally induced position variations are approximately out of phase with the ocean tide, such that the glacier position is advanced at low tide, and retarded at high tide, with respect to the position expected for the mean flow speed.

Moreover, in summer of 2006, the downglacier part of Helheim, extending ∼4 km behind the calving front, was observed to show a vertical response to tidal forcing (see Figure 4.2), indicating that this region of the glacier was afloat. However, in 2007 and 2008, sites in similar locations did not exhibit a vertical response to the tides. Furthermore, in 2006, the sites that exhibit a vertical response to the tides also present a tidal response in the cross-flow component of motion, indicating that the floating section of the glacier changed its direction of flow with the tide. Figure 4.2 also shows that the tidal variations in the three components of flow decrease in amplitude with distance from the calving front, as one would expect for a distance-attenuating response.

In what follows, we present, in turn, the analysis of the response of the glacier to the ocean tides in the three components of flow. During the 2006 campaign, the sites in the downglacier region were operated for short time periods of a few days. Instead, in 2007 and 2008, most of the sites were deployed for a period of 1–2 months, enabling the study of the temporal dependence of the glacier's tidal response.

4.3 GPS tidal analysis

To characterize the response of the glacier to the ocean tide, we perform an admittance analysis that also includes a time delay between the forcing and the glacier's response.We perform a least-squares fit to the geodetic position estimates using a model $y(t)$ that includes an offset x_0 at the reference epoch t_0, a mean glacier flow velocity v, a mean glacier acceleration a, when needed, and an admittance (scaling) parameter A, relating the ocean tide height $T(t)$ to deviations in glacier displacement from the mean flow:

$$y(t, \Delta t) = x_0 + v(t - t_0) + \frac{1}{2}a(t - t_0)^2 \pm A\ T(t - \Delta t) + \epsilon(t), \tag{4.1}$$

where $\epsilon(t)$ is the error in the position estimates. Since, the response of the glacier in the horizontal components of flow are out of phase with the ocean tide, we reverse the sign of the tide when fitting these components. The admittance parameter is thus the ratio between the amplitude of the tidal response of the glacier and the amplitude of the ocean tide. In the least-squares fit we down-weight the GPS observations corresponding to non-fixed segments of data (see Section 2.5.4).

We estimate the time delay Δt between the ocean tide and the response of the glacier by performing a χ^2 grid search of the model described above at 5-minute time steps (higher temporal resolutions are not warranted by the data), for delays between -4 h and 4 h. In this analysis, the best-fit time delay is given by the minimum χ^2 per degree of freedom, χ^2_ν. Each of the time delays fitted to a given timeseries has a corresponding best-estimate of x_0, v, a, and A. Thus, the resulting parameters from the tidal analysis are the best-fit parameters for the estimated time delay. The fitting procedure is done in two iterations. In the first iteration 4-sigma outliers to the best-fit model are identified. In the second iteration the fits are repeated excluding the outliers. For illustration purposes, Figure 4.3 shows a χ^2_ν curve for sites SN06 and SN05 and a comparison between vertical position estimates and modeled tidal response for the minimum χ^2_ν and a $\Delta t = 0$ h.

We analyze the data in independent batches, normally one UT day in duration since that is the characteristic length of the position estimates that result from the GPS data processing (see Chapter 2). This scheme ensures that potential systematic errors related to day-boundary crossing do not leak into our analysis. Furthermore, since we observe variation of the tidal parameters values over time, as it is further explained below, the analysis of longer time periods is not warranted. We perform fits to ad hoc time periods when more complicated dynamic signals occur, such as those related to glacial earthquakes or other non-constant accelerations. The RMS of the residuals to these fits ranges in general between ~1 cm and ~7 cm. Larger RMS are found associated with timeseries that contain significant non-tidal glacier flow variations. In comparison, total glacier motion at the location of these sites over one day is typically 10–24 m horizontaly. Two examples of such fits are shown in Figure 4.3.

To assess the significance of the admitted tidal signal term for a given day and site, we compare the model described in Equation 4.1 with a constant-speed model that does not include a tidal signal, by means of an F-test at 95% confidence (see Appendix D.1).

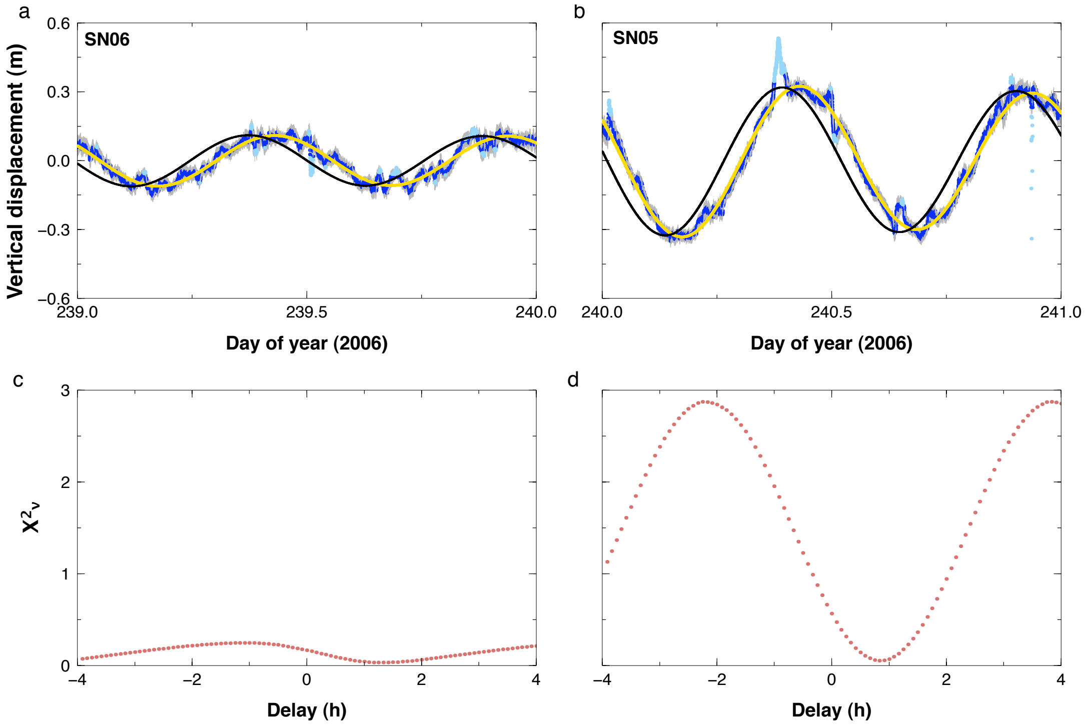

Figure 4.3: (Top) Blue dots show vertical position of site relative to mean speed for (a) site SN06 on day 239 (2006) and (b) site SN05 on day 240 (2006). Yellow line shows modeled tidal response for the minimum χ^2_ν. Black line is the modeled tidal response corresponding to zero time delay. (Light blue dots are outliers and are not used in the least-squares fit.) The RMS of the residuals to such fits are (a) 24 mm and (b) 43 mm. (Bottom) χ^2_ν as a function of time delay for the fits performed to the timeseries above.

This enables us to discern whether there is a tidal response at the sites furthest from the calving front or not. We also evaluate with the same type of test the need for an acceleration parameter in each of the fits by comparing the model results with and without this parameter. In most cases involving the along-flow horizontal component, we find that the F-test favors a model that includes a constant acceleration. The example from 2008 shown in Figure 4.2 clearly illustrates the need for an acceleration parameter.

The size of the error bar for the time delay estimates depends on the steepness of the χ^2_ν curve as a function of time. Since the error bar comprises the time delay estimates that fall in a χ^2_ν range of values that are less than 5% probable in an F-test sense, the sharper the steepness of the curve, the smaller the size of the error, and vice versa. The error of the parameters estimated with the least-squares fit are scaled by the χ^2_ν as explained in Appendix D.2.

4.4 Results

In this section we present the results pertaining to the tidal analysis of the GPS data acquired at Helheim Glacier during the summers of 2006–2008. First, we present the results for the time delay of the tidal response, then we describe its spatial variation throughout the glacier, and its temporal variation over long and short timescales.

4.4.1 Time delay of the tidal response

Our analysis shows that the response of the glacier is delayed with respect to the ocean tide in Sermilik Fjord. In the GPS tidal analysis, the time delay of the response of the glacier with respect to the ocean tide in each of the days is given by the minimum χ^2_ν in the grid search (see Figure 4.3), as explained above. This yields a time delay of the glacier response in general between 0 and 4 hours with respect to the ocean tide. (A positive delay means that the glacier response lags the tide, as one would expect, though that information was not used as constraint in the fitting procedure.) The error of the individual-day estimates of time delay range between 5 minutes and several hours, with the error being larger, the smaller the amplitude of the tidal signal is.

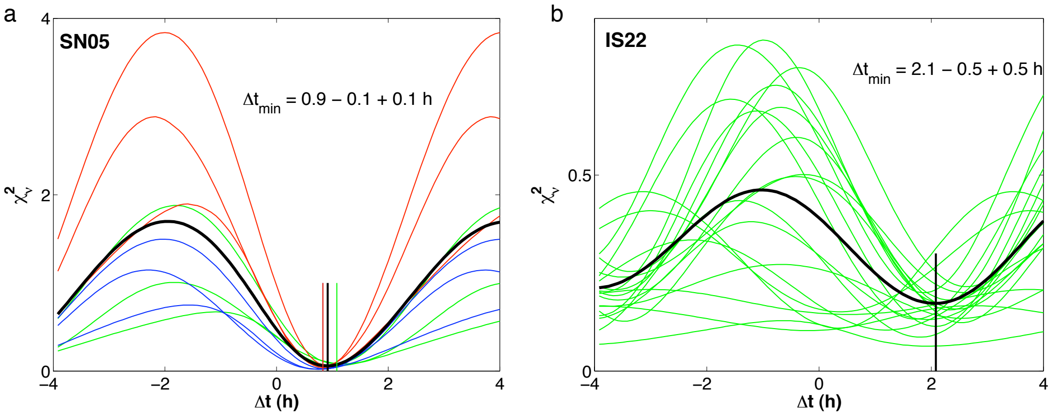

Figure 4.4: χ^2_ν as a function of time delay for (a) site SN05 in 2006 (3 days) and (b) site IS22 in 2007 (19 days), for the fits in the (green) along-flow, (blue) cross-flow, (red) vertical components of motion, and (black) best-fit time delay for all days and components. Vertical lines mark the best-fit time delay for each of the three components and for all of them (Δt_{min}).

However, a variation in the time delay as a function of time (and over the different components of motion, when these present tidal response) for a given site is not required by the data. We tested this by estimating a normalized mean χ^2_ν curve for each of the sites. Figure 4.4 shows two examples of individual and mean χ^2_ν curves. We compared the fits to the data given by the parameters corresponding to the minimum of the mean χ^2_ν curve with the fits given by the individual-day estimates of time delay. Since the residuals to such fits do not differ significantly (generally less than ∼5 mm in RMS) we conclude that a single time delay for each site and all days (and components, when warranted), given by the minimum of the normalized mean χ^2_ν curve, explains well the tidal variations observed. The best-fit parameters for each individual daily timeseries are given by the minimum of the mean χ^2_ν curve. The error of the best-fit time delay is estimated in the same way as the error of the individual-day time delays (see Appendix D.1).

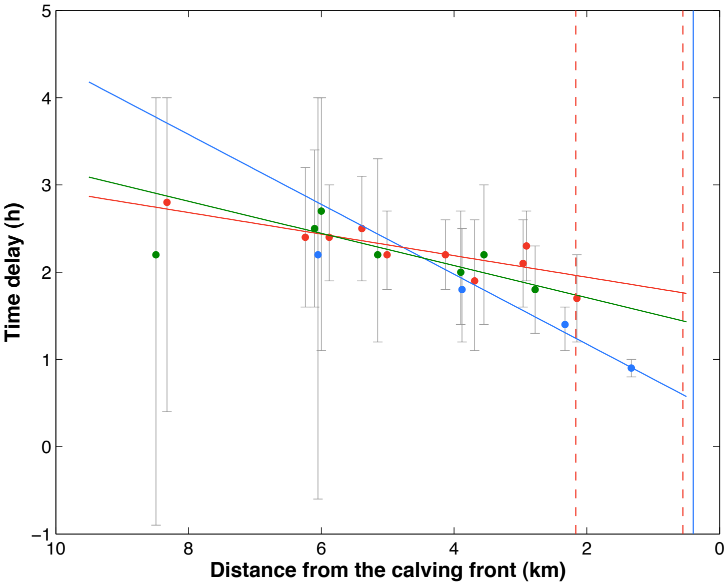

Figure 4.5: Time delay of the response of the glacier to ocean-tidal forcing as a function of distance from the calving front in (blue) 2006, (red) 2007, and (green) 2008. Distances are with respect to calving front position on day July 31, 2008 (day of year 213). Vertical lines: calving front positions on (solid) days 242 for 2006 and (dashed) 185 for 2007 (color coded as dots).

The time delays we estimate for all days (and flow components) for each of the sites range between ∼0.9–2.8 h. The observed initial variation over time in the range of 0–4 h is in most cases, within the error, consistent with the best-fit time delay obtained with the mean χ^2_ν curve. Significantly different time delay estimates are attributed to non-tidal flow variations or noise that are not modeled by the GPS tidal analysis.

Table 4.2: Weighted mean time delay of the response of the glacier to the ocean tide in each of the years for the components indicated, where A refers to along-flow, C to cross-flow, and U to vertical.

Year	Components	Time delay (h)
2006	ACU	1.0±0.1
2007	A	2.2±0.2
2008	A	2.0±0.3

Furthermore, the estimated time delays for all sites from a given summer campaign are, within the error, consistent with each other. The weighted-mean time delay for the response in each of the summer campaigns is given in Table 4.2. The mean delay of the response of the glacier to the ocean tides was 1.0±0.1 h during summer 2006, and 2.2±0.2 h and 2.0±0.3 h in 2007 and 2008, respectively. Thus, our results indicate that the glacier responded to the tides with a shorter delay in 2006 than in 2007 or 2008. In 2006, the glacier contained a short floating tongue, unlike in summers of 2007 and 2008.

Since the error of the time delay estimates increases as the amplitude of the tidal response decreases, sites upglacier do not provide hard constraints to attempts at modeling the delay. However, since there is a hint of a dependency of the time delay estimates on distance from the calving front (Figure 4.5), we tested a linear model as the simplest possible variation. A weighted least-squares fit to the time delay estimates using a linear model for the variation of the delay with distance from the calving front yields a propagation of the time delay in the upglacier direction of 0.4±0.2 h/km in 2006, 0.1±0.1 h/km in 2007, and 0.2±0.1 h/km in 2008 (errors are 3-σ), thus barely significant.

4.4.2 Spatial variation of the tidal response

We observe vertical tidal modulations during the two short observing periods at the lower part of Helheim Glacier in 2006, indicating that this region of the glacier was afloat (Figure 4.2). The vertical response of the glacier is ∼30–40% of the full tidal range at the site located closest to the calving front, and attenuates at $\lesssim$6 km behind the calving front. For example, the vertical response for days of year 238–241 (Figure 4.2) is

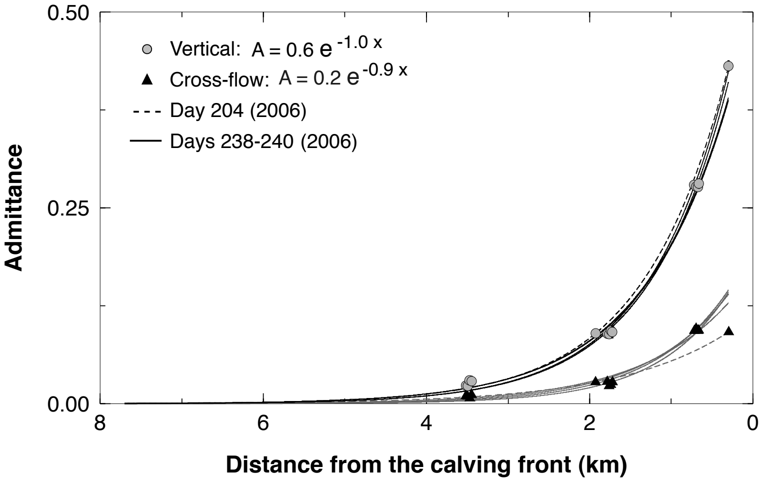

Figure 4.6: Admittance amplitude A of vertical (circles) and cross-flow (triangles) response to ocean-tidal forcing as a function of distance x from the calving front position on day of year 242 (2006) for the short-term ice sites in 2006 (see Figure 1.4). Lines are best fit (in a least-squares sense) to the data using an exponential function (see text) for days 204 (dashed) and 238–241 (solid) in 2006. All 1-σ error bars are smaller than the size of the markers.

∼60 cm peak-to-peak at the location of site SN05 (∼700 m behind the calving front), it is largely attenuated at site SN07 (~3.5 km behind the calving front), and not present at SN08 (~6 km upglacier from the calving front). These observations indicate that during this period, the grounding line at Helheim must have been located between ~3.5 and ~6 km behind the calving front. (Distances to the calving front are with respect to terminus position on day of year 242 in 2006, as derived from a satellite image acquired on that day.)

Figure 4.6 shows the admittance amplitude of the vertical response as a function of distance to the calving front. The admittance analysis reveals that the amplitude of the vertical response to the tides decays exponentially with distance from the calving front. Therefore, we fit an exponential function to the admittance amplitude of all sites in the center flowline of the glacier, $A(x) = A_0 e^{-kx}$, where A is the admittance amplitude, x the distance to the calving front, A_0 the admittance at the calving front, and k is the decay constant, or the inverse of the scale length for the admittance to be reduced by a factor e. The fits for different days are very consistent (see Figure 4.6), with a mean value (over all days) for the exponential decay constant of 1.0±0.1 km^{-1}, an admittance amplitude at the calving front of 0.6±0.2, and an RMS of the residuals to these fits of ~0.01, in admittance amplitude. We also tested a power-law fit to the vertical admittance amplitude as a function of distance (not shown). This model is discarded since it gives ~6 times worse results than the exponential decay function.

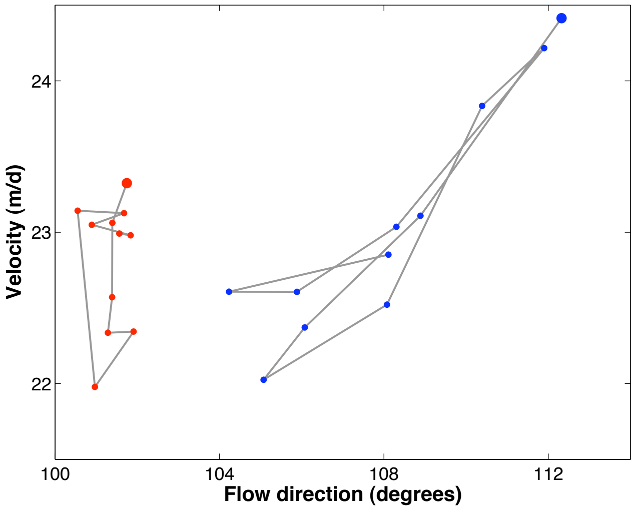

Figure 4.7: Velocity as a function of flow direction for (blue) site SN05 on day 238 (2006), which presented a tidal response in the cross-flow component, and (red) site IS22 on day 200 (2007), which did not. Each of the dots is an estimate corresponding to a fit to 2 h of data. Dots are joined with a line to show progression of time, with largest dot identifying first epoch.

We also observe a tidal response in the horizontal cross-flow component where a vertical tidal response is present in summer 2006 (see Figure 4.2). No other sites or times present a tidal-induced response in the cross-flow component of motion. Figure 4.7 shows estimates of horizontal velocity versus the azimuth for one day, in batches of 2 h each, and for two sites, one that presents a cross-flow tidal signal, SN05, and one which does not, IS22. The figure shows that site SN05 changes from maximum speed and maximum azimuth to minimum speed and azimuth. The change in flow direction observed at this site is of ∼8 degrees azimuth angle, over the course of a day. Instead, site IS22 varies from minimum to maximum speed, with minimal change in direction, less than ∼1 degree azimuth angle. These results indicate that the floating section of the glacier also changed its direction of flow with the tide.

Figure 4.6 shows that the amplitude of such modulations also decays exponentially with distance from the calving front, with a mean scale length of 0.9±0.2 km^{-1}, and an admittance amplitude at the calving front of 0.2±0.1. Figure 4.6 also shows that an exponential decay with similar scale lengths describes the spatial dependence of the amplitude of the vertical and cross-flow components, though the former is clearly larger.

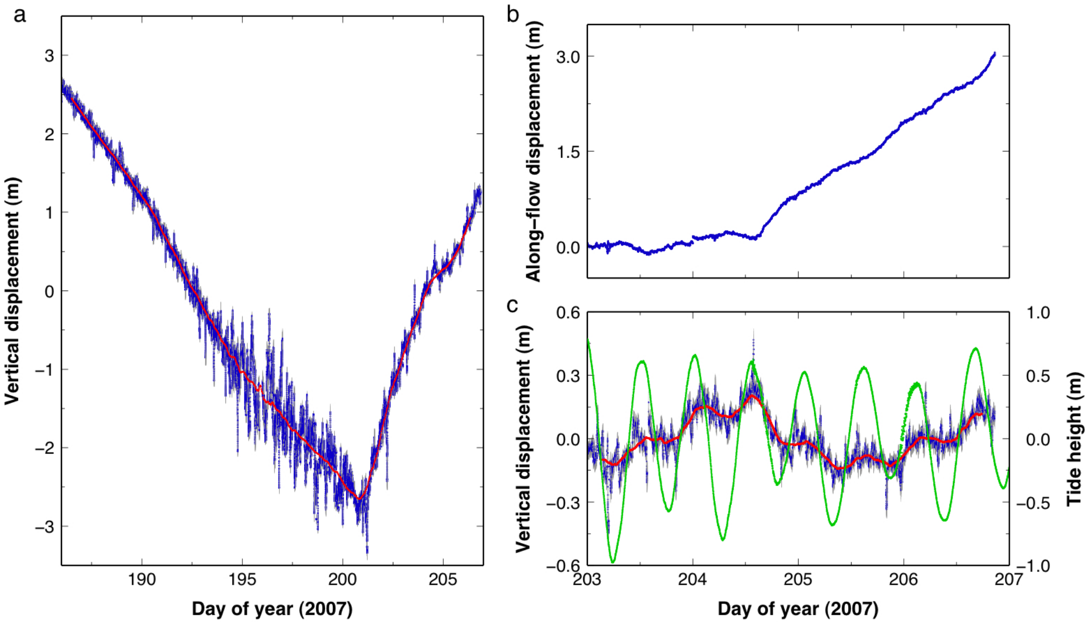

Figure 4.8: (a) Blue dots: Vetical position of site closest to the calving front (IS20), spanning days 186–207 (2007). Red line are the smoothed position estimates using a 24-hr averaging running window. (b and c) Blue dots: Along-flow (b) and vertical (c) position residuals for the site closest to the calving front (IS20), spanning days 203–207 (2007). The position residuals in the along flow are with respect to mean speed on day 203, and in the vertical component, with respect to mean vertical motion for the period 203–207. Red line are the smoothed position estimates using a 6-hr averaging running window. Green line is the tide height in Sermilik Fjord as measured with the tide gauge.

As already mentioned, the sites that operated in the lower part of Helheim in 2007, in general, do not present a vertical response to the tides, thus indicating that the glacier was basically grounded during that summer. (See Figure 4.2 for an example encompassing three days at the beginning of the season.) A notable exception is the site located closest to the calving front in 2007, site IS20 (see Figure 1.5). This site flowed closest to the calving front than any other site during the three seasons, and was retrieved in a mid-campaign visit (on day of year 206) at just tens of meters from the terminus. Figure 4.8(a) shows that after a gradual downwards flow of ~30 cm/d since its deployment, IS20 reverted its vertical direction of flow on day 201 and initiated a large, steady uplift of ~70 cm/d. None of the rest of GPS sites show a vertical uplift concomitant with that of IS20. Furthermore, our analysis indicates that this site transitioned from grounded to floating at some time during the period 194–203. The position estimates present no vertical response to the tides prior to day ~194 (see Figure 4.2 for an example during days 186–189). Figure 4.8(c) shows a vertical tidal response to the tides of ~10% the full tidal range from day 203 until the time of its retrieval. The larger scatter of position estimates for the period 194–203, relative to times prior and after, prevents us from discerning whether the glacier was experiencing or not tidal bending during that period. At about day 204.6, site IS20 shows as well a step-like increase in horizontal velocity not present in the rest of sites (Figure 4.8(b)). One day after site IS20 was retrieved, there was a large calving event at Helheim Glacier associated with a glacial earthquake (and reported in Nettles et al. (2008)). This calving event caused the terminus to retreat by ~1.3 km, as shown by the analysis of MODIS images around these days (Nettles et al., 2008), thus calving off the location where IS20 was operating prior to its retrieval.

In summer 2008, we observe small (less than 3% of the full tidal range) vertical tidal modulations for the sites located closest to the calving front (Figure 4.9). The observed vertical tidal response is limited basically to site IS40 (see Figure 1.6) and to the time periods of maximum ocean tide.

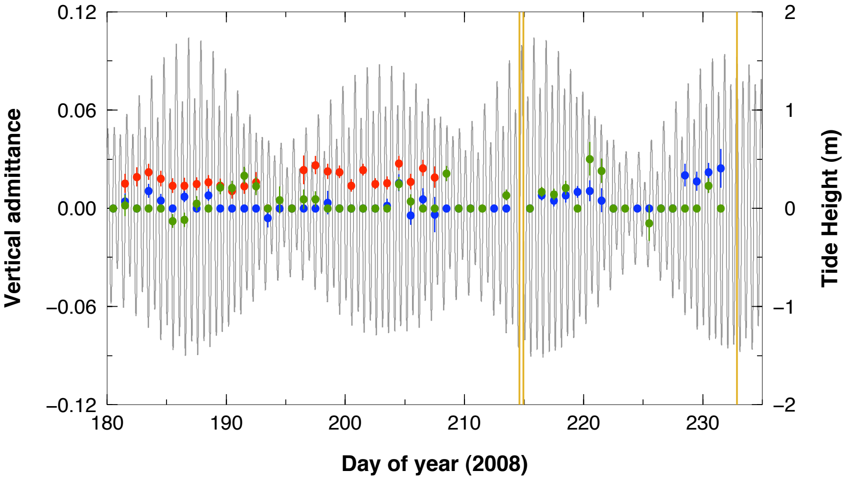

Figure 4.9: Dots: Admittance amplitude for the response of the glacier to the ocean tide in the vertical component, for the three GPS stations located closest to the calving front in summer 2008. Grey line: Modeled tide at Sermilik Fjord. Yellow lines indicate the times of glacial earthquakes.

We do not observe cross-flow tidal variations in 2007 or 2008. However, since the vertical response during these years is small compared to 2006, and the cross-flow response is in turn smaller than the vertical (see Figure 4.6), the level of variations in that component, if present, is below the precision of our position estimates.

During 2006–2008, the position deviations from mean flow in the along-flow component of the sites located in the lower part of Helheim Glacier are dominated by tidal variations. The horizontal response to tidal forcing is observed over the region extending from the terminus, past the glacier bend, and up to at least positions across from the static station NUN1 on the southwestern elbow of the glacier margin (see Figures 1.4–1.6). Figure 4.2 shows an example encompassing three days during each of the campaigns for the four sites located closest to the calving front. The tidally-induced position variations in the along-flow direction are approximately out of phase with the ocean tide. Therefore, the flow of Helheim Glacier is modulated by the ocean tides such that the glacier position is advanced at low tide, and retarded at high tide, with respect to the position expected for the mean flow speed. The amplitude of such modulations is always less than ~10 cm and, as was the case with the vertical and cross-flow components, decays with increasing distance from the calving front.

The horizontal flow of the glacier is modulated by the tides regardless of whether the glacier is floating, as in 2006, or mainly grounded, as in 2007 and 2008. For example, in 2006, the along-flow tidal modulations are observed in the region extending from the terminus to upglacier site SN08 (see Figure 1.4, lack of data around the glacier elbow during this year prevents us from sampling the tidal response in that region). Note that during this time the grounding line was located between sites SN07 and SN08, as inferred from the vertical response. In 2007, tidal variations are observed up to site IS26 (see Figure 1.5). The estimated admittance amplitude for the response at this site is in general significant (the amplitude is always less than ~2 cm) but for some days, generally coinciding with the times when the response of the glacier in the rest of sites is lowest, the signal is within the noise. The same behavior is observed for site IS45 in 2008 (see Figure 1.6), located in a similar location to where IS26 was located the previous year. In 2008 we also observe tidal flow modulations even further upglacier, up to site IS61. However the admittance analysis indicates that the signal is significant only for very few days at this site, when the response of the glacier, as observed for the rest of sites, is largest.

The admittance analysis also shows that the amplitude of the flow modulations decays exponentially with distance from the calving front, as was the case with the vertical and cross-flow components (see Figure 4.6). To illustrate this behavior, Figure 4.10 shows the admittance amplitude as a function of distance to the calving front for the three-day examples in Figure 4.2, that is, days of year 238–240 in 2006, 186–188 in 2007, and 204–206 in 2008. The days shown in this figure have been chosen for its proximity to the time when a position of the calving front is available, day 242 in 2006, day 185 in 2007, and day 213 in 2008. (In 2008, position timeseries were not complete for the days close to 213, hence the larger time separation.) For these three time periods in 2006–2008, the location of the calving front in the fjord (see Figures 1.4–1.6) and the amplitude of the ocean tide (see Figure 4.2) are quite similar. We fit an exponential model (best fit in a least-squares sense) to the admittance amplitude of all sites, independently for each year. In these fits we have not used the sites located farther than ~10 km from the calving front since these sites have very small tidal response and sometimes yield negative admittance estimates, which is physically unrealistic (i.e., the glacier responds to tidal forcing and not the other way around). We estimate, for each of the years, (inverse) scale lengths of $k = 0.43 \pm 0.08$ km^{-1} in 2006, 0.24 ± 0.07 km^{-1} in 2007, and 0.24 ± 0.10 km^{-1} in 2008, and admittance amplitudes at the calving front of $A_0 = 0.08 \pm 0.02$ in 2006, 0.05 ± 0.02 in 2007, and 0.05 ± 0.02 in 2008 (errors are 3-σ). The residuals to these fits have an RMS<0.005 in admittance. It seems interesting to note that the year when the glacier was floating, 2006, the response at the calving front was larger than when grounded, in 2007 and 2008, as one would expect, but that the decay constant was almost double, thus the response decaying to $1/e$ in half the distance. (The day-to-day variation within each year is discussed below.)

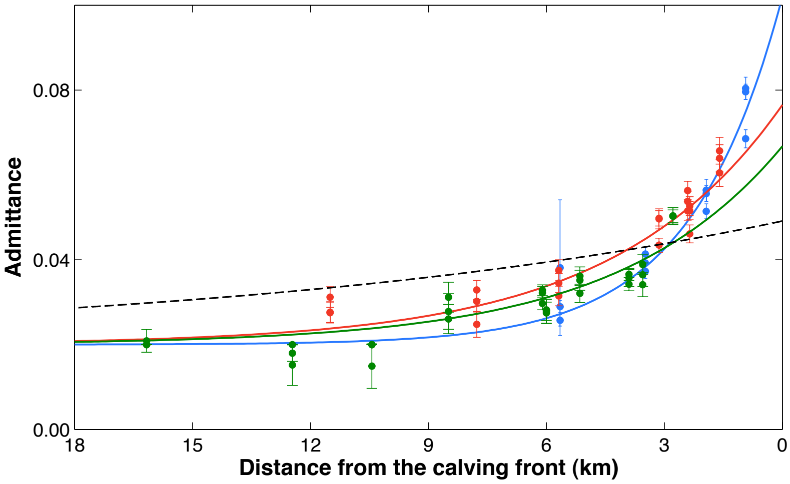

Figure 4.10: Admittance amplitude of the along-flow response to ocean-tidal forcing as a function of distance from the calving front, for days 238-240 in 2006 (blue), 186–188 in 2007 (red), and 204–206 in 2008 (green). Distances are with respect to calving front positions on days 242 in 2006, 185 in 2007, and 213 in 2008. Solid lines are best fit (in a least-squares sense) to the data using an exponential function (sites located >10 km from the calving front have not been used in the fit). Error bars are 1-σ. Dashed line is the admittance predicted by model from Anandakrishnan & Alley (1997). This model does not fit our observations, as further explained in Section 4.5.

A power-law fit to the admittance amplitude $A(x) = A_0 x^{-\alpha}$, where α is the power-law index, and A_0 an amplitude factor, with units km$^{\alpha}$ when the distance to the calving front x is in km, also fits the data well (Figure 4.11). For the fits performed to the data shown in Figure 4.10, the power-law index ranges between 1.0 ± 0.3 and 1.2 ± 0.4, and the amplitude A_0, between 0.06 ± 0.03 km$^{1.1}$ and 0.09 ± 0.05 km$^{1.3}$. However, the RMS of the

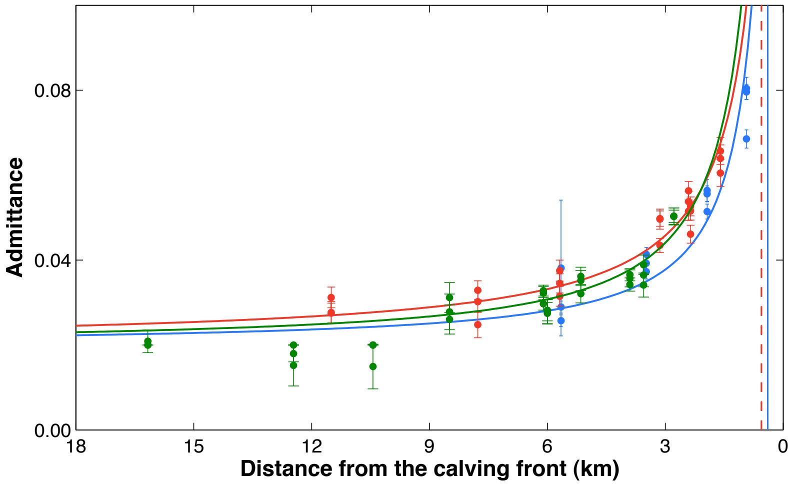

Figure 4.11: Same as in Figure 4.10, except here the solid lines are best fit (in a least-squares sense) to the data using a power-law function.

residuals to these fits is ∼3–5 times larger than the exponential fits. Also, the power-law fit decays slower than the exponential decay, and thus predicts a response of >0.01 in admittance at upglacier positions where no tidal response is observed (at distances >18 km from the calving front).

4.4.3 Temporal variation of the tidal response

We next focus on the temporal variability of the admittance over the longer timescale, which is warranted in 2007 and 2008. Figure 4.12 shows the daily estimates of the admittance amplitude as a function of time for the three sites located closest to the calving front in 2007 and 2008. Figure 4.12(a) includes sites IS20, IS21, and IS22 during the time period 186–206 in 2007. These sites were repositioned to occupy locations ∼3 km upglacier from their original positions, and renamed to IS35, IS36, and IS38 (see Figure 1.5). The three sites, included in Figure 4.12, operated in their relocated positions during the period 209–235, 2007 (see Figure 1.5). Figure 4.12(b) includes sites IS40, IS41, and IS42 (see Figure 1.6) during the period 181–231 in 2008 (IS40, was retrieved on day 207). The figure also shows the ocean tide height as predicted by model AOTIM-5, and the time when glacial earthquakes, associated with large caving events, occurred (Nettles et al., 2008).

The admittance of the along-flow tidal modulations is highly time varying over time periods of a few days. Perhaps most evident in Figure 4.12 are the abrupt increases in admittance amplitude coinciding with the times of glacial earthquakes. (These variations are further explained in Chapter 5.) Focusing on the variation over the longer timescale and avoiding the days around glacial earthquakes, Figure 4.12 shows that the admittance also presents a periodic signature, suggesting that the glacier responds non-linearly to the tidal force. The admittance varies with a period of ∼15 days, suggesting a response to the 14.7-days period modulation of the ocean tide. This semi-monthly admittance amplitude response is markedly asymmetric, characterized by a long phase of increase that begins shortly after the neap tide and lasts ∼11–13 days, plateaus over a few-days time between after the spring tide and before the next neap tide, and then drops quickly in ∼2–4 days, beginning at approximately the same time of the neap tide, before starting a new fortnight cycle. Therefore, the along-flow tidal response maxima and minima occur around the times of the neap tide, at about 2 days before and after the times of the neap tide, respectively.

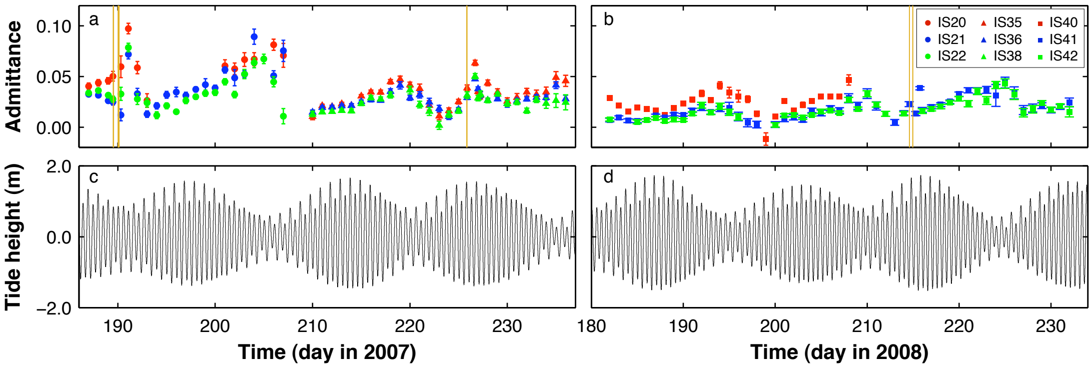

Figure 4.12: Top: Admittance amplitude for the response of the glacier to the ocean tide in the along-flow component, for the three GPS stations located closest to the calving front in (a) 2007 and (b) 2008, yellow lines indicate the times of glacial earthquakes. Bottom: Modeled tide at Sermilik Fjord.

There is a hint, in 2008, when sites IS41 and IS42 where operated continuously during 50 days, of a small secular trend in the admittance amplitude of these sites, perhaps due to a general decrease in glacier length over the summer. We thus fit a linear model to the admittance data of sites IS41 and IS42 (independently) over three complete cycles. (We used complete cycles and not the entire timeseries to minimize the effect of not modeling the periodic signal on the parameter estimates; we chose not to include an asymmetric, sawtooth periodic pattern in our model at this stage to avoid unnecessary complexity.) We perform the fit to data from days of year 181–225, and 187–231. The mean rate of increase of admittance amplitude is ∼0.0004±0.0001 d^{-1}, which though seemingly significant, should be taken cautiously given the model simplicity. (In 2007, the sites had to be repositioned in a mid-campaign visit, which added on to the scatter associated with the larger glacial earthquake signals, does not not justify any attempt to search for a secular trend.)

We have performed several tests and error analyses to assess whether the periodic variation observed in the along-flow admittance amplitude is a real physical response of the glacier, or an artifact. In the remainder of this section, we describe these tests in turn.

4.4.3.1 Tidal admittance analysis using the observed tide

There is the possibility that the temporal variation in the tidal admittance results from an error in the AOTIM-5 modeled tide used in the GPS tidal analysis. A discrepancy between the modeled and the "true" tide that is temporally varying would result in a temporally varying admittance, even if the glacier's response to the tides were constant. Assuming that the tide observed at the cove location (see Figure 4.1(a)) is a good representation of the true tide at the glacier terminus, Figure 4.1(b) shows that the difference between the modeled and observed tide indeed varies over time.

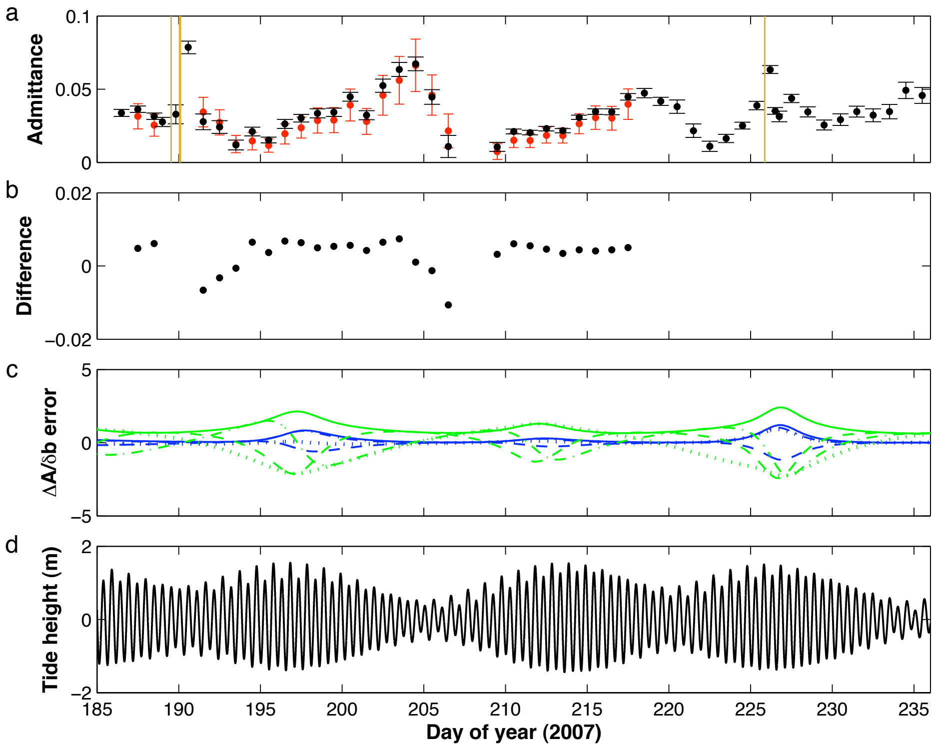

Figure 4.13: (a) Estimated admittance using (black) the modeled tide and (red) the observed tide for sites IS22 (days 186–206, 2007) and IS35 (days 209–235, 2007). Yellow lines indicate the times of glacial earthquakes. (b) Difference between the two estimates of admittance. (c) Normalized error in estimated admittance ΔA due to an error δb in the amplitudes of the tidal constituents. Green and blue lines show the errors due to the 4 principal constituents in the semidiurnal and diurnal bands, respectively. (d) Modeled tide.

To quantify the effect of the discrepancy between the modeled and observed tide on the estimates of admittance, we have performed the tidal analysis detailed in Section 4.3 but using for the ocean tide height variations, $T(t)$ in Equation 4.1, the observed tide instead of the modeled tide. We have done this test for the time periods during which the water-pressure gauge operated in Sermilik Fjord in 2007. Figure 4.13(a) shows the results of admittance with respect to the observed and modeled tide for sites IS22 and IS35. We selected these two sites because they have the least noisy estimates among the sites that present the largest tidal signal and they operated at the time when the water-pressure tide gauge operated. Figure 4.13(b) shows the difference between estimates from both analyses. The figures show that the ∼15-day periodic variation in admittance is present in the results from both analyses. The difference in admittance between the two analyses is ∼20%, mainly due to the higher amplitude of the observed tide. Also, the structure of the temporal variation of the admittance estimates and of their differences are dissimilar.

4.4.3.2 Analysis of the impact of errors in the ocean-tide model

The analysis shown above demonstrates that the temporal variation in admittance is predicted by both the observed and modeled tide. However, the tide gauge was located at a distance of ∼35 km from the glacier's terminus. Thus, there still exists the possibility that the observed and modeled tide do not describe well the tide at the glacier's front. For this reason, we have conducted a theoretical analysis of the effects of errors in the ocean-tide model on the least-squares estimates of admittance (Davis, 2010).

We consider for simplicity that the model fitted to the position estimates is

$$y(t) = A\ T(t) + \epsilon(t), \tag{4.2}$$

where A is the admittance, $T(t)$ is the ocean tide height, and $\epsilon(t)$ is the error in the position estimates. The tide T is given by the tidal constituents i as

$$T(t) = \sum_i b_i \cos(2\pi n_i f_i t + \phi_i), \tag{4.3}$$

where b_i and ϕ_i are the amplitudes and phases of the tidal constituents, $n_i f_i$ are the frequencies of the tidal constituents in the diurnal ($n_i = 1$) and semidiurnal ($n_i = 2$) bands. The amplitudes, phases, and frequencies of the eight principal tidal constituents at Sermilik Fjord as predicted by the ocean tide model AOTIM-5 are given in Table 4.1.

If we assume there is an error $\Delta T(t)$ in the tide models, and A is estimated using least squares, the error ΔA in the admittance is given by

$$\Delta A = (H^T \Lambda^{-1} H)^{-1} H^T \Lambda^{-1} \Delta T, \tag{4.4}$$

where H is the matrix of partial derivatives, or design matrix, which for this simplified model is $H = T$, Λ is the covariance matrix of the errors in the observations which, for simplicity, we will assume it is diagonal and that all observation errors σ are the same such that $\Lambda = \sigma^2 I$, and ΔA and ΔT are the vectors containing the errors for each time epoch in the admittance and tide height, respectively.

An error in the amplitude of the q-th constituent of the tidal model causes an error in the tidal model given by

$$\Delta T(t) = \delta b_q\ \cos(2\pi n_q f_q t + \phi_q). \tag{4.5}$$

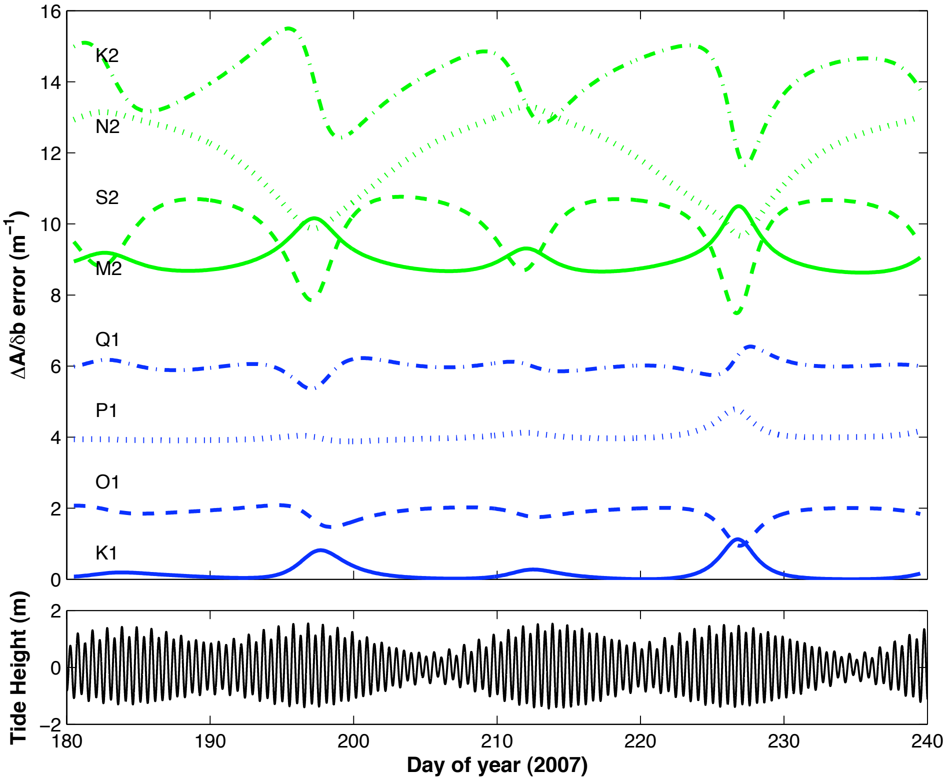

Figure 4.14: (Top) Normalized error in admittance ΔA due to an error δb in the amplitudes of the tidal constituents for days 180–240 in 2007. The error is expressed as $\Delta A/\delta b$. Green and blue lines show the errors due to the 4 principal constituents in the semidiurnal and diurnal bands, respectively. Lines are arbitrarily offset by 2 m^{-1} for clarity. (Bottom) Modeled tide.

Since our least squares analysis is performed in each UT day independently, we can define $t = t_0 + t'$ with $-1/2 \le t' \le 1/2$, where t_0 is the reference epoch for each UT day, and t' is the time that varies during the day relative to the reference epoch. Therefore, if t_j are the observation epochs,

$$H^T H = \sum_j [T(t_j)]^2 \simeq \frac{1}{\Delta t} \int_{-1/2}^{1/2} dt' \left[T(t_0 + t')\right]^2 \tag{4.6}$$

$$H^T \Delta T = \sum_j T(t_j) \Delta T(t_j) \simeq \frac{1}{\Delta t} \int_{-1/2}^{1/2} dt' T(t_0 + t')\, \Delta T(t_0 + t'), \tag{4.7}$$

where we have approximated the sum over all epochs with the integral. After doing the calculations above (detailed in Appendix E), we obtain that the expression for the error in the estimated admittance is

$$\Delta A = \delta b_q \left[\frac{\sum_i b_i \delta_{n_i,n_q} \cos\left[2\pi n_i (f_i - f_q) t_0 + (\phi_i - \phi_q)\right]}{\sum_{i,k} b_i b_k \delta_{n_i,n_k} \cos\left[2\pi n_i (f_i - f_k) t_0 + (\phi_i - \phi_k)\right]} \right]. \tag{4.8}$$

The expression above shows that the error in the admittance can vary with day at specific frequencies. We have evaluated the error in the admittance (using the expression above) caused by an error Δb_i in the amplitudes of each of the eight principal tidal constituents of tidal model AOTIM-5. The results for the error in admittance caused by each of the tidal constituents are shown in Figure 4.13(c) and Figure 4.14, normalized by the error δb_i. We find that the errors in the admittance, ΔA, have dominant frequencies around 15 days and are maximum around the times of spring tides.

Figure 4.13 summarizes the tests detailed above. Figure 4.13(a) shows that the ~15 day variation in admittance is present in the analysis of both the observed and modeled tide. Moreover, although there are differences in the estimated admittances from these two analyses, these do not account for all the observed variation in admittance, nor has it the same temporal structure. Furthermore, Figure 4.13(c) shows that though an error in the amplitude of the tidal constituents can cause an admittance error with a ~15-day periodicity, the temporal variation of such errors is not in phase with the variation in the admittance. Whereas the error in admittance due to an error in the modeled tide peaks generally around the spring tide (or between the neap and spring tides), the estimated admittance peaks ~2 days before neap tide. Taken together, these results suggest that the glacier response to the ocean tidal forcing is not linear with the tide height but contains a ~15-day-period variation during the time of our observations.

4.4.3.3 Example of temporal variation in tidal admittance

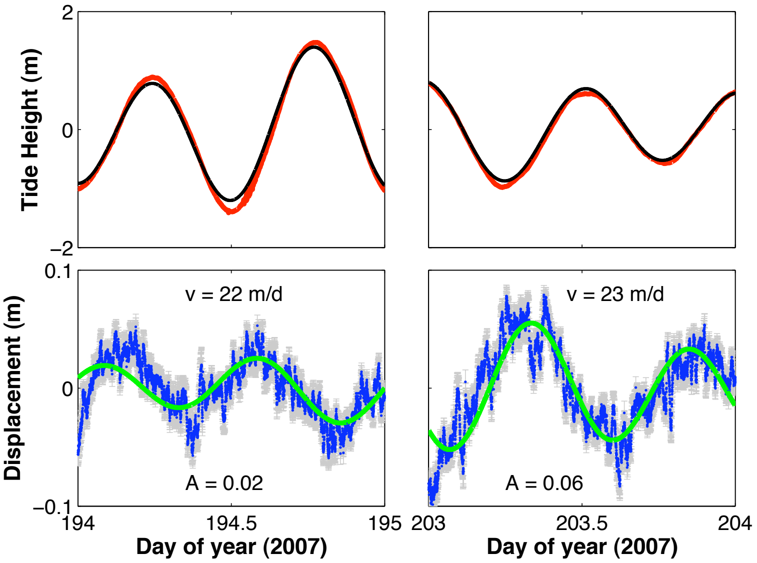

Figure 4.15: (Top) Red and black lines show the observed and modeled tide, respectively. (Bottom) Blue dots show position of site IS22 relative to mean speed. Green line shows modeled tidal response. Results shown are for days (left) 194 and (right) 203 in 2007, showing variation in tidal response over time.

The observed variation in admittance peaks ∼2 days before the neap tide, so that the amplitude of the tidal response of the glacier is sometimes of higher amplitude around neap tide than at spring tide. To illustrate that even just by visual inspection we can observe a variation in the tidal response over time we compare the tide and position observations and model results for two separate days. We chose two days so that the first would have a large tide and low admittance and the second, small tide and high admittance. Figure 4.15 shows an example comparing a day with spring ocean tide and nearly minimum admittance to a day with neap ocean tide and close to maximum admittance. This example clearly shows that there is indeed a variation in the tidal response of the glacier over time.

4.5 Discussion

The vertical response of the glacier to the ocean tides, observed over a significant section of the glacier only during summer 2006, suggests that the glacier had thinned and developed a short floating tongue during this period, already indicated by other studies (e.g., Howat et al., 2005). Our observations also suggest that from the summer of 2006 to the summer of 2007 the glacier thickened, at least in its lower part. Since Helheim's calving front position in the fjord did not vary significantly during 2006–2008 (despite the episodes of significant retreat, the terminus position at the beginning of summers of 2007 and 2008 was very near its position at the end of summer 2006, see Figures 1.4–1.6), we attribute the lack of significant vertical response to the tides in 2007 and 2008 to the possibility that Helheim Glacier had thickened. A simple calculation yields that the glacier will be afloat where its height above sea level is less than

$$h = H_i - H_w = H_w\left(\rho_w/\rho_i - 1\right), \tag{4.9}$$

where H_i and H_w are the ice thickness and the bedrock depth below sea level, respectively, at the grounding line, ρ_i and ρ_w are the densities of ice and seawater, and we have applied the flotation condition at the grounding line, that is, $H_i\rho_i = H_w\rho_w$. In the summer of 2006 we observe vertical response of the glacier to the ocean tides up to ∼5 km behind the calving front. H_w varies over this distance between ∼625–750 m (Joughin et al., 2008b) (see Figure 1.3). The flotation condition requires the height above sea level of the lower ∼5 km of the glacier to be less than h∼81–97 m. Lidar measurements from summer 2007 yielded a height of the calving front above sea level of 70–150 m, with the height varying across the glacier (L. Stenseng, private communication). Stearns & Hamilton (2007) estimated thinning rates for Helheim during the period of 2002–2005 of 7–44 m/yr. In 2005–2008 the rate of change in surface elevation changed from negative to positive, amounting to 11 m/yr in 2006–2007 (Murray et al., 2010). This suggests that the possibility of Helheim thinning from below the flotation threshold (h ∼81–97 m) in summer 2006 to above such threshold in 2007 is plausible, but requires the glacier to have been close to the flotation threshold during this period. The transition of site IS20 from grounded to floating during summer 2007 and the small vertical response of site IS40 during some periods in 2008 suggest that in fact the glacier was close to the flotation threshold. Comparison between position measurements from GPS sites deployed in similar locations in summers of 2006–2008 yield higher vertical positions by ∼7–15 m in 2007 and 2008, with respect to 2006. However these results should be taken with caution because location of sites are only approximately reoccupied from one summer campaign to the next, and the surface of Helheim Glacier is highly irregular, with the lower part of the glacier mainly composed of ice pinnacles that can result in thickness variations of several meters over a distance of a few tens of meters.

Furthermore, the vertical uplift and acceleration of site IS20 and its transition from grounded to floating during the last days that this site operated, together with the fact that a day after its retrieval a large-scale calving event calved off the location where IS20 was operating, suggests that the icebergs at Helheim Glacier start to vertically respond to the ocean tides before completely detaching from the glacier. This hypothesis is in agreement with the observation that the retreat of Helheim Glacier took place by means of the release of large tabular icebergs in 2006, when the glacier had developed a short floating tongue, and of smaller unstable icebergs in 2007 and 2008, when the glacier was basically grounded (further explained in Chapter 5). These observations suggest that the vertical response of the glacier to the ocean tides, play an important role in the weakening of the glacier terminus and the subsequent formation of icebergs, as had been previously suggested by calving models (e.g., van der Veen, 1996; Benn et al., 2007a,b).

Our results indicate that the tidal admittance analysis performed on daily timeseries describes well the tidal response of the glacier, both in the vertical and horizontal components, and thus that the ice deformation varies linearly with variations in the applied stress over daily timescales. This suggests that the ice responds elastically to tidal variations (e.g., Anandakrishnan & Alley, 1997; Gudmundsson, 2007). That is, that the variation in driving stress or shear stress (since these balance in steady state), $\Delta\tau$, is proportional to variations in hydrostatic pressure,

$$\Delta\tau = K\rho_w g T(t), \tag{4.10}$$

where K is a constant of proportionality, ρ_w is the density of sea water, g is the acceleration due to gravity, and $T(t)$ is the tidal height.

The out-of-phase response of the glacier to tidal forcing in the along-flow component is usually interpreted as resulting from stress fluctuations on the terminus caused by variations in hydrostatic pressure associated with the ocean tides (e.g., Anandakrishnan & Alley, 1997). A comparison between expected variations in speed due to tidally induced changes in driving stress (e.g., Howat et al., 2005) and the observed variations in speed due to tidal forcing generally supports this hypothesis at Helheim Glacier. For a site flowing at ∼20 m/d we observe an amplitude of the tidal variations in displacement of a maximum of ∼5–10 cm (see Figure 4.12). This corresponds to a variation in speed (given by $2\pi nf \sim 4\pi$ d^{-1} times the variation in displacement, where nf is the frequency of the tide) of ∼3–6%. On the other hand, we investigate the change in driving stress and speed caused by the tidal variation in sea level. As the tide rises and falls, the normal stress due to hydrostatic pressure acting on the calving front increases and decreases, respectively. The difference in force ΔF_w between high (h_h) and low (h_l) tide is given by (e.g., Anandakrishnan & Alley, 1997):

$$\Delta F_w = F_h - F_l = \frac{\rho_w g}{2}\left(h_h^2 - h_l^2\right) = \rho_w g h_w \Delta h_w, \tag{4.11}$$

where h_w is the mean sea level, and Δh_w is the tidal range. The difference in driving stress between high and low tide is given by $\Delta F_w/L$, where L is the length over which the tidal forcing acts. We follow the force-balance analysis in Howat et al. (2005), where it is used that glacier speed is proportional to mean effective driving stress τ_e to a power n. For glaciers like Helheim, where the margins provide most of the resistance to flow, $n \sim 3$ (Paterson, 1994). Then, the increase in flow speed at low tide with respect to mean sea level (m) can be quantified:

$$\frac{v_l}{v_m} = \left[\frac{\tau_e + \Delta F_w/2/L}{\tau_e}\right]^3 \tag{4.12}$$

where we have used that at low tide there is an increase in driving force with respect to the mean sea level of $\Delta F_w/2/L$. Assuming that the length over which the tidal forcing acts is $L{\sim}12$ km (suggested by our observations) and that the mean effective driving stress at Helheim is $\tau_e \sim 170$ kPa (Howat et al., 2005), these calculations yield a variation in speed between low and mean tide of ~1%, compared to our observed maximum of ~3–6%. Thus, as previously mentioned, the similarity between the results of this simple calculations and our observations suggests that the out-of-phase response of the glacier with respect to the ocean tide is a result of variations in hydrostatic pressure at the glacier terminus due to the ocean tide.

Despite that the glacier deformation varies linearly with variations in tidal stress, the glacier responds with a time delay to the forcing of ~1–2 h, which suggests some source of viscous resistance. Moreover, an exponential function describes well the decay of the tidal response of the glacier with distance from the calving front in the three components of flow.

The model by Anandakrishnan & Alley (1997), where the glacier is modeled as a purely elastic beam flowing solely by deformation of the viscous till bed, predicts an out-of-phase tidal response in the along-flow direction. Furthermore, in this model, the response of the glacier decays exponentially with distance and is delayed with respect to the forcing. The model predicts a horizontal tidal displacement w_x given by

$$w_x(x,t) = -\frac{P_0}{\sqrt{2}kE}e^{-kx}\cos(\omega t - kx + \pi/4), \tag{4.13}$$

where x is distance from the grounding line, t is time, E and H are ice elasticity and thickness, respectively, η and h_b are the till's viscosity and thickness, P_0 and ω are the amplitude and frequency of the stress fluctuations acting on the terminus due to tidal forcing, and $k = \sqrt{\frac{\omega\eta}{2EHh_b}}$.

Helheim Glacier presents some fundamental disagreements with this model, namely the source of the viscous resistance, since fast-flowing glaciers as Helheim flow by sliding over their beds. However, since the spatial dependence and phase relation are generally in good agreement with our observations, we have compared this model to our observations. We use an elastic modulus of 3×10^9 Pa (Paterson, 1994), an ice thickness of 800 m, and a semidiurnal tidal forcing of 1 m amplitude, for which we deduce an amplitude for the tidal pressure acting on the calving front of $P_0 = \frac{\Delta F_w}{2h_w}$ ~12.5 kPa. Lacking information for Helheim on the till parameters η and h_b, we use the values in Anandakrishnan & Alley (1997) for Ice Stream C. We obtain a value for the admittance at the calving front of ~0.04, which is a slightly lower admittance than the values obtained from the exponential fits to our position estimates (~0.05–0.08). However, the scale length predicted by the model of ~0.07 km^{-1} is 4–6 times smaller than the observed at Helheim. Figure 4.10 shows the admittance as a function of distance predicted by this model. A higher scale length could be obtained by means of a higher value of η/h_b, however this would further decrease the amplitude of the response. Thus, we conclude that the model of Anandakrishnan & Alley (1997) does not fit the observed tidal admittance at Helheim Glacier.

Our observations show that the response of the glacier to tidal forcing is delayed by ~1–2 h with respect to the ocean tide. A delay in the tidal response has also been observed at other glaciers and ice streams (e.g., Dietrich et al., 2007; Anandakrishnan et al., 2003). The response of Helheim Glacier occurred ~1 h earlier in 2006, when the glacier front was afloat, possibly due to a reduction of the ice-bedrock friction. There is also a slight hint of an increase in the delay of the response with distance from the calving front.

The model of Anandakrishnan & Alley (1997) also predicts a delay at the location where the tidal forcing is applied, of $\pi/4/\omega$, where ω is the frequency of the tide. Such a delay in this model results from the requirement that the resistance to flow is viscous, combined with the glacier ice being elastic. (A purely elastic response with no viscous resistance is in phase with the tide.) On the other hand, the model of Anandakrishnan & Alley (1997) predicts a time dependence for the horizontal displacement given by $sin(\omega t - kx - \pi/4)$. This model predicts a time delay of the response with respect to the tide as a function of distance to the calving front of:

$$\Delta t = \frac{kx + \pi/4}{\omega}, \tag{4.14}$$

which for Helheim yields a delay of the response at the calving front of 1.5 h and a further delay of k/ω ~0.5–0.8 h/km upglacier, for the range of k values that fit our estimates. Although the predicted time delay at the terminus is in good agreement with the observed at Helheim, the response observed upglacier (0.1–0.4 h/km) travels ~1–8 times faster than the model predictions.

We also test a model in which glacier speed v also depends non-linearly on the driving stress, balanced by a resisting shear stress τ_b. The model is perturbed by ocean tides such that tidal stresses $\Delta\tau$ are proportional to tidal amplitude $T(t)$ and a glacier-position-dependent function $K(x)$ (Gudmundsson, 2007; King et al., 2010):

$$v = C\tau_b^n \tag{4.15}$$

$$v = \bar{v} + \Delta v \tag{4.16}$$

$$\tau_b = \bar{\tau}_b + \Delta\tau = \bar{\tau}_b + K(x)\,\rho_w\,g\,T(t), \tag{4.17}$$

where $\bar{v}$ is the mean speed, Δv is the variation in speed due to the ocean tides, and $\bar{\tau}_b$ is the mean shear stress. This model, using $n \sim 3$, is analogous to the force-balance approach we used above to deduce the variation in speed at the terminus, but introducing the dependence of the response with distance, $K(x)$. The equations above yield a variation in speed due to the ocean tides of

$$\Delta v = C\left(3\Delta\tau^2\bar{\tau}_b + 3\Delta\tau\bar{\tau}_b^2 + \Delta\tau^3\right). \tag{4.18}$$

We use $\bar{\tau}_b = 170$ kPa for Helheim (Howat et al., 2005). A simple force balance analysis (see Equations 4.11 and 4.12) yields $K(0) = -h_w/L$, where h_w is the mean sea water depth at the calving front (h_w ~700 m at Helheim) and L is the length over which tidal forcing acts (L ~12 km). We find that this model predicts a variation in speed of ~1% at the calving front. The maximum tidally induced variation in speed observed at Helheim is ~3–6% (corresponding to a displacement amplitude of ~5–10 cm). We use an exponentially decaying function $K(x)$ with x the distance from the calving front, and a scale length of ~0.24 km^{-1} (based on our observations). Figure 4.16 shows that these calculations predict a tidal response of the same order of magnitude but smaller than the observed, specially at the sites closest to the calving front. Gudmundsson (2007) also observes values of $K(0)$ larger than predicted and argues that at Rutford Ice Stream the tidal perturbation of the basal shear stress could be primarily related to tidal flexure stresses (also proportional to $T(t)$ but of larger amplitude (Holdsworth, 1969)), rather than to the hydrostatic stress variations. This could explain the larger tidal flow response at Helheim during summer 2006, when the glacier had developed a short floating tongue. However, it can not explain the observations compared to the model in Figure 4.16, since these are for summer 2007, when the glacier was basically grounded. Thus, these results need further investigation.

Furthermore, our observations indicate that the glacier is highly variable in its horizontal response to the tides. The along-flow tidal response presents a non-linear response to the tides of ~15 days period. Neither of these models explains the observed temporal variation in admittance. Gudmundsson (2007) showed that his model predicted a non-linear response at Rutford Ice Stream that caused a fortnightly variation in the speed of the glacier. However the higher driving stress at Helheim Glacier (~170 kPa) compared to Rutford Ice Stream (~21 kPa (Gudmundsson, 2007)) reduces the non-linear component of the variation in speed in Equation 4.18, so that, the non-linear variation in the mean speed of the glacier predicted by Gudmundsson (2007) is negligible in the case of Helheim Glacier.

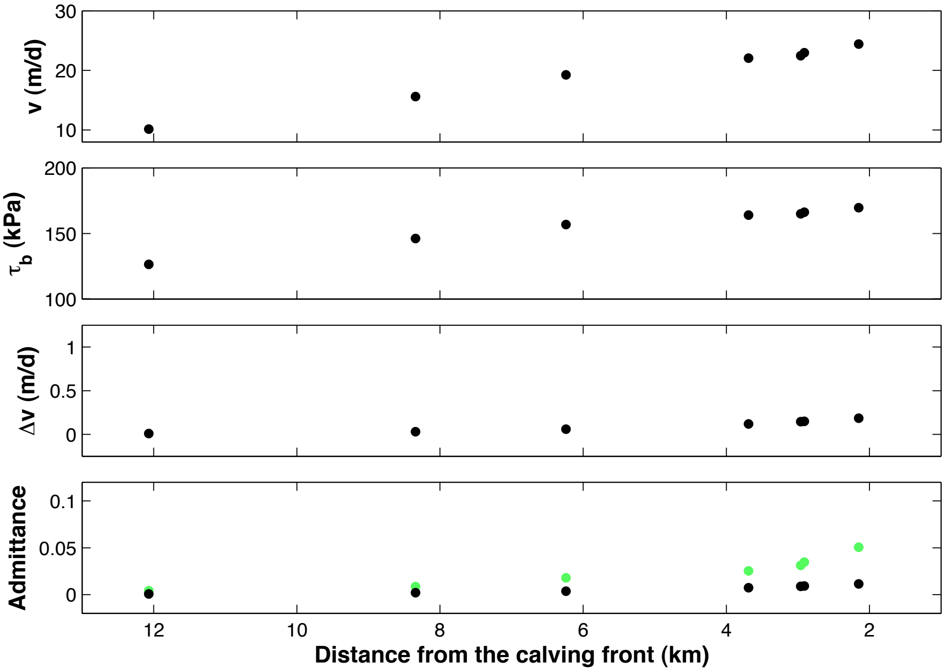

Figure 4.16: (a) Estimated mean summer speed for sites IS20–IS26 in 2007. (b) Estimated basal shear stress from mean speed using $\bar{\tau}_b = 170$ kPa near the calving front and $v = C\bar{\tau}_b^3$. (c) Modeled variation in speed Δv due to tidal stresses. (d) (black) Modeled tidal admittances in displacement and (green) estimated tidal admittance from observations.

The classical models for vertical elastic or elastic and viscoplastic tidal deformation (e.g., Holdsworth, 1969; Lingle et al., 1981) do not predict well the spatial variation of the vertical tidal response observed at Helheim (see Figure 4.17). In these studies the glacier is modeled as a uniform long beam, pinned at one end, subject to a uniform load, and floating in seawater. For these models to fit the data well, the grounding line (or pinned point) would have to be placed downglacier of a Helheim site (SN07) that shows a vertical response. We fit the observations of vertical admittance amplitude for sites SN05–SN08 deployed during days of year 238–241 in 2006, using the model by Lingle et al. (1981). We require the grounding line to be at a mid distance between SN07, which showed vertical response, and SN08, which did not. We perform fits for different glacier thickness values. Figure 4.17 shows the result for an ice thickness of 800 m. We find that best-fit parameters for the observations at Helheim yield a negligible viscoplastic component, and a Young modulus for ice of $\sim 1.3 \times 10^{10}$ Pa, thus at least ~40% larger than accepted values for glacier ice. However, these models use a boundary condition for long floating tongues, and may therefore not be appropriate for Helheim in its current configuration. Further investigation is needed to explain the observed vertical response to ocean tides at Helheim Glacier.

Our observations indicate that the tidal response in the horizontal component when the lower part of Helheim Glacier was floating (in 2006) differs slightly from the response when the glacier was basically grounded. When the glacier was afloat the response was of higher amplitude but decayed faster with distance from the calving front. This suggests that the reduction in friction, likely caused by the detachment of the glacier tongue from the fjord bed, plays a role in the tidal response. This is also suggested by the lower time delay in the response of the glacier. Alternatively, as explained above, the horizontal tidal flexure stresses could add on to the hydrostatic stress variations, resulting in a larger perturbation to the basal shear stress (Holdsworth, 1969; Gudmundsson, 2007).

The tidal variation in the cross-flow component indicates that the sites change its direction of flow as the tide rises and falls. The fact that the cross-flow tidal signal is observed in 2006 only where a vertical response to the tides is present, for sites SN05–SN07, and the lack of cross-flow tidal signal during 2007 and 2008, when no significant vertical response is observed, suggests a link between these two dynamic responses. The similarity between the scale length of the exponential decay of both responses further suggests the link between the cross-flow and vertical responses. The change in flow direction of the sites with the tide could be indicating that the deflection of the glacier was not uniform across the glacier's width, possibly due to a difference in glacier thickness across its width, causing a tilt in the floating ice tongue as it rose and fell. A similar effect was observed in Ice Stream D by Anandakrishnan et al. (2003).

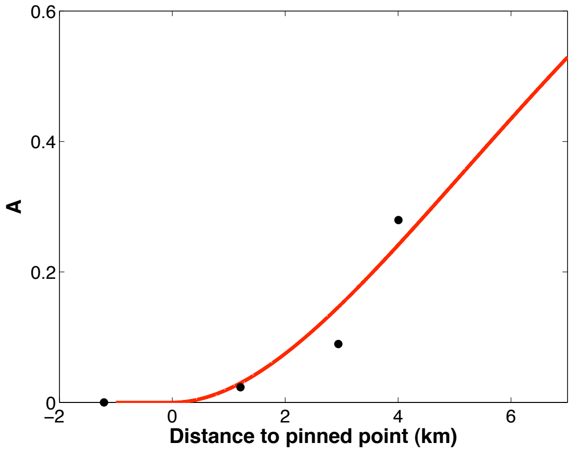

Figure 4.17: Admittance amplitude for the vertical response of the glacier to the tides as a function of distance to the grounding line. Black dots are observations at Helheim. Red line shows the vertical displacement predicted by the model of Lingle et al. (1981) and best-fit parameters for an ice thickness of 800 m. The model does not explain the observations well. The error bars for the admittance are smaller than the size of the dots.

4.6 Summary

We have used the extensive GPS-based positioning data set collected at Helheim Glacier during the summers of 2006–2008 to characterize the glacier response to the ocean tide. The position deviations from mean flow in the along-flow component of the sites located in the lower ∼12–16 km of Helheim Glacier are dominated by tidal variations that are out of phase with the ocean tide. In summer 2006, the lower ∼4–5 km of the glacier also showed a vertical response to the tides, accompanied by a response in the direction perpendicular to flow.

The admittance analysis indicates that the tidal response of the glacier is delayed by ∼1–2 h with respect to the tides. The response occurred ∼1 h earlier in 2006, when the glacier front was afloat, possibly due to lower friction at the base of the glacier.

The vertical and cross-flow responses to the tides, observed only during summer 2006, suggest that the glacier had thinned and developed a short floating tongue during this period. The along-flow tidal response of the glacier is out of phase with the ocean tide. We interpret this as resulting from stress fluctuations on the terminus caused by tidal variations in hydrostatic pressure (e.g., Anandakrishnan and Alley, 1997; Gudmundsson, 2007).

The tidal admittance parameters in all three components show an exponential decay with distance from the calving front. Although the model of Gudmundsson (2007) describes the overall spatial variation of tidal admittance we observe, the shape of the admittance decay is not explained well.

Furthermore, the response in the along-flow component varies over time with a periodicity of ∼15 days and can increase abruptly as a response to large calving events associated with glacial earthquakes.

Chapter 5

Flow variations at Helheim Glacier related to glacial earthquakes and calving

A major objective that prompted the field-based observational campaigns conducted at Helheim Glacier was to identify the source mechanism of glacial earthquakes and to study their related glacier dynamic response. These recently unveiled type of seismic events, epicentered on large outlet glaciers (with an uncertainty of ∼20 km), mainly on the Greenland Ice Sheet, but incompatible with standard tectonic earthquake models, are characterized by seismic magnitudes ranging between 4.6–5.1, and long periods of more than 30 s (Ekström et al., 2003, 2006; Tsai & Ekström, 2007; Nettles & Ekström, 2010). Modeling suggested at first that a plausible explanation for glacial earthquakes were episodes of sudden and short-lived accelerations of large volumes of the glaciers trunks for distances of meters to decimeters (Ekström et al., 2003). Magnitudes of 4.6–5.1 are equivalent to a mass-slide product of $0.1\text{–}20\times10^{14}$ kg m (Ekström et al., 2006). The ambiguity on the mass and distance can best be resolved using high-precision geodetic methods such as GPS, which motivated the consolidation of the project at Helheim Glacier. The temporal pattern of occurrence of these events, marked by a strong seasonality with most of the events taking place during summer, and a dramatic increase in the frequency of events over the years 2000–2005, suggested they were linked to changing glacier dynamics and accelerating mass loss from the Greenland Ice Sheet, in relation to environmental conditions (Ekström et al., 2006). In Greenland, the number of events per year increased gradually from an average of 10 in 1993–2000 to 33 in 2005. However, during the period 2006–2008 the glacial earthquake activity decreased to levels similar to 2003–2004 (Nettles & Ekström, 2010).

Later investigations demonstrated that glacial earthquakes occur close in time to sudden episodes of large-scale calving events (Joughin et al., 2008a; Nettles et al., 2008; Amundson et al., 2008). As examined in detail in this chapter, the geodetic field experiment conducted by Nettles et al. (2008) at Helheim Glacier showed that the glacial

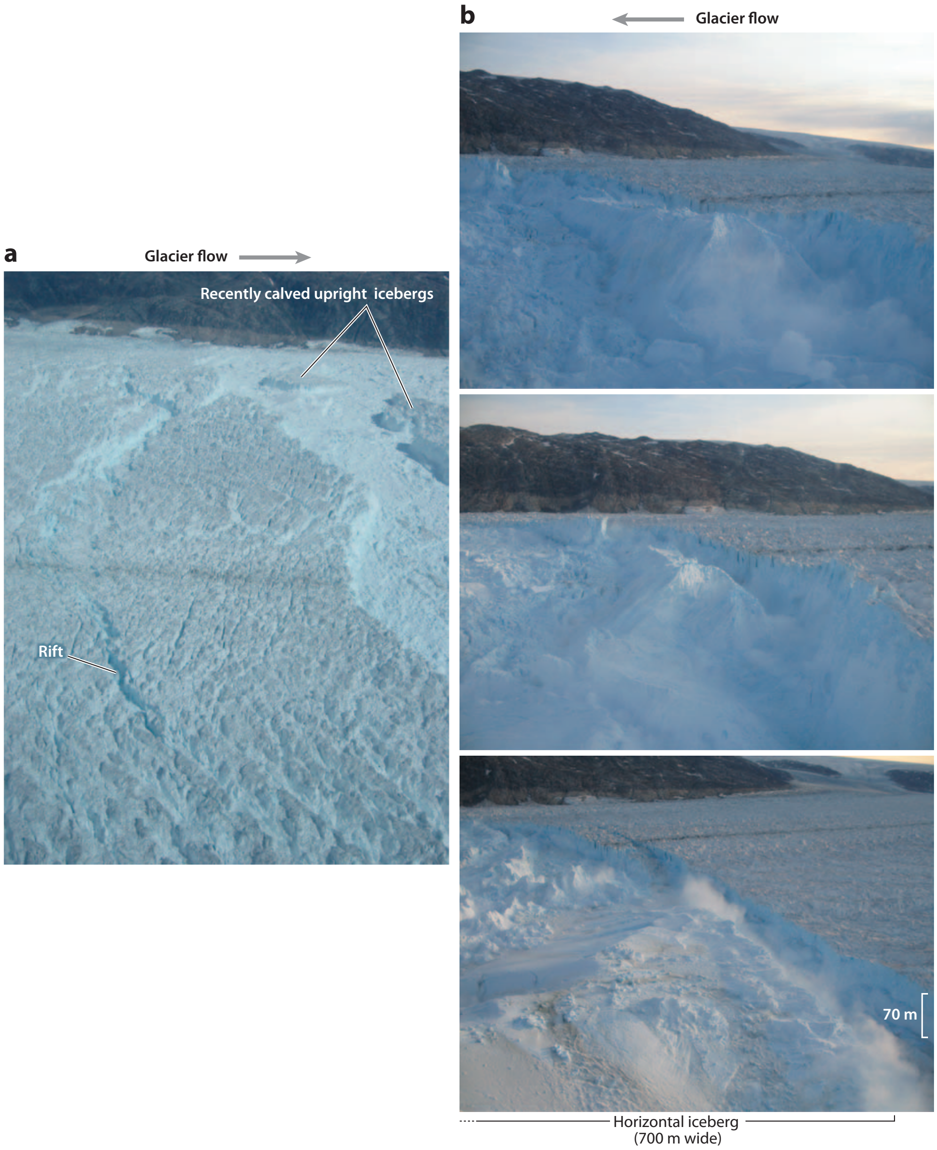

Figure 5.1: Pictures showing two different types of large-scale calving events at Helheim Glacier. (a) Large tabular icebergs calved at the glacier, image from July 25, 2006. Glacier flow in this image is from left to right. (b) Calving event from August 19, 2008, involving an unstable iceberg that overturns (time progresses from top to bottom images, with the bottom image taken ∼3 minutes after the top image), generating a glacial earthquake. Glacier flow in this image is from right to left. From Nettles & Ekström (2010).

earthquakes and calving events were also temporally linked to moderate but abrupt speedups of the glacier, rather to steps in glacier displacement as first suggested by Ekström et al. (2003, 2006). However, the observed glacier accelerations represent a force too small to generate the observed seismic radiation. The observations (Nettles et al., 2008; Amundson et al., 2008) and modeling (Tsai et al., 2008; Nettles & Ekström, 2010) imply that glacial earthquakes are generated by the calving process. The earthquakes are only detected where marine-terminating outlet glaciers are present and in association with the calving of large-scale and unstable icebergs. Icebergs which are narrower in the along-flow direction than are high, overturn against the glacier ice front while calving, accelerating away from the glacier and transmitting a force to the calving front or directly to the fjord seafloor (Tsai et al., 2008; Nettles & Ekström, 2010). The variation in earthquake activity during the period 1993-2008 tracks the ice-front retreat activity in Greenland. The seasonality of the events is explained by the general pattern of retreat and advance from Greenland outlet glaciers, which tend to advance in the wintertime and to retreat during the summertime, by means of a few large-scale calving events with associated glacial earthquakes (Joughin et al., 2008a; Nettles & Ekström, 2010).

We found that the glacier accelerations associated with glacial earthquakes and large-scale calving events were also linked to sudden and transient increases in the flow response to ocean tidal forcing (de Juan et al., 2010b). The transient nature of such behavior and its temporal relation to strain-rate variations associated with the glacial-earthquake speedups suggested that this response was linked to a temporal reduction of the ice-bedrock friction, possibly driven by a disruption of the subglacial drainage system.

The dynamic short-timescale response of the glacier's surface in relation to glacial earthquakes and calving events was first reported by Nettles et al. (2008). In Section 5.1 we expand the results presented in Nettles et al. (2008) to show the geodetic observations of glacier deformation associated with several glacial earthquakes detected at Helheim Glacier during the summers of 2006–2008, and characterize the dynamic response of the glacier associated with glacial earthquakes. In Section 5.2 we present and expand the results reported in de Juan et al. (2010b), where we analyzed the temporal and sudden increase in ocean tidal response associated with glacial earthquakes.

5.1 Glacier speedup related to glacial earthquakes and calving

During the summer of 2006, although several retreats of the calving front were detected (Joughin et al., 2008a), no glacial earthquakes occurred at Helheim Glacier. During the observing period of the GPS network in 2007, six glacial earthquakes were detected at Helheim, clustered in three different time periods. Finally, only two glacial earthquakes separated by a few hours occurred during the GPS observing period at Helheim in summer 2008. Some lower magnitude earthquakes, generally occurring close in time to larger earthquakes, have been identified with an interactive detection procedure developed by M. Nettles (private communication). Table 5.1 shows the time of occurrence of large and small glacial earthquakes during the GPS observing periods at Helheim Glacier.

Table 5.1: Time of occurrence, magnitude M_{SW} (Ekström, 2006), and detection method of the glacial earthquakes detected at Helheim during the observing periods of the GPS networks deployed during the Arctic summers of 2006–2008. "S" refers to the standard automatic procedure described by Ekström et al. (2003) and Ekström (2006), and "E" refers to the interactive mode used for earthquakes too small to be detected with the standard procedure.

Year	**Day of year**	**Time (UTC)**	**Magnitude (M_{SW})**	**Detection Method**
2007	189	12:58:24	4.7	S
2007	189	21:33:10	—	E
2007	190	01:08:16	4.8	S
2007	190	02:32:10	4.5	E
2007	190	02:42:08	4.7	S
2007	196	03:48:30	—	E
2007	201	05:49:40	—	E
2007	207	22:42:48	4.7	S
2007	209	02:18:20	—	E
2007	225	18:42:20	—	E
2007	225	20:37:52	4.8	S
2008	214	14:43:20	4.8	S
2008	214	23:00:40	4.8	S
2008	232	21:05:28	4.8	S

5.1.1 Method and Results

The time of occurrence of teleseismically detected glacial earthquakes were indicated by yellow bars in Figures 3.8 and 3.9. The mean daily velocity estimates of the GPS sites from the networks in summer 2007 and 2008, shown in these figures, reveal that the earthquakes are closely correlated in time with increases in speed. Such accelerations occur on timescales shorter than a day and in general happen coherently throughout the length of the glacier. The speed recovers partially 1–2 days after the glacial earthquakes. Nevertheless, specially in summer 2007, glacial earthquakes result in an unrecovered increase in speed that appears to last throughout the season. Other variations in speed, similar to the ones caused by the earthquakes, at least from the perspective of daily estimates, take place at times when no earthquakes are registered. However, the characteristics of such speed increases are markedly different from the ones related to glacial earthquakes, as will be shown in this and later chapters. The largest increase in speed during the summers of 2006–2008 was registered in 2007 in association with three major glacial earthquakes that took place in an interval of $\sim$14 h on days of year 189–190. One glacial earthquake in 2007 took place during a mid-campaign field visit on day 207, when there was no GPS cover at the lower part of the glacier. And finally, two more glacial earthquakes took place in mid August, on day of year 225, in 2007, causing an increase in speed similar to the ones associated with the event at the beginning of the season but of smaller magnitude. In 2008 only two glacial earthquakes, on day of year 214, occurred during the observing period of the GPS network. The increase in speed associated with such events was smaller than in the previous year.

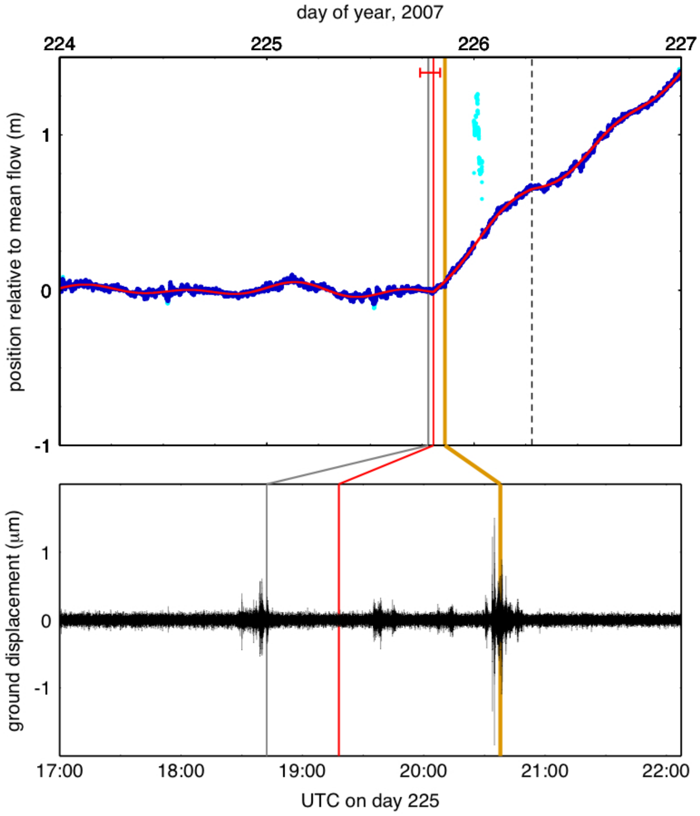

Figure 5.2: (Top) Along-flow position estimates relative to the mean speed prior to the speedup and glacial earthquake for site IS38 and spanning three days in 2007, days 224-227. Red line shows estimated fit to the position timeseries with our preferred model (see text) and light blue dots indicate 4-σ outliers. Vertical lines indicate the time of (yellow) a teleseismically detected glacial earthquake, (grey) a smaller glacial earthquake, (red) the estimated time of the change in speed of the glacier with its corresponding error bar, and (black, dashed) the time of a second change in speed. (Bottom) Displacement seismogram recorded at Isortoq station, ~100 km from Helheim. From Nettles et al. (2008).

The high-accuracy, high-time-resolution estimates of glacier position allow us to investigate these events in greater detail. Figure 5.2 shows the position estimates of station IS38, located near the calving front (see Figure 1.5), during three days encompassing the time of the glacial earthquake that occurred near the end of day 225 in 2007. An additional smaller earthquake, detected with enhanced methods, took place ~2 h before the teleseismic earthquake. The position estimates are shown relative to the mean flow prior to the speedup. The figure shows that the speedup happened in a step-wise fashion at a time close to the time of the earthquakes. The speed of this site transitioned from

21.7 m/d before the earthquake to 23 m/d following the earthquake (Nettles et al., 2008).

The exact timing of the change in speed can be achieved by means of several approaches. However, the sinusoidal variations in speed related to the ocean tidal response complicate the analysis. An empirical orthogonal function (EOF) analysis, which decomposes the signal into orthogonal basis functions, yielded that the step-wise increase in speed and the tidal response of the glacier could not be separated into different temporal eigenfunctions, indicating that both geophysical responses have the same spatial variability and therefore are somehow linked (Davis et al., 2008). Had these two responses been separated in different EOF modes, a better estimation of the time of the change in flow speed would have been possible, however the tidal variations need to be taken into account in the time estimation. One way of estimating the time of the change in velocity is performing a χ^2 search for the time when a step-like change in velocity (modeled as a heaviside step function) takes place. In this approach, where each site's timeseries is analyzed independently, the simplest model to fit the timeseries during the three-day estimation period is one that includes a velocity prior to the time of velocity change, a heaviside step function for the change in velocity, a final velocity, a combination of diurnal and semidiurnal cosines and sines to fit the tidal variations, and a position offset:

$$\begin{aligned} f(t) = x_0 + v\,t + H(t-t_1)\,\Delta v_1 + A_s\,\cos(\omega_s t) + C_s\,\sin(\omega_s t) + \\ A_d\,\cos(\omega_d t) + C_d\,\sin(\omega_d t), \end{aligned} \tag{5.1}$$

where t is the time since the reference epoch, x_0 is the position offset at the reference epoch, v is the velocity prior to the glacial earthquake, Δv_1 is the increase in velocity after the earthquake, t_1 is the times of the change in velocity, $H(t)$ is the heaviside step function, ω_s and ω_d are the semidiurnal and diurnal frequencies, A_s and C_s, are the tidal parameters in the semidiurnal band, and A_d and C_d, the tidal parameters in the diurnal band. In this procedure we estimate the parameters that best describe the data in a least-squares sense and calculate the postfit χ^2 residual for a given range of times of speed-change. We take as the time of the change in speed the one that minimizes the χ^2 of postfit residuals. However, the timeseries are better described by a model that allows for a second heaviside change in speed to account for a small change in speed observed $\sim$12 h after the first change in speed, and a linear variation over time of the amplitudes of the sinusoidal variations fitted:

$$\begin{aligned} f(t) = x_0 + v\,t + H(t-t_1)\,\Delta v_1 + H(t-t_2)\,\Delta v_2 + \\ (A_s + B_s t)\,\cos(\omega_s t) + (C_s + D_s t)\,\sin(\omega_s t) + \\ (A_d + B_d t)\,\cos(\omega_d t) + (C_d + D_d t)\,\sin(\omega_d t), \end{aligned} \tag{5.2}$$

where Δv_2 is the decrease in velocity, t_2 is the time of the second change in velocity, B_s and D_s are the tidal rate parameters in the semidiurnal band, and B_d and D_d, the tidal rate parameters in the diurnal band. Such approach is our preferred model since it improves the fit to the timeseries with respect to the simplest model at a statistically significantly level (>99% confidence) (Nettles et al., 2008).

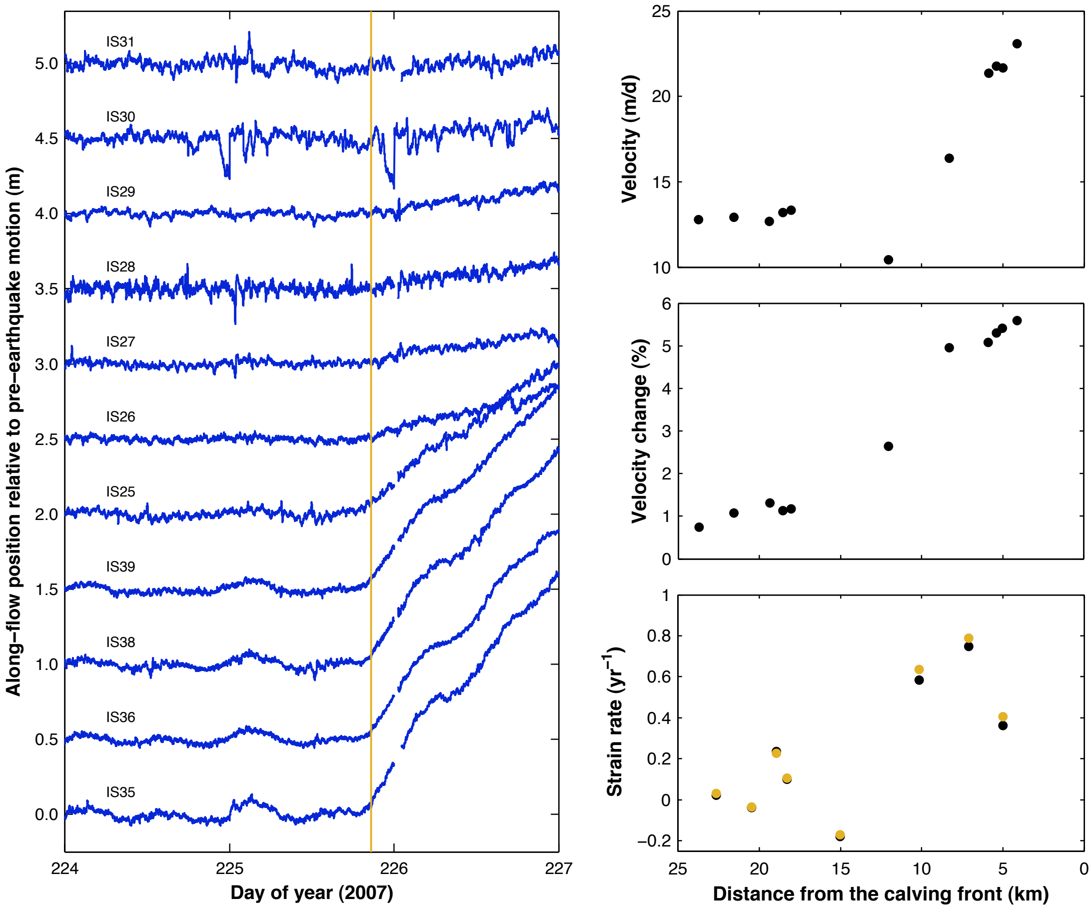

Figure 5.3: Left: Along-flow position estimates relative to mean speed prior to the speedup and glacial earthquake for all sites and spanning three days in 2007, days 224-227. The timeseries are offset by 0.5 m for each site for clarity. Sites are plotted, bottom to top, from closest to the calving front to farthest upglacier. The yellow line indicates the time of the teleseismically detected glacial earthquake. Right: (Top) Horizontal speed of all sites prior to the glacial earthquake, (middle) relative change in speed associated with the glacial earthquake, and (bottom) longitudinal strain rate (black) before the glacial earthquake and (yellow) after the earthquake, as a function of the distance of the sites to the calving front position on day of year 213 in 2008.

Figure 5.2 shows the time for the change in speed estimated with the preferred of our techniques, with its corresponding error bar that comprises the estimates from the rest of approaches (Nettles et al., 2008). The time of the speedup is indistinguishable from the time of the first enhanced-detection earthquake, and happened ~80 min earlier than the large earthquake (Nettles et al., 2008). The position estimates for the rest of sites in the network are shown in Figure 5.3. The figure shows that the step-wise increase in speed happens approximately coherently across the network. Figure 5.3 also shows that the amplitude of the change in velocity decreases with increasing distance from the calving front, from a ~6% increase at a site located ~4 km from the calving front to ~1% increase ~24 km upglacier. The variation over distance of the speed change happens primarily in the lower ~15 km of the glacier. Therefore, as shown in Figure 5.3, the glacial earthquake also causes a change in longitudinal strain rate, specially significant in the lower part of the glacier. The longitudinal strain rates shown in Figure 5.3 are calculated from pairs of consecutive sites located approximately on the center flowline of the glacier.

The change in velocity is observed for all sites in the network, that is, up to ~20 km from the calving front. The analysis of the position data from all the sites shows that on average the increase in speed happened first at the sites downglacier from IS25, that is, sites IS35–IS25 (see Figure 1.5), and slightly later at the sites upglacier (Nettles et al., 2008). However, the uncertainties in the estimated speedup time, which are larger for smaller changes in velocity, i.e., for the sites located farther upglacier, prevent from distinguishing a propagation pattern of the speedup.

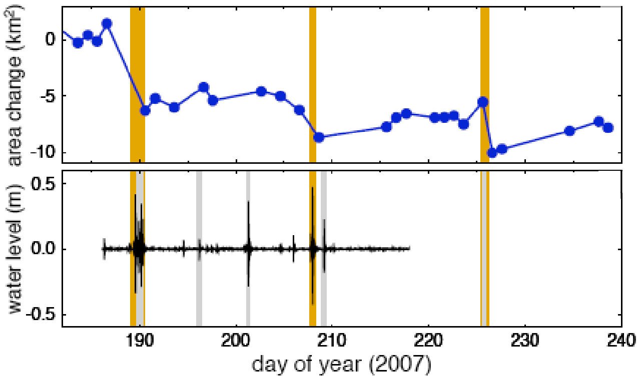

Figure 5.4: (Top) Cumulative change in glacier area at Helheim with respect to total area on day of year 180 in 2007, as derived from MODIS images. (Bottom) Ocean water level with respect to mean water height, recorded with a tide gauge at Sermilik Fjord (position of the tide gauge shown in Figure 1.2) and filtered to eliminate variations due to ocean tides. Vertical lines indicate the occurrence of (yellow) teleseismically-detected glacial earthquakes and (grey) smaller earthquakes detected with enhanced methods. From Nettles et al. (2008).

The times of the glacial earthquakes are also coincident with large calving events, which are currently understood to be the source mechanism for the seismic events. While the time of an earthquake can be determined very accurately (less than 1 minute) and the exact time of the glacier speedup can be determined to within a few hours, the timing of a calving event has much lower precision. The position of the calving front is mapped at near-daily intervals during the GPS observation period using cloud-free images from the Moderate Resolution Imaging Spectroradiometer (MODIS). The cumulative change in glacier area is shown in Figure 5.4. Large steps towards negative values are present near the times of the glacial earthquakes and indicate the occurrence of large calving events. The time resolution of the MODIS images depends on the atmospheric conditions and is limited for the time periods studied here to 1–4 days. An episode of retreat of the calving front, as deduced from MODIS images, can be a consequence of one or more calving events, associated with one or several glacial earthquakes. However, the collapse of a large iceberg into the fjord also causes small tsunamis. Nettles et al. (2008) used tide gauge records filtered between 200 and 4000 s to eliminate long period variations due ocean tides, shown in Figure 5.4, and hand-picked tsunami arrivals to help constrain the time of occurrence of the large-scale calving events to within a few minutes.

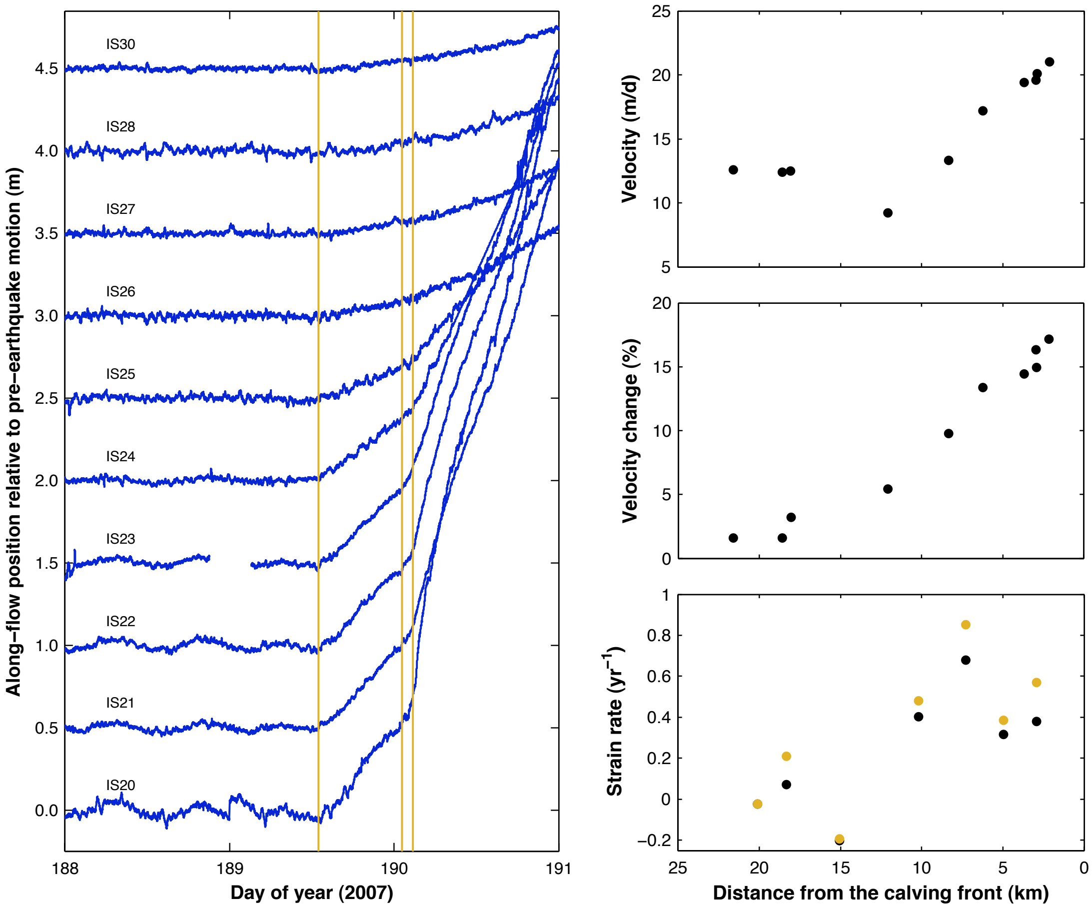

Figure 5.5: Same as in Figure 5.3, except here for days 188-191 (2007), encompassing three glacial earthquakes.

The position estimates for the changes in speed related to other glacial earthquake events show similar behavior. Figure 5.5 shows the position estimates for all sites during three days surrounding the time of three large glacial earthquakes that occurred during days of year 189–190 in 2007. In this case the first of the earthquakes happened approximately half a day earlier than the other two earthquakes. The position estimates show similar behavior to the event analyzed above, except in this case with two step-wise speedups closely correlated in time with the timing of the glacial earthquakes. Again, the acceleration is observed throughout the length of the glacier, and its amplitude decreases with increasing distance from the terminus. The speedup registered during these days, of up to ∼18% at the site located ∼2 km from the calving front, is the largest change in speed observed during the 2006–2008 observational field campaigns at Helheim Glacier, and coincides also with the time when the largest number of glacial earthquakes were detected. Analysis of MODIS images showed that during this time the calving front of the glacier retreated by ∼1.3 km, with an associated area loss of ∼6 km^2 (Nettles et al., 2008). In comparison, events of terminus retreat associated with glacial earthquakes during the period 2001-2005 in general happened in steps of more than ∼0.5 km and less than ∼1 km (Joughin et al., 2008a). The change in longitudinal strain rate associated with this event is also the largest registered during the period 2006–2008 (see Figure 5.5).

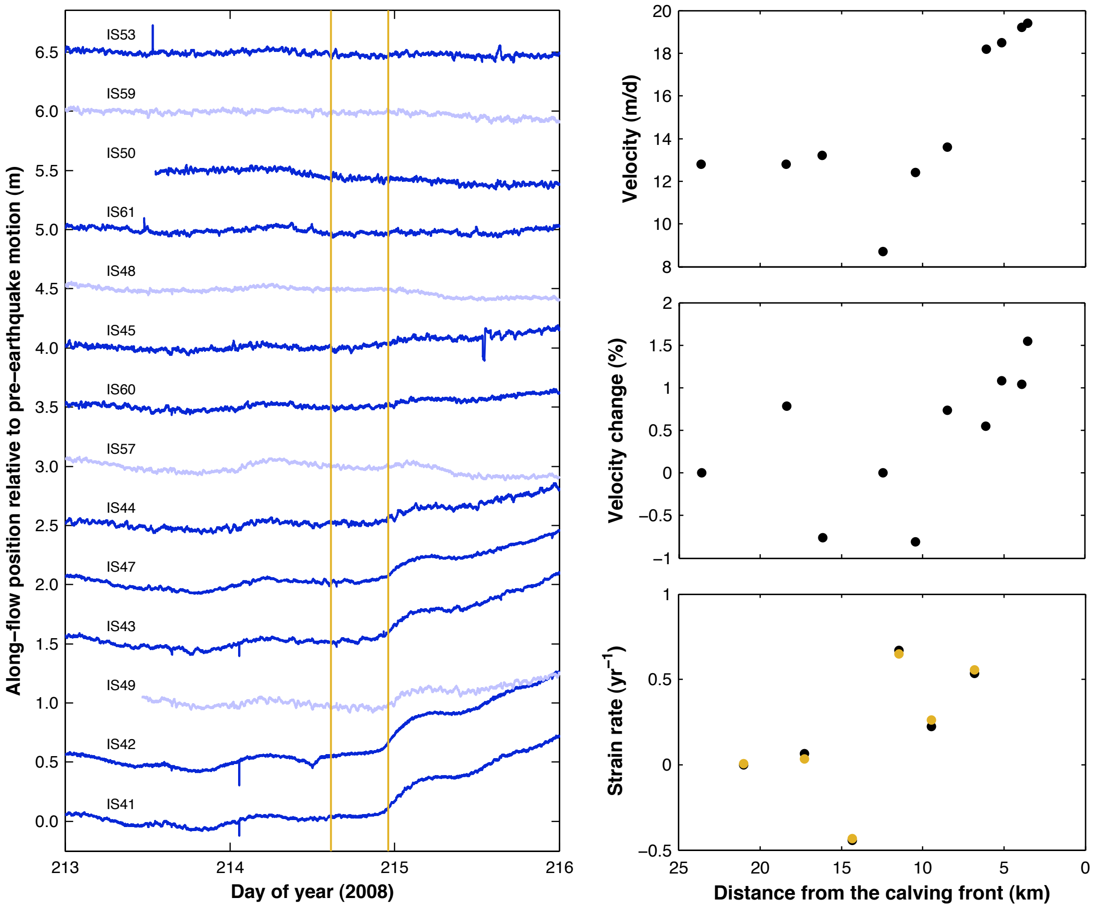

Figure 5.6: Same as in Figure 5.3, except here for days 213-216 (2008), encompassing two glacial earthquakes. Timeseries shown in a lighter color correspond to sites located on the glacier's tributary.

A similar glacial earthquake event that happened in 2008, on day 214, shown in

Figure 5.6, yielded a more moderate speedup. The change in speed was not significantly larger than the daily increase in speed registered on the days prior to the glacial earthquakes (see Figure 3.9), although in the case of glacial earthquakes the change happens nearly instantaneously, while other changes happen gradually. Also, in this case the speedup was not detected at the farthest upglacier sites, and despite the two earthquakes were separated in time by ∼8 h, only the second earthquake seems to have associated a step-wise change in speed. In general during the summer of 2008 the flow of the glacier was slower and the changes in speed were less important compared to the previous summer, as detailed in Chapter 3.

The site located closest to the calving front on the tributary, site IS49, shows a change in speed associated with the earthquake similar to that observed in the main trunk. However, sites located on Helheim's tributary but farther upglacier present a markedly different flow behavior characterized by a decrease in speed a few hours after the earthquakes. Additional observations suggest that this behavior is motivated by an atypical drainage event of meltwater from the surface to the base of the tributary. This issue is addressed further in Section 6.2.

5.1.2 Summary and Discussion

Glacial earthquakes manifest in the GPS position timeseries of the glacier's surface as site-dependent flow-speed increases. No obvious coseismic offset in displacement takes place at the time of the glacial earthquakes, rather there is a step in flow velocity, discarding the initial hypothesis that the source mechanism of glacial earthquakes was the sliding of a large part of the glacier by a few meters.

Observations indicate that the dynamics of the calving terminus at large fast flowing outlet glaciers in Greenland varies seasonally, in general advancing in winter and retreating during the summer (Joughin et al., 2008a; Amundson et al., 2008). The retreat happens in several discrete events where large-scale icebergs detach from the glacier. When the icebergs produced are tall, in comparison with their along-flow length, they become unstable and overturn against the ice front as they calve, exerting a force on the glacier and solid earth and producing glacial earthquakes (Tsai et al., 2008; Nettles & Ekström, 2010). The acceleration of the iceberg mass along ∼10–100 m represents a mass-sliding product sufficient to explain the production of a glacial earthquake (Nettles & Ekström, 2010). The iceberg height, and thus the glacier thickness, is likely the most important control on the glacial earthquake magnitude since it determines the translation distance of the iceberg as it overturns (Nettles & Ekström, 2010).

During 2006 the summer retreat at Helheim occurred in a series of discrete episodes that involved large icebergs (Joughin et al., 2008a). This, combined with our observations that during 2006 Helheim had developed a floating tongue (see Chapter 4), suggests that during this summer the retreat of the calving front occurred through the detachment of large tabular-like icebergs that do not overturn and thus do not generate glacial earthquakes. Our observations indicate that in summer 2007 the grounding line was located very near the calving front, which again made possible the calving of unstable slab-like icebergs, and thus the occurrence of glacial earthquakes.

Geodetic observations at Helheim Glacier from Arctic summers in 2007 and 2008 revealed that the calving events and associated glacial earthquakes correlate in time with sudden increases in glacier flow speed, that take place coherently throughout the length of the glacier (Nettles et al., 2008). The magnitude of the speed change decreases with increasing distance from the calving terminus, so that a sudden change in longitudinal strain rate also takes place associated with the glacial earthquake. A similar study at Jakobshavn Isbræ on the Greenland West Coast, led to analogous conclusions on the relation between glacial earthquakes, calving, and flow acceleration (Amundson et al., 2008). The observed change in speed is likely to be caused by the loss of ice at the calving front, which reduces resistance to flow and increases the glacier's effective driving stress (Howat et al., 2005; Nick et al., 2009).

The change in speed recovers partially after the glacial earthquake but these events in general cause a sustained velocity increase. Whether such speed increases are sustained over the winter, and how much can they account for the overall yearly speed increase of the glacier is not clear yet.

5.2 Sudden increase in tidal response linked to glacial earthquakes, calving, and acceleration

In Chapter 4 we examined the response of Helheim Glacier to the ocean tides. We analyzed the temporal and spatial dependence of the admittance of the response of the glacier to the ocean tide. Typically, tidal admittance amplitudes vary little from day to day, periodic variations related to the non-linear response of the glacier to the ocean tides happen in a relatively gradual mode, especially while the response is increasing (see Chapter 4).

However, following glacial earthquakes, the tidal admittance can increase suddenly by a factor of as much as ~2.5. The onset of the intensified tide-modulated flow coincides with the step-like increases in speed and longitudinal strain rate associated with glacial earthquakes. However, the transitory nature of this intensified response, with a duration of 1–2 days, contrasts with the sustained higher flow speeds that follow many earthquakes. We conclude, based on the temporal relation with strain-rate variations, that the enhanced response to the ocean tides may be explained by a temporary disruption of the subglacial drainage system and a concomitant reduction of the friction at the ice-bedrock interface.

The results presented in this section were originally published in de Juan et al. (2010b) and have been expanded here to show this glacial-earthquake associated behavior in more detail.

5.2.1 Method

For the periods around glacial earthquakes times, the analysis of the tidal modulations is performed using the approach described in 4.3 with some adjustments. Glacial earthquakes are associated with step-like increases in velocity, which the tidal analysis method does not model. Therefore, for days when one or several earthquakes occurred, instead of analyzing the data in one-day batches, we analyze shorter time periods bounded by the times of the earthquakes. We concatenate days when necessary, to ensure long enough periods of time that enable the fit of the tidal model. We eliminate data from ∼1 h prior and subsequent to earthquake times since the change in velocity does not happen precisely at the time of the earthquake but very close in time (see Section 5.1). Finally, we use the simplest model to fit such short time periods of data, i.e., we do not estimate an acceleration parameter.

For example, in 2007, during days 189–190 (July 8–9), five earthquakes were detected at Helheim at the times shown in Table 5.1. For the analysis of these glacial earthquakes, we have fitted independently with the model described in 4.3 the following time periods: (1) day 189, 0–12h; (2) day 189, 14–24h; (3) day 190, 4–24h. Thus, we have ignored the second earthquake that occurred on day 189 at 21:33, since it was detected using "enhanced" methods and does not have a clear velocity increase associated with it (see Figure 5.5). Also, since the three earthquakes detected on day 190 happened very close in time, we do not attempt to analyze the periods in between these earthquakes, as such short time periods prevent from estimating the tidal parameters. The rest of earthquakes are analyzed using a similar approach.

5.2.2 Results

The along-flow tidal response of Helheim Glacier presents a ∼15-day period variation, possibly associated with the modulation of the ocean tide height of the same period, as shown in Chapter 4. Such variations are small and happen in a gradual mode, so that variations from day to day are at most of a factor of ∼1.5. However, we find that following glacial earthquakes, the along-flow tidal response increases nearly instantaneously by a factor of as much as ∼2.5. As described earlier, glacial earthquakes are also associated with step-wise increases in glacier speed. The magnitude of such speedups decreases with distance from the calving front, resulting as well in an increase in longitudinal strain rate, specially in the lower part of the glacier, where tidal response is observed.

Figure 5.7 shows the increase in tidal response associated with the glacial earthquakes that occurred on days of year 189–190 (2007). GPS site IS22 was chosen to illustrate this response for its proximity to the calving front and because it has good quality position estimates throughout this period. Following the two glacial earthquakes on day 190, the admittance of the tidal signal at this site increased by a factor of ∼2.5, coincident with an increase in velocity of ∼2 m/d. The first of the earthquakes shown in this figure, on day 189, that was of lower magnitude and produced a smaller change in flow speed, is also associated with a smaller change in tidal response (see estimated admittances in

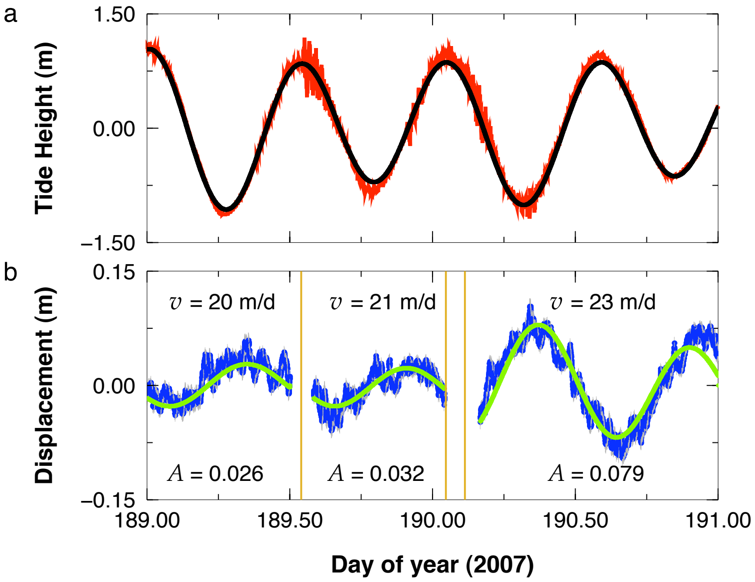

Figure 5.7: (a) Black line shows predicted ocean tide at an ocean location near the mouth of Sermilik Fjord (Figure 4.1). Red line shows observed tide within the fjord. (b) Blue dots show estimates of horizontal position (site IS22) along the direction of glacier flow relative to a best-fit mean speed v, for three time periods separated by glacial earthquakes. Green line shows tidal function fitted to these estimates, with admittances A. The RMS misfit is less than 16 mm for the examples shown. Yellow lines indicate the times of glacial earthquakes. From de Juan et al. (2010b).

Figure 5.7). From visual inspection of Figure 5.7, it is clear that the increase in tidal response happens nearly immediately following the time of the earthquakes. Usually, in the analysis of the tidal signals bounded by glacial earthquakes we do not take into account ∼1 h prior and subsequent to the time of the glacial earthquakes. However, for this example, we extended the time period before the second set of earthquakes to include the first hour of day 190 (approximately until the time of the first earthquake on day 190, see Table 5.1). This allows us to confirm that no significant change in tidal admittance happened before the time of the earthquakes. As expected, the ocean-tide record varies smoothly and continuously throughout the period of increased tidal response (Figure 5.7(a)), so that the increase in tidal response can not be attributed to a change in the ocean tide. Also, the small tsunamis caused by the calving process and reported in Nettles et al. (2008) attenuate well before the tidal response recovers.

The enhanced tidal response lasts for one to two days after the glacial earthquake. Furthermore, the decrease in tidal response is usually temporally linked to a deceleration of the glacier. Figure 5.8 illustrates this for the case of site IS22. In Figure 5.8(a) the tidal model fitted to day 190 (excluding the time of the glacial earthquakes) is propagated forward in time for day 191. In Figure 5.8(b) the opposite is done, the model fitted to

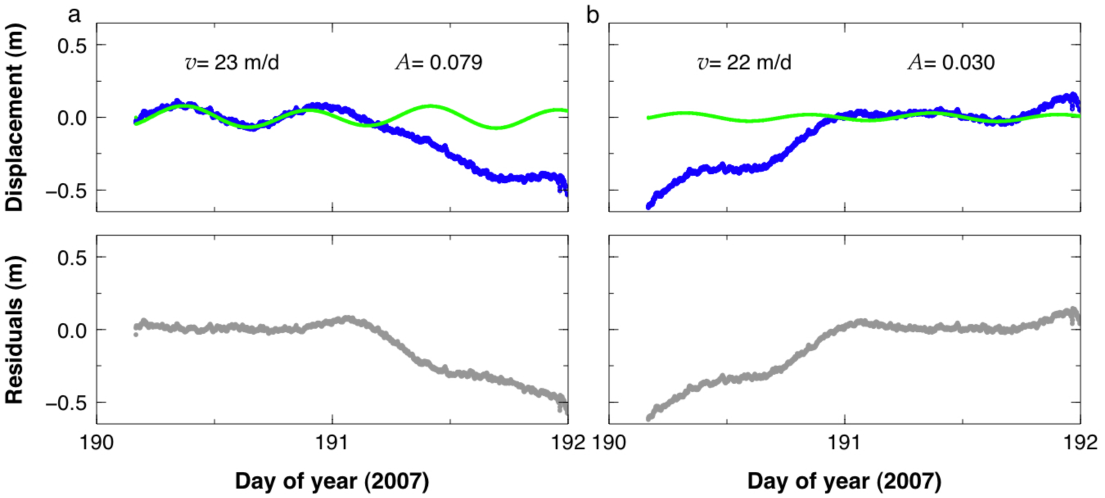

Figure 5.8: Blue dots show estimates of along-flow position (site IS22) relative to mean speed v. Green line shows tidal function fitted to the estimates with admittances A. Lower panels show the residuals to each of the tidal functions fitted. The mean speed and tidal function fitted are derived from the fit to (a) day 190 (excluding the time of the glacial earthquakes), propagated forward in time, and (b) day 191 propagated backward in time.

day 191 is propagated backward in time for day 190. The figure shows how a step-like decrease in velocity happened at a time around the day boundary of 190–191. The figure also shows that the tidal response decreased at approximately the same time, the tidal response on day 191 is overestimated by the model from day 190, and vice versa, the response on day 190 is underestimated by the model parameters from day 191. However, while the tidal response recovers almost to pre-earthquake values, the flow speed only recovers partially, as discussed in Section 5.1.

Figure 5.9 shows as a function of distance to the calving front, the admittance amplitude for sites IS20–IS26 (see Figure 1.5) for two days before the glacial earthquakes (187 and 188), day 190 after the glacial earthquakes, and day 191. As detailed in Chapter 4, and exponential function describes well the decay of the response with distance from the calving front. The increase in tidal response following the earthquakes and its subsequent decrease almost to pre-event values is consistent for all sites, and the exponential decay of the response is maintained throughout the process. This figure also shows that, the change in tidal response is largest for the site closest to the calving front and progressively smaller with increasing distance from the calving front. Therefore, like the change in flow velocity (Nettles et al., 2008), the change in tidal admittance associated with glacial earthquakes decreases with distance upglacier.

Other glacial earthquakes present consistent behavior. For example, Figure 5.10 shows the tidal response increase, following two glacial earthquakes on day 225, for the site located closest to the calving front, IS35.

In Figure 5.11 these results are extended to show the change in response for all of the

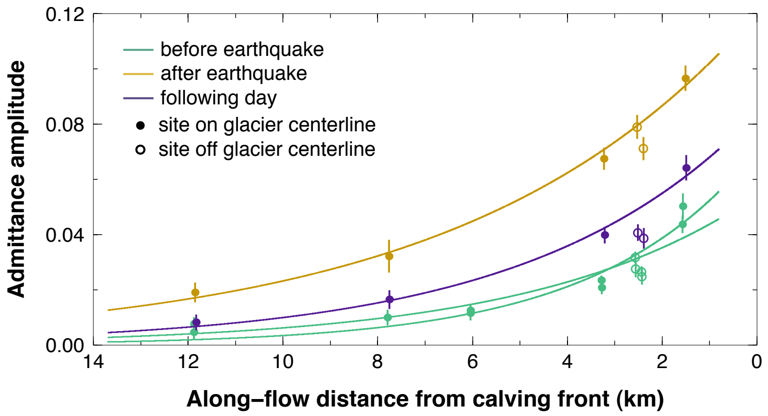

Figure 5.9: Admittance of along-flow response to ocean-tidal forcing as a function of distance from the calving front position on day 185 (2007), fitted with an exponential function, for four days encompassing the time of the glacial earthquakes on days 189 and 190. The sites located off the glacier centerline are not included in the exponential fit. From de Juan et al. (2010b).

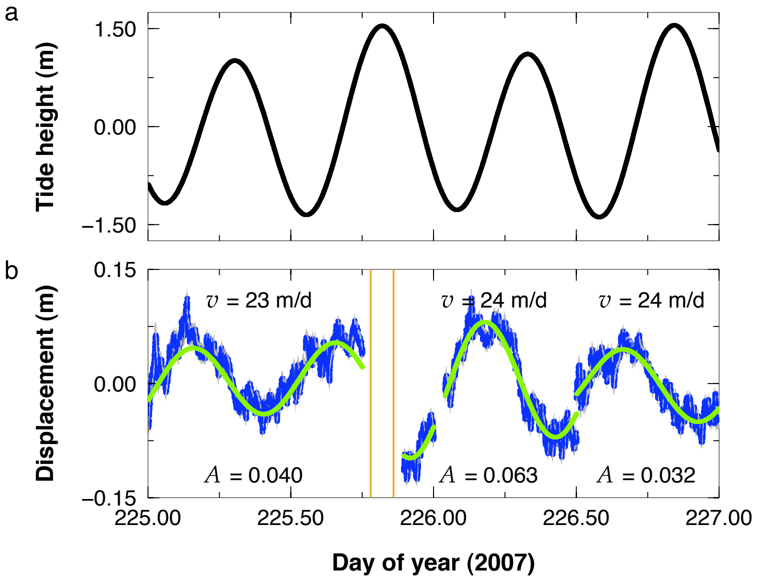

Figure 5.10: Same as in Figure 5.7, except here for site IS35 and days 225–227 in 2007. For this period there are no ocean tide observations available. Outliers after the day boundary 225–226 have been eliminated.

glacial earthquakes detected during the Arctic summer seasons of 2007–2008, when six large glacial earthquakes occurred (Nettles et al., 2008), clustered in three different time periods: two in summer 2007 and one in summer 2008. This figure also provides a broader view since it shows, for each of the glacial-earthquake periods, the tidal admittance amplitude for the four sites located closest to the calving front (see Figures 1.5-1.6) during 7-day time periods encompassing the time of the glacial earthquakes. The example shown in Figures 5.7–5.9 and 5.11(a), from days 189–190 in 2007 and encompassing three earthquakes, is associated with the largest increase in velocity and largest increase in tidal response. The other events show consistent behavior, albeit of less amplitude, both in tidal response increase and velocity increase, specially for the case in 2008. In 2008 glacier flow was slower and less variable, as detailed in Chapter 3. There is no noticeable change in tidal response after the first earthquake on day 214 (2008), and the change in response is very moderate after the second earthquake on the same day, both results are in agreement with the corresponding changes in velocity. The events from 2007–2008 occurred for different positions of the calving front in the fjord, discarding any relation of the enhanced tidal response with a singularity in the fjord geometry.

In general, all of the GPS sites that present tidal response show consistent behavior during glacial-earthquake events. However, there are some exceptions. For example, while after the earthquakes on days 190 (2007) all of the sites show a large increase in tidal response (see Figure 5.9 and Figure 5.11(a)), after the smaller earthquake on the previous day, only sites IS20 and IS22 show a response, indicating that either only part of the glacier responded to this event, or that the signal-to-noise ratio is not large enough for the sites further from the calving front than IS22.

Figure 5.11 also shows that after 1–2 days following the glacial earthquakes, the tidal response decays to pre-event values, usually at the same time that the glacier velocity also decays. However, unlike the tidal response, the glacier velocity typically recovers only partially. An exception is the decrease in tidal response after the earthquakes on day 225 in 2007, which happened only ∼16 hours following the earthquakes (Figure 5.10) and coincided with a very slight change in flow speed of the glacier, a larger decrease in speed followed the next day (Figure 5.11(b)).

Overall, we find that both the magnitude of the change in tidal response following a glacial earthquake and its subsequent decrease correlate with the changes in flow speed observed at those times. Figure 5.12 shows the correlation between the admittance-amplitude change and the velocity change (the linear correlation coefficient is of 0.86, statistically significant at >99% level).

5.2.3 Discussion

Our results indicate that the enhanced response of the glacier to ocean tidal forcing is temporally related to the increase in flow speed and longitudinal strain rates that follow glacial-earthquake calving. Moreover, we take the temporal relationship between the partial flow deceleration and associated decrease in strain rate, approximately one to two days after the glacial earthquakes, and the recovery of the tidal response to steady-state values to be further evidence of this coupled relationship. Although the tidal stress is applied at the glacier terminus, the change in sensitivity to tidal forcing is observed at least 12 km upglacier after a glacial-earthquake calving event, indicating a coupling

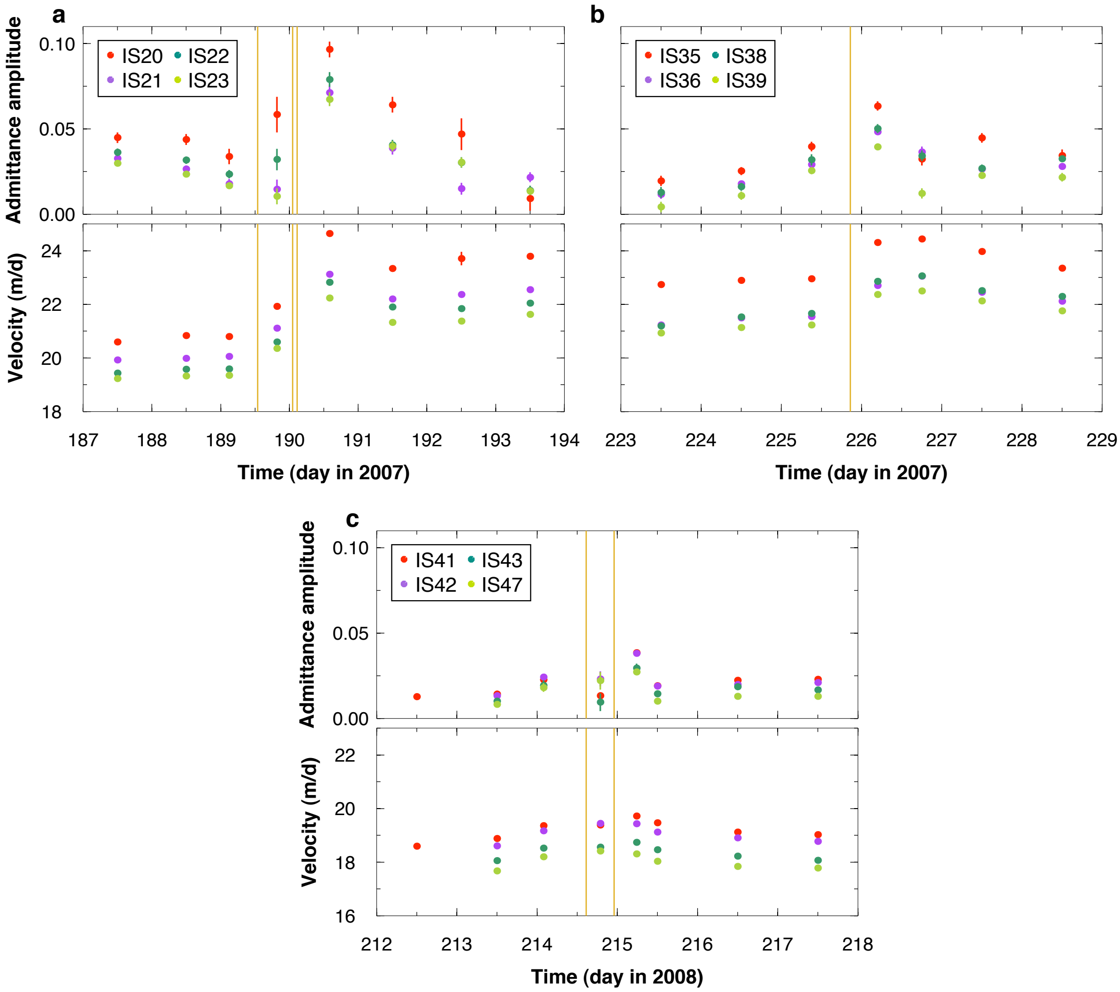

Figure 5.11: Admittance amplitudes for the glacier response to the ocean tide in the along-flow component of motion, and velocity of the four GPS stations located closest to the calving front (see Figures 1.4–1.6) for seven days encompassing the time of glacial earthquakes (yellow lines) in (a and b) 2007 and (c) 2008. (Note the change in scale in the lower panel of Figure 5.11(c).) Uncertainties are plotted as vertical bars. Expanded from de Juan et al. (2010b).

of flow characteristics over at least this distance.

Since the response decays exponentially with distance from the terminus, one could expect the retreat of the calving front associated with glacial earthquakes to cause an increase in the glacier's response to ocean tides. In a similar way, long-term loss of ice at the glacier terminus causes sustained flow-speed increases (Joughin et al., 2004; Thomas, 2004; Howat et al., 2005; Nettles et al., 2008). However, the loss of ice itself is unlikely to be the cause of the increased tidal response, since the rapid recovery of admittance amplitudes to pre-event values demonstrates that the change in distance to the calving front is not the primary control on the temporal variation in glacier tidal

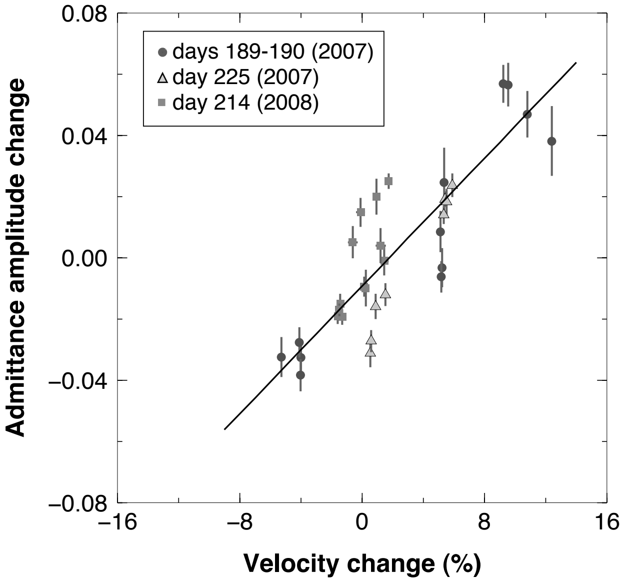

Figure 5.12: Correlation between admittance-amplitude change and fractional velocity change for the four sites located closest to the calving front, with best linear fit (black line; correlation coefficient of 0.86). Values are plotted for each of the two days following the glacial earthquakes on days 189 and 190, 2007, day 225, 2007, and day 214, 2008. Uncertainties are plotted as horizontal and vertical bars. For many estimates, error bars are smaller than the size of the symbols.

response. The possibility of the recovery being caused by glacier front re-advancement is also discarded, because the rate of advance is limited by the speed of glacier flow and the recovery happens very fast. Thus, the transient nature of the enhanced tidal response is an important characteristics in terms of understanding the mechanism that drives it. Following this argument, a temporary decrease in resistance at the glacier bed would enable the glacier to respond with higher amplitude to the tides.

Following large calving events associated with glacial earthquakes, the glacier experiences an increase in surface velocity and strain rate. Since fast-moving outlet glaciers flow mainly by basal sliding, we expect a change in strain rate at the glacier surface to lead to a similar change at the glacier base. We propose that the change in basal strain rate can disrupt the subglacial hydrologic system in such a way that the basal water pressure is increased, similarly to what occurs in a glacier surge, enabling an enhanced response of the glacier to the tides.

The reorganization of the basal hydrological system has shown to act as a mechanism for glacier surges (Kamb et al., 1985; Kamb, 1987). In a non surge stage, meltwater is discharged subglacially through one or several large tunnels where the water pressure is below the ice overburden pressure, and thus such conduits are kept open by frictional melting. In the surging stage, the subglacial drainage system is instead formed by large cavities linked by small channels distributed across the glacier bed width, which need to be at high pressure to keep the conduits open, so that the high flow velocities observed during a surge are caused by the basal water pressure in the cavities approaching the ice overburden pressure.

Even though the velocity of fast-flowing outlet glaciers is less sensitive than that of ice sheets to enhanced meltwater input (Joughin et al., 2008a; van de Wal et al., 2008) it has been shown that they can respond to fluctuations in melt (Joughin et al., 2008a; Andersen et al., 2010). At Helheim Glacier, observations indicate a significant sensitivity to added runoff from surface melt. Velocity variations of up to ∼5% have been found to be correlated with melt fluctuations with a 1-day time lag, the correlation being more significant near the front of the glacier (Andersen et al., 2010). A recent study shows that it is the increase in water input variability that drives the dynamic switching between subglacial channels and cavities and leads to glacier acceleration (Schoof, 2010).

Although nothing is known about the subglacial hydrologic system at Helheim Glacier, our observations indicate the presence of large volumes of basal meltwater, especially at the lower part of the glacier where the high strain rates cause extensive crevassing, providing an efficient conduction of runoff from the glacier surface to the bed. This, in combination with the runoff that is likely drained from upstream towards the terminus and the fact that the region is near flotation, makes this part of the glacier more sensitive to added water input (Andersen et al., 2010). The fact that the glacier flow speed responds to added runoff suggests that the subglacial drainage system consists, at least in part, of small channels or linked cavities that are at high-pressure, and that if low-pressure tunnels exist they are insufficient to carry away the excess meltwater, and are probably destroyed rapidly through advection due to the high flow speeds, as suggested by Kamb et al. (1985).

We propose that the subglacial drainage system at Helheim, which very likely consists, at least in part, a distributed system of linked cavities, is disrupted by the increase in basal strain rate associated with a glacial-earthquake speedup, reducing the volume of water that can be accommodated in subglacial channels and increasing basal water pressure in the cavities, further lubricating the ice-bedrock interface and enabling the glacier to enhance its response to the tides. The disruption of the hydrological system is expected to be temporary, with more efficient drainage re-established as strain rate is reduced. Furthermore, this effect would not only increase the tidal response of the glacier, but would also cause a temporary additional acceleration, above the longer-term speedup caused by the loss of resisting forces at the terminus, that would recover at the same time as the tidal response. This agrees with our observations.

The large calving events associated with glacial earthquakes involve one or several icebergs overturning, and displacing large volumes of water, as observed at Helheim and Jakobshavn Glaciers (Nettles et al., 2008; Amundson et al., 2008). If, as a result of calving, additional water were injected upglacier into the subglacial hydrologic system, this could provide a supplementary mechanism for a rapid increase in tidal response that would be followed by a rapid return to steady-state conditions as the extra water exits the glacier front, though this is highly speculative.

Alternatively, the nonlinear rheology of the ice may provide a mechanism for enhanced response to tidal forcing as velocity and strain rate increase.

5.2.4 Summary

It has been shown that the flow of the lower part of Helheim Glacier presents tidal variations. The response of the glacier to the ocean tides-related variations in hydrostatic pressure varies gradually with a 15-day periodicity, as detailed in Chapter 4. However, in this chapter we have shown that the tidal flow response can also increase abruptly by as much as a factor of ∼2.5 following a glacial earthquake and associated calving event. The enhanced tidal response lasts only 1–2 days, after which the tidal flow variations return to pre-earthquake state.

The temporal relation between this enhanced tidal response and the speedup and increase in longitudinal strain rate associated with glacial-earthquake calving, and also between the recovery of the tidal response and a partial deceleration of the glacier, suggest a link between these events.

Given the transient nature of the enhanced tidal response, and its link to strain rate variations, we propose that a temporary decrease in the resistance at the glacier bed, possibly caused by the disruption of the basal drainage system and the consequent increase in basal water pressure, could explain these observations.

Chapter 6

Flow variations at Helheim Glacier associated with meltwater drainage

In general the flow speed of Helheim Glacier remains constant from day to day or varies in a moderate and gradual fashion. However, at several specific times during the summer, more or less abrupt changes in flow speed take place. Some of these changes occur in relation to large calving events and associated with glacial earthquakes, as described in Chapter 5. Others present a different flow character and occur at times when no glacial earthquakes are detected. Here we analyze some of these changes in speed that we interpret as the glacier response to the supply of large volumes of water to the subglacial drainage system.

The basal hydraulic system can be formed by large channels at low pressure that provide fast drainage, or by distributed systems at high pressure that consist of cavities linked by narrow passageways that provide slow drainage (Kamb, 1987; Fowler, 1987). Most likely, the drainage system is formed by a combination of both types of systems. The flow speed of the glacier and the amount of water supplied to the bed, among other factors, control which type of system is active. (A more extended description of the types of subglacial drainage systems is given in Chapter 1, Section 1.3.1.) In fast-moving glaciers that flow basically by sliding, the subglacial drainage system consists, at least in part, of a distributed system (Hooke, 2005), since separation between the bed and the ice occurs where bedrock bumps are located. It is also possible for the subglacial drainage system to transition from one configuration to the other depending on the discharge conditions, as demonstrated to occur in relation to surging glaciers (Kamb, 1987).

The presence of meltwater at the ice-bedrock interface provides basal lubrication. Increased basal water pressure provided by increased water supply to the basal drainage system can cause the glacier to separate from the bedrock, reducing friction and thus increasing sliding velocity (e.g., Zwally et al., 2002; Das et al., 2008; Bartholomaus et al., 2008; Schoof, 2010).

Recent modeling shows that increased but steady rates of meltwater supply to the bed of the ice sheet and glaciers is not sufficient to cause acceleration, and even can lead to deceleration since above a critical rate of water flow a channelized system at low pressure forms (Schoof, 2010). Instead, it is the variation in water supply which leads to increased ice flow through the transition to a distributed system or even in a channelized system, since conduits adjust their size slowly and may not have the capacity to accommodate a sudden increase in water supply (Schoof, 2010).

An important increase in water supply are those caused by the sudden drainage of supraglacial lakes. These lakes can drain rapidly when they establish a connection to the englacial drainage system. Such events have been observed to cause the acceleration of the ice sheet (Das et al., 2008). However, there still is no evidence for this process taking place at the large outlet glaciers in Greenland, nor it is known its contribution to the summer increase in speed observed at these glaciers.

The flow speed of Helheim Glacier is sensitive to variations in meltwater runoff, as demonstrated by Andersen et al. (2010). The variations in melt at Helheim, estimated from a surface energy balance model and validated against field observations of ablation, correlate well with the surface variations in speed observed with GPS. The velocity response of the glacier, of ∼4% relative to mean speed, is delayed, relative to the melt signal, by ∼12–36 h (Andersen et al., 2010).

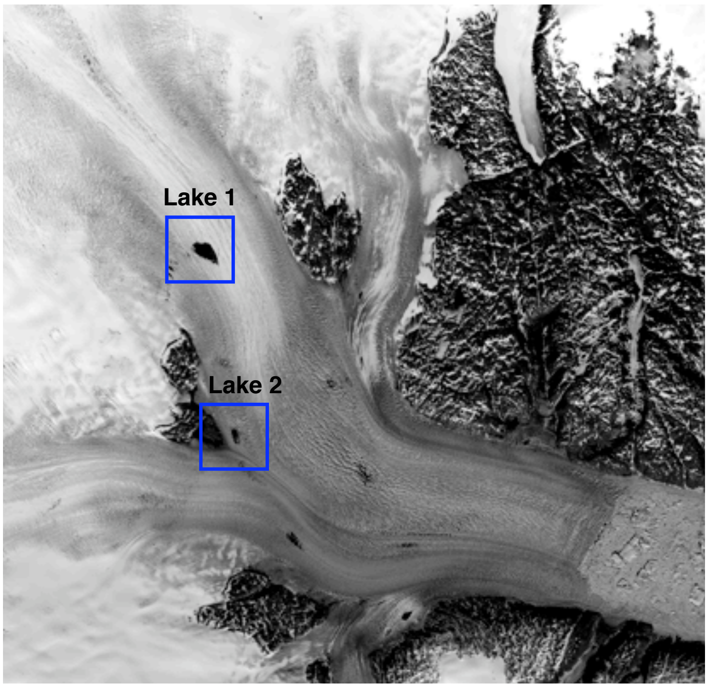

Figure 6.1: Advanced Land Observing Satellite (ALOS) image of Helheim Glacier from June 22, 2008 (day of year 174) showing the location of two supraglacial lakes which are referred to in this chapter.

During the field-based campaigns conducted in 2006–2010 we observed that meltwater accumulates at Helheim forming several melt ponds or supraglacial lakes on its surface. These type of lakes tend to occupy approximately the same location each summer (Sneed & Hamilton, 2007), probably influenced by the topography of the glacier bed. In several occasions these lakes have been observed to transition from full to drained over the course of a summer. During the summer of 2009 we recorded the drainage of one of such lakes with the use of a water-pressure tide gauge. In several occasions during the Arctic summers of 2007–2008 we recorded geodetic observations that suggest the flow response of the glacier to one of such drainage events.

In this chapter we present evidence for three events concerning the drainage of supraglacial lakes and analyze their effect on the dynamics of Helheim Glacier. The first of such events took place during days of year 228–233 in 2007, the second happened on the glacier's tributary during days of year 213–216 in 2008, approximately one day prior to a glacial earthquake, and finally a third event was recorded with the use of a water-pressure gauge. Figure 6.1 shows the location of the two supraglacial lakes at the surface of Helheim Glacier where these events take place. A quantitative, more rigorous version of the still somewhat qualitative preliminary results presented here is currently underway.

6.1 Speedup and slowdown, rise and fall at Helheim Glacier

This section presents a qualitative study of the GPS position timeseries at Helheim Glacier for days of year 228–233 in 2007 (August 16–21). The motion of the glacier relative to the mean flow, as measured by these timeseries, undergoes a distinct speedup phase followed by a slowdown episode. Concomitant with the speedup and slowdown is a rise and fall of the glacier, particularly at locations upglacier from the bend at Helheim Glacier.

These deviations from mean flow appear markedly different from the speedup events already reported by Nettles et al. (2008) and associated with glacial earthquakes. Indeed, this is a quiescent time period at Helheim in terms of glacial earthquakes, with the closest events detected occurring five days earlier, on day of year 225.

6.1.1 Observations of horizontal flow

Figure 6.2 shows the along-flow position variations of the GPS sites at Helheim Glacier during days 228–233 in 2007 with respect to the mean flow on day 228. The timeseries in the figure are dominated by a large departure from mean glacier motion, showing a large and rapid increase followed by a smaller decrease.

During day of year 228, the glacier flowed at approximately constant velocity (zero position on Figure 6.2 corresponds to mean motion on day 228 for each site), and begun a slight speedup during the final hours of day 228 that was followed by a more signif-

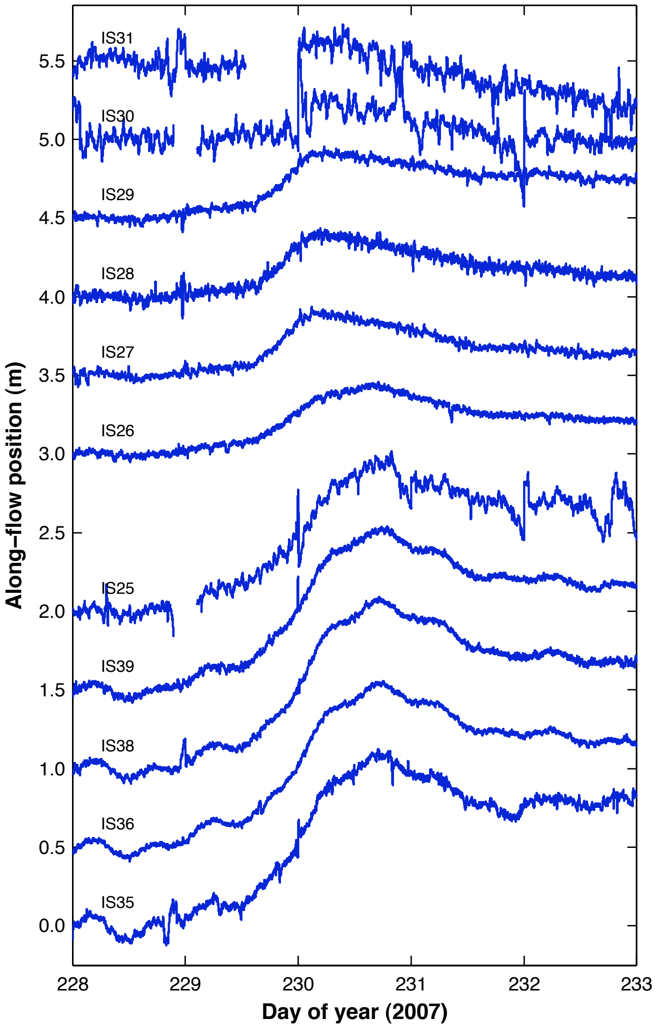

Figure 6.2: Along-flow position estimates relative to mean speed on day 228 for all sites and spanning five days in 2007, days 228–233. Each timeseries is arbitrarily offset by 0.5 m vertically for clarity. Sites are plotted, bottom to top, from closest to the calving front to farthest upglacier within the main glacier.

icant acceleration which took place after 229.5. Both speedups appear to happen in a step-like fashion for the sites upglacier from IS26 and in a more gradual mode for the sites downglacier. (See network map in Figure 1.5 for the location of the sites.) Some hours after the beginning of day 230, the sites upglacier (IS29, IS28, IS27) recorded a pronounced step-like slowdown after which they returned to flow at a constant speed for the rest of the day. As for the slowdown, the site at the glacier bend (IS26) and the sites closer to the calving front (IS25, IS39, IS38, IS36, IS35) present a different behavior in comparison with the sites upglacier. At these later sites the deceleration phase is more extended in time and appears to happen gradually or at least in a two-step fashion.

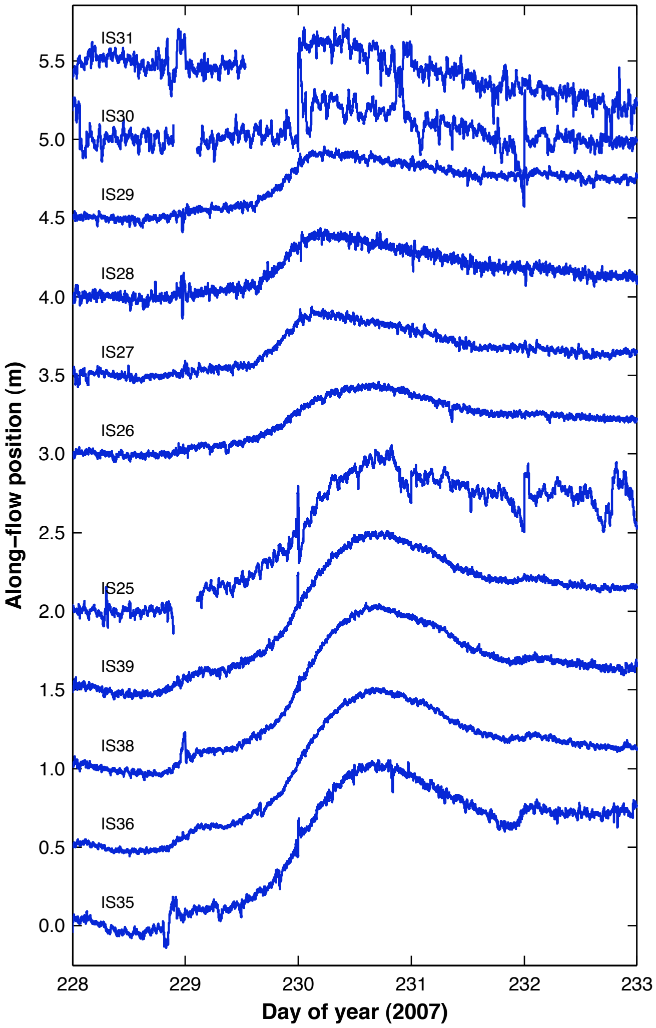

Figure 6.3: Same as in Figure 6.2 where we have corrected the position estimates of sites IS35–IS39 for the tidal response of the glacier.

When comparing these two groups of sites, we should take into account that the flow of the sites located between the bend in the glacier geometry and the calving front is modulated by the tides in the fjord. The semidiurnal signal in the timeseries is a delayed flow response of the glacier to the tides in Sermilik Fjord, as demonstrated in Chapter 4. However, IS26 in general does not show a significant tidal signal but has the same kind of deceleration behavior as the sites downglacier. Therefore, we are confident that the difference in behavior between these two regions of the glacier is not only caused by the flow response to the ocean tides. We have corrected the timeseries for the tidal response, estimated using the procedure detailed in Section 4.3. The corrected timeseries, shown in Figure 6.3, still contain some residual tidal signal, however it is very small compared to the larger and lower frequency accelerations discussed in this section. Based on the corrected timeseries, we can conclude that for the sites downglacier from IS26, the slowdown on day 230 happens gradually. The sites downglacier begin to slow down at approximately the same time the sites upglacier experience the step-like slowdown (230–230.25), but the maximum deceleration happens ∼6–12 h later.

Figures 6.2 and 6.3 show that the magnitude of the acceleration is larger for the sites located downglacier from site IS25 than for sites located upglacier. And that, although the position estimates of sites IS30 and IS31 are noisier than for other sites (some very noisy estimates are edited out), they also exhibit a speedup and slowdown. Nevertheless, the timing of the changes in speed is not resolvable for these two sites. The cross-flow component of motion (not shown) does not show any signal that could indicate changes in flow direction during these time period.

Summarizing, during this period three abrupt changes in flow speed happened, spanning two days. An increase in flow speed, happening at least in two steps, is followed by a decrease in speed that happened in two steps upglacier, and in a gradual mode downglacier. The flow behavior of the glacier is markedly different in the upglacier and downglacier regions. The magnitude of the speed increase is one of the largest during 2007 summer (see Figure 3.8), specially for the sites located upglacier where the speedups caused by perturbations at the calving front and associated with glacial earthquakes are largely mitigated compared to the sites located closer to the calving front. In contrast, for this event, the velocity change shows very clearly in the timeseries for all sites. Also, in contrast with the calving-event speedups, the acceleration downglacier does not exhibit a step-wise behavior.

6.1.2 Observations of vertical flow

Figure 6.4 shows the vertical component of motion for the same sites (except for IS30 and IS31) and days. This figure reveals that sites upglacier from the bend were lifted by ∼10–15 cm. (Unfortunately, timeseries of IS30 and IS31 are too noisy during this time period to discern whether they present any significant change in vertical position, or not.) Sites IS27–IS29 started to lift up at a time slightly earlier than the time when the glacier experienced its maximum acceleration (229.5) and they reached its maximum vertical position and started to drop shortly before the sites upglacier experienced the slowdown (230). Moreover, the onset and maximum vertical uplift of site IS26 seems to occur half a day later than for sites IS27–IS29. We do not observe a vertical displacement at sites IS25 and IS35–IS39. Also, the displacement at IS26 is of lower amplitude than at IS27–IS29. The vertical uplift observed during this time period is a unique event in the 2007 timeseries.

6.1.3 Meltwater pulse hypothesis

We use a basal meltwater pulse originated upglacier and traveling downglacier as a working hypothesis for explaining these observations. The vertical uplift of first sites IS27–IS29 and later IS26 suggests such a mechanism (Zwally et al., 2002; Das et al.,

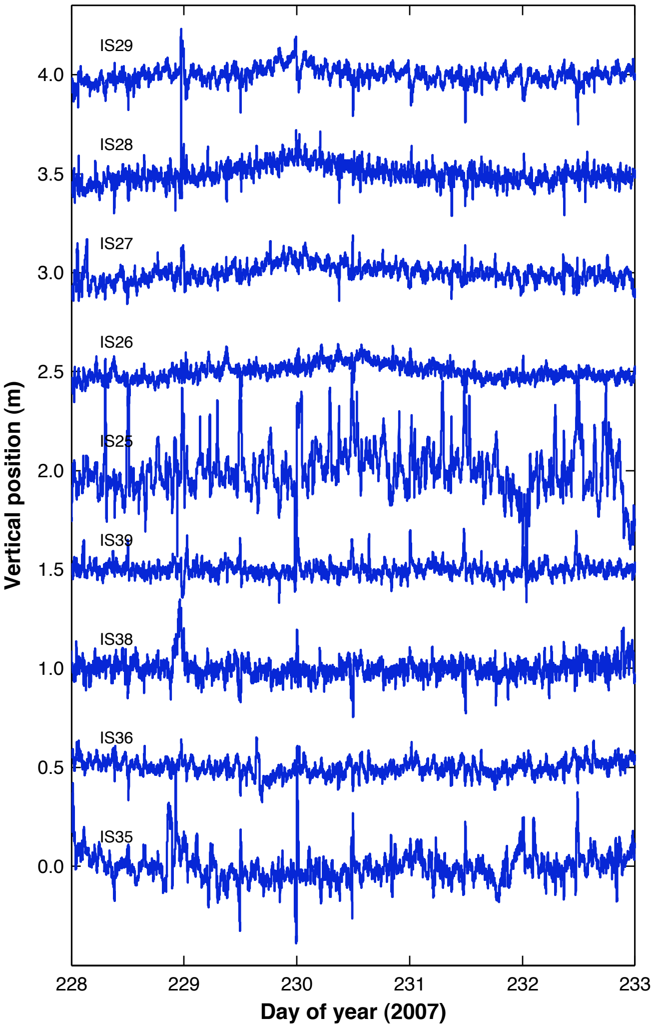

Figure 6.4: Vertical position residuals to the mean motion for same sites (except for IS30 and IS31) and days as in Figure 6.2.

2008). This meltwater pulse would have caused the water pressure in the subglacial cavities to rise sufficiently to overcome the ice-overburden pressure, and thus, to cause the glacier to lift and speedup. Once the glacier had begun to lift, a larger flux of water would have caused the ice to separate further from the bed until the maximum volume of subglacial water in the cavities was reached. Then, as the water was drained through the subglacial drainage system, the ice surface would have begun to decrease, returning the glacier to its original vertical position. The maximum horizontal acceleration of the ice upglacier at Helheim took place shortly after the glacier began to lift in this area but before it reached its maximum vertical position. Iken et al. (1983) observed that during rapid uplifts experienced by Unteraargletscher, the maximum horizontal velocity coincided with maximum upward velocity, that is, with maximum water pressure, but not with maximum uplift caused by the maximum water volume in the cavities. This implies that the pressure of water, and not its volume, is what controls the horizontal velocity during these events. Shortly after sites IS27–IS29 at Helheim glacier began to drop and before they reached their original vertical position, the ice in this region decelerated.

We hypothesize that when the acceleration of the ice upstream took place, the speedup pulse was propagated downstream, and the sites downglacier also accelerated. The propagation speed of this pulse was probably fast enough that we can not resolve it, in agreement with the observations of the propagation of speedups related to glacial earthquakes. Also, the sites downglacier decelerate when the sites upglacier decelerate (some hours after 230). Nevertheless, the downglacier sites continue decelerating until the pulse of meltwater travels through the bend in the glacier and below IS26. The fact that the vertical displacement at IS26 is of lower amplitude than at IS27–IS29 might indicate that the effect of the meltwater pulse decreases as it flows downglacier possibly because the water is more narrowly distributed upglacier and the water flux is spread as it travels downglacier. On the other hand, the subglacial channels and linked cavities can probably accommodate larger volumes of water underneath the part of the glacier closer to the calving front, due to the larger presence of meltwater in this region. The same flux of water through a wider channel or spread over a larger number of channels or cavities might not cause water pressure in subglacial conduits to rise sufficiently to lift the glacier. This would explain the fact that IS25 and IS35–IS39 do not show vertical uplift. Also, this would cause the deceleration of sites IS25 and IS35–IS39 to take place more or less simultaneously to the deceleration of site IS26, when the ice around IS26 returned to its original vertical position.

The fact that the glacier experienced a slight acceleration at the end of day 228, before the vertical uplift of the glacier, indicates that at that time meltwater was being drained to the bed and was reducing the friction between the glacier and its bed. Therefore, the meltwater drainage event should have begun some time during day 228. When water reached and lubricated the bed, the glacier accelerated slightly while the water began to fill the subglacial cavities. Once the cavities were full (around 229.25–229.5) the water pressure in them had increased sufficiently to allow the glacier to lift, and as more water kept flowing into the cavities the ice separated further from the bed, up to 15 cm when the maximum volume of water in the cavities was reached.

Considering the half day between the maximum uplift at sites IS27–IS29 and site IS26, and taking into account that the distance between them is $\sim$6 km, the meltwater pulse would have traveled downglacier at a velocity of $\sim$14 cm/s, which is $\sim$500 times faster than the mean glacier flow at the calving front.

The fact that the accelerations are larger for the sites located downglacier from the bend in the glacier could be because the glacier flows faster and is weaker in this part and hence responds with higher amplitude to perturbations.

6.1.4 Simple hydrological model

We can use the GPS observations and the interpretation above to sketch a conceptual hydrological model that allows us to calculate a minimum meltwater volume involved in the speedup and slowdown of Helheim Glacier.

Since we observe that IS27–IS29 lift at the same time, we consider a cavity of length the distance between IS27 and IS29, that is, 1.4 km. The width of this cavity is a total unknown, except that it cannot be larger than the ∼7 km width of the glacier at those locations, which seems unrealistically large for a cavity. The only other evidence towards a smaller width is the large velocity gradient measured in 2006 between site IS06, on a position similar to IS27–IS29, and IS05 and IS07, 1–2 km off the center axis. Thus, suggesting a standard deep and narrow U-shaped glacier valley. Lacking conclusive information, we assume 0.5 km as the approximate width for the cavity. Of course, instead of such a large cavity, the subglacial drainage system in this area could be formed of several interconnected smaller cavities. However, for the purpose of estimating an approximate water volume responsible for this event, we consider the simplest case with a unique large cavity. The height of the cavity at the time when it held the maximum water volume was the original height of the cavity prior to rise (for the water pressure in the cavity to exceed the ice-overburden pressure, the cavity needs to be full) plus the maximum vertical uplift experienced by the ice surface, 15 cm. It took approximately 9 hours for the water in the cavity to raise to a height of 15 cm (the time between when the glacier started to lift until it reached the maximum vertical position). Since the time between when the water reached and lubricated the bed (which we hypothesize that happened concomitant with the first slight acceleration of the glacier) and when the cavity was full and begun to lift was about 6 hours, and considering a constant water flow in the cavity filling process, we estimate that the water level in the cavity rose 10 cm until it was full. Hence, the total height of water volume input by the meltwater pulse in the cavity, when the ice was at its maximum vertical position, was 25 cm.

For such a hypothetical cavity, the maximum water volume contained in it (when the ice was in its maximum vertical position) would be 175000 m^3. This is a lower bound since it does not take into account the water that had already left the cavity and was traveling downglacier while the cavity was being full. If this meltwater event were to be caused by the drainage of a supraglacial lake, which have typical depths of about 4 m in the Greenland Ice Sheet (Sneed & Hamilton, 2007), the surface of the lake would be at least 0.04 km^2.

Figure 6.5 shows MODIS images from the days surrounding the time of these events. Although the resolution of these images does not allow to make definite conclusions, they suggest that a supraglacial lake located near the position of site IS29 but off the center axis of the glacier (Lake 1 in Figure 6.1) was present on images taken on days 227 and 228, but not on images from days 231 and 234. Unfortunately, the images between days 228 and 231 are cloudy, which does not allow to further constrain the time of the lake drainage. The lake ocupies at least 6 ± 3 pixels in the images, which correspond to an

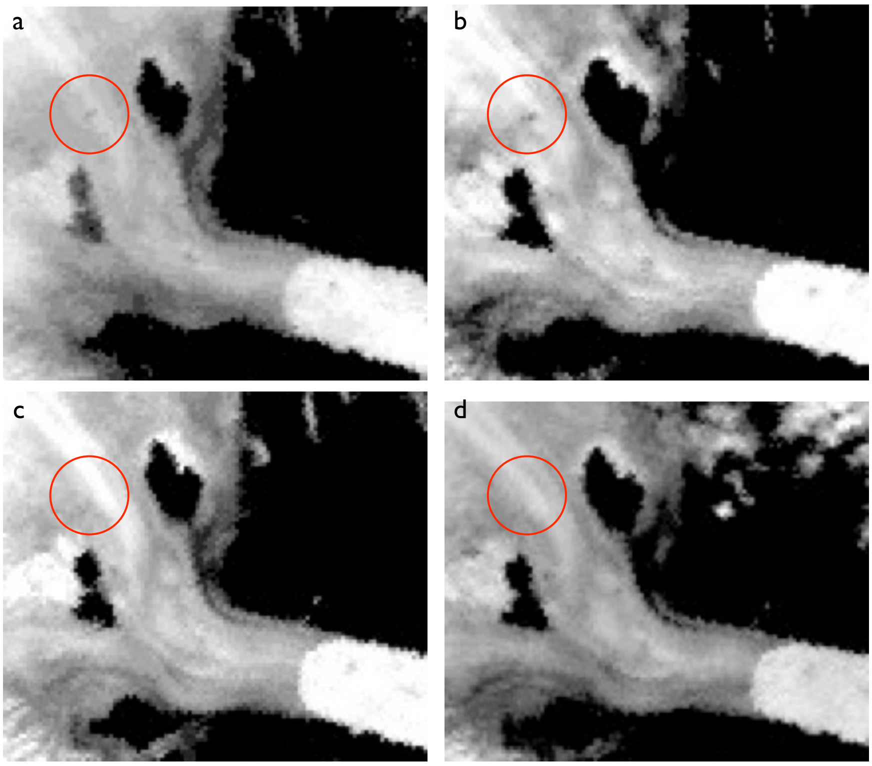

Figure 6.5: MODIS images of the Helheim Glacier area from days around the time of the hypothetical meltwater pulse event. Images are from (a) day 227, 14:55, (b) day 228, 13:45, (c) day 231, 14:30, and (d) day 234, 15:00 (2007). The position of the supraglacial lake is indicated by a red circle.

area of 0.4 ± 0.2 km^2. Measurements at this lake during summer 2009 (see Section 6.3) indicate that the depth of the lake was in general >6 m. Therefore, a total or partial drainage of this lake would provide sufficient water to fill the hypothetical subglacial cavity and to cause the vertical uplift of the glacier.

The proximity of this lake to the sites that experience the largest vertical uplift (see Figure 1.5) makes it a plausible candidate for the initiation of the hypothetical meltwater pulse event. During the time of these events, no glacial earthquake was detected, the closest large calving event is the one on day 225. It is also important to note that the relative magnitude of the speedup between sites upglacier and downglacier is the lowest of the 2007 summer. Also, the change in speed is observed at the sites furthest upglacier, IS30 and IS31. And, furthermore, this is the only time in the 2007 summer campaign that a vertical uplift of a part of the glacier was observed. All these pieces of evidence support the hypothesis that what caused the speedup and slowdown, and the rise and fall signal that traveled from upstream towards the calving front was a meltwater pulse caused by the drainage of the supraglacial lake located upstream at Helheim Glacier (Lake 1 in Figure 6.1).

6.2 Rise and fall at Helheim Glacier preceding a calving event

6.2.1 Observations

We turn now to a second hypothetical meltwater event. Figure 6.6 shows the along-flow position estimates of the GPS sites at Helheim Glacier during three days encompassing the time of two glacial earthquakes registered on day 214, 2008 (already presented in Section 5.1). The sites on the main trunk of the glacier present a step-like speedup very close in time to the time of the second glacial earthquake. (See Figure 1.6 for a map of the GPS sites during this period.) Such response is consistent with that observed in relation to other glacial earthquakes in the previous year, albeit of lower amplitude. However, the sites located on the tributary (see Figure 1.6) suggest a different response. The site on the tributary located closest to the calving front, site IS49, presents the same type of response as the sites on the main trunk of the glacier, but of smaller amplitude. However, sites IS57, IS48, IS58, and IS59, located progressively farther upglacier in the tributary, present a markedly different flow character. These sites undergo a phase of speedup, happening ∼1–1.5 days before the earthquakes, followed by a slowdown that takes place in two steps, one happening before the earthquakes, the second hapenning after the earthquakes. These events seem to happen in a gradual mode during a period of ∼2–3 days. Their character is similar to that presented in the previous section for days 228–233 in 2007 and hypothetically linked to the drainage of a supraglacial melt pond, although of smaller magnitude.

Figure 6.7 shows the vertical component of site position variation for the same sites presented in Figure 6.6. The vertical timeseries reveal that site IS58, located on the edge between the main trunk and the tributary and very close to the nunatak, experienced a vertical uplift concomitant with the changes in speed observed at this and other sites in the tributary. The site started to rise at the end of day 213, achieved its maximum vertical height ∼6 h after the beginning of day 214, when it started to fall until it recovered its original vertical position, ∼1 day later. No other site in the tributary or the main trunk presents such a vertical uplift concomitant with that of site IS58.

Although some other vertical departures from mean flow are observed at site IS58 during the observing period in summer 2008, in association also with changes in speed, there is no other signal as large and clear as the one observed for these days.

6.2.2 Hydrological hypothesis

Following the same line of thought as for the events registered on days 228–233 in 2007, we interpret this signal as a meltwater pulse that would have entered the subglacial drainage system not far from site IS58, causing the water pressure at the bed to increase and causing the vertical uplift of this site. As to why no other site in the network registered such an uplift, we believe this is explained by the location of IS58. Since site IS58 was deployed near the edge between the main trunk and the tributary and just a few

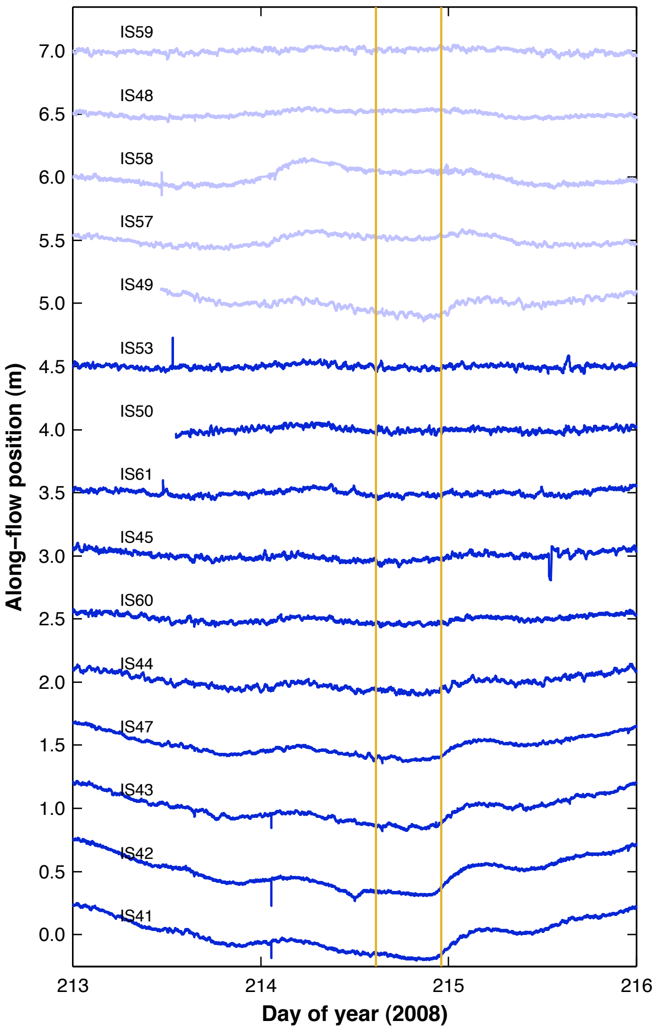

Figure 6.6: Along-flow position estimates relative to mean speed for all sites (except for three sites located upglacier on the main trunk) and spanning three days in 2008, days 213–216. Timeseries shown in a lighter color correspond to sites located on Helheim's tributary. The timeseries are offset by 0.5 m for each site for clarity. Sites are plotted, bottom to top, from closest to the calving front to farthest upglacier within the main glacier, and then within the tributary. Yellow lines indicate the time of glacial earthquakes.

kilometers from the nunataks, the glacier in this region is presumably thinner compared to the ice below the rest of sites, generally deployed on the centerline of the glacier or tributary and far from the glacier walls. Therefore, lifting this part of the glacier requires less hydraulic pressure. Furthermore, the site is located downglacier enough that the subglacial drainage system in this region probably accommodates easily large volumes of water, thus the water pressure at the bed rapidly decreases as the water pulse travels away from the location where it entered the subglacial drainage system. Also, the source for

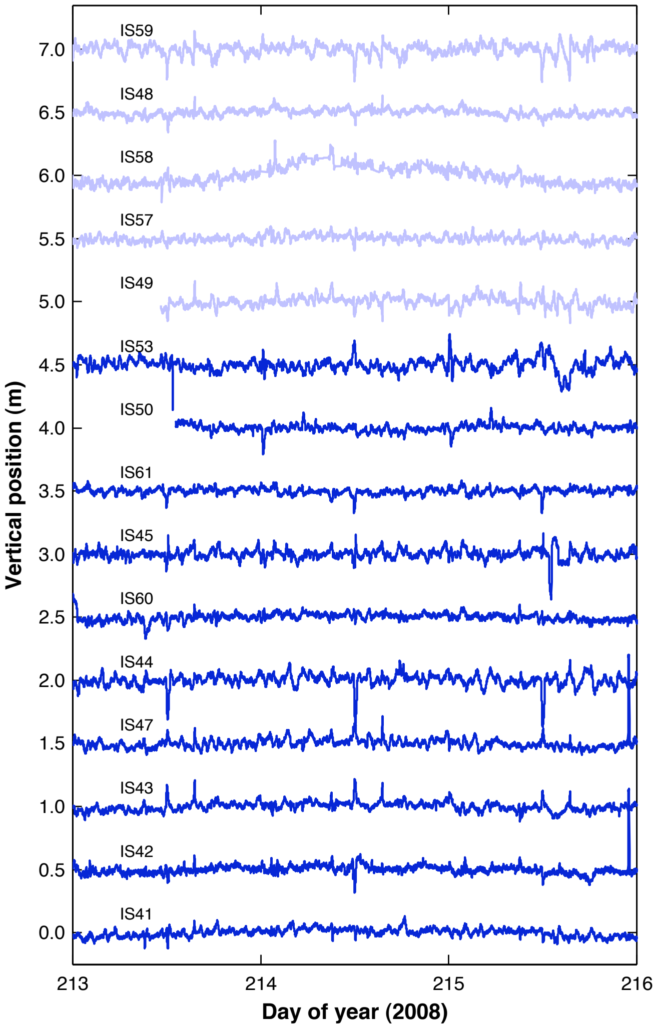

Figure 6.7: Vertical position residuals to the mean motion for same sites and days as in Figure 6.6.

the meltwater pulse was probably located not far from site IS58. A plausible candidate is a supraglacial melt pond that some times forms ~1–2 km upglacier the location of IS58, and close to the nunataks (Lake 2 in Figure 6.1). This lakes appears clearly on the LANDSAT image of Helheim Glacier from 2001 (see Figures 1.4–1.6). The lake is also present in an ALOS image from the beginning of summer 2008 (Figure 6.1). We estimated a surface for the lake in this image (of higher resolution than the MODIS images) of ~0.6 km^2.

The fact that this event happened close in time to the glacial earthquakes on day 214 may not be a coincidence. This hypothetical meltwater pulse originated just ~14–16 km from the calving front. Furthermore, there is no other signal of meltwater pulse or of glacial-earthquake and calving-event associated speedup as clear as this one during the entire summer of 2008. This suggests that the drainage of large volumes of water may play a role in triggering at least some of the glacial-earthquake generating calving events, either by their effect on the dynamics of the glacier, in this case of the tributary, or by the drained meltwater itself contributing, when it comes out the front, to the detachment of the ice that is calved. Indeed, in several occasions water is observed to come out the front of the glacier prior to a large calving event, as registered in the photographic images of the front of the glacier.

Unfortunately, although the lake is sometimes observed in MODIS images, available daily, because of its proximity to the glacier walls, it is sometimes shadowed by the nunataks, depending on the position of the glacier in the satellite swath. Therefore, these images do not allow to verify the presence or absence of this lake at Helheim Glacier.

6.3 Record of the drainage of a supraglacial lake at Helheim Glacier

In summer 2009 we deployed a water-pressure gauge at one of the melt ponds that forms each summer at Helheim Glacier. It forms always in approximately the same location, in the upglacier region of Helheim Glacier (Lake 1 in Figure 6.1). We believe the drainage of this lake was responsible for the speedup and slowdown registered during days 228–233 in 2007 (Section 6.1). Such lakes tend to repeat their position from year to year, influenced by the glacier bed topography.

At the time when the pressure gauge was deployed, on day 178 (June 27), the melt pond contained a large volume of water. At the time of its retrieval, on day 234 (August 22), all the water had drained. Figure 6.8 shows the lake's water level variations measured by the pressure gauge. This sensor records variations in pressure, which we convert to water height by using the density of fresh water and using as reference for zero-level, the pressure recorded at the time when the lake had drained. The recorded data shows high variability in the lake's water level, including partial drainages, terminated by an abrupt and complete drainage of the lake on day 217 (August 5).

During the period between days 178–216, the water height in the lake at the position of the pressure gauge ranged from ∼11 to ∼6 m. (It should be taken into account that the maximum water height recorded by the sensor may not be the maximum water depth of the lake since the pressure gauge was very likely not deployed in the deepest part of the lake.) During this period, the record shows some episodes of gradual filling and drainage and also some water height variations that are much more abrupt, happening within a few hours. The clearest examples of such sudden variations are the ones from days 205 and 212. On day 205 a sudden partial drainage took place that lasted ∼2 h and lowered the lake level by ∼2–3 m. This drainage was followed by a period of quiescence until day 212, when the lake underwent a rapid drainage followed by and increase in the water level, all taking place in less than ∼3 h. These sudden increases in water level could be caused by the outflow of pressurized water that returns to the glacier surface when the pressure in the subglacial drainage system increases above a certain threshold. There is

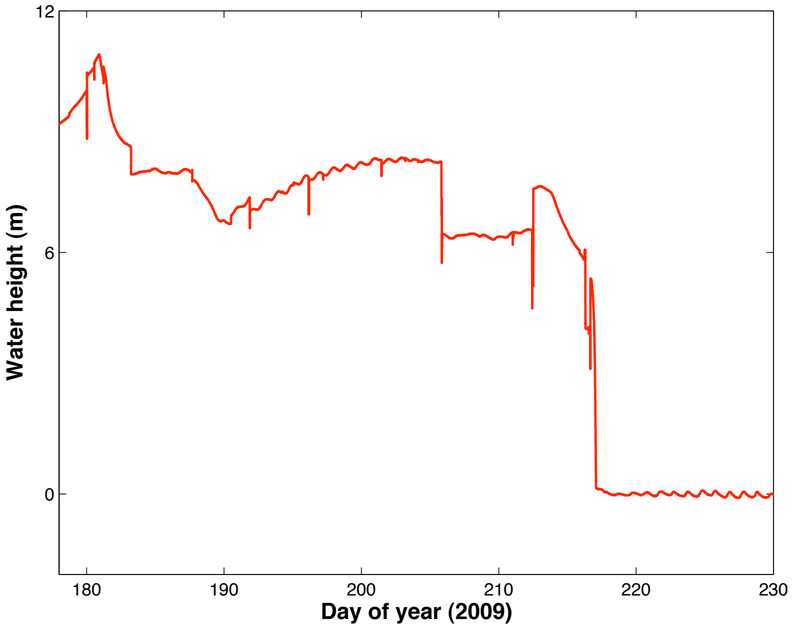

Figure 6.8: Water height in the supraglacial lake located in the upglacier part of Helheim (see Figure 6.1) during the period a water-pressure sensor operated, days of year 178–234, in 2009.

also the possibility that the sudden water level increase was, at least partially, spurious. Also, diurnal variations during quiescence periods are possibly caused by variations in atmospheric pressure.

The final drainage of the lake, taking place during days 216–217, happened in several distinct steps. Figure 6.9 is a zoom in of the period when the final drainage took place. An initial and abrupt drainage was followed by ∼9–10 h of stabilization, and then by a refilling of the lake returning its level to a level similar to the one registered before the initial partial drainage. Shortly after, the lake begun to drain steadily for a period of ∼10 h until it drained completely. Such a time period for the drainage of a melt pond is in agreement with the time the glacier was observed to uplift during days 229–231 in 2007 (see Section 6.1).

Unfortunately, lacking external validation, we cannot conclusively determine the level of error in these estimates, and thus we do not make further use of them. They however support the hypothesis that significant and rapid lake drainage events are conceivable. Furthermore, lake drainage at this location was confirmed in 2006 and 2009 by visual inspection. In 2006, a pressure gauge was lost in this pond to a sudden drainage event. Also, the comparison between the lake's water level records and the geodetic observations of glacier flow from summer 2009 requires the processing of L1-only GPS data, and thus is left for future research.

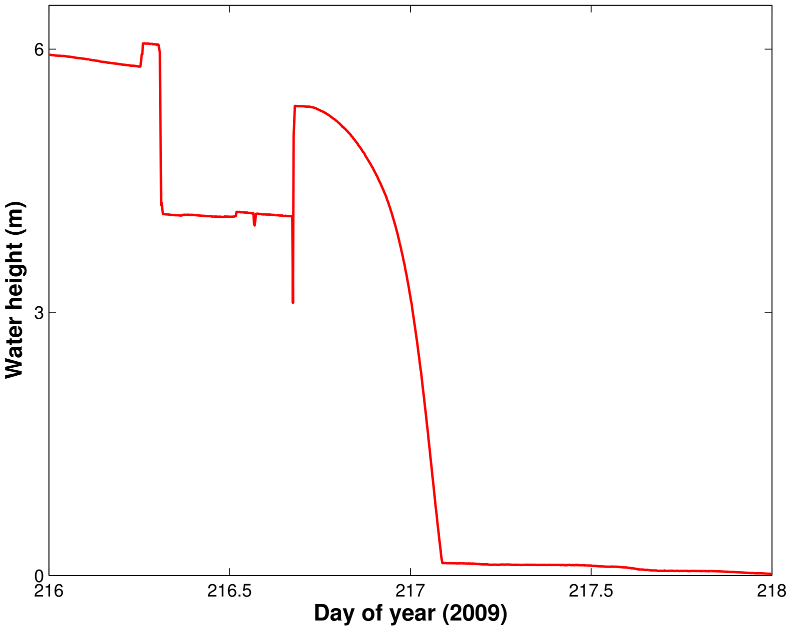

Figure 6.9: Zoom in of Figure 6.8 for days of year 216–218, during which the lake drained completely.

6.4 Summary

The observations presented in this chapter demonstrate that the speed of Helheim Glacier can vary rapidly at times when no large calving events associated with glacial earthquakes occur. The vertical uplift observed at some sites, concomitant with changes in glacier speed, suggest that such variations in ice flow speed are associated with episodes of high water pressure in the subglacial drainage system, which result in the glacier lifting and accelerating. Also, the character of these variations in speed is markedly different from those observed in association with glacial earthquakes. An increase in basal water pressure sufficient to cause the acceleration of the glacier can be caused by a sudden and large variation in the meltwater supply to the bed (Schoof, 2010). We hypothesize that such increase in meltwater supply is of supraglacial lake origin. Large supraglacial lakes have been observed to drain and cause the acceleration of the ice sheet (Das et al., 2008). At Helheim, several melt ponds form each summer season in approximately the same location. One of such lakes, located in the upglacier region, has been observed to drain in several occasions. In 2009 we deployed a water-pressure gauge in this lake that allowed us to record its evolution over the course of one and a half months, including its complete drainage in early August. Furthermore, in 2008 one of these events occurred approximately 1 day prior to a large calving event and glacial earthquake, suggesting that the dynamic response of the glacier to the increase in basal water pressure could also have played a role in triggering the calving event.

The results presented here are rather qualitative and require further analysis, which is in progress. This study, although at a preliminary stage, already highlights the importance of lakes that form on the surface of large Greenland outlet glaciers in triggering important variations in their flow speed. A detailed study of the response of the glacier to such events can yield important results pertaining to the glacier's hydrologic system.

Chapter 7

Conclusions

7.1 Summary of work

In this thesis we have undertaken the processing of the high-rate, high-precision GPS data acquired during the summers of 2006–2008 at several locations on the surface of Helheim Glacier. We have detailed the processing method used, and we have assessed the precision of the position estimates obtained with such techniques. We have also analyzed the several sources of errors that affect our solutions, such as ionospheric errors, reference frame errors, and systematic errors associated with the processing technique, the quality of the data, and multipath.

We have used the extensive GPS data set to characterize the general state of the flow of Helheim Glacier by investigating the mean kinematics of the glacier during the summers of 2006–2008, from mean seasonal to daily timescales. We have characterized the spatial variation of the mean summer flow over the region where our GPS network extended and its consistency from year to year. We have also studied, in each of the seasons, the temporal dependence of the mean daily velocity at each of the sites, and its spatial coherence throughout the glacier. And we have analyzed the results in relation to satellite-imagery observations from previous years and from the same time period.

The high-precision of the high-rate GPS observations collected at Helheim Glacier enables us to study in great detail the sub-daily deviations from mean flow and their spatio-temporal variation. In this respect, one of the main parts of the work presented in this thesis is centered in the characterization of the flow response of Helheim Glacier to the ocean tides. We study the tidal response of the glacier over daily, to monthly, to seasonal timescales. We use the observed and modeled ocean tide at Sermilik Fjord to perform a fit to the tidal signals observed in the horizontal and vertical components of the daily position timeseries, and we study the spatial and temporal variation of the parameters that characterize the tidal response of the glacier. We compare our observations to the predictions of several models that study the tidal bending and tidal flow variations of glaciers.

The sub-daily deviations from mean flow include, at some specific times, large and abrupt changes in speed, in general coherent throughout the length of the glacier. We present the geodetic observations of glacier deformation associated with several glacial earthquakes that occurred during the summers of 2006–2008. We characterize the glacial earthquake-associated dynamic response, consisting on step-wise speedups. We also analyze in detail the tidal response around the times of glacial earthquakes. We describe and study the sudden and transient increases in ocean tidal response of the glacier observed in association with these events and analyze them in relation to the change in the flow behavior of the glacier.

Finally, we present a preliminary study of speed increases that happen at times when no glacial earthquakes are detected and present a different flow character than those associated with the earthquakes. We analyze some of these changes in speed which have characteristics that suggest they are caused by the sudden drainage of lakes that form at the surface of Helheim Glacier by accumulation of meltwater. We also present the record of one of such drainages.

7.2 Conclusions

The Helheim project demonstrates the feasibility of obtaining continuous high-rate position measurements at the surface of a fast-flowing glaciers with a GPS network. This method allows to characterize the surface deformation of the glacier with high precision (at the cm-level) and with a temporal resolution higher than with any other technique used in glaciology, and thus, to study the dynamics of glaciers at temporal scales not explored before. We have estimated that the high-rate position solutions of fast-flowing ice sites at Helheim Glacier, processed with respect to a static reference site deployed on the rock margins of the glacier, have a precision of ∼1–2 cm in the horizontal component, and ∼2–5 cm in the vertical component. We have also shown that the quality of the solutions is highly dependent on the ability of the processing software of resolving and fixing all the phase ambiguities to integer values, which in turn depends on the quality of the data, specially near day boundaries. The position estimates from a given site show a high-frequency, low-amplitude variations that repeat over consecutive days, suggesting that a substantial part of the systematic errors observed in the timeseries are associated with multipath.

The analysis of the GPS position estimates from Helheim Glacier reveal that during the summers of 2006–2008 the speed of the glacier ranged from ∼24 m/d near the terminus to ∼4 m/d at ∼37 km upglacier. In general, the flow speed gradually increases from upstream towards the calving front, so that extending flow, with high positive longitudinal strain rates, dominates over the majority of the glacier's extension. However, at the bend of the glacier, where the ice changes its direction of flow from southeast to due east, there exists a region of compressing flow. Sites located just a few kilometers offset from the center flowline have similar speeds that those located at the same distance from the calving front but in the center. However, speeds rapidly decrease near the margins, indicating that lateral shear strains are high.

The estimated mean speed of Helheim Glacier during summers of 2006–2008 was ∼20% lower than in 2005, similar to estimates from 2003, and higher than in 2000. The inter-annual variations in speed during the summers of 2006–2008, when the speed remained approximately constant, were also much less important than the dramatic variations reported during the period 2002–2006 (Howat et al., 2007). The slowdown observed at Helheim Glacier is consistent with observations at other southeast Greenland glaciers, and appears to have been regulated by sea surface temperature (Murray et al., 2010). However, the glacier was most active during the summer of 2007, when the lower ∼12 km of the glacier flowed slightly faster than in 2006 and 2008. The speed was also more variable in 2007, with the most numerous and largest variations in speed taking place during this summer season. This reactivation of Helheim during summer 2007, not observed at other glaciers, also coincides with a warm water anomaly between Greenland and Iceland in July 2007 (Murray et al., 2010), suggesting that the flow regime of Helheim Glacier is highly sensitive to ocean conditions (Straneo et al., 2010). In most cases, specially in summer 2007, the velocity of the GPS sites on the glacier gradually increases throughout the season, mainly due to external forcings, such as changes in the boundary conditions or increase in sea and atmosphere temperatures, but in part also due to the advection of the sites into regions of faster flow regime.

At the sites located in the lower ∼12–16 km of the glacier we observe semi-diurnal sinusoidal variations in the along-flow position residuals to linear motion, and also during some periods, in the vertical and cross-flow components of motion. Such semi-diurnal variations correlate with the ocean tide in Sermilik Fjord but are delayed with respect to it. Thus, we interpret these variations as the response of the glacier to ocean tidal forcing.

During the summers of 2006–2008, for the sites located in the lower ∼16 km of the glacier, the diplacement deviations from mean flow in the along-flow component are dominated by tidal variations that are out of phase with the ocean tide. The glacier position advances at low tide and retards at high tide with respect to mean flow. Such variations are at most of ∼10 cm in amplitude and result from the variations in hydrostatic pressure as the tide rises and falls (e.g., Anandakrishnan & Alley, 1997; Gudmundsson, 2007), as indicated by the comparison of the observed variations in speed and the expected due to the tidally induced variations in driving stress (Howat et al., 2005; Gudmundsson, 2007).

In 2006 the lower ∼4–5 km of the glacier were also observed to show vertical response to the ocean tides, indicating that this region of the glacier was afloat during this period. The response had an amplitude of ∼30–40% of the full tidal range at the site located closest to the calving front and attenuated $\lesssim$6 km behind the calving front. In general, sites located in similar locations in 2007 and 2008 do not show vertical response to the tides. However, in 2007, the site located closest to the calving front was observed to transition from grounded to floating, suggesting that the glacier was very close to flotation during this period. We attribute the observed change in vertical response from 2006 to 2007 to the possibility that the glacier had thickened. Moreover, in 2006 the sites that present vertical tidal response also exhibit tidal response in the cross-flow component, indicating that the glacier changed slightly its direction as the tide rose and fell, suggesting a link between the vertical and the cross-flow responses. Lacking detailed bathymetric information we interpret the cross-flow variations as due to differential vertical response to ocean tides across the glacier.

The admittance analysis yields that the tidal response of the glacier is delayed with respect to the ocean tides by ∼1–2 h. The response occurred ∼1 h earlier in 2006, when the glacier was afloat, suggesting that lower friction during this period caused the glacier to respond more rapidly. The admittance of the response decays exponentially with distance from the calving front in the three components of flow. Furthermore, the tidal response in the along-flow component is highly time varying. It presents a gradual variation with a ∼15-day periodicity that suggests a non-linear response of the glacier to the ocean tides. Also, abrupt changes in tidal response are observed at the time of large calving events associated with glacial earthquakes (de Juan et al., 2010b).

During the observing period of our GPS network, and specially in summer of 2007, the flow speed of the glacier experienced abrupt increases, normally followed by total or partial decreases. In general, such variations in speed happened coherently throughout the length of the glacier, and its magnitude decreased upstream. Some of the variations in speed are temporally linked to the occurrence of glacial earthquakes (Nettles et al., 2008). These type of earthquakes are now known to be generated by large calving events that produce tall unstable icebergs that overturn against the ice front as they calve (Tsai et al., 2008; Nettles & Ekström, 2010).

In summer 2006, since Helheim Glacier had developed a short floating tongue, its retreat occurred by calving of large tabular icebergs that do not overturn, and thus do not cause glacial earthquakes. In 2007, the glacier had re-grounded, which made possible the calving of unstable icebergs and the production of glacial earthquakes. Several glacial earthquakes occurred at Helheim during the summers of 2007 and 2008, clustered in three different time periods. All of them manifest on the glacier's surface as sudden increases in flow speed (Nettles et al., 2008), likely caused by the reduction in resisting forces at the calving front and the increase in effective driving stress (e.g., Howat et al., 2005; Nick et al., 2009). The magnitude of the change in speed, which occurs coherently throughout the length of the glacier, decreases with increasing distance from the calving front. Therefore, glacial earthquakes also cause sudden changes in the glacier's longitudinal strain rate. The speed recovers partially after the glacial earthquake, but in some cases the event causes a sustained increase in velocity (Nettles et al., 2008).

As indicated above, the along-flow tidal response presents a long-period variation, in general changing gradually. However, following glacial earthquakes, and coinciding with the step-like increases in speed, the tidal admittance increases suddenly by a factor of as much as ∼2.5 (de Juan et al., 2010b). The intensified tidal response only lasts for 1–2 days, in contrast with the speed variation that only recovers partially approximately at the same time that the tidal response recovers. Due to the transient nature of the response, the loss of ice associated with the glacial earthquake is unlikely to be the cause of the increase in tidal response. Instead, a temporary decrease in flow resistance would enable the glacier to respond with higher amplitude to the tides. We hypothesize that the abrupt change in longitudinal strain rate associated with glacial earthquakes may cause a disruption of the subglacial drainage system, similar to that observed in surging glaciers (Kamb, 1987). Such a disruption would increase the basal water pressure, reducing the friction at the ice-bedrock interface, and enabling the observed enhanced response of the glacier to the ocean tides (de Juan et al., 2010b). Such disruption is expected to be temporary, with the re-establishment of a more efficient drainage once the strain rate is reduced.

Other large increases in flow speed happen when no glacial earthquakes are detected. Their flow character suggests that they are originated by the drainage of meltwater lakes. Such lakes form on the surface of the glacier by accumulated meltwater, and tend to occupy the same location each summer. These speed increases occur concomitant to a rise and fall at the sites located nearby one of such lakes, which suggests that the variations in flow speed are associated with episodes of high water pressure in the subglacial drainage system. Furthermore, the character of the variations in speed is markedly different from that observed in association with glacial earthquakes. The position timeseries suggest that these increases in speed originate upglacier or near the sites that exhibit the vertical displacement. We hypothesize that these increases in glacier flow speed are associated with the sudden drainage of one of these lakes, which increases basal water pressure, allowing the glacier to lift and accelerate. In 2008, one of such events occurred $\sim$1 day before a large calving event and glacial earthquake were detected, suggesting that the drainage of meltwater lakes might have played a role in triggering some of the calving events. Satellite MODIS images from around the time of one of such events show that the lake is present in the images before the event, but not in the images from some days after the event. In 2009 we deployed a water-pressure gauge in one of such lakes, which enabled the study of its evolution, including its complete drainage that was observed to occur over the course of one day.

Most of the speed increases at Helheim Glacier are observed to occur temporally and spatially coherent throughout the glacier's length, indicating that a change in the boundary conditions, whether it is localized at the glacier terminus, like in the case of glacial earthquakes (Nettles et al., 2008), or at the base of the glacier and originated upglacier, like in the drainage of a supraglacial lake, the speed response of the glacier is transmitted throughout the length of the glacier. Also, both the long period and the sudden variations in tidal response occur coherently in the region of the glacier that exhibits tidal response. These results demonstrate that the glacier is capable of responding rapidly and coherently to external forcing, and highlight the need for understanding the role that these rapid changes play in the overall evolution of the ice sheet in a changing climate.

This thesis demonstrates that continuous high-rate and high-precision position estimates at the surface of large outlet glaciers provide valuable information on the flow character of the glacier at a wide range of timescales. Such measurements can help understand the variations in glacier flow induced by small and constant forcings, such as the ocean tides, and also by large and sudden changes in boundary conditions, such as glacial-earthquake related calving events and sudden drainage of large volumes of meltwater. Characterizing such responses helps improve our understanding of the role that external forcing plays in the acceleration and retreat of large outlet glaciers in Greenland.

7.3 Future work

Following the investigations described in this thesis, a number of studies could be taken up. For example, further research involving detailed (finite-element) numerical modeling could help better understand the observed tidal response of the glacier. Such modeling would also contribute to unravel key information on rheological properties and dynamic response of Helheim Glacier to other external forcings. We are currently in the process of describing in a paper for publication the findings related to the response of Helheim Glacier to the ocean tides, including testing some simple models, and this study is ongoing work.

As for the results presented here on the response of the glacier to sudden changes in basal water pressure, they are preliminary, but a more quantitative analysis is underway.

Furthermore, the field-based campaigns at Helheim Glacier lasted until the summer of 2010 and, starting in 2008, were extended to Kangerdlugssuaq Glacier, also located in the southeast coast of Greenland, to north of Helheim. Starting in 2008 a network of new high-accuracy, low-cost GPS receiving systems was operated on both glaciers. These new GPS systems were also operated over winter. However, the data collected by these systems consists of single frequency (L1-only) GPS observations. The processing of such data requires the development of a new software package, which is currently underway. The analysis of this data, including both the extension over time at Helheim and to a second glacier in many ways similar to Helheim and spatially close to it, should provide important information on the dynamic evolution of Greenland's fast-flowing outlet glaciers.

Appendices

Appendix A

Specifications for the geophysical sensors deployed at Helheim Glacier

A.1 Dual-frequency GPS systems

The GPS systems deployed on ice at Helheim Glacier include antenna, receiver, batteries, solar panel, and an environmentally hardened enclosure (see Figure A.1). The receiver and batteries are stored in a suitcase-sized waterproof box, and the solar panels are attached on to the surface of the box. The antenna lies separately on a tripod. Both the box and antenna are anchored to a pole drilled into the ice.

Almost all of the systems are Trimble NetRS or Trimble R7 receivers and Trimble Zephyr antennas. Only some of the receivers are Trimble 5700 (see Appendix B for a list of the GPS systems deployed in each of the summer campaigns). The sampling rate is limited by the storage capacity of the receivers. We operated the Trimble NetRS at one sample per 5 seconds (i.e., 0.2 Hz), and the R7 and 5700 at one sample per second (i.e., 1 Hz). All of the receivers have dual-frequency tracking capability, they track carrier phases L1 and L2, P code pseudorange P1 and P2, pseudorange C/A, in most of the cases also the raw signal strength for the phase observations S1 and S2, and in some cases the Doppler frequency D1 and D2. Raw data was stored in Trimble proprietary binary format, and then converted to RINEX (receiver independent exchange) observation format, prior to processing. The receivers are low power consumption (~4 W with antenna). Solar panels represent the best way to deal with long-term power issues in this environment. The power systems for each GPS system comprise a 40 W photovoltaic panel, two 18 Ah batteries for energy storage, and a charge controller to prevent the battery from overcharging. The antennas were mounted on ~20 cm high aluminum tripods.

The static reference GPS stations (see Figure A.2) also include antenna, receiver, batteries, and solar panel. A Trimble NetRS receiver and Trimble Zephyr antenna were used for reference stations NUN1 in 2006, and NUN1 and NUN2 in 2008. In 2007, NUN1 and NUN2 had Trimble R7 receivers and Zephyr antennas. In 2006, NUN2 and HEL1 were Javad Lexon receivers and Javad Regant antennas. Finally, in 2008, HEL2 was a Trimble NetRS receiver and Trimble Dorne Margolin antenna. All of these receivers tracked double frequency observations. These sites were built following general advise by unavco (facility.unavco.org/project_support/project_support.html).

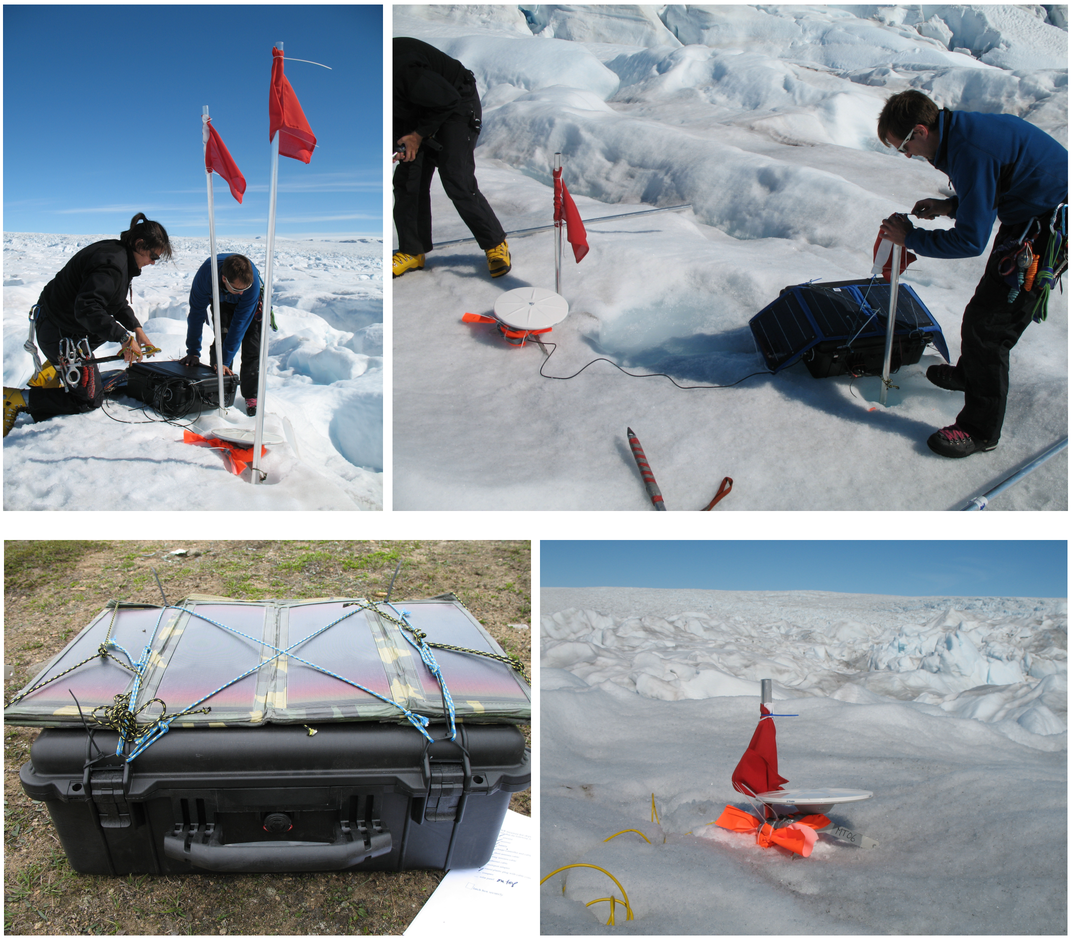

Figure A.1: (Top) Pictures of GPS stations deployed on ice, and (bottom) close up view of (left) solar panel attached to the surface of the receiver box and (right) GPS antenna on a tripod.

A.2 Water-pressure gauges

For recording the ocean tide in Sermilik Fjord during summer seasons 2006–2008 we used a Global Water WL16-U pressure transducer and data logger. The pressure transducer, that is housed in a weather-resistant enclosure, is connected with a cable to the data logger, which was placed on land. The logger also includes an atmospheric pressure sensor to correct the pressure measured by the transducer for the inverse barometer effect. We operated it at one sample per minute.

The water-pressure gauge that was operated in a melt pond in 2009 (see Figure 1.2) was a U20-001-01 HOBO 30-Foot Depth Data Logger. This water-pressure gauge can be

Figure A.2: Pictures of a GPS reference static station deployed at Helheim on the glacier margins during summer 2006.

operated in a water depth up to ∼9 m, which is enough for the depth of this glacier melt pond. Due to a lower storage capacity, we had to configure this logger to measure once every 4 minutes in order to ensure its operation during the entire campaign.

Appendix B

GPS systems deployed at Helheim Glacier

Table B.1: Site name, deployment location (latitude and longitude), time of deployment and retrieval in day of year, number of days for which the site operated correctly, and type of receiver and antenna for the sites deployed during the field campaign of summer 2006.

Site	Lat	Lon	Depl.	Retr.	Days	Receiver	Antenna
IS01	66.4553	-38.3991	180	241	39	Trimble NetRS	TRM41249.00
IS02	66.4594	-38.4250	179	237	35	Trimble NetRS	TRM41249.00
IS03	66.4354	-38.4324	181	183	3	Trimble NetRS	TRM41249.00
IS05	66.4648	-38.4704	180	183	4	Trimble NetRS	TRM41249.00
IS06	66.4696	-38.4415	179	240	29	Trimble 5700	TRM41249.00
IS07	66.4701	-38.4147	180	240	60	Trimble NetRS	TRM41249.00
IS08	66.5058	-38.4402	180	241	61	Trimble NetRS	TRM41249.00
IS09	66.4848	-38.4725	179	181	3	Trimble NetRS	TRM41249.00
IS10	66.4712	-38.5093	181	240	37	Trimble NetRS	TRM41249.00
IS11	66.4990	-38.5060	179	240	27	Trimble NetRS	TRM41249.00
IS13	66.5229	-38.5476	179	238	57	Trimble NetRS	TRM41249.00
IS15	66.5391	-38.5677	179	238	59	Trimble NetRS	TRM41249.00
IS16	66.5423	-38.7363	180	228	27	Trimble NetRS	TRM41249.00
IS17	66.5784	-38.6454	180	238	36	Trimble NetRS	TRM41249.00
IS18	66.5843	-38.5424	180	182	3	Trimble NetRS	TRM41249.00
IS19	66.5947	-38.6661	180	238	36	Trimble NetRS	TRM41249.00
SN03	66.3624	-38.1406	203	204	2	Trimble NetRS	TRM41249.00
SN04	66.3696	-38.1710	203	206	4	Trimble NetRS	TRM41249.00
SN05	66.3667	-38.1469	237	241	5	Trimble NetRS	TRM41249.00
SN06	66.3695	-38.1681	237	241	5	Trimble NetRS	TRM41249.00
SN07	66.3722	-38.2019	237	241	5	Trimble NetRS	TRM41249.00
SN08	66.3799	-38.2468	238	241	4	Trimble NetRS	TRM41249.00

Continued on Next Page . . .

Table B.1 – Continued

NUN1	66.4202	-38.4800	178	241	50	Trimble NetRS	TRM41249.00
NUN2	66.4834	-38.3722	180	240	60	JNS LEXON_GGD	JPSREGANT_DD_E
HEL1	66.4012	-38.2156	179	240	61	JNS LEXON_GGD	JPSREGANT_DD_E

Table B.2: Same as in Table C.1, except for the sites deployed during the field campaign of summer 2007.

Site	**Lat**	**Lon**	**Depl.**	**Retr.**	**Days**	**Receiver**	**Antenna**
IS20	66.3686	-38.1711	185	206	22	Trimble R7	TRM41249.00
IS21	66.3778	-38.1831	185	206	22	Trimble R7	TRM41249.00
IS22	66.3627	-38.1922	185	206	22	Trimble NetRS	TRM41249.00
IS23	66.3724	-38.2037	185	206	22	Trimble NetRS	TRM41249.00
IS24	66.3812	-38.2555	185	206	22	Trimble NetRS	TRM41249.00
IS25	66.3884	-38.3034	185	236	52	Trimble NetRS	TRM41249.00
IS26	66.4157	-38.3493	185	236	52	Trimble R7	TRM41249.00
IS27	66.4610	-38.4238	185	235	51	Trimble NetRS	TRM41249.00
IS28	66.4634	-38.4339	185	235	51	Trimble NetRS	TRM41249.00
IS29	66.4707	-38.4441	207	235	30	Trimble NetRS	TRM41249.00
IS30	66.4857	-38.4724	185	235	51	Trimble NetRS	TRM41249.00
IS31	66.4991	-38.5069	185	235	51	Trimble NetRS	TRM41249.00
IS35	66.3737	-38.2162	208	236	29	Trimble NetRS	TRM41249.00
IS36	66.3847	-38.2317	208	236	29	Trimble R7	TRM41249.00
IS38	66.3699	-38.2447	208	236	29	Trimble NetRS	TRM41249.00
IS39	66.3773	-38.2539	208	236	29	Trimble NetRS	TRM41249.00
NUN1	66.4201	-38.4801	186	236	51	Trimble R7	TRM41249.00
NUN2	66.4834	-38.3719	207	224	12	Trimble R7	TRM41249.00

Table B.3: Same as in Table C.1, except for the sites deployed during the field campaign of summer 2008. HEL2 was installed on August 24, 2007 and is still operating.

Site	**Lat**	**Lon**	**Depl.**	**Retr.**	**Days**	**Receiver**	**Antenna**
IS40	66.3717	-38.1849	180	207	28	Trimble NetRS	TRM41249.00
IS41	66.3823	-38.2018	180	231	52	Trimble R7	TRM41249.00
IS42	66.3641	-38.2170	180	231	52	Trimble NetRS	TRM41249.00
IS43	66.3750	-38.2396	189	231	43	Trimble R7	TRM41249.00
IS44	66.3891	-38.3051	182	231	50	Trimble R7	TRM41249.00
IS45	66.4174	-38.3484	179	231	53	Trimble R7	TRM41249.00
IS46	66.3844	-38.2534	182	212	31	Trimble R7	TRM41249.00
IS47	66.3657	-38.2636	182	231	50	Trimble R7	TRM41249.00
IS48	66.3722	-38.4544	179	231	53	Trimble NetRS	TRM41249.00
IS49	66.3504	-38.2496	182	231	39	Trimble R7	TRM41249.00
IS50	66.4602	-38.4297	179	231	45	Trimble R7	TRM41249.00
IS51	66.4628	-38.4462	179	233	55	Trimble NetRS	TRM41249.00
IS53	66.4996	-38.4919	183	231	49	Trimble R7	TRM41249.00
IS54	66.5395	-38.5834	189	213	25	Trimble R7	TRM41249.00
IS55	66.5955	-38.6722	189	231	43	Trimble R7	TRM41249.00
IS56	66.3495	-38.2002	190	211	22	Trimble R7	TRM41249.00
IS57	66.3548	-38.3330	189	231	43	Trimble R7	TRM41249.00
IS58	66.3834	-38.4174	189	231	43	Trimble R7	TRM41249.00
IS59	66.3763	-38.6047	189	231	43	Trimble R7	TRM41249.00
IS60	66.3999	-38.3372	189	231	43	Trimble R7	TRM41249.00
IS61	66.4428	-38.4027	189	231	43	Trimble R7	TRM41249.00
IS62	66.4799	-38.4666	190	231	42	Trimble NetRS	TRM41249.00
NUN1	66.4202	-38.4792	179	233	55	Trimble NetRS	TRM41249.00
NUN2	66.4833	-38.3722	180	233	54	Trimble NetRS	TRM41249.00
HEL2	66.4012	-38.2157	–	–	–	Trimble NetRS	TRM29659.00

Appendix C

Kinematics of GPS systems deployed at Helheim Glacier

Table C.1: Site name, distance to calving front position on day of year 213 (2008), mean summer horizontal speed, $v \pm \epsilon_v$, and flow direction with respect to North, for the sites deployed during the summer of 2006. (For sites with less than 3 days of data we take estimates from daily solutions.)

Site	**dist (km)**	v **(m/d)**	ϵ_v **(m/d)**	**dir (degrees)**
IS01	16.83	12.35	0.01	156
IS02	17.84	13.60	0.01	156
IS03	15.91	13.55	1.12	166
IS05	19.61	11.31	0.57	149
IS06	19.19	13.11	0.10	156
IS07	18.79	12.46	0.05	157
IS08	22.50	2.30	0.01	182
IS09	21.76	13.75	0.01	138
IS10	21.54	7.13	0.01	129
IS11	23.54	13.27	0.01	138
IS13	26.83	11.94	0.06	140
IS15	28.94	8.97	0.06	148
IS16	34.12	3.80	0.01	115
IS17	34.65	5.47	0.01	141
IS18	32.41	3.29	0.01	167
IS19	36.70	4.11	0.01	148
SN03	1.33	23.58	0.01	108
SN04	2.89	22.06	1.36	105
SN05	1.33	23.29	0.29	108
SN06	2.33	21.34	0.27	105
SN07	3.88	19.94	0.28	101
SN08	6.05	18.30	0.65	95

Table C.2: Same as in Table C.1, except for sites deployed during the field campaign of summer 2007.

Site	**dist (km)**	v **(m/d)**	ϵ_v **(m/d)**	**dir (degrees)**
IS20	2.15	24.42	0.03	106
IS21	2.91	22.95	0.04	102
IS22	2.96	22.45	0.06	101
IS23	3.69	22.05	0.06	101
IS24	6.24	19.25	0.08	95
IS25	8.33	15.60	0.02	109
IS26	12.06	10.13	0.01	133
IS27	18.05	13.14	0.01	156
IS28	18.57	13.02	0.12	156
IS29	19.38	12.68	0.02	156
IS30	21.59	12.86	0.01	139
IS31	23.74	12.73	0.05	138
IS35	4.13	23.32	0.05	99
IS36	5.01	21.86	0.04	98
IS38	5.39	22.00	0.05	95
IS39	5.88	21.55	0.05	95

Table C.3: Same as in Table C.1, except for sites deployed during the field campaign of summer 2008.

Site	dist (km)	v (m/d)	ϵ_v (m/d)	dir (degrees)
IS40	2.78	19.97	0.01	103
IS41	3.55	18.66	0.08	101
IS42	3.90	18.50	0.08	97
IS43	5.15	18.10	0.01	96
IS44	8.49	13.27	0.12	111
IS45	12.46	8.61	0.10	136
IS46	6.00	16.36	0.03	95
IS47	6.10	17.74	0.13	93
IS48	14.48	8.39	0.01	91
IS49	4.85	13.84	0.03	88
IS50	18.39	12.80	0.02	155
IS51	18.95	12.10	0.12	154
IS53	23.62	12.71	0.01	138
IS54	29.90	7.93	0.03	138
IS55	37.27	3.97	0.14	145
IS56	2.78	17.00	0.05	101
IS57	8.69	11.54	0.16	107
IS58	13.57	10.58	0.16	117
IS59	21.27	6.63	0.01	74
IS60	10.44	12.13	0.16	130
IS61	16.17	13.00	0.01	164
IS62	21.20	12.44	0.18	145

Appendix D

Analysis of ocean tides modulation of glacier flow

D.1 F-test

The χ^2 per degree of freedom, χ^2_ν, of the fit to observations $y_1, ..., y_N$ by a model with M parameters is given by

$$\chi^2_\nu = \frac{1}{\nu} \sum_i^N \frac{1}{\sigma_i^2} (y_i - \widehat{y})^2, \tag{D.1}$$

where σ_i are the observation errors, ν is the number of degrees of freedom $\nu = N - M$, and $\widehat{y}$ is the modeled response.

Then, given two different models fitted to the same set of observations, with number of parameters M_1 and M_2, where $M_2 > M_1$, and degrees of freedom ν_1 and ν_2, respectively, the problem of determining which model describes the data better can be approached as a statistical hypothesis test between them, where the appropriate statistic is an F statistic, or F-test described as (e.g., Bevington, 1969),

$$\widehat{F} = \frac{\chi^2_{\nu,1}}{\chi^2_{\nu,2}}. \tag{D.2}$$

Under the null hypothesis here represented by the simpler model (i.e., the model with less number of parameters, or M_1), the statistic $\widehat{F}$ is F distributed with ν_1 and ν_2 degrees of freedom. Since $\widehat{F}$ is the ratio of two random variables, each being χ^2_ν distributed, a large difference between them would lead to a large value of $\widehat{F}$ and indicate that the null hypothesis can be rejected. We define F_{95} as the F value corresponding to degrees of freedom ν_1 and ν_2 for which the probability (given by the F-distribution) of getting an F larger or equal to F_{95} by chance is 5%. Then, if the F-test yields that $\widehat{F} > F_{95}$, the more complex model, corresponding to ν_2 degrees of freedom, is needed to explain the data. Otherwise, both models fit the data well and the more complex model is not warranted.

We also use the F-test to estimate the error of the time delay of the tidal response. The limits of the error bar for the time delay are the time-delay estimates corresponding to $F_{95} \times \chi^2_\nu$, that is the maximum χ^2_ν for which the more complex model is warranted (at 95% confidence level).

D.2 Degree of correlation of the GPS data

The parameters estimated in the GPS tidal analysis are scaled by the χ^2_ν as indicated below:

$$\widetilde{\epsilon} = \epsilon \sqrt{\chi^2_\nu \, DOC}, \tag{D.3}$$

where ϵ is the estimated error, $\widetilde{\epsilon}$ is the scaled error, and DOC is the degree of correlation of the observations fitted by the model.

In general, the tidal fits are performed to timeseries which are normally one UT day in duration. Since in our processing method we estimate the position of the sites every 15 seconds, the number of degrees of freedom is ν ~5760.

However, the data has some degree of autocorrelation. One can define the DOC as the number of epochs in the timeseries that are autocorrelated to 50%. This can be estimated by performing an autocorrelation of a timeseries, the width of the peak centered on zero-delay at an autocorrelation of 0.5 will be the degree of autocorrelation. Figure D.1 shows an example of an autocorrelation test for a timeseries of an ice site at Helheim Glacier. We estimate the width of the central peak to be ~50–100 epochs, which corresponds to ~12–24 min. Therefore, based on this autocorrelation pattern, for the data collected at Helheim Glacier we estimate the degree of correlation to be 100.

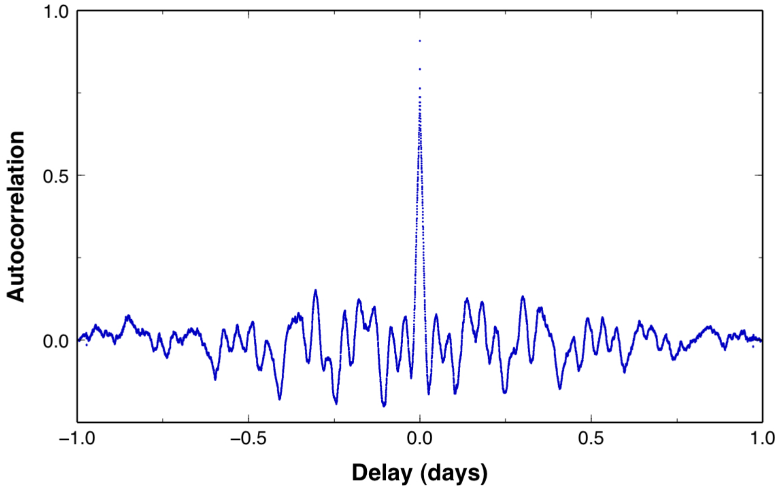

Figure D.1: Autocorrelation as a function of time delay for site IS07 and day 206 in 2006.

Appendix E

Theoretical ocean-tide model error analysis

In order to evaluate the sum in Equation 4.6 we compute the product

$$\begin{aligned}
\big[T(t_0+t')\big]^2 &= \sum_{i,k} b_i b_k \cos(2\pi n_i f_i (t_0+t') + \phi_i)\cos(2\pi n_k f_k (t_0+t') + \phi_k) \\
= \sum_{i,k} b_i b_k &\big[\cos(2\pi n_i f_i t' + \phi_i)\cos(2\pi n_i f_i t_0) - \sin(2\pi n_i f_i t' + \phi_i)\sin(2\pi n_i f_i t_0)\big] \\
&\times \big[\cos(2\pi n_k f_k t' + \phi_k)\cos(2\pi n_k f_k t_0) - \sin(2\pi n_k f_k t' + \phi_k)\sin(2\pi n_k f_k t_0)\big] \\
&= \sum_{i,k} b_i b_k \,[\; C_i C_k \cos(2\pi n_i f_i t' + \phi_i)\cos(2\pi n_k f_k t' + \phi_k) \\
&\quad - C_i S_k \cos(2\pi n_i f_i t' + \phi_i)\sin(2\pi n_k f_k t' + \phi_k) \\
&\quad - S_i C_k \sin(2\pi n_i f_i t' + \phi_i)\cos(2\pi n_k f_k t' + \phi_k) \\
&\quad + S_i S_k \sin(2\pi n_i f_i t' + \phi_i)\sin(2\pi n_k f_k t' + \phi_k)\;]
\end{aligned} \tag{E.1}$$

where we have defined $C_i = \cos(2\pi n_i f_i t_0)$ and $S_i = \sin(2\pi n_i f_i t_0)$. We make the approximation that $f_i t' \approx f_o t'$ where f_o is 1 cicle per sidereal day. The integration in Equation 4.6 yields that terms with $n_i \neq n_k$ vanish, resulting in

$$\begin{aligned}
H^T H = \frac{1}{2\Delta t} \sum_{i,k} b_i b_k \delta_{n_i,n_k} \,[\; & C_i C_k \cos\Delta\phi_{i,k} + C_i S_k \sin\Delta\phi_{i,k} \\
& - S_i C_k \sin\Delta\phi_{i,k} + S_i S_k \cos\Delta\phi_{i,k}\;]
\end{aligned} \tag{E.2}$$

where $\Delta\phi_{i,k} = \phi_i - \phi_k$. Combining trigonometric terms in Equation E.2 the integration in Equation 4.6 finally yields

$$H^T H = \frac{1}{2\Delta t} \sum_{i,k} b_i b_k \delta_{n_i,n_k} \cos\left[2\pi n_i (f_i - f_k) t_0 + (\phi_i - \phi_k)\right]. \tag{E.3}$$

Similarly, using Equation 4.5, the sum in Equation 4.7 is given by

$$\begin{aligned} T(t_0+t')\,\Delta T(t_0+t') &= \delta b_q\, \cos(2\pi n_q f_q(t_0+t')+\phi_q) \sum_i b_i \cos(2\pi n_i f_i(t_0+t')+\phi_i) \\ &= \delta b_q \sum_i b_i \left[C_q \cos(2\pi n_q f_q t'+\phi_q) + S_q \sin(2\pi n_q f_q t'+\phi_q)\right] \\ &\qquad \times \left[C_i \cos(2\pi n_i f_i t'+\phi_i) + S_i \sin(2\pi n_i f_i t'+\phi_i)\right], \end{aligned} \tag{E.4}$$

which, with similar algebra as that of the used above, yields

$$H^T \Delta T = \frac{1}{2\Delta t}\delta b_q \sum_i b_i \delta_{n_i,n_q} \cos\left[2\pi n_i(f_i - f_q)t_0 + (\phi_i - \phi_q)\right]. \tag{E.5}$$

Appendix F

List of papers to scientific journals and major meetings by the author

F.1 Published (peer-reviewed)

Andersen, M. L., Larsen, T., Nettles, M., Elosegui, P., van As, D., Hamilton, G. S., Stearns, L. A., Davis, J. L., Ahlstrøm, A. P., de Juan, J., Ekström, G., Stenseng, L., Khan, S. A., Forsberg, R. & Dahl-Jensen, D., 2010. Spatial and temporal melt variability at Helheim Glacier, East Greenland, and its effect on ice dynamics. *Journal of Geophysical Research*, **115**, F04041

de Juan, J., Elósegui, P., Nettles, M., Larsen, T. B., Davis, J. L., Hamilton, G. S., Stearns, L. A., Andersen, M. L., Ekström, G., Ahlstrøm, A. P., Stenseng, L., Khan, S. A. & Forsberg, R., 2010b. Sudden increase in tidal response linked to calving and acceleration at a large Greenland outlet glacier. *Geophysical Research Letters*, **37**, L12501

Nettles, M., Larsen, T. B., Elósegui, P., Hamilton, G. S., Stearns, L. A., Ahlstrøm, A. P., Davis, J. L., Andersen, M. L., de Juan, J., Khan, S. A., Stenseng, L., Ekström, G. & Forsberg, R., 2008. Step-wise changes in glacier flow speed coincide with calving and glacial earthquakes at Helheim Glacier, Greenland. *Geophysical Research Letters*, **35**, L24503

F.2 In preparation

de Juan, J., Elósegui, P., Nettles, M., Davis, J. L., Larsen, T. B., Hamilton, G. S. & Stearns, L. A., in preparation(a). Ocean tides modulation of flow at Helheim Glacier, East Greenland, using high-rate GPS. *Journal of Geophysical Research*

de Juan, J., Elósegui, P., Nettles, M., Davis, J. L., Larsen, T. B., Hamilton, G. S. & Stearns, L. A., in preparation(b). Flow variations at Helheim Glacier induced by the drainage of supraglacial lakes. *Journal of Glaciology*

F.3 Contributions to major international meetings

de Juan, J., Elosegui, P., Nettles, M., Davis, J. L., Larsen, T., Hamilton, G. S. & Stearns, L. A., 2010a. GPS measurements of flow variations at a large Greenland outlet glacier due to ocean tidal forcing. *AGU Fall Meeting Abstracts*, A516

de Juan, J., Elosegui, P., Nettles, M., Davis, J. L., Larsen, T., Ahlstrøm, A., Andersen, M. L., Ekstrom, G., Forsberg, R., Hamilton, G. S., Khan, S. A., Schild, K. M., Stearns, L. A. & Stenseng, L., 2009a. Ocean tides modulation of flow at Helheim Glacier, East Greenland, observed using GPS. *AGU Fall Meeting Abstracts*, 90 (52)

de Juan, J., Elosegui, P., Nettles, M., Davis, J. L., Larsen, T. B., Ahlstrom, A. P., Andersen, M. L., Ekstrom, G., Forsberg, R., Hamilton, G. S., Khan, S. A., Schild, K., Stearns, L. A. & Stenseng, L., 2009b. Flow modulation by ocean tides at Helheim Glacier, East Greenland, observed using GPS. *EGU General Assembly 2009*, **11**, EGU2009–8329–3

de Juan, J., Elosegui, P., Davis, J. L., Nettles, M. & Larsen, 2008a. Analysis of ionospheric errors and correction techniques in high-rate GPS glaciology. *EGU General Assembly 2008*, **10**, EGU2008–A–04190

de Juan, J., Elosegui, P., Nettles, M., Larsen, T. B., Davis, J. L., Ahlstrøm, A. P., Andersen, M. L., Ekström, G., Forsberg, R., Hamilton, G. S., Khan, S. A., Schild, K. M., Stearns, L. A. & Stenseng, L., 2008b. Sub-daily glacier flow variations at Helheim Glacier, East Greenland, using GPS. *AGU Fall Meeting Abstracts*, 89 (53)

Appendix G

Resum de la tesi

Aquesta tesi presenta un estudi de l'aplicació de tècniques GPS (Sistema de posicionament global) per a l'estudi de la dinàmica d'una de les glaceres que flueix més ràpid del món, la glacera Helheim, localitzada a la costa sud-est de Groenlàndia. L'alt mostreig i l'alta precisió de les estimacions de posició GPS ens permet estudiar en detall la dinàmica d'aquestes glaceres en una ampli ventall d'escales temporals, des de interanual a subdiària.

Les principals glaceres de base marina de Groenlàndia han duplicat la seva contribució al nivell del mar durant la darrera dècada (Rignot & Kanagaratnam, 2006; Velicogna, 2009). La velocitat de flux d'aquestes glaceres s'ha incrementat, seguit del seu aprimament, retrocés del termini i la pèrdua de les seves llengües flotants (e.g., Joughin et al., 2004; Howat et al., 2005; Luckman et al., 2006; Stearns & Hamilton, 2007). L'informe de l'IPCC del 2007 (Lemke et al., 2007) va assenyalar que els models actuals per a les prediccions de la futura pujada del nivell del mar no tenen en compte els ràpids canvis dinàmics dels corrents de gel i les glaceres. Les observacions de què aquestes glaceres poden experimentar ràpids canvis en la velocitat impliquen que les prediccions d'augment del nivell del mar realitzades pels models actuals estan subestimades, i posa de relleu la necessitat de comprendre els mecanismes pel ràpid flux d'aquestes glaceres en un clima canviant. El vessament d'aigua de desglaç des de la superfície a la base de les glaceres ha demostrat tenir una influència molt important en la velocitat del flux i en la descàrrega de gel de les glaceres, mitjançant l'augment de la pressió de l'aigua basal i la lubricació de la capa entre el gel i la base de la glacera (Zwally et al., 2002; Das et al., 2008; Schoof, 2010). Les glaceres de base marina també han demostrat ser molt sensibles a canvis en el seu termini (on es produeix el despreniment d'icebergs, anomenat "calving front"), que poden iniciar fases dramàtiques d'acceleració, aprimament, i retrocés (Howat et al., 2005; Stearns & Hamilton, 2007; Amundson et al., 2008; Nettles et al., 2008; Nick et al., 2009). Observacions recents indiquen que les glaceres situades al sud-est i oest de Groenlàndia són molt sensibles a les condicions de l'oceà (Holland et al., 2008; Murray et al., 2010), suggerint que la temperatura de la superfície del mar és un factor essencial en la regulació de la dinàmica d'aquests glaceres.

Les dades de la xarxa sísmica mundial (GSN) van revelar l'existència d'un tipus de terratrèmols no-tectònics i telesísmics que es localitzava sota de grans capes de glaceres de base marina a Groenlàndia, l'Antàrtida i Alaska (Ekström et al., 2003, 2006; Tsai & Ekström, 2007). Els anomenats "terratrèmols glacials" es caracteritzen per tenir una alta magnitud sísmica (entre 4.6 i 5.1) i, a diferència dels terratrèmols tectònics, per l'emissió d'ones de llarg període (35 a 150 s). Durant el període comprès entre 1993 i 2005, 184 terratrèmols glacials van ser detectats a Groenlàndia. El nombre d'esdeveniments per any va començar a augmentar al 2002. D'altra banda, hi ha una forta estacionalitat en la taxa d'ocurrència d'aquests esdeveniments, que són més freqüents durant els últims mesos d'estiu. L'estacionalitat i la freqüència cada vegada major dels terratrèmols glacials i la seva coincidència amb els canvis en el comportament de les glaceres de Groenlàndia, suggeria una connexió entre aquests dos mecanismes (Ekström et al., 2006). Posteriorment s'ha demostrat que aquests terratrèmols estan temporalment vinculats al despreniment o "calving" de grans icebergs al termini de grans glaceres de base marina que, al ser molt inestables, bolquen dintre de l'aigua, (Joughin et al., 2008b; Nettles et al., 2008; Amundson et al., 2008), suggerint que els terratrèmols estan generats pel procés de "calving".

La glacera Helheim, una de les glaceres més grans de Groenlàndia, que es troba a la costa sudoriental, representa al voltant del 20% del cabal total de descàrrega de l'est de Groenlàndia (Rignot & Kanagaratnam, 2006). La glacera, que flueix a velocitats d'alguns metres per dia, ha experimentat canvis significatius durant l'última dècada. Ha passat per períodes de important retrocés, acceleració i aprimament (Howat et al., 2005; Stearns & Hamilton, 2007), alhora que canvis similars es produïen en altres glaceres del sud-est de Groenlàndia. El balanç de massa de la glacera Helheim es va reduir de positiu ($\sim$4 km^3 gel/any) durant el període 1996-2000 a negatiu ($\sim$-12 km^3 gel/any) en el 2005, el que va representar el 5% de la pèrdua de massa total de Groenlàndia durant aquell any (Rignot & Kanagaratnam, 2006). La glacera va accelerar en el seu termini de 22 m/d fins a 30 m/d entre 2000 i 2005 (Howat et al., 2005). Durant aquest mateix període, la posició del calving front va retrocedir uns 7.5 km.

L'estudi dels terratrèmols glacials i de la seva relació amb el flux de les glaceres va motivar la consolidació d'un projecte multidisciplinari per estudiar el comportament de les grans glaceres de base marina de Groenlàndia. La glacera Helheim va ser seleccionada per dur-hi a terme una sèrie de campanyes d'observació per diverses raons. Primer de tot, té una història recent de canvis ràpids en la seva dinàmica, però, a diferència de la glacera Jakobshavn Isbræ, la dinàmica de Helheim no s'havia estudiat abans amb observacions in-situ. També, aquesta glaciera va tenir una alta productivitat de terratrèmols glacials en el període 1996-2005 (12 sismes van ser detectats a Helheim el 2005). Finalment, és logísticament menys complexa que altres glaceres. Per poder analitzar la dinàmica de la glacera Helheim en alt detall, incloent-hi els terratrèmols recentment descoberts, utilitzem dades GPS recollides en la superfície de la glacera Helheim durant els estius àrtics de 2006–2008. El projecte de Helheim demostra la viabilitat d'obtenir mesures de posicionament de forma continua i amb alt mostreig en la superfície de glaceres altament dinàmiques. Aquest mètode permet caracteritzar la deformació de la superfície de la glacera amb alta precisió (al nivell de centímetres) i amb una resolució temporal més gran que amb qualsevol altra tècnica utilitzada en glaciologia, i per tant, permet estudiar la dinàmica de les glaceres en escales temporals no explorades fins a l'actualitat.

En aquesta tesi s'ha dut a terme el processament de les dades GPS d'alta precisió adquirides durant els estius de 2006–2008 en diversos llocs de la superfície de la glacera Helheim. El processament de les dades GPS s'ha fet utilitzant el software TRACK, el mòdul de processament cinemàtic de GAMIT (Chen, 1998). Hem detallat el mètode de processament utilitzat, i hem avaluat la precisió de les estimacions de posició obtingudes amb aquestes tècniques. També hem analitzat les diverses fonts d'errors que afecten les nostres solucions, com ara els errors deguts a la ionosfera, els errors deguts al sistema de referència, i errors sistemàtics associats a la tècnica de processament, a la qualitat de les dades, i al fenòmen de "multipath".

Hem estimat que les solucions de posició d'alt mostreig d'estacions a la superfície de la glacera, fluint a velocitats de varis metres per dia i processades respecte a una estació de referència estàtica als marges de roca de la glacera, tenen una precisió de ∼1–2 cm a la component horitzontal, i ∼2–5 cm en la component vertical. També hem demostrat que la qualitat de les solucions depèn en gran mesura de la capacitat del software de processament de resoldre i fixar totes les ambigüitats de fase a un valor enter, el que depèn en gran mesura de la qualitat de les dades, especialment prop dels límits entre dies. Les estimacions de posició d'una estació i dia específics mostren una variació de baixa amplitud i alta freqüència, que es repeteix en dies consecutius, i que suggereix que una part substancial dels errors sistemàtics en les solucions es deuen al "multipath".

Hem utilitzat l'ampli conjunt de dades GPS recollit a la glacera Helheim per caracteritzar l'estat general del seu flux, investigant la cinemàtica mitjana de la glacera durant els estius de 2006–2008, des d'escales temporals interanuals a diàries. Hem caracteritzat la variació espacial del flux mitjà en la regió on vam instal·lar la xarxa GPS i hem analitzat la seva consistència d'any en any. També hem estudiat, en cada un dels estius, la dependència temporal de la velocitat mitjana diària en cada una de les estacions, i la seva coherència espacial al llarg de la glacera. Hem analitzat els resultats en relació a les observacions d'imatges per satèl·lit d'anys anteriors i del mateix període de temps.

L'anàlisi de les solucions de posició revelen que durant els estius de 2006–2008 la velocitat de la glacera va variar entre ∼24 m/d, prop de la part terminal de la glacera fins a ∼4 m/d a una posició ∼37 km glacera amunt. La Figura G.1 mostra la velocitat horitzontal mitjana durant els estius de 2006–2008 per a les estacions GPS instal·lades a la glacera Helheim. Cadascuna de les fletxes en aquesta figura mostra la velocitat mitjana horitzontal i la direcció de flux de cada una de les estacions per al període de temps durant el qual van romandre a la glacera. En general, la velocitat del flux augmenta gradualment des de la part alta de la glacera fins al "calving front", de manera que un flux extensiu, amb alts valors positius de velocitat de deformació longitudinal, domina sobre la major part de la glacera. No obstant, en la zona on el flux de la glacera canvia de direcció de sud-est cap a est, hi ha una regió de flux compressiu. Les estacions ubicades a pocs quilòmetres de la línia central de flux tenen velocitats similars a les situades a la mateixa distància des del "calving front", però al centre. No obstant, les velocitats disminueixen considerablement prop dels marges, indicant que els estressos de fricció laterals són elevats.

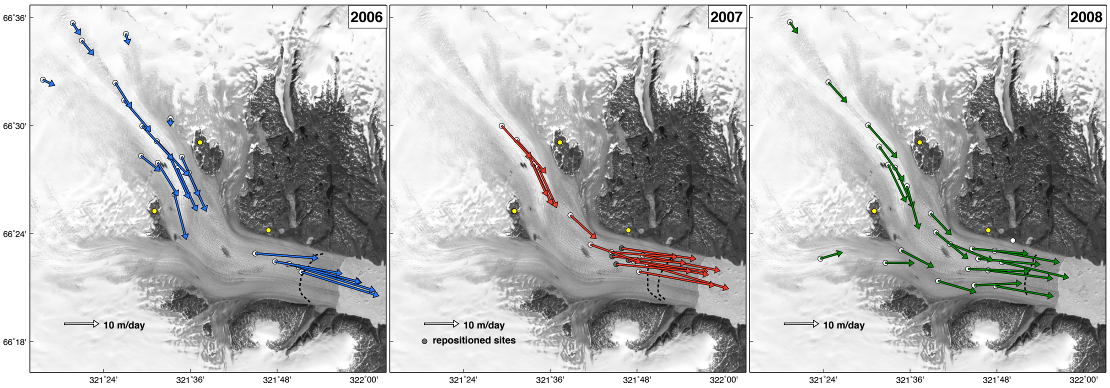

Figure G.1: Velocitat horizontal mitjana de les estacions en gel a la glacera Helheim durant l'estiu de (esquerra) 2006, (enmig) 2007 i (dreta) 2008. Els punts indiquen la posició de instal·lació de (blanc) estacions en gel, i (groc) estacions estàtiques de referència. La direcció de les fletxes indica la mitjana de la direcció de flux, i la mitjana de la velocitat horizontal ve indicada per la longitud de les fletxes. Per referència, veure una flexta a la base de la figura, amb una escala de 10 m/d. Línies discontínues mostren la posició del "calving front" en els dies d'any 242 en el 2006; (línia de més a l'est) 185 i (línia de més a l'oest) 236 en el 2007; i 213 en el 2008.

La velocitat mitjana estimada de la glacera Helheim durant els estius de 2006–2008 és ∼20% menor que la del any 2005, similar a les estimacions pel 2003, i superior a la de l'any 2000. Les variacions interanuals de la velocitat durant els estius de 2006–2008, quan la velocitat de la glacera es va mantenir aproximadament constant, van ser molt menys importants que les dramàtiques variacions documentades durant el període 2002–2006 (Howat et al., 2007). La desacceleració observada a Helheim durant aquest període és consistent amb les observacions realitzades en altres glaceres al sud-est de Groenlàndia, i sembla haver estat regulada per la temperatura de la superfície del mar (Murray et al., 2010). No obstant, la glacera va ser més activa durant l'estiu del 2007, quan els últims ∼12 km de la glacera van fluir lleugerament més ràpid que en el 2006 i 2008. La velocitat va ser també més variant durant el 2007, les variacions més nombroses i de més amplitud en la velocitat van tenir lloc durant aquest estiu. La Figura G.2 mostra la velocitat horitzontal diària de totes les estacions en cadascuna de les campanyes d'estiu del 2006–2008. La reactivació de Helheim durant l'estiu de 2007, que no es va observar en altres glaceres, també coincideix amb una anomalia en la temperatura de la superfície de l'oceà entre Groenlàndia i Islàndia el juliol de 2007 (Murray et al., 2010), el que suggereix que el règim de flux de la glacera Helheim és molt sensible a les condicions de l'oceà (Straneo et al., 2010). En general, i especialment en l'estiu de 2007, la velocitat de la glacera augmenta gradualment en el transcurs de l'estiu, degut probablament en gran mesura a forçaments externs, com ara canvis en les condicions de contorn al "calving front" o a la base de la glacera, o bé canvis en la temperatura de l'atmosfera o l'oceà, però en part

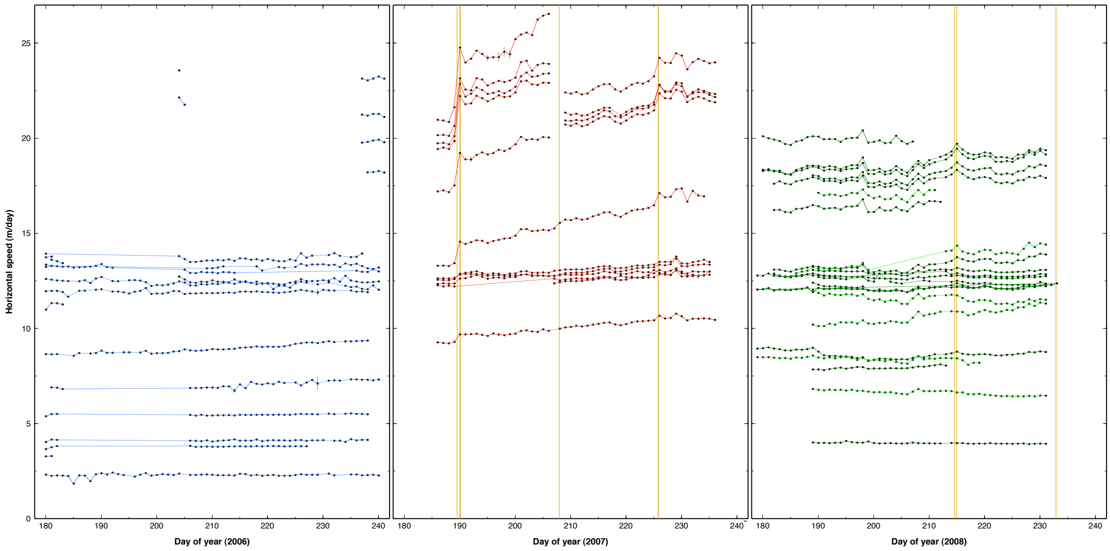

Figure G.2: Velocitat horizontal mitjana diària de les estacions en gel operades a la glacera Helheim durant les campanyes d'estiu de (esquerra) 2006, (enmig) 2007, i (dreta) 2008. Les estimacions de velocitat corresponents a cada estació estan connectades amb una línia per claretat, una línia continua connecta dies consecutius, s'utilitza una línia discontinua quan hi ha observacions que falten o la qualitat de les dades no permetia estimar la velocitat amb confiança suficient. En la majoria dels casos les barres d'error són més petites que el tamany dels símbols. Barres grogues indiquen el temps de terratrèmols glacials detectats telesísmicament.

també a causa de l'advecció de les estacions a regions de règim amb flux més ràpid.

L'alta precisió i l'alt mostreig de les observacions GPS recollides a la glacera Helheim ens permet estudiar en detall les desviacions sub-diàries respecte al flux mitjà i la seva variació espai-temporal. En aquest sentit, una de les parts principals del treball presentat en aquesta tesi es centra en la caracterització de la resposta del flux de la glacera a les marees oceàniques. L'estudi dels efectes de pertorbacions conegudes, com les marees oceàniques, sobre el flux de les glaceres poden proporcionar informació valuosa sobre la naturalesa de la resposta dinàmica i sensibilitat de les glaceres a canvis en les seves condicions de contorn.

En les estacions situades en la part baixa de la glacera, ∼12–16 km darrera del "calving front" s'observen variacions sinussoïdals semi-diürnes en els residus de posició al flux mitjà, i també durant alguns períodes, en la component vertical de moviment (veure Figura G.3). Aquestes variacions semi-diürnes estan correlacionades amb la marea oceànica al fiord Sermilik, però estan retardades respecte a la mateixa. Interpretem aquestes variacions com la resposta de la glacera al forçament de les marees oceàniques. Hem estudiat la resposta de la glacera a les marees a escales temporals que van des de diàries, a mensuals, a interanuals. Utilitzem la marea oceànica observada i modelada en el fiord on descarrega els icebergs la glacera Helheim, el fiord Sermilik, per a realitzar un ajust a les senyals de marees observades en les components horitzontals i verticals de sèries temporals diàries de posició. Estudiem la variació espacial i temporal dels paràmetres que caracteritzen la resposta de la glacera a les marees. Comparem les nostres observacions amb les prediccions de diversos models que estudien les variacions de flux i la flexió de les glaceres en resposta a les marees.

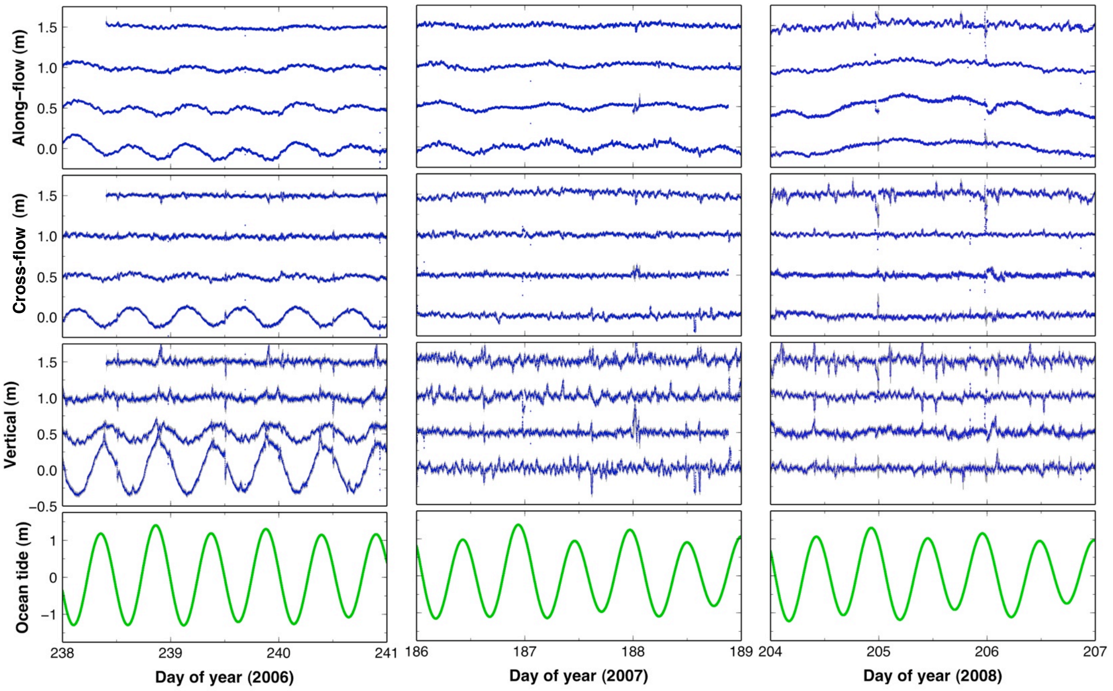

Figure G.3: Punts blaus: Exemple de posició d'estacions GPS relativa al flux mitjà en (dalt) la direcció de flux, (enmig) la perpendicular a la direcció de flux, i (sota) la direcció vertical, estimada cada 15 segons. Es mostren les quatre estacions localitzades al centre de la glacera i més properes al "calving front", durant un període de tres dies en (esquerra) el 2006, (enmig) 2007, i (dreta) 2008. Les sèries temporals estan decalades en cada panell per claretat, amb les estacions mostrades des de més propera al "calving front" (sota), fins a la més llunyana (dalt). Línia verda: Marea oceànica predita al fiord Sermilik amb el model AOTIM-5 (Padman & Erofeeva, 2004).

Durant els estius de 2006–2008, les estacions ubicades en la part més baixa de la glacera, als darrers ∼16 km, les desviacions respecte del desplaçament mitjà en la component del moviment al llarg de flux estan dominades per variacions de marea que estan en contrafase amb la marea oceànica. La posició de la glacera avança en marea baixa i es retarda en marea alta respecte a la mitjana del flux. Aquestes variacions són com a màxim de ∼10 cm d'amplitud, i les interpretem com la resposta a les variacions en la pressió hidrostàtica quan la marea puja i baixa (e.g., Anandakrishnan & Alley, 1997; Gudmundsson, 2007). La comparació de les variacions observades en velocitat i les variacions esperades degut a les variacions en l'esforç conductor ("driving stress") (Howat et al., 2005; Gudmundsson, 2007) en general suporten aquesta hipòtesi.

Al 2006, els ∼4–5 km inferiors de la glacera presenten una resposta vertical a les marees, el que indica que aquesta regió de la glacera estava en flotació durant aquest període. La resposta té una amplitud del ∼30–40% de l'amplitud total de la marea en l'estació situada més a prop del “calving front” i s'atenua $\lesssim$6 km darrere del mateix. En general, estacions situades en llocs similars el 2007 i 2008 no mostren una resposta vertical a les marees. No obstant això, el 2007, a l'estació més propera al “calving front” observem la seva transició d'estar a terra ferme a estar en flotació, la qual cosa suggereix que la glacera estava molt a prop de la flotació durant aquest període. Atribuïm el canvi observat en la resposta vertical del 2006 al 2007 a la possibilitat de què la glacera hagués augmentat en grossor. D'altra banda, al 2006 les estacions que presenten resposta vertical a les marees mostren també resposta a les marees en el component perpendicular al flux de la glacera, el que indica que la glacera canviava lleugerament la seva direcció mentre la marea pujava i baixava, i doncs suggerint un vincle entre el flux vertical i el flux perpendicual.

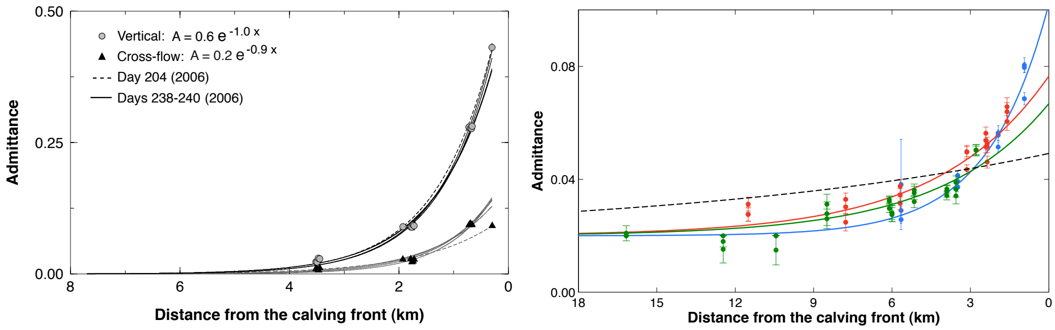

Figure G.4: Amplitud de la resposta de la glacera a les marees en funció de la distància al “calving front” en les components (esquerra) vertical (cercles) i perpendicular a la direcció del flux (triangles) en l'estiu del 2006, i (dreta) en la direcció del flux en els estius de 2006 (blau), 2007 (vermell) i 2008 (verd). Les línies són els millor ajusts (en mínims quadrats) a les dades utilitzant una funció exponencial.

L'anàlisi dut a terme mostra que la resposta de la glacera a les marees està retardada respecte a elles entre 1 i 2 h. La resposta es produïa ∼1 h abans en el 2006, quan la glacera estava en flotació, suggerint que la reducció de la fricció en la base durant aquest període va propiciar que la glacera respongués més ràpidament al forçament de les marees. L'amplitud de la resposta decau exponencialment amb la distància des del “calving front” en les tres components del flux (veure Figura G.4). A més, la resposta a les marees en la component al llarg de flux és molt variable en el temps. Presenta una variació gradual amb una periodicitat d'aproximadament 15 dies, que suggereix una resposta no lineal de la glacera a les marees oceàniques (veure Figura G.5). A més, s'observen canvis abruptes en la resposta de la glacera a la marea coincidents amb el despreniment d'icebergs que bolquen i generen terratrèmols glacials (de Juan et al., 2010b).

Les desviacions sub-diàries respecte el flux mitjà inclouen, especialment durant el 2007, canvis en la velocitat que es produeixen de manera sobtada. En general, aquestes

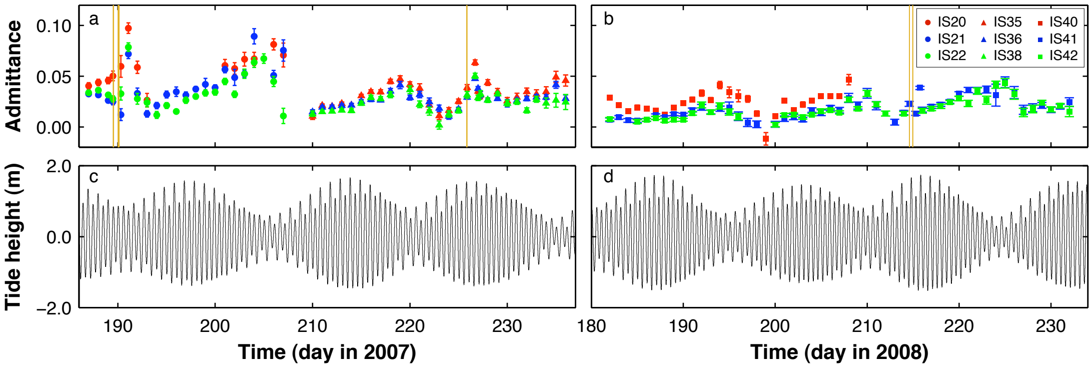

Figure G.5: Dalt: Amplitud de la resposta de la glacera a la marea oceànica en la direcció del flux, per les tres estacions GPS més properes al "calving front" en el (esquerra) 2007 i (dreta) 2008, línies grogues indiquen el temps de terratrèmols glacials. Sota: Marea modelada al fiord Sermilik.

variacions en la velocitat succeeixen de forma coherent al llarg de la glacera, i la seva magnitud disminueix glacera amunt, quan més enfora es troben les estacions del "calving front". Algunes de les variacions en velocitat estan relacionades temporalment amb la producció de terratrèmols glacials (Nettles et al., 2008). Aquest tipus de terratrèmols són generats per esdeveniments glacials en els que es desprenen icebergs alts i inestables que bolquen contra el front de la glacera (Tsai et al., 2008; Nettles & Ekström, 2010). En la tesi presentem les observacions GPS de la deformació de la glacera associades amb diversos terratrèmols glacials que es van produir durant els estius de 2006–2008. Caracteritzem la resposta dinàmica de la glacera associada als terratrèmols, que consisteix en un augment sobtat de velocitat quasi instantani. També s'analitza en detall la resposta de la glacera a les marees al voltant dels temps dels terratrèmols glacials. Descrivim i estudiem l'augment sobtat i transitori en la resposta de la glacera a les marees en associació amb aquests esdeveniments i els analitzem en relació al canvi en el comportament del flux de la glacera.

En l'estiu de 2006, quan la glacera Helheim havia desenvolupat una curta llengua flotant, el retrocés de la glacera es produïa mitjançant el despreniment d'icebergs tabulars, els quals són estables i per tant no causen terratrèmols glacials. Al 2007, la glacera tornava a estar recolzada sobre terra, i això va fer possible el despreniment d'icebergs més alts que amples i per tant inestables, i doncs la producció de terratrèmols glacials. Diversos terratrèmols glacials van ocórrer a Helheim durant els estius de 2007 i 2008, centrats en tres períodes de temps diferenciats. Tots ells es manifesten a la superfície de la glacera com un augment sobtat del velocitat de flux (Nettles et al., 2008), probablement causats per la reducció en les forces de fricció al "calving front" (e.g., Howat et al., 2005; Nick et al., 2009). A la Figura G.6 es mostra un exemple de l'augment de la velocitat de la glacera Helheim associat a un terratrèmol glacial. La magnitud del canvi en la velocitat, que es dóna coherentment al llarg de la glacera, disminueix amb la distància

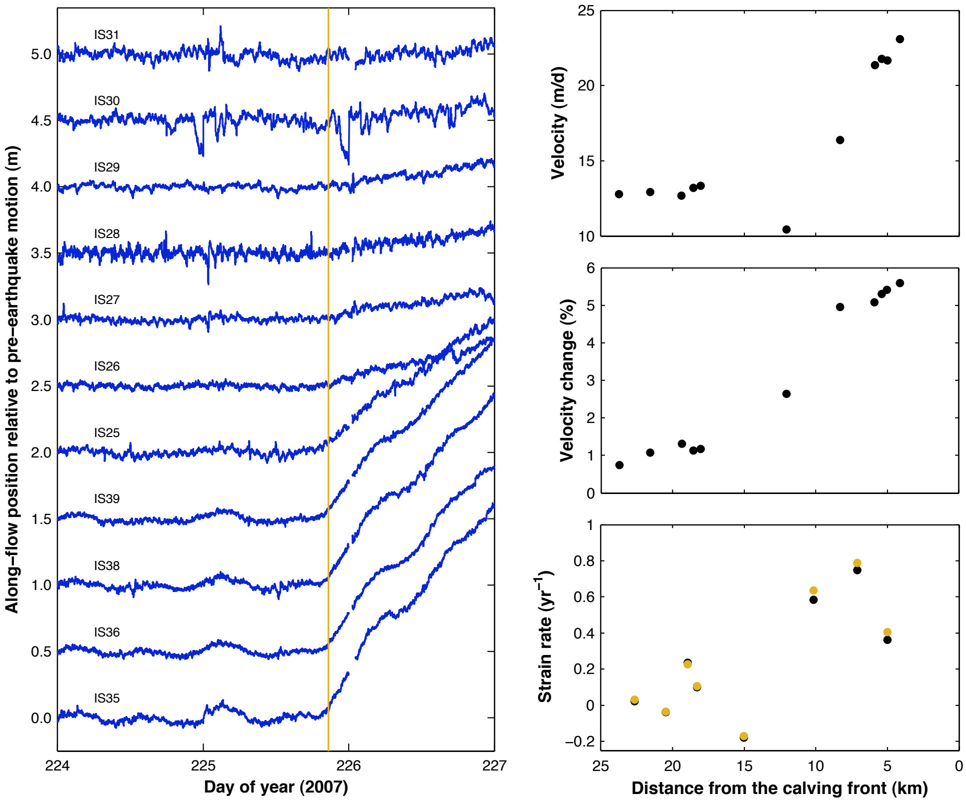

Figure G.6: Esquerra: Estimacions de posició en la direcció de flux relatius a la velocitat d'abans de l'acceleració sobtada i terratrèmol glacial per totes les estacions i durant tres dies en el 2007, dies 224–227. Les sèries temporals estan decalades per 0.5 m per cada estació per claretat. Les estacions es mostren, de baix a dalt, des de més propera a més llunyana del "calving front". La línia groga indica el temps del terratrèmol glacial. Dreta: (Dalt) Velocitat horizontal de les estacions abans del terratrèmol glacial, (enmig) canvi en velocitat relatiu associat amb el terratrèmol glacial, i (sota) velocitat de deformació longitudinal (negre) abans i (groc) després del terratrèmol i despreniment de gel, en funció de la distància de les estacions a la posició del "calving front" en el dia 213 en el 2008.

des del "calving front". Per tant, els terratrèmols glacials també causen canvis sobtats en la velocitat de deformació (strain rate) longitudinal (veure Figura G.6). La velocitat es recupera parcialment després del terratrèmol glacial, però en la majoria dels casos, l'esdeveniment provoca un augment permanent en la velocitat (Nettles et al., 2008).

Com s'ha esmentat anteriorment, la resposta de la glacera a les marees en la component al llarg del flux presenta una variació amb un període de ∼15 dies, en general canviant gradualment (veure Figura G.5). Però, seguit dels terratrèmols glacials i coincidint amb l'augment de la velocitat, l'amplitud de la resposta a la marea augmenta sobtadament per un factor de fins a ∼2.5 (de Juan et al., 2010b). La Figura G.7 mostra l'augment de la resposta a les marees associat als terratrèmols glacials que es van produir

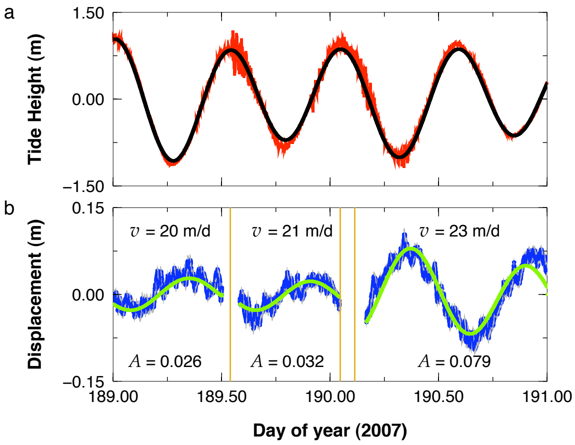

Figure G.7: (a) La línia negra mostra la marea oceànica predita al fiord glacial. La línia vermella mostra la marea observada. (b) El punts blaus mostren la posició horitzontal en la direcció de flux relatiu a la velocitat mitjana v, per tres períodes de temps separats per terratrèmols glacials. La línia verda mostra la funció de marea ajustada als estimats, amb amplitud relativa A. Els RMS (root-mean-square) dels residus a l'ajust és menor que 16 mm per els exemples mostrats. Les línies grogues indiquen el temps dels terratrèmols glacials. Figura de de Juan et al. (2010b).

en els dies 189-190 de l'any 2007. La resposta intensificada a les marees només dura 1–2 dies, en contrast amb la variació de velocitat que només es recupera parcialment aproximadament al mateix temps que es recupera completament la resposta a la marea. A causa de la seva naturalesa transitòria, la pèrdua de gel relacionada amb el terratrèmol glacial és poc probable que sigui la causa de l'augment de la resposta a la marea. En canvi, una disminució temporal en la resistència al flux permetria a la glacera respondre amb major amplitud a la marea. La nostra hipòtesi és que el canvi sobtat en la velocitat de la glacera i en la velocitat de deformació longitudinal, relacionats amb els terratrèmols glacials, poden causar una pertorbació en el sistema de drenatge subglacial, similar a l'observada en les glaceres "surging" (Kamb, 1987). Aquesta perturbació incrementaria la pressió de l'aigua basal, reduiria la fricció en la interfície gel-base, i permetria l'augment observat de la resposta a les marees (de Juan et al., 2010b). Aquestes pertorbacions s'espera que siguin transitòries, amb el restabliment d'un drenatge més eficient una vegada que la velocitat de deformació es redueix.

Finalment, es presenta un estudi preliminar sobre les variacions en la velocitat de la glacera que es produeixen en moments en que no es registren terratrèmols glacials i que presenten un caràcter diferent que no pas les associades amb els terratrèmols. Analitzem alguns d'aquests canvis en la velocitat que tenen característiques que suggereixen que són causades pel desguàs sobtat d'aigua de desglaç. Aquesta aigua s'acumula en llacs que es formen a la superfície de la glacera, i tendeixen a ocupar el mateix lloc cada estiu. Aquests increments de velocitat es produeixen concomitants amb un ascens i descens vertical en les estacions situades a prop dels llacs esmentats, cosa que suggereix que les variacions en

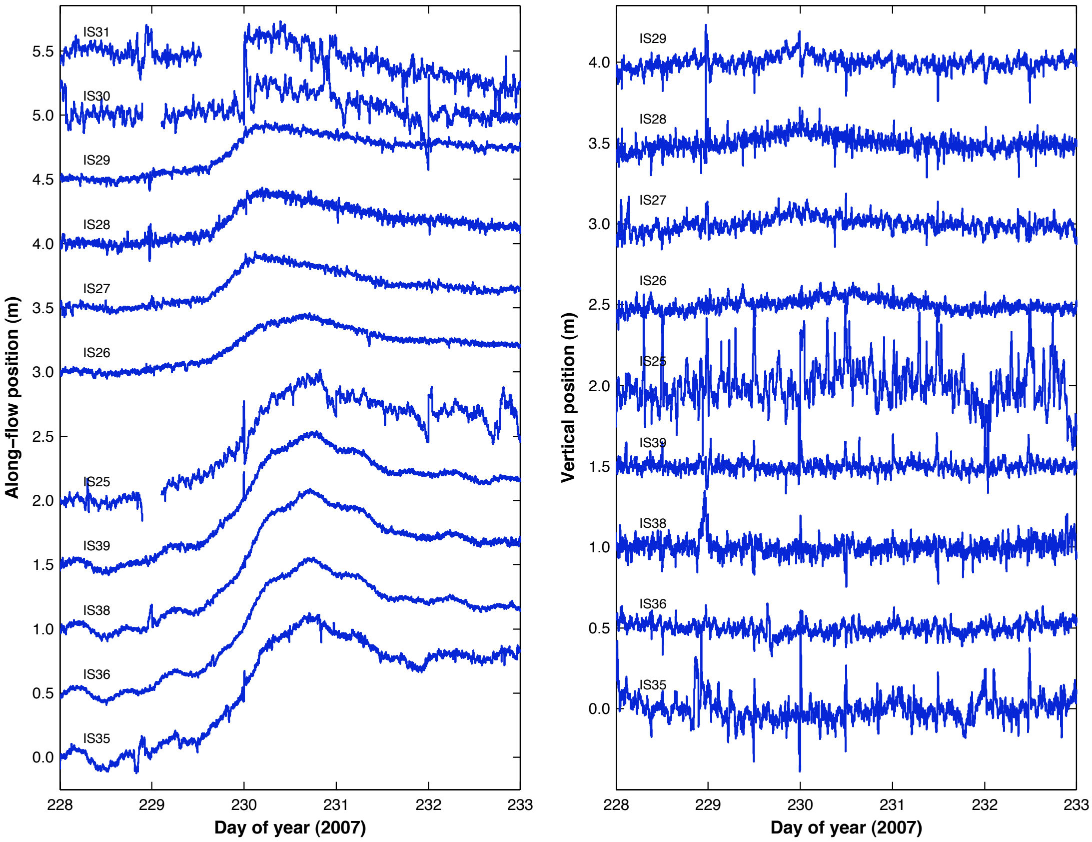

Figure G.8: Posició relativa a la velocitat mitjana en el dia 228 en (esquerra) la direcció del flux i (dreta) direcció vertical per totes les estacions i durant 5 dies en el 2007, dies 228–233. Les sèries temporals estan decalades per 0.5 m per cada estació per claretat. Les estacions es mostren, de baix a dalt, des de més propera a més llunyana del "calving front", en la glacera i el seu tributari.

la velocitat de flux estan relacionades amb episodis d'alta pressió d'aigua en el sistema de drenatge subglacial. D'altra banda, el caràcter de les variacions en la velocitat és molt diferent de l'observat en associació amb els terratrèmols glacials. Les sèries temporals de posició suggereixen que aquests augments en la velocitat s'inicien en la part alta de la glacera o prop de les estacions que mostren el desplaçament vertical. La Figura G.8 mostra la posició en la direcció del flux i la posició vertical de les estacions GPS a Helheim durant un d'aquests esdeveniments. La nostra hipòtesi és que aquests augments en la velocitat de flux de les glaceres estan associats amb el drenatge sobtat d'un llac, el que augmenta la pressió basal de l'aigua, permetent que la glacera s'aixequi i acceleri. Durant el 2008 es va detectar un d'aquests esdeveniments ~1 dia abans d'un gran despreniment de gel i un terratrèmol glacial, el que suggereix que el drenatge dels llacs formats a la superfície de la glacera podrien jugar un paper important en el desencadenament d'alguns dels esdeveniments al "calving front". Imatges del satèl·lit MODIS de l'època d'un d'aquests esdeveniments mostren que el llac està present en les imatges abans de l'esdeveniment, però no en les imatges d'alguns dies després. Al 2009, també vam operar un mareògraf en un dels esmentats llacs, el que va permetre l'estudi de la seva evolució, incloent el seu drenatge complet que es va produir en el transcurs d'un dia.

La majoria de les variacions en la velocitat es produeixen de manera consistent temporal i espacialment al llarg de la longitud de la glacera, el que indica que un canvi en les condicions de contorn, ja sigui localitzat al termini de la glacera o "calving front", com en el cas dels terratrèmols glacials (Nettles et al., 2008), o bé a la base de la glacera i originat en la part alta, com en el drenatge d'un llac, la resposta de la glacera es transmet a través tota la seva extensió. A més, tant les variacions graduals com les variacions sobtades en la resposta a les marees oceàniques, es produeixen també de manera coherent a la regió de la glacera que presenta la resposta a la marea. Aquests resultats demostren que la glacera és capaç de respondre ràpidament i de manera consistent a forces externes, i posa de relleu la necessitat de comprendre el paper que aquests canvis ràpids poden exercir en l'evolució global de la capa de gel en un clima canviant.

Aquesta tesi demostra que les mesures de posició d'alta precisió i d'alt mostreig en la superfície de les glaceres ofereixen informació valuosa sobre el caràcter del flux de la glacera en una ampli ventall d'escales de temps. Aquestes mesures poden ajudar a comprendre les variacions en el flux de les glaceres induïdes per forces petites i constants, com les marees oceàniques, i també pels canvis grans i sobtats en les condicions de contorn, com ara els terratrèmols glacials o esdeveniments relacionats amb el calving front i el drenatge sobtat de grans volums d'aigua de desglaç. La caracterització d'aquestes respostes ajuda a entendre el paper que juguen els forçaments externs en l'acceleració i el retrocés de les glaceres de base marina de Groenlàndia.

Bibliography

Abdalati, W. & Steffen, K., 2001. Greenland ice sheet melt extent: 1979-1999. *Journal of Geophysical Research*, **106**, 33983–33988.

Alley, R. B., Clark, P. U., Huybrechts, P. & Joughin, I., 2005a. Ice-Sheet and Sea-Level Changes. *Science*, **310**, 456–460.

Alley, R. B., Dupont, T. K., Parizek, B. R. & Anandakrishnan, S., 2005b. Access of surface meltwater to beds of sub-freezing glaciers: preliminary insights. *Annals of Glaciology*, **40**, 8–14.

Amundson, J. M., Fahnestock, M., Truffer, M., Brown, J., Lüthi, M. P. & Motyka, R. J., 2010. Ice mélange dynamics and implications for terminus stability, Jakobshavn Isbræ, Greenland. *Journal of Geophysical Research (Earth Surface)*, **115**, F01005.

Amundson, J. M., Truffer, M., Lüthi, M. P., Fahnestock, M., West, M. & Motyka, R. J., 2008. Glacier, fjord, and seismic response to recent large calving events, Jakobshavn Isbræ, Greenland. *Geophysical Research Letters*, **35**, L22501.

Anandakrishnan, S. & Alley, R. B., 1997. Tidal forcing of basal seismicity of ice stream C, West Antarctica, observed far inland. *Journal of Geophysical Research*, **102**, 15183–15196.

Anandakrishnan, S., Voigt, D. E., Alley, R. B. & King, M. A., 2003. Ice stream D flow speed is strongly modulated by the tide beneath the Ross Ice Shelf. *Geophysical Research Letters*, **30**(7), 1361.

Andersen, M. L., 2010. *Surface melt, dynamics and seismicity at Helheim Glacier, East Greenland*. Ph.D. thesis, Faculty of Science, University of Copenhagen.

Andersen, M. L., Larsen, T., Nettles, M., Elosegui, P., van As, D., Hamilton, G. S., Stearns, L. A., Davis, J. L., Ahlstrøm, A. P., de Juan, J., Ekström, G., Stenseng, L., Khan, S. A., Forsberg, R. & Dahl-Jensen, D., 2010. Spatial and temporal melt variability at Helheim Glacier, East Greenland, and its effect on ice dynamics. *Journal of Geophysical Research*, **115**, F04041.

Bartholomaus, T. C., Anderson, R. S. & Anderson, S. P., 2008. Response of glacier basal motion to transient water storage. *Nature Geoscience*, **1**, 33–37.

Benn, D. I., Hulton, N. R. J. & Mottram, R. H., 2007a. 'Calving laws', 'sliding laws' and the stability of tidewater glaciers. *Annals of Glaciology*, **46**, 123–130.

Benn, D. I., Warren, C. R. & Mottram, R. H., 2007b. Calving processes and the dynamics of calving glaciers. *Earth Science Reviews*, **82**, 143–179.

Bevington, P. R., 1969. *Data reduction and error analysis for the physical sciences*. McGraw-Hill.

Bindoff, N. L., Willebrand, J., Artale, V., Cazenave, A., Gregory, J., Gulev, S., Hanawa, K., Quéré, C. L., Levitus, S., Nojiri, Y., Shum, C., Talley, L. & Unnikrishnan, A., 2007. *Observations: Oceanic Climate Change and Sea Level*. Cambridge University Press, Cambridge.

Bindschadler, R. A., King, M. A., Alley, R. B., Anandakrishnan, S. & Padman, L., 2003. Tidally Controlled Stick-Slip Discharge of a West Antarctic Ice Stream. *Science*, **301**, 1087–1090.

Chen, G., 1998. *GPS kinematic positioning for the airborne laser altimetry at Long Valley, California*. Ph.D. thesis, Massachusetts Institute of Technology, Cambridge, Mass.

Chen, J. L., Wilson, C. R. & Tapley, B. D., 2006. Satellite Gravity Measurements Confirm Accelerated Melting of Greenland Ice Sheet. *Science*, **313**, 1958–1960.

Choi, K., Bilich, A., Larson, K. M. & Axelrad, P., 2004. Modified sidereal filtering: Implications for high-rate GPS positioning. *Geophysical Research Letters*, **31**, L22608.

Das, S. B., Joughin, I., Behn, M. D., Howat, I. M., King, M. A., Lizarralde, D. & Bhatia, M. P., 2008. Fracture Propagation to the Base of the Greenland Ice Sheet During Supraglacial Lake Drainage. *Science*, **320**, 778–781.

Davis, C. H., Li, Y., McConnell, J. R., Frey, M. M. & Hanna, E., 2005. Snowfall-Driven Growth in East Antarctic Ice Sheet Mitigates Recent Sea-Level Rise. *Science*, **308**, 1898–1901.

Davis, J. L., 2010. Theoretical effects of error in the ocean-tide model on least-squares estimates of admittance. Tech. rep., Lamont-Doherty Earth Observatory, Columbia University (unpublished).

Davis, J. L., Elosegui, P., de Juan, J., Nettles, M., Ahlstrom, A., Andersen, M. L., Ekstrom, G., Forsberg, R., Hamilton, G., Khan, A., Larsen, T., Stearns, L. & Stenseng, L., 2008. Determining the Timing of Helheim Glacial

Earthquakes from Glacier-Based GPS Time Series. *AGU Fall Meeting Abstracts*, 89 (53).

Davis, J. L., Elosegui, P., Hamilton, G., Stearns, L., Langer, M., Nettles, M. K. & Larsen, T. B., 2007. Mechanisms for Tidally Induced Glacier Deformation and Flow Variations, East Greenland. *AGU Fall Meeting Abstracts*, 88 (52).

Davis, J. L., Herring, T. A., Shapiro, I. I., Rogers, A. E. E. & Elgered, G., 1985. Geodesy by radio interferometry - Effects of atmospheric modeling errors on estimates of baseline length. *Radio Science*, **20**, 1593–1607.

de Juan, J., Elosegui, P., Davis, J. L., Nettles, M. & Larsen, 2008a. Analysis of ionospheric errors and correction techniques in high-rate GPS glaciology. *EGU General Assembly 2008*, **10**, EGU2008–A–04190.

de Juan, J., Elosegui, P., Nettles, M., Davis, J. L., Larsen, T., Ahlstrøm, A., Andersen, M. L., Ekstrom, G., Forsberg, R., Hamilton, G. S., Khan, S. A., Schild, K. M., Stearns, L. A. & Stenseng, L., 2009a. Ocean tides modulation of flow at Helheim Glacier, East Greenland, observed using GPS. *AGU Fall Meeting Abstracts*, 90 (52).

de Juan, J., Elosegui, P., Nettles, M., Davis, J. L., Larsen, T., Hamilton, G. S. & Stearns, L. A., 2010a. GPS measurements of flow variations at a large Greenland outlet glacier due to ocean tidal forcing. *AGU Fall Meeting Abstracts*, A516.

de Juan, J., Elosegui, P., Nettles, M., Davis, J. L., Larsen, T. B., Ahlstrom, A. P., Andersen, M. L., Ekstrom, G., Forsberg, R., Hamilton, G. S., Khan, S. A., Schild, K., Stearns, L. A. & Stenseng, L., 2009b. Flow modulation by ocean tides at Helheim Glacier, East Greenland, observed using GPS. *EGU General Assembly 2009*, **11**, EGU2009–8329–3.

de Juan, J., Elósegui, P., Nettles, M., Davis, J. L., Larsen, T. B., Hamilton, G. S. & Stearns, L. A., in preparation(a). Ocean tides modulation of flow at Helheim Glacier, East Greenland, using high-rate GPS. *Journal of Geophysical Research*.

de Juan, J., Elósegui, P., Nettles, M., Davis, J. L., Larsen, T. B., Hamilton, G. S. & Stearns, L. A., in preparation(b). Flow variations at Helheim Glacier induced by the drainage of supraglacial lakes. *Journal of Glaciology*.

de Juan, J., Elosegui, P., Nettles, M., Larsen, T. B., Davis, J. L., Ahlstrøm, A. P., Andersen, M. L., Ekström, G., Forsberg, R., Hamilton, G. S., Khan, S. A., Schild, K. M., Stearns, L. A. & Stenseng, L., 2008b. Sub-daily glacier flow variations at Helheim Glacier, East Greenland, using GPS. *AGU Fall Meeting Abstracts*, 89 (53).

de Juan, J., Elósegui, P., Nettles, M., Larsen, T. B., Davis, J. L., Hamilton, G. S., Stearns, L. A., Andersen, M. L., Ekström, G., Ahlstrøm, A. P., Stenseng, L., Khan, S. A. & Forsberg, R., 2010b. Sudden increase in tidal response linked to calving and acceleration at a large Greenland outlet glacier. *Geophysical Research Letters*, **37**, L12501.

Dietrich, R., Maas, H., Baessler, M., Rülke, A., Richter, A., Schwalbe, E. & Westfeld, P., 2007. Jakobshavn Isbræ, West Greenland: Flow velocities and tidal interaction of the front area from 2004 field observations. *Journal of Geophysical Research (Earth Surface)*, **112**, F03S21.

Dupont, T. K. & Alley, R. B., 2005. Assessment of the importance of ice-shelf buttressing to ice-sheet flow. *Geophysical Research Letters*, **32**, L04503.

Eanes, R. J. & Bettadpur, S., 1995. The CSR 3.0 global ocean tide model. Tech. Rep. CSR-TM-95-06, Center for Space Research.

Echelmeyer, K., Clarke, T. S. & Harrison, W. D., 1991. Surficial glaciology of Jakobshavns Isbræ, West Greenland: Part I. Surface morphology. *Journal of Glaciology*, **37**, 368–382.

Egbert, G. D., Bennett, A. F. & Foreman, M. G. G., 1994. TOPEX/POSEIDON tides estimated using a global inverse model. *Journal of Geophysical Research*, **99**, 24821–24852.

Ekström, G., 2006. Global Detection and Location of Seismic Sources by Using Surface Waves. *The Bulletin of the Seismological Society of America*, **96**, 1201–1212.

Ekström, G., Nettles, M. & Abers, G. A., 2003. Glacial Earthquakes. *Science*, **302**, 622–624.

Ekström, G., Nettles, M. & Tsai, V. C., 2006. Seasonality and Increasing Frequency of Greenland Glacial Earthquakes. *Science*, **311**, 1756–1758.

Elgered, G., Davis, J. L., Herring, T. A. & Shapiro, I. I., 1991. Geodesy by radio interferometry - Water vapor radiometry for estimation of the wet delay. *Journal of Geophysical Research*, **96**, 6541–6555.

Elosegui, P., Davis, J. L., Jaldehag, R. K., Johansson, J. M., Niell, A. E. & Shapiro, I. I., 1995. Geodesy Using the Global Positioning System: The Effects of Signal Scattering. *Journal of Geophysical Research*, **100**, 9921–9934.

Elósegui, P., Davis, J. L., Johansson, J. M. & Shapiro, I. I., 1996. Detection of transient motions with the Global Positioning System. *Journal of Geophysical Research*, **101**, 11249–11262.

Elosegui, P., Nettles, M., Davis, J. L., Hamilton, G. S., Larsen, T. B. et al., 2008. Determining glacier flow with novel polar GPS systems. *AGU Fall Meeting Abstracts*, 89 (53).

Elosegui, P., Nettles, M., de Juan, J., Davis, J. L., Hamilton, G. S. & Larsen, T. B., 2009. An up-close examination of tidewater outlet-glacier flow and glacial earthquakes using GPS. *EGU General Assembly 2009, held 19-24 April, 2009 in Vienna, Austria*, **11**, EGU2009–8915–3.

Fountain, A. G., Jacobel, R. W., Schlichting, R. & Jansson, P., 2005. Fractures as the main pathways of water flow in temperate glaciers. *Nature*, **433**, 618–621.

Fountain, A. G. & Walder, J. S., 1998. Water flow through temperate glaciers. *Reviews of Geophysics*, **36**, 299–328.

Fowler, A. C., 1987. A theory of glacier surges. *Journal of Geophysical Research*, **92**, 9111–9120.

Gogineni, S., Tammana, D., Braaten, D., Leuschen, C., Akins, T., Legarsky, J., Kanagaratnam, P., Stiles, J., Allen, C. & Jezek, K., 2001. Coherent radar ice thickness measurements over the Greenland ice sheet. *Journal of Geophysical Research*, **106**, 33761–33772.

Gudmundsson, G. H., 2006. Fortnightly variations in the flow velocity of Rutford Ice Stream, West Antarctica. *Nature*, **444**, 1063–1064.

Gudmundsson, G. H., 2007. Tides and the flow of Rutford Ice Stream, West Antarctica. *Journal of Geophysical Research (Earth Surface)*, **112**, F04007.

Hamilton, G. S., Khan, S. A., Schild, K. M., Stearns, L. A., Nettles, M., Ahlstrøm, A. P., Andersen, M. L., Davis, J. L., Ekström, G., Elósegui, P., Forsberg, R., de Juan, J., Larsen, T. B. & Stenseng, L., 2008. Iceberg Calving and Flow Dynamics at Helheim Glacier, East Greenland, from Time-Lapse Photography. *AGU Fall Meeting Abstracts*, 89 (53).

Hamilton, G. S., Stearns, L. A., Elósegui, P., Davis, J. L., Nettles, M., Ahlstrøm, A. P., Khan, S. A., Langer, M., Stenseng, L., Ekström, G., Forsberg, R., Jørgensen, T. M. & Larsen, T. B., 2006. Tidal Modulation of Ice Flow on Kangerdlugssuaq and Helheim Glaciers, East Greenland, from High-Rate GPS Measurements. *AGU Fall Meeting Abstracts*, 87 (52).

Herring, T. A., 1992. Modeling atmospheric delays in the analysis of space geodetic data. *Proceedings of the Symposium on Refraction of Transatmospheric Signals in Geodesy*, **36**, 157–164.

Herring, T. A., King, R. W., McClusky, S. & King, M. A., 2008. Workshop on Processing and Analysis of GPS Data with GAMIT/GLOBK/TRACK.

Hofmann-Wellenhof, B., Lichtenegger, H. & Collins, J., 1994. *GPS: Theory and Practice*. Springer-Verlag Wien New York. 3rd Edition.

Holdsworth, G., 1969. Flexure of a floating ice tongue. *Journal of Glaciology*, **8**, 385–397.

Holland, D. M., Thomas, R. H., de Young, B., Ribergaard, M. H. & Lyberth, B., 2008. Acceleration of Jakobshavn Isbræ triggered by warm subsurface ocean waters. *Nature Geoscience*, **1**, 659–664.

Hooke, R. L., 2005. *Principles of Glacier Mechanics*. Cambridge University Press. 2nd Edition.

Hoque, M. M. & Jakowski, N., 2008. Estimate of higher order ionospheric errors in GNSS positioning. *Radio Science*, **43**, RS5008.

Howat, I. M., Joughin, I., Fahnestock, M., Smith, B. E. & Scambos, T. A., 2008. Synchronous retreat and acceleration of southeast Greenland outlet glaciers 2000-06: ice dynamics and coupling to climate. *Journal of Glaciology*, **54**, 646–660.

Howat, I. M., Joughin, I. & Scambos, T. A., 2007. Rapid Changes in Ice Discharge from Greenland Outlet Glaciers. *Science*, **315**, 1559–1561.

Howat, I. M., Joughin, I., Tulaczyk, S. & Gogineni, S., 2005. Rapid retreat and acceleration of Helheim Glacier, east Greenland. *Geophysical Research Letters*, **32**, L22502.

Iken, A., Röthlisberger, H., Flotron, A. & Haeberli, W., 1983. The uplift of Unteraargletscher at the beginning of the melt season – a consequence of water storage at the bed? *Journal of Glaciology*, **29**, 28–47.

Johannessen, O. M., Khvorostovsky, K., Miles, M. W. & Bobylev, L. P., 2005. Recent Ice-Sheet Growth in the Interior of Greenland. *Science*, **310**, 1013–1016.

Joughin, I., Abdalati, W. & Fahnestock, M., 2004. Large fluctuations in speed on Greenland's Jakobshavn Isbræ glacier. *Nature*, **432**, 608–610.

Joughin, I., Das, S. B., King, M. A., Smith, B. E., Howat, I. M. & Moon, T., 2008a. Seasonal Speedup Along the Western Flank of the Greenland Ice Sheet. *Science*, **320**, 781–783.

Joughin, I., Howat, I., Alley, R. B., Ekstrom, G., Fahnestock, M., Moon, T., Nettles, M., Truffer, M. & Tsai, V. C., 2008b. Ice-front variation and tidewater behavior on Helheim and Kangerdlugssuaq Glaciers, Greenland. *Journal of Geophysical Research (Earth Surface)*, **113**, F01004.

Joughin, I., Smith, B. E., Howat, I. M., Scambos, T. & Moon, T., 2010. Greenland flow variability from ice-sheet-wide velocity mapping. *Journal of Glaciology*, **56**, 415–430.

Kalman, R. E., 1960. A New Approach to Linear Filtering and Prediction Problems. *Transactions of the ASME-Journal of Basic Engineering*, **82**(Series D), 35–45.

Kamb, B., 1987. Glacier surge mechanism based on linked cavity configuration of the basal water conduit system. *Journal of Geophysical Research*, **92**, 9083–9100.

Kamb, B., Raymond, C. F., Harrison, W. D., Engelhardt, H., Echelmeyer, K. A., Humphrey, N., Brugman, M. M. & Pfeffer, T., 1985. Glacier Surge Mechanism: 1982-1983 Surge of Variegated Glacier, Alaska. *Science*, **227**, 469–479.

King, M. A., Murray, T. & Smith, A. M., 2010. Non-linear responses of Rutford Ice Stream, Antarctica, to semi-diurnal and diurnal tidal forcing. *Journal of Glaciology*, **56**, 167–176.

Krabill, W., Hanna, E., Huybrechts, P., Abdalati, W., Cappelen, J., Csatho, B., Frederick, E., Manizade, S., Martin, C., Sonntag, J., Swift, R., Thomas, R. & Yungel, J., 2004. Greenland Ice Sheet: Increased coastal thinning. *Geophysical Research Letters*, **31**, L24402.

Lemke, P., Ren, J., Alley, R. B., Allison, I., Carrasco, J., Flato, G., Fujii, Y., Kaser, G., Mote, P., Thomas, R. H. & Zhang, T., 2007. *Observations: changes in snow, ice and frozen ground*. Cambridge University Press, Cambridge.

Lingle, C. S., Hughes, T. J. & Kollmeyer, R. C., 1981. Tidal flexure of Jakobshavns Glacier, West Greenland. *Journal of Geophysical Research*, **86**, 3960–3968.

Luckman, A. & Murray, T., 2005. Seasonal variation in velocity before retreat of Jakobshavn Isbræ, Greenland. *Geophysical Research Letters*, **32**, L08501.

Luckman, A., Murray, T., de Lange, R. & Hanna, E., 2006. Rapid and synchronous ice-dynamic changes in East Greenland. *Geophysical Research Letters*, **33**, L03503.

Marini, J. W., 1972. Correction of satellite tracking data for an arbitrary tropospheric profile. *Radio Science*, **7**, 223–231.

Meier, M. F. & Post, A., 1987. Fast tidewater glaciers. *Journal of Geophysical Research*, **92**, 9051–9058.

Milne, G. A., Gehrels, W. R., Hughes, C. W. & Tamisiea, M. E., 2009. Identifying the causes of sea-level change. *Nature Geoscience*, **2**, 471–478.

Moon, T. & Joughin, I., 2008. Changes in ice front position on Greenland's outlet glaciers from 1992 to 2007. *Journal of Geophysical Research (Earth Surface)*, **113**, F02022.

Motyka, R. J., Hunter, L., Echelmeyer, K. A. & Connor, C., 2003. Submarine melting at the terminus of a temperate tidewater glacier, LeConte Glacier, Alaska, U.S.A. *Annals of Glaciology*, **36**, 57–65.

Murray, T., Scharrer, K., James, T. D., Dye, S. R., Hanna, E., Booth, A. D., Selmes, N., Luckman, A., Hughes, A. L. C., Cook, S. & Huybrechts, P., 2010. Ocean regulation hypothesis for glacier dynamics in southeast Greenland and implications for ice sheet mass changes. *J. Geophys. Res.*, **115**(F3).

Murray, T., Smith, A. M., King, M. A. & Weedon, G. P., 2007. Ice flow modulated by tides at up to annual periods at Rutford Ice Stream, West Antarctica. *Geophysical Research Letters*, **34**, L18503.

Nettles, M., Ahlstrøm, A. P., Elósegui, P., Hamilton, G. S., Khan, S. A., Andersen, M. L., Stearns, L. A., Stenseng, L., Davis, J. L., Ekström, G., Forsberg, R.and Jørgensen, T. & Larsen, T. B., 2006. Helheim 2006: Integrated geophysical observations of glacier flow. *AGU Fall Meeting Abstracts*, 87 (42).

Nettles, M. & Ekström, G., 2010. Glacial Earthquakes in Greenland and Antarctica. *Annual Review of Earth and Planetary Sciences*, **38**, 467–491.

Nettles, M., Larsen, T. B., Elósegui, P., Hamilton, G. S., Stearns, L. A., Ahlstrøm, A. P., Davis, J. L., Andersen, M. L., de Juan, J., Khan, S. A., Stenseng, L., Ekström, G. & Forsberg, R., 2008. Step-wise changes in glacier flow speed coincide with calving and glacial earthquakes at Helheim Glacier, Greenland. *Geophysical Research Letters*, **35**, L24503.

Nick, F. M., van der Veen, C. J., Vieli, A. & Benn, D. I., 2010. A physically based calving model applied to marine outlet glaciers and implications for the glacier dynamics. *Journal of Glaciology*, **56**, 781–794.

Nick, F. M., Vieli, A., Howat, I. M. & Joughin, I., 2009. Large-scale changes in Greenland outlet glacier dynamics triggered at the terminus. *Nature Geoscience*, **2**, 110–114.

Niell, A. E., 1996. Global mapping functions for the atmosphere delay at radio wavelengths. *Journal of Geophysical Research*, **101**, 3227–3246.

Otero, J., Navarro, F. J., Martin, C., Cuadrado, M. L. & Corcuera, M. I., 2010. A three-dimensional calving model: numerical experiments on Johnsons Glacier, Livingston Island, Antarctica. *Journal of Glaciology*, **56**, 200–214.

Padman, L. & Erofeeva, S., 2004. A barotropic inverse tidal model for the Arctic Ocean. *Geophysical Research Letters*, **31**, L02303.

Park, K., Elósegui, P., Davis, J. L., Jarlemark, P. O. J., Corey, B. E., Niell, A. E., Normandeau, J. E., Meertens, C. E. & Andreatta, V. A., 2004. Development of an antenna and multipath calibration system for Global Positioning System sites. *Radio Science*, **39**, RS5002.

Paterson, W. S. B., 1994. *The Physics of Glaciers*. Elsevier. 3rd Edition.

Payne, A. J., Vieli, A., Shepherd, A. P., Wingham, D. J. & Rignot, E., 2004. Recent dramatic thinning of largest West Antarctic ice stream triggered by oceans. *Geophysical Research Letters*, **31**, L23401.

Reeh, N., Lintz Christensen, E., Mayer, C. & Olesen, O. B., 2003. Tidal bending of glaciers: a linear viscoelastic approach. *Annals of Glaciology*, **37**, 83–89.

Reeh, N., Mayer, C., Olesen, O. B., Lintz Christensen, E. & Højmark Thomsen, H., 2000. Tidal movement of Nioghalvfjerdsfjorden glacier, northeast Greenland: observations and modelling. *Annals of Glaciology*, **31**, 111–117.

Rignot, E., Box, J. E., Burgess, E. & Hanna, E., 2008. Mass balance of the Greenland ice sheet from 1958 to 2007. *Geophysical Research Letters*, **35**, L20502.

Rignot, E., Casassa, G., Gogineni, P., Krabill, W., Rivera, A. & Thomas, R., 2004. Accelerated ice discharge from the Antarctic Peninsula following the collapse of Larsen B ice shelf. *Geophysical Research Letters*, **31**, L18401.

Rignot, E. & Kanagaratnam, P., 2006. Changes in the Velocity Structure of the Greenland Ice Sheet. *Science*, **311**, 986–990.

Rignot, E., Koppes, M. & Velicogna, I., 2010. Rapid submarine melting of the calving faces of West Greenland glaciers. *Nature Geoscience*, **3**, 187–191.

Röthlisberger, H., 1972. Water pressure in intra- and subglacial channels. *Journal of Glaciology*, **11**, 177–203.

Saastamoinen, J., 1972. Contributions to the theory of atmospheric refraction. *Bulletin Geodesique*, **46**, 279–298.

Scambos, T. A., Bohlander, J. A., Shuman, C. A. & Skvarca, P., 2004. Glacier acceleration and thinning after ice shelf collapse in the Larsen B embayment, Antarctica. *Geophysical Research Letters*, **31**, L18402.

Schmid, R., Mader, G. & Herring, T., 2005. From relative to absolute antenna phase center corrections, in Celebrating a Decade of the International GPS Service. In M. Meindl, ed., *Workshop and Symposium 2004*, 209– 221. Astron. Inst., Univ. of Berne, Berne, Switzerland.

Schoof, C., 2010. Ice-sheet acceleration driven by melt supply variability. *Nature*, **468**, 803–806.

Sneed, W. A. & Hamilton, G. S., 2007. Evolution of melt pond volume on the surface of the Greenland Ice Sheet. *Geophysical Research Letters*, **34**, L03501.

Sohn, H., Jezek, K. C. & van der Veen, C. J., 1998. Jakobshavn Glacier, West Greenland: 30 years of spaceborne observations. *Geophysical Research Letters*, **25**, 2699–2702.

Stearns, L. A. & Hamilton, G. S., 2007. Rapid volume loss from two East Greenland outlet glaciers quantified using repeat stereo satellite imagery. *Geophysical Research Letters*, **34**, L05503.

Stearns, L. A., Hamilton, G. S. & Reeh, N., 2005. Multi-decadal record of ice dynamics on Daugaard Jensen Gletscher, East Greenland, from satellite imagery and terrestrial measurements. *Annals of Glaciology*, **42**, 53–58.

Straneo, F., Hamilton, G. S., Sutherland, D. A., Stearns, L. A., Davidson, F., Hammill, M. O., Stenson, G. B. & Rosing-Asvid, A., 2010. Rapid circulation of warm subtropical waters in a major glacial fjord in East Greenland. *Nature Geoscience*, **3**, 182–186.

Teunissen, P. J. G. & Kleusberd, A., 1998. *GPS for Geodesy*. Springer. 2nd Edition.

Thomas, H. R., 2004. Force-perturbation analysis of recent thinning and acceleration of Jakobshavn Isbrae, Greenland. *Journal of Glaciology*, **50**, 57–66.

Thomas, R. H., 2007. Tide-induced perturbations of glacier velocities. *Global and Planetary Change*, **59**, 217–224.

Thomas, R. H., Abdalati, W., Frederick, E., Krabill, W. B., Manizade, S. & Steffen, K., 2003. Investigation of surface melting and dynamic thinning on Jakobshavn Isbrae, Greenland. *Journal of Glaciology*, **49**, 231–239.

Thompson, A. R., Moran, J. M. & Swenson, G. W., 1986. *Interferometry and synthesis in radio astronomy*. Wiley-Interscience, New York.

Tsai, V. C. & Ekström, G., 2007. Analysis of glacial earthquakes. *Journal of Geophysical Research (Earth Surface)*, **112**, F03S22.

Tsai, V. C., Rice, J. R. & Fahnestock, M., 2008. Possible mechanisms for glacial earthquakes. *Journal of Geophysical Research (Earth Surface)*, **113**, F03014.

van de Wal, R. S. W., Boot, W., van den Broeke, M. R., Smeets, C. J. P. P., Reijmer, C. H., Donker, J. J. A. & Oerlemans, J., 2008. Large and Rapid Melt-Induced Velocity Changes in the Ablation Zone of the Greenland Ice Sheet. *Science*, **321**, 111–113.

van der Veen, C. J., 1996. Tidewater calving. *Journal of Glaciology*, **42**, 375–385.

van der Veen, C. J., 2007. Fracture propagation as means of rapidly transferring surface meltwater to the base of glaciers. *Geophysical Research Letters*, **34**, L01501.

Vaughan, D. G., 1995. Tidal flexure at ice shelf margins. *Journal of Geophysical Research*, **100**, 6213–6224.

Velicogna, I., 2009. Increasing rates of ice mass loss from the Greenland and Antarctic ice sheets revealed by GRACE. *Geophysical Research Letters*, **36**, L19503.

Velicogna, I. & Wahr, J., 2006. Measurements of Time-Variable Gravity Show Mass Loss in Antarctica. *Science*, **311**, 1754–1756.

Walters, R. A. & Dunlap, W. W., 1987. Analysis of time series of glacier speed: Columbia Glacier, Alaska. *Journal of Geophysical Research*, **92**, 8969–8975.

Wiens, D. A., Anandakrishnan, S., Winberry, J. P. & King, M. A., 2008. Simultaneous teleseismic and geodetic observations of the stick-slip motion of an Antarctic ice stream. *Nature*, **453**, 770–774.

Zwally, H. J., Abdalati, W., Herring, T., Larson, K., Saba, J. & Steffen, K., 2002. Surface Melt-Induced Acceleration of Greenland Ice-Sheet Flow. *Science*, **297**, 218–222.